Advanced Treatment Methods of Melanoidin for the Effective Remediation of Distillery Spentwash

A

Thesis Submitted

In Fulfilment of the Requirements

for the degree of

DOCTOR OF PHILOSOPHY

by

Rahul Verma

(Roll no. 166152005)

Under the supervision of

Prof. Lalit Mohan Pandey & Prof. Lal Mohan Kundu

February - 2023

Centre for the Environment

Indian Institute of Technology Guwahati

Guwahati-781039, Assam, India

Dedicated

To

My Family

INDIAN INSTITUTE OF TECHNOLOGY GUWAHATI

भारतीय प्रौद्योगिकी संस्थान गुवाहाटी

Center for the environment, Guwahati 781039, Assam, India

पर्यावरण केंद्र, गुवाहाटी 781039, असम, भारत

DECLARATION

It is to declare that the content embodied in this thesis entitled **"Advanced Treatment Methods of Melanoidin for the Effective Remediation of Distillery Spentwash"** is the result of investigations carried out by me at the **Centre for the Environment, Indian Institute of Technology, Guwahati, Assam, India** under the supervision of **Prof. Lalit Mohan Pandey** & **Prof. Lal Mohan Kundu** for the award of the **Doctor of Philosophy**. The work has not been submitted elsewhere for any degree or diploma of any institute or university. I wish to state that to the best of my knowledge and undertaking nothing in this report amounts to plagiarism.

In keeping with the general practice of reporting scientific observations, due acknowledgments have been made wherever the work described is based on the findings of other investigators.

Date: 15th February 2023

RAHUL VERMA

Centre for the Environment

Indian Institute of Technology, Guwahati

Guwahati – 781039, Assam, India

INDIAN INSTITUTE OF TECHNOLOGY GUWAHATI

भारतीय प्रौद्योगिकी संस्थान गुवाहाटी

Center for the environment, Guwahati 781039, Assam, India

पर्यावरण केंद्र, गुवाहाटी 781039, असम, भारत

CERTIFICATE

This is to certify that the thesis entitled **"Advanced Treatment Methods of Melanoidin for the Effective Remediation of Distillery Spent Wash"** submitted by **Mr. Rahul Verma (Roll No.: 166152005)** for the award of the **degree of Doctor of Philosophy,** is an authentic record of results obtained from the research work carried out under the supervision and guidance at the **Centre for the Environment, Indian Institute of Technology Guwahati, Assam, India.** The thesis has fulfilled all requirements as per the regulations of the Institute and has reached the standard required for submission. The work documented in this thesis has not been submitted to any other University or Institute for the award of any degree.

Thesis Supervisor

Prof. Lalit Mohan Pandey
Professor
Department of Bioscience and Bioengineering
IIT Guwahati
Guwahati – 781039
Assam, India

Thesis Co-supervisor

Prof. Lal Mohan Kundu
Professor
Department of Chemistry
IIT Guwahati
Guwahati – 781039
Assam, India

ACKNOWLEDGEMENT

First and foremost, I am the most profound gratitude to my Ph.D. supervisors, **Prof. Lalit Mohan Pandey** and **Prof. Lal Mohan Kundu** for believing in me and providing me the opportunity to work on such an excellent topic. I am very much inspired by their rich experience and knowledge and approach to problems, immense patience, and extreme care. They have taught me, both consciously and unconsciously, the importance of hard work and patience. I am highly obligated to them for their persistent devotion and willingness. I could not have imagined having a better advisor and mentor than them. I enjoyed every moment of working under their supervision and learned many things from them. It is truly a dream come true for me to have them as supervisors.

I would like to thank my Doctoral Committee members, **Prof. Senthilkumar Sivaprakasam (committee chairman)** from the Department of Biosciences and Bioengineering, **Prof. Chandan Das** from the Department of Chemical Engineering and **Prof. Shyam Prosad Biswas** from the Department of Chemistry for their research-oriented teaching, which helped me during my Ph.D. I take this opportunity to thank all the faculty members for their valuable suggestions and cooperation during my course work.

I would like to thank former Director **Prof. Gautam Biswas** and current Director **Prof T. G. Sitharam**, IITG, for providing the necessary facilities and a conducive academic environment.

I am highly obliged to the **Centre for The Environment**, Indian Institute of Technology Guwahati, for giving me this opportunity to be a part of this prestigious Institution. I am extremely grateful to the former Heads of the Centre for The Environment **Prof. Vikas Kumar Dubey**, **Prof. Mihir Kumar Purkait** and current Head **Prof. Utpal Bora**, all faculty members, scientific officer **Dr. Deepmoni Deka**, technical staffs **Mr. Partha Protim Bakal**, **Mr. Rajiv Kumar Gogoi**, **Mr. Kaustubh Rakshit** and **Mr. Mridul Das** for their kind co-operation during the entire course of my research period. My acknowledgment also goes to the **Ministry of Human Resource Development (MHRD)**, India for financial support throughout my research tenure.

I am very thankful to the **Central Instrument Facility (CIF)** of the Indian Institute of Technology Guwahati for allowing me to conduct my analyses using various sophisticated

instruments such as NMR, BET, LC-MS, TGA, MALDI-ToF, FETEM and FESEM-EDX which has been very important in this research work. In this regard, I would like to acknowledge all the members of CIF for their assistance. I am gratified to the Department of **Biosciences and Bioengineering (BSBE)** at the Indian Institute of Technology Guwahati for allowing me to analyze the samples for surface tension measurements, reactor operations and contact angle measurements. My acknowledgment goes to the **Department of Chemical Engineering** of the Indian Institute of Technology Guwahati for allowing me to powder UV, BET and TGA analysis.

I would like to acknowledge **DCM Shriram Ltd, a sugar cane molasses-based distillery plant in Hardoi, India,** to prove the sugar-cane molasses and industrial-based real spentwash samples.

I also extend my special thanks to my seniors **Dr. Abshar Hasan**, **Dr. Poulami Datta**, and **Dr. Varun Saxena** for their guidance in the initial days of my research. They helped me by providing the proforma of annual progress reports, synopsis reports and various presentations. I appreciate the efforts of my lab-mates **Ms. Swati**, **Ms. Gayatri**, **Mr. Aquib**, **Mr. Aman**, **Mr. Rushikesh**, **Mr. Vivek**, **Mr. Anurag**, **Ms. Mehak**, **Mr. Gyan**, **Mr. Ravi** and **Mr. Mohit** from the **Biointerface and Environmental Engineering (BIEEL) laboratory**.

I express my gratitude towards my seniors and lab mates in the Centre for the Environment, **Dr. Gopi Kiran**, **Dr. Lalit Goswami**, **Dr. Nanendra Naik**, **Dr. Papu Kumar Naik**, **Dr. Kamalesh Verma**, **Dr. Smruti Ranjan Dash**, **Dr. Paulomi Bose**, **Dr. Sayanti Ghosh**, **Mr. Smonath Chanda**, **Mr. Rajneesh Kumar**, **Mr. Tanmay Dutta**, **Mr. Prithwi Chayan Chatterjee**, **Mr. Abhishek Singh**, **Mr. Prabhat Kumar Patel**. **Ms. Jinat Aktar**, **Mrs. Jyoti Kainthola**, **Ms. Nivedhitha S**, **Ms. Payal Mazumder**, **Ms. Deepa Sachan**, **Mrs. Deepti Nair** and all members for providing me technical and moral support and all the laughs and joyful moments.

My special thanks to **Ms. Swati Sharma**, **Dr. Poulami Datta** and **Dr. Papu Kumar Naik** who helped me a lot during the research work.

Finally, I would like to express my sincere gratitude to my family, father **Sri Ram Baran Verma**, mother **Smt. Kalavati Devi**, sisters **Sita Verma, Anita Verma** and Brother **Anurag Verma**. Whose blessings and never-ending support are the real stimulus that constantly inspires me to do my best. Last but not least, my deepest gratitude goes to my wife, **Mrs. Jyoti Kumari Mahato** for her

constant encouragement, endless sacrifices and patience, sincere prayers, continuous support, and motivation to complete this thesis work.

I would like to thank all the people who contributed in some way to the work described in this thesis and supported me in completing my Ph.D. Working on this Ph.D. has been an unforgettable experience for me and it would not be possible without these people.

Above all, I would like to thank the "**Almighty GOD**" for blessing me and providing me the unseen moral support that directed me through my good as well as hard times.

Rahul Verma

Abstract

The melanoidin-containing wastewater, particularly distillery spentwash possesses very high loads of chemical oxygen demand (COD) and other organic and inorganic pollutants. The discharge of this dark brown colour wastewater to water bodies results in eutrophication, reduction of dissolved oxygen level, obstruction of sunlight penetration, inhibition of photosynthesis of aquatic plants and groundwater contamination. The treatment efficacies of the conventional methods are quite low due to the poor biodegradability of melanoidin. In this regard, the present study explores adsorption, advanced oxidation process, and photocatalysis to remove melanoidin from wastewater. In addition, the bioprocessing of molasses to produce alternative metabolite biosurfactants has been investigated to decrease the pollution load of wastewater. Chapter 1 and chapter 2 demonstrate the introduction and literature review on melanoidin removal in distillery spentwash.

In chapter 3, low-cost bio-sorbents were prepared from different plant sources and further amine-modified by forming self-assembled monolayers (SAMs). The experimental parameters like temperature, pH and adsorbent doses have been optimized by RSM-CCD for the maximum removal of melanoidin. Amine-modified *Phyllanthus emblica* leaf resulted in the maximum adsorption of melanoidin (616 mg g^{-1}). These adsorbents were tested for reusability and retained their adsorption capacity up to the 5^{th} consecutive adsorption/desorption cycle.

In chapter 4, the photochemical degradation of melanoidin has been investigated by the photo-Fenton process. The experimental parameters such as temperature, time, H_2O_2 and Fe concentrations were optimized. At the optimized condition (34°C, 117 min, 158 mM of H_2O_2 and 0.74 mM of Fe), the 99 ± 1 % degradation of 1 % w/v of melanoidin solution was observed along with 88 ± 2 % of COD reduction.

Chapter 5 investigates the photocatalytic degradation of melanoidin using different photocatalysts such as ZnO, TiO_2, Fe doped ZnO (FZO) and WO_3. The FZO and synthesized WO_3 nanoparticles were investigated with excellent results under UV light and visible light illumination, respectively, for melanoidin degradation. The FZO showed 98 ± 0.5 % and 85 ± 2 % of melanoidin and COD reduction, respectively of 1 % (w/v) of initial melanoidin concentration at the optimized conditions: 34 °C, contact time of 117 min, 163 mM of H_2O_2 and 261 ppm of FZO. Similarly, the WO_3 showed 99 ± 1 % of colour and 93 ± 1 % of COD reductions, at 0.5 % (w/v) of initial melanoidin concentration under the optimized conditions. These photocatalysts also displayed complete degradation of 4 % (v/v) of real spentwash and excellent reusability for multiple cycles.

In the last chapter (Chapter 6), microbial utilization of molasses has been investigated to produce biosurfactants using an isolated inherent microbe *Bacillus subtilis* RSL-2. At the optimized conditions, a large biosurfactant concentration of 12.34 ± 0.1 g L^{-1} was obtained. The produced biosurfactant was identified to be lipopeptide in nature. Further, a reactor study was performed in a 5 L bioreactor, and the biosurfactant concentration was enhanced to 13.92 g L^{-1}. The produced wastewater had 75 to 80 times lower COD value as compared to distillery spentwash.

Table of Contents

	List of Tables	(x)
	List of Figures	(xiii)
	Abbreviations	(xviii)
	Symbols	(xxi)
Chapter 1	**Introduction**	1
1.1	Objectives	3
1.2	Thesis outline	4
Chapter 2	**Literature Review**	6
2.1	Introduction	7
2.2	Distilleries in India, process description for ethanol production and waste generation	7
2.3	Characteristics of distillery effluent	9
2.4	Distillery effluent treatment technologies	10
2.5	Conclusions	44
Chapter 3	Melanoidin removal by biosorption using low-cost and biogenic adsorbents	46
3.1	Introduction	46
3.2	Materials and methods	49
3.3	Results and discussion	56
3.4	Conclusions	95
Chapter 4	Treatment of melanoidin and real spentwash samples using advanced oxidation processes	96
4.1	Introduction	97
4.2	Materials and methods	98
4.3	Results and discussion	102
4.4	Conclusions	122
Chapter 5	Photocatalytic degradation of melanoidin under UV/Visible light illumination	123

5.1	Introduction	124
5.2	Materials and methods	127
5.3	Results and discussion	134
5.4	Conclusions	175
Chapter 6	Exploring molasses as a sole nutrient for the production of alternative metabolite biosurfactants	177
6.1	Introduction	178
6.2	Materials and methods	180
6.3	Characterization of biosurfactant	186
6.4	Results and discussion	189
6.5	Conclusions	217
Chapter 7	Overall conclusion and future scope	219
7.1	Overall conclusion	219
7.2	Future Scope	220
	Appendices	224
	References	240
	Research output	263

List of Tables

Table No.	Title	Page no
Table 2.1	General characteristics of untreated raw distillery spentwash	10
Table 2.2	Performances of various AOPs along with energy requirements	25
Table 2.3	Literature review of photocatalytic degradation of distillery effluents	28
Table 2.4	A detailed list of bacteria, fungi, and yeast tried for decolorization of distilled effluent	33-34
Table 2.5	List of reactors used for decolorization of distillery effluent	39
Table 2.6	Comparisons study of different treatment methods of distillery wastewater	44
Table 3.1	Isotherm/kinetic/thermodynamic models, linear expression forms, and their plots	54
Table 3.2	Experimental and predicted values of melanoidin decolourization at different experimental set-ups of independent variables for amine-modified PELP, CLLP and TILP (Temperature, pH and adsorbent concentration) in RSM-CCD	63-65
Table 3.3	Comparison of correlation coefficient value (R^2) and significance of the ANOVA model by the lesser p-value and higher F-value for amine-modified PELP, CLLP and TILP	66
Table 3.4	ANOVA table of quadratic models for PELP, CLLP and TILP	66-67
Table 3.5	Comparison of Langmuir, Freundlich, Temkin and D-R isotherm models for the sorption of melanoidin on amine-modified PELP, CLLP and TILP	74
Table 3.6	Different adsorbents used for melanoidin removal and their maximum adsorption capacity	76
Table 3.7	Comparison of kinetic studies of melanoidin adsorption on modified PELP, CLLP and TILP	82
Table 3.8	Comparison of intraparticle diffusion analysis of amine-modified PELP, CLLP and TILP	82

Table 3.9	Thermodynamic parameters for melanoidin adsorption on amine-modified leaves	85
Table 3.10	Elemental analysis (wt %) of amine-modified PELP, CLLP and TILP before and after adsorption of melanoidin	92
Table 3.11	Comparison study of COD and colour reduction of melanoidin and real spentwash samples by amine-modified PELP, CLLP and TILP	93
Table 4.1	Expressions of the kinetic and thermodynamic models used to fit the experimental data	102
Table 4.2	The experimental set-ups of four independent variables along with actual and predicted response values	105
Table 4.3	ANOVA table of quadratic model for melanoidin degradation	106
Table 4.4	The kinetic parameters obtained by fitting the experimental data to the first-order kinetic model at different conditions of the photo-Fenton process	112
Table 4.5	Thermodynamic investigation of melanoidin degradation and its characteristics under RSM-optimized conditions	113
Table 4.6	Comparison of the current study and experimental circumstances with several types of wastewater treated by the photo-Fenton procedure	118-121
Table 5.1	Independent Variables and their ranges were scrutinized in the RSM-CCD design	131
Table 5.2	Plots for graphical representations of the kinetic and thermodynamic models	132
Table 5.3	Kinetic parameters of melanoidin degradation using WO_3 photocatalyst at the optimized conditions along with control experiments in the dark	161
Table 5.4	Thermodynamic parameters during melanoidin degradation using WO_3 photocatalyst at the optimized conditions	161
Table 5.5	The kinetic parameters for photocatalytic degradation of melanoidin using FZO at optimized conditions along with control experiments	169

Table 5.6	Thermodynamic parameters for photocatalytic degradation of melanoidin using FZO at optimized conditions	169
Table 5.7	Comparison of relevant studies for decolorization and COD reduction of melanoidin containing wastewater	174
Table 6.1	Experimental and predicted values of ST, biosurfactant concentration and biomass with respect to independent variables (pH, temperature and molasses concentration) in RSM-CCD runs	191
Table 6.2	Quadratic model fitting to the experimental parameters with ANOVA analysis	193
Table 6.3	List of biosurfactant production ability of *Bacillus sp*. using molasses as whole substrate/C source	197
Table 6.4	Comparison of the ability of selected bacterial strains to utilize molasses as the sole nutrient source in 3 different growth modes	201
Table 6.5	Various studies utilizing molasses for the production of biosurfactants	207

LIST OF FIGURES

Figure No	Title	Page no
Figure 2.1	Steps of alcohol production and spentwash generation	8
Figure 2.2	Adsorption on the surface of an adsorbent	12
Figure 2.3	Classifications of AOPs	15
Figure 2.4	Mechanism of wet air oxidation (WAO) process	19
Figure 2.5	WAO of biomethanated distillery wastewater	20
Figure 2.6	Advanced oxidation process and the degradation processes of organic pollutants	23
Figure 3.1	FTIR spectra of unmodified and amine-modified PELP, CLLP and TILP	57-58
Figure 3.2	Thermostability analysis of amine-modified PELP, CLLP and TILP	59-60
Figure 3.3	3D response surface plots of amine-modified PELP, CLLP and TILP for the melanoidin adsorption considering their independent parameters as temperature, pH and concentration of adsorbent	68-69
Figure 3.4	FESEM images of modified PELP, CLLP and TILP; before and after adsorption of melanoidin	70-71
Figure 3.5	Fitting and comparison of Langmuir, Freundlich, Temkin and D-R isotherm models of melanoidin adsorption with experimental data of amine-modified PELP	75
Figure 3.6	Kinetic model fitting of experimental data for the melanoidin adsorption and comparison with Pseudo-first-order, Pseudo-second-order and Elovich isotherm models and their parameters	78
Figure 3.7	Fitting of intraparticle diffusion kinetic model to experimental data of the melanoidin adsorption on modified PELP, CLLP and TILP indicating rapid adsorption and intraparticle diffusion	79-80
Figure 3.8	Decolorization of melanoidin at optimized condition by PELP, CLLP and TILP before and after amine-modification at their respective RSM optimized conditions	81

Figure 3.9	Thermodynamic analysis of melanoidin adsorption on amine-modified PELP, CLLP and TILP	84
Figure 3.10	Adsorption-desorption efficiency of modified PELP, CLLP and TILP up to 5th consecutive cycles	86
Figure 3.11	Analysis of adsorption mechanism through FTIR spectra on PELP, CLLP and TILP	87-88
Figure 3.12	Zeta potential values of melanoidin, unmodified and modified PELP, CLLP and TILP at different pH	90-91
Figure 3.13	The difference in the colour of samples before and after the adsorption of spentwash and melanoidin by amine-modified PELP, CLLP and TILP at optimized conditions	94
Figure 4.1	Photo-Fenton reactor equipped with UV light source	99
Figure 4.2	3D response surface plots with their respective independent variables to maximize the degradation of melanoidin by photo-Fenton process	107
Figure 4.3	Degradation of melanoidin and COD reduction at RSM-optimized conditions	108
Figure 4.4	Comparison of melanoidin degradation (%) estimated through HPLC and UV-Spectrophotometer methods	108
Figure 4.5	Consequence of solution pH on melanoidin degradation at photo-Fenton optimized condition	109
Figure 4.6	The fitting of first-order kinetic models of experimental data obtained at the optimized conditions	111
Figure 4.7	Thermodynamic investigation of melanoidin degradation at RSM-optimized conditions	113
Figure 4.8	Change in concentrations of Fe, Fe(II), Fe(III) ions and pH of the solution during the melanoidin degradation process	115
Figure 4.9	Performance of optimized photo-Fenton conditions on actual spentwash samples	117
Figure 5.1	UV–vis diffused reflectance spectra and Bandgap calculation by the Tauc's plot of different nanoparticles	135

Figure 5.2	XRD spectra of synthesized WO_3 nanoparticles calcinated at different temperatures along with the reference WO_3 sample	137
Figure 5.3	FTIR spectra of reference WO_3 and synthesized WO_3 nanoparticles at different calcined temperatures	139
Figure 5.4	Raman spectra of synthesized WO_3 nanoparticles calcined at different temperatures	140
Figure 5.5	FETEM micrographs of synthesized WO_3@700 ℃ nanoparticles	142
Figure 5.6	FESEM images of (A) Reference WO_3 and synthesized WO_3 calcinated at (B) 300 ℃, (C) 500 ℃, (D) 700 ℃ and (E) 900 ℃.	143
Figure 5.7	Energy-dispersive X-ray spectroscopy of (A) Reference WO_3 sample and (B) Synthesized WO_3@700 ℃ sample	144
Figure 5.8	Zeta potential values of WO_3 photocatalysts and melanoidin at different pH values. The surface charge of WO_3 photocatalysts was found to be -21 ± 1 mV confirming its colloidal stability. The point of zero charge (pzc) of melanoidin was estimated as 6.9	145
Figure 5.9	XRD spectra of synthesized FZO nanoparticles confirm the formation of the desired nano-assembly	146
Figure 5.10	FTIR spectra of synthesized FZO nanoparticles	147
Figure 5.11	Raman spectra of synthesized FZO nanoparticles	148
Figure 5.12	FETEM images of (A-B) synthesized FZO nanoparticles, (C) Atomic crystal planes and (D) SAED pattern	149
Figure 5.13	FESEM image of synthesized FZO nanoparticles	150
Figure 5.14	Energy-dispersive X-ray spectroscopy of synthesized FZO sample	150
Figure 5.15	Zeta potential values of FZO photocatalysts and melanoidin at different pH values	151
Figure 5.16	Effect of initial melanoidin concentrations and calcination temperature of WO_3 on melanoidin degradation	153
Figure 5.17	Degradation of the melanoidin and COD reduction at RSM optimized conditions by WO_3	155
Figure 5.18	Comparison of melanoidin degradation using HPLC analysis and UV-Spectrophotometer	156

Figure 5.19	Effects of solution pH on the melanoidin degradation using WO_3 photocatalyst at the optimized conditions	157
Figure 5.20	Degradation kinetics of melanoidin at optimized conditions WO_3	159
Figure 5.21	Thermodynamic analysis of melanoidin degradation using WO_3 photocatalyst at the optimized conditions	160
Figure 5.22	Degradation of the melanoidin and COD reduction at RSM optimized condition of FZO	163
Figure 5.23	Comparison of melanoidin degradation using HPLC and UC-Spectrophotometer analysis at optimized conditions of FZO	164
Figure 5.24	Effect of solution pH on photocatalytic degradation of melanoidin using FZO at the optimized conditions	165
Figure 5.25	The photocatalytic degradation kinetics of melanoidin using FZO under UV irradiation at optimized conditions	167
Figure 5.26	Thermodynamic analysis during photocatalytic degradation of melanoidin using FZO at optimized conditions	168
Figure 5.27	Reusability study of synthesized WO_3 nanoparticles	170
Figure 5.28	Schematic diagram of the photocatalytic mechanism for melanoidin degradation	171
Figure 5.29	Application of the developed combinations of WO_3/H_2O_2/Visible and FZO/H_2O_2/UV at the respective RSM optimized conditions of the decolourization of a real spentwash samples	173
Figure 5.30	Antibacterial activity of WO_3 and FZO nanoparticles on real wastewater sample (spentwash) for removal of microbes	175
Figure 6.1	Growth profile of *Bacillus subtilis* RSL-2 bacteria	190
Figure 6.2	3D response surface plots for the biomass, ST and biomass concentration considering their independent parameters as pH, temperature and concentration of molasses	194
Figure 6.3	Profile of ST, dry biomass, biosurfactant production and residual sugar at the optimized conditions in shake-flask study	195

Figure 6.4	Growth and sugar utilization ability of *Bacillus subtilis* RSL-2 in batch bioreactor study using 5 % (w/v) molasses as a sole nutrient source	200
Figure 6.5	Growth profile of *B.subtilis* RSL-2 in a semicontinuous mode reactor with intermittent feeding of 14.05 g L^{-1} per 8 h of incubation	202
Figure 6.6	Change in bacterial specific growth rate (μ) with time in the batch and sequential fed-batch bioreactor study	204
Figure 6.7	Functional group analysis of the produced biosurfactant by FTIR and ^{1}H NMR	209
Figure 6.8	LC–MS and MALDI TOF analysis for the produced biosurfactan	211
Figure 6.9	The reduction in surface tension with increased biosurfactant shows the CMC value for crude biosurfactant	212
Figure 6.10	Oil displacement test and emulsification activity of produced biosurfactant	213
Figure 6.11	The surface charge of produced biosurfactant at various pH values	214
Figure 6.12	Thermostability analysis of produced biosurfactant using TGA	216
Figure 6.13	Analysis of wettability alteration by contact angle analysis of Molasses media, Cell-free supernatant and produced biosurfactant at CMC value	217

Abbreviations

3D	Three Dimensional
AC	Activated Carbon
ANOVA	Analysis of Variance
AOP	Advanced Oxidation Process
APHA	American Public Health Association
ASBR	Anaerobic Sequencing Batch Reactor
BBD	Box–Behnken Design
BET	Brunauer–Emmett–Teller
BOD	Biological Oxygen Demand
CCD	Central Composite Design
CLLP	Citrus Limon Leaves Powder
CMC	Critical Micelle Concentration
COD	Chemical Oxygen Demand
Conc	Concentration
CPCB	Central Pollution Control Board
CSTR	Continuous Stirred Tank Reactors
DCB	Dry Cell Biomass
df	Degree of Freedom
DLS	Dynamic Light Scattering
DWW	Distillery Wastewater
E_{24}	Emulsification index after 24 h incubation
EDX	Energy dispersive X-ray Spectroscopy
Eq	Equation
FESEM	Field Emission Scanning Electron Microscope
FETEM	Field-Emission Transmission Electron Microscope
Fig	Figure
FTIR	Fourier Transform Infrared Spectroscopy
FZO	Iron Doped Zinc Oxide
HPLC-UV	High Performance Liquid Chromatography-UV detector

hr	Hour
HRT	Hydraulic Retention Time
ICDD	International Centre for Diffraction Data
INR	Indian Rupee
LB	Luria Bertani Broth
LCMS	Liquid Chromatography–Mass Spectrometry
MALDI-TOF	Matrix-Assisted Laser Desorption/Ionization-Time of Flight
Min	Minute
mM	Mili-Molar
MSW	Melanoidin Containing Spentwash
MW	Molecular Weight
NMR	Nuclear Magnetic Resonance
OD	Optical Density
OLR	Organic Loading Rate
PELP	Phyllanthus Emblica Leaves Powder
ppm	Parts Per Million
Ref	Reference
rpm	Revolutions Per Minute
RSM	Response Surface Methodology
RT	Retention Time
SAMs	Self-Assembled Monolayers
SBR	Sequencing Batch Reactor
ST	Surface Tension
TDS	Total Dissolved Solids
Temp	Temperature
TGA	Thermal Gravimetric Analysis
TILP	Tamarindus Indica Leaves Powder
TiO_2	Titanium Oxide
TOC	Total Organic Carbon
TS	Total Solids
TSS	Total Suspended Solids

TVS	Total Volatile Solids
UASB	Upflow Anaerobic Sludge Blanket
USEPA	U.S. Environmental Protection Agency
UV	Ultraviolet
VSS	Volatile Suspended Solids
WAO	Wet Air Oxidation
WHO	World Health Organization
WO_3	Tungsten Oxide
XRD	X-ray Powder Diffraction
ZnO	Zinc Oxide
CFU	Cell Forming Unit

Symbols

%	Percentage
z_i	Valency
Ψ_d	Zeta-Potential (mV)
<	Smaller than
>	Greater than
ϵ	Polanyi potential related to the equilibrium constant ($mol^2\ J^{-2}$)
°C	Degree Celsius
b_T	Temkin Constant Related to the Heat of Adsorption ($J\ mol^{-1}$)
C_0	Initial substrate concentration ($mg\ L^{-1}$)
C_e	Equilibrium Substrate Concentration ($mg\ L^{-1}$)
C_e	Equilibrium Concentration of Adsorbate ($g\ L^{-1}$)
F	Faraday's constant
h	Initial Adsorption Rate of Pseudo-Second-Order ($mg\ g^{-1}\ min^{-1}$)
k_0	Zero Order Rate Constant
k_0	Zero-Order Reaction Rate Constants ($Mole\ L^{-1}\ Sec^{-1}$)
k_1	First Order Rate Constant (h^{-1})
k_1	Pseudo-First-Order Rate Constant (min^{-1})
k_2	Pseudo-Second-Order Rate Constant ($g\ mg^{-1}\ min^{-1}$)
K_{ad}	Adsorption Energy Constant ($mol^2\ J^{-2}$)
k-Da	Kilodaltons (molecular weight)
K_f	Freundlich Constant ($mg\ g^{-1}$)
K_L	Langmuir Isotherm Constant ($L\ mg^{-1}$)
K_T	Temkin Isotherm Equilibrium Coefficient ($L\ g^{-1}$)
m/z	Mass to Charge Ratio
n	Adsorption Intensity $(L\ g^{-1})^{1/n}$
q_e	Adsorption at Equilibrium Time ($mg\ g^{-1}$)
q_m	Maximum Adsorption Capacity ($mg\ g^{-1}$)
q_t	Adsorption at Time t ($mg\ g^{-1}$)
q_t	Concentration at a Time Interval ($mg\ g^{-1}$)

R	Universal Gas Constant (8.314 J mol^{-1} K^{-1})
R^2	Correlation Coefficient
T	Temperature (K)
t	Time
V	Volume of Solution (mL)
W	Weight of the Adsorbent (mg)
$Y_{P/S}$	Biosurfactant Yield
$Y_{x/s}$	Biomass Yield
α	Adsorption Rate (mg g^{-1} min^{-1})
β	Elovich Constant (g mg^{-1})
δ	Chemical Shift (ppm) in NMR
ΔG	Change in Gibbs free energy (J mol^{-1})
ΔH	Change in Enthalpy (J mol^{-1})
ΔS	Change in Entropy (J mol^{-1} K^{-1})
θ	Half of the Diffraction Angle/Bragg angle
μ	Specific Growth Rate

Chapter 1

Introduction

The entire world is facing the major water crisis of land and groundwater quality issues in the twenty-first century [1]. The World Health Organization (WHO 2015) has reported that about 1.1 billion people do not have adequate drinking water [2]. Urbanization, industrialization and uncontrolled increase in the global population are the main cause of over-exploitation of groundwater [3]. The chemical and biochemical industries are quite water-intensive and thus generate a huge quantity of wastewater. Distilleries are one of the water-intensive industries and generate about 12-15 times of effluent per litre of alcohol produced. The disposal of untreated water into the environment is a significant source of water pollution. The consumption of this contaminated water is the leading cause of death and numerous health-related issues worldwide. Hence, the wastewater needs to be treated to meet the prescribed standards for discharge or reuse.

Further, by-products of agro-based industries are rich in carbon contents, which are being extensively utilized in fermentation (biochemical) industries. Sugarcane is a global crop and is cultivated in most countries. After Brazil, India is the second-largest sugar-producing country using sugarcane [4]. Molasses and bagasse are the main by-products of these sugar industries. There are a lot of industries that use molasses, such as distilleries, fermentation industries, sugar mills, and other molasses-based businesses. Molasses is the primary source of alcohol production in India. Indian distilleries use molasses as a raw material (carbon source) to produce ethanol by the microbial fermentation process [5]. Molasses is a dark brown coloring compound that is a by-product of the sugar industry. It contains melanoidin compounds produced by the Maillard reaction at 140 °C - 150 °C temperature by combining amino acids and sugar [6]. For example, melanoidin is produced by the glucose and

glycine reaction at 125 °C for 2 h [5]. Melanoidins are very high molecular weight organic compounds (mw of 40 kDa - 40,000 kDa). At the higher concentrations, the melanoidin compound is genotoxic and cytotoxic [7]. The distilleries generate two types of wastewater. The first is spentwash produced during the distillation of fermented broth containing alcohol. The second one is wastewater generated by the washing of fermenters, cooling towers, boilers, etc. The primary source of the dark brown color of distillery wastewater is the melanoidin compound produced by the non-enzymatic chemical reaction (Maillard reaction) [8].

The melanoidin-containing wastewater (spentwash) possesses very high loads of biological oxygen demand (BOD), chemical oxygen demand (COD), other organic and inorganic pollutants along with acidic pH [5]. This makes it highly polluted wastewater. Thus, the Ministry of Environment, Forest and Climate Change, India, has categorized these industries in the “red category.” The discharge of untreated melanoidin-containing wastewater in water bodies or land causes hazardous and carcinogenic effects on living and non-living systems [9]. Its release into the environment leads to the soil, groundwater and river water contaminations, eutrophication and hampering the photosynthesis rate of aquatic plants. This reduces the penetration of sunlight into water bodies and inhibits the quality and production of crops [3, 6]. On the other hand, if directly disposed of on land, it decreases the soil's alkalinity, which causes inhibition of seed germination and low quality of crop production [3]. The central pollution control board (CPCB) places distilleries among India's topmost polluting industries. Hence, treatment is a mandatory requirement before these effluents are released to the ecosystem.

Various physical, chemical and biological methods have been applied to treat distillery wastewater. Biological techniques such as bacterial, fungal, and algal treatment methods have been applied to remove the melanoidin compounds before discharging them into the environment [9]. However, the

treatment efficacies of these methods are quite low due to the poor biodegradability of melanoidin [10]. Thus various alternatives to conventional methods such as the use of activated carbon, electrochemical degradation, integrated biochemical adsorption, oxidation, coagulation, membrane filtration, have been applied for melanoidin removal [11]. However, due to the high organic loadings and the presence of melanoidin chemicals in the water, the efficacy of the above treatment procedures is severely hampered [3, 12]. The drawbacks of these methods include higher operational and maintenance costs, a requirement of a large number of chemicals, generation of by-products (secondary waste) in large amounts and various harmful effects on the ecosystem.

The present thesis explores various physical, chemical and biological methods to manage the distillery spentwash. Firstly, adsorption, advanced oxidation process, and photocatalysis have been investigated to remove melanoidin followed by the treatment of real from wastewater (spentwash). In addition, the bioprocessing of molasses to produce alternative metabolite biosurfactants has been investigated to decrease the pollution load of wastewater. The objectives of this thesis are formulated accordingly.

1.1. Objectives

With the aim to bridge the knowledge lacuna as discussed in Chapter 2, the objectives of the thesis are as follows:

1. Melanoidin removal by biosorption using low cost and biogenic adsorbents
2. Treatment of melanoidin and real spentwash samples using advanced oxidation processes
3. Photocatalytic degradation of melanoidin under UV/Visible light illumination
4. Exploring molasses as a sole nutrient for the production of alternative metabolite biosurfactants

1.2. Thesis Outline

The thesis has been arranged into seven chapters based on the above-mentioned four objectives. A chapter-wise thesis outline is briefed as follows:

Chapter 2

This chapter reviews existing literature on the present status of distillery effluents and their physicochemical and biological methods applied for the treatment of molasses-based distillery wastewater, along with their potential and limitations.

Chapter 3

In this chapter, *Phyllanthus emblica*, *Citrus limon* and *Tamarindus indica* leaves have been explored to remove synthetic melanoidin. The surface of these leaf powders was modified by amine (self-assembled monolayers) SAMs to improve the adsorption properties. The experimental conditions (pH, temperature and adsorbent dose) were optimized using the Response Surface Methodology-Central Composite Design (RSM-CCD) to maximize the adsorption capacity.

Chapter 4

The photochemical degradation of melanoidin has been investigated in this chapter by the photo-Fenton process. The experimental parameters such as temperature, time, H_2O_2 and Fe(II) concentrations were optimized. At the optimized condition, degradation of melanoidin solution was observed associated with COD reduction**.** The experimental data were fitted for kinetics and thermodynamic analysis.

Chapter 5

In this chapter, photodegradation of melanoidin and distillery spentwash were investigated. Various nanomaterials such as ZnO, TiO_2, Fe doped ZnO (FZO) and WO_3 were tested for the photocatalytic

degradation of the melanoidin under different light conditions. The degradation efficiency of the real spent wash samples was also studied at the optimized conditions.

Chapter 6

This chapter explores sugarcane molasses as the sole nutrient source (media) for biosurfactant production using an isolated inherent microbe, *Bacillus subtilis* RSL-2. This study puts forward the potential waste to strategic wealth applications through microbial fermentation of molasses.

Chapter 7

This chapter summarizes the overall conclusions of the present research work and also suggests the possible directions to extend the research work in the future.

Chapter 2

Literature review

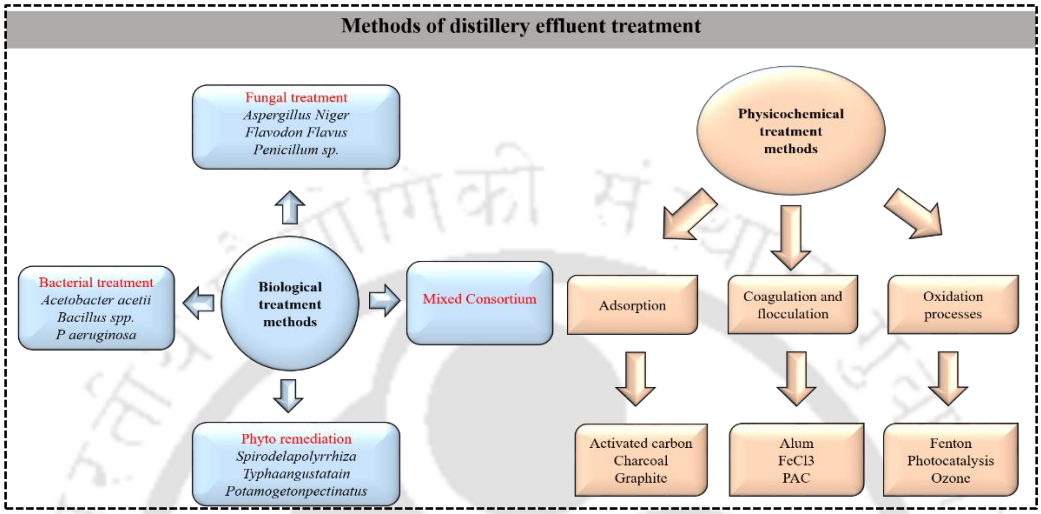

*(Decontamination of distillery spentwash through advanced oxidation methods. Advanced Oxidation Processes for Effluent Treatment Plants, **Rahul Verma**, L.M. Kundu, and L.M. Pandey. 2021, Elsevier. p. 103-117)*

This chapter reviews existing literature on the present status of distillery effluents and their physicochemical and biological methods applied for the treatment of molasses-based distillery wastewater, along with their potential and limitations. In distilleries, ethanol production generates a large amount of highly polluted brown-colored acidic spentwash. If discharged without treatment, it causes the death of aquatic flora and fauna, lowers the pH of the soil and water, contaminates the water and soil, and hinders the use of water for humans, animals and plants. In order to minimize the effect of spentwash, it is necessary to treat it (decontaminate) before discharging. Mostly, the anaerobic digestion process is applied by industries to treat spentwash. However, the conventional methods have reached their limits due to very high organic loadings and the presence of melanoidin

compounds. AOPs have emerged as efficient methods for the reclamation of organic pollution and have been explored for the treatment of distillery spentwash.

2.1. Introduction

The distilleries are one of the most polluting industries on the planet, as it generates a significant amount of wastewater every year. Extensive amounts of organic and inorganic pollutants, in addition to toxic heavy metals and their oxides, are detected in distillery effluent wastewater. This has significant ramifications on the ecosystem as well as human health.

In order to successfully remove melanoidin from water while also decreasing the levels of COD and BOD in the water, several physiochemical (adsorption, coagulation-flocculation, oxidation, membrane filtration etc.) and biological (bacterial, fungal, and algal) treatment processes have been applied.

2.2. Distilleries in India and process description for ethanol production and waste generation

India has more than 350 distilleries, mainly in Andhra Pradesh, Haryana, Uttar Pradesh, Tamil Nadu and Maharashtra [3]. Molasses-based distilleries play an essential role in the world economy and generate highly polluted wastewater, called spentwash, which contains very high COD and other pollutants. The annual ethanol production in India is $>4.27 \times 10^9$ L. Subsequently, effluent generated by this is $>53.2 \times 10^{10}$ L, i.e., at the rate of 12 to 15 L spentwash produced per L of alcohol production. A detailed flow diagram of spentwash production in a distilleries has been shown in Figure 2.1 [13].

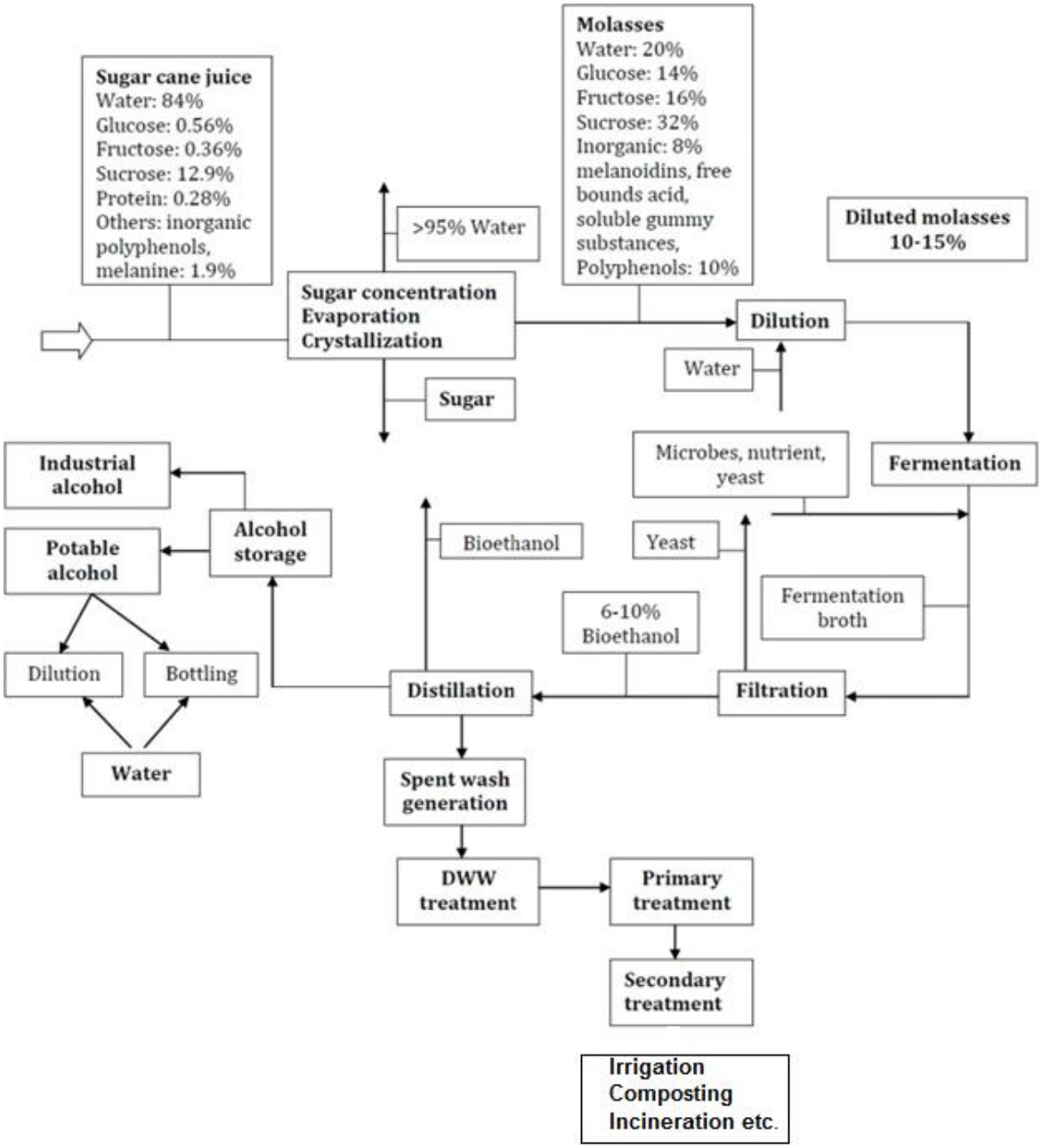

Fig. 2.1: Steps of alcohol production and spentwash generation [Adopted from [12]].

2.3. Characteristics of distillery effluent

Molasses-based distilleries play an essential role in the world economy and generate highly polluted wastewater, called spentwash, which contains high COD (110k-190k mgL^{-1}) and BOD (50k-90k mg L^{-1}). The general characteristic of untreated distillery effluent is shown in Table 2.1 [14] [15]. The high molecular weight of melanoidin (40kDa to 40000kDa) and elemental composition depend on the Maillard reaction conditions, temperature, pH, concentration, reaction time, etc. The Maillard reaction produces small molecules to large polymers. The consumption of higher concentrations can produce a genotoxic and cytotoxic effect on cells [7, 16, 17]. The melanoidin-containing effluents are harmful to the environment because they have high COD and BOD loads. These effluents have a dark brown colour that is very hard for bacteria and other organisms to break down. People use dark brown sludge as fertilizer after diluting it several times with water to get rid of the colored water. As a result, the resources of freshwater got contaminated. Another big problem caused by distillery wastewater is that the pH level of the streams drops. This leads to more organic waste and an obnoxious smell. The waste from distilleries is a big problem for water quality in some parts of the country and direct disposal into land or soil causes polluting the environment.

Table 2.1: General characteristics of untreated raw distillery spentwash [Adopted from [15]].

Parameters	Range (mg L^{-1})
pH	3.0-4.5
BOD_5	50,000-90,000
COD	110,000-190,000
Total volatile solids (TVS)	80,000-120,000
Total suspended solids (TSS)	13,000-150,000
Total dissolved solids (TDS)	90,000-150,000
Total solids (TS)	110,000-190,000
Sulphate	7500-9000
Phosphate	2500-2700
Total nitrogen	5000-7000
Chloride	8000-8500
Phenols	8000-10,000

2.4. Distillery effluent treatment technologies

Various physicochemical and biological methods have been investigated and applied to achieve the discharge standard of melanoidin-containing wastewater. Different conventional physicochemical methods such as activated carbon, electrochemical degradation, integrated biochemical adsorption, oxidation, coagulation, membrane filtration, photocatalytic degradation, Fenton and photo-Fenton processes have been applied for the treatment of melanoidin containing wastewater [3, 11]. The biological treatment technology utilized microbial activity (Bacteria, Algae, Fungi, Enzymatic activity, etc.) for the effective treatment of melanoidin-containing wastewater [18].

2.4.1. Physico-chemical Treatment technologies for distillery wastewater

Before discharging, various physical and chemical treatment processes have effectively treated distillery wastewater. In physicochemical treatment methods, the color pigments are removed either by the breakdown of pigments or by concentrating the color into sludge. The physiochemical process involved coagulation, flocculation, adsorption, electrocoagulation, advanced oxidation processes, catalysis, membrane filtration, etc. [19].

2.4.1.1. Distillery effluent treatment through adsorption

In a physicochemical treatment method, adsorption is the most applied technique for pollutants and color removal. It is a surface-based phenomenon in which the organic and inorganic contaminants from wastewaters are removed by attaching them to the surface of the adsorbent. Adsorption on the activated carbon (AC) surface mainly treats ions, metals, specific organic pollutants, and color (Figure 2.2). AC is used as an effective adsorbent due to its microporous structure, high surface area, a very high degree of surface reactivity, and a very high degree of adsorbent capacity [20]. An extensive literature has been published on the studies of the use of the adsorbent such as chemically modified/treated powdered activated carbon, biochar, sugarcane bagasse, chitosan activated charcoal, etc., for distillery wastewater (DWW) treatment. [12]. Activated carbon and commercially available activated carbon prepared by various agriculture waste, sugarcane bagasse, etc. are also used to decolorize melanoidin. In a study, commercially available activated carbon with a surface area of 1400 m^2 g L^{-1} was used on a packed bed to anaerobically treat spentwash. Almost 90 % decolorization was achieved [21]. Lalov *et al.* used chitosan in the amount of 10 g L^{-1} as at a concentration of adsorbent for the contact time of 30 min. The effective treatment of diluted DWW found 98 % in

color removal 99 % in COD reduction [22]. Further, Mane *et al.* have testified 50 % color removal from distillery effluent using chemically modified sugarcane bagasse in a concentration of 0.5 g per100 mL in wastewater using chloride hydrochloride and 3-chloro-2-hydroxypropyl trimethyl ammonium chloride (CHPTAC) and 2-diethyl laminoethyl (DEAE) for the treatment of distillery effluent. [23]. Shivayogimathand *et al.* reported 89.8 % TDS, 95.4 % COD, and 62.83 % color reduction from distillery wastewater using activated bagasse carbon [24].

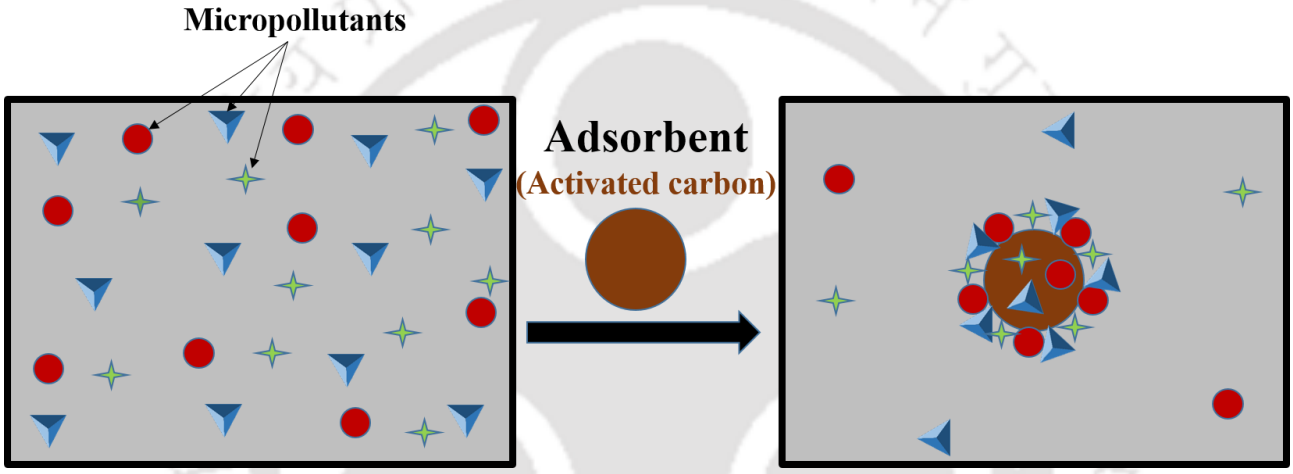

Fig. 2.2: Adsorption on the surface of an adsorbent.

2.4.1.2. Distillery effluent treatment through coagulation and flocculation

The coagulation and flocculation process is widely used for wastewater treatment to separate the suspended molecules by neutralizing the positive and negative charge. The particles attached to each other form the larger particle (Flocs). Generally, the coagulation process is an expensive process in the form of chemicals and as well as sludge disposal. Thus, the industries required the development of new and low-cost alternative techniques for wastewater treatment. Migo *et al.* used a polymer of ferric hydroxy sulfate, a commercially available inorganic flocculant for the treatment of distillery-based wastewater; the treatment resulted in 87 % decolorization of biomethanated effluent [25]. Alum

and iron salts were used with coagulation and were ineffective for melanoidin color removal. Further, they used lime and ozone to treat anaerobically digested distillery effluent, resulting in 67.6 % color removal and 82.5 % COD removal using an optimum dosage 10 g L^{-1} in a 30 min time duration. $FeCl_3$ and $AlCl_3$ were also used for melanoidin pigments decolorization of bio-methanated effluent and showed 76 % removal of total organic carbon and about 93 % in color [26].

2.4.1.3. Distillery effluent treatment through the oxidation process

AOPs are proven to be excellent methods for the decontamination of wastewater, which are based on the in-situ formation of extremely reactive and strong oxidizing radicals. Hydroxyl radicals (•OH) and ozone (O_3) are very powerful oxidants and oxidise the organic and inorganic compounds present in wastewater [27]. Once O_3 is dissolved in water, it reacts with the organic compounds present in wastewater. The reaction occurs in two different ways, (1) By the indirect reaction with available organic compounds through the formation of free radicals and (2) Direct oxidation. This promising technology has been explored for the treatment of distillery effluent. AOPs are found to quickly degrade the melanoidin pigments into their intermediate products, depending on the treatment period and concentration. There are many oxidation processes used for the colour removal and decontamination of distillery spent wash such as O_3, Fenton's reagent, H_2O_2 and O_3 combined with H_2O_2. Fenton reagent is a mixture of iron salts and hydrogen peroxide, which generates •OH radicals in the homogenous reaction. These •OH radicals decompose the organic compounds, which leads to decolorization and COD removal [28].

2.4.1.3.1 AOPs: Principles and applications

AOPs is a well-defined process involved in the formation and use of nonselective powerful $\bullet OH$ radicals in large quantities, which oxidize a large number of organic compounds present in the wastewater. •OH radicals have the second strongest oxidation potential after fluorine radical. However, fluorine radicals are not applied for the decontamination of effluent wastewater treatment due to its highly toxic nature. Hence, •OH radicals have been broadly used for AOPs because of its non-toxicity. Further, the AOPs reaction mechanisms are classified into two categories [29].

(a) Production of free OH radicals

(b) The oxidation of organic molecules by free radicals

The highly reactive free radicals are generated by the use of hydrogen peroxide (H_2O_2), ozone (O_3), iron salts, semiconductors with ultraviolet light (UV). These generated radicals react with organic pollutants and convert them into CO_2 and H_2O. On the basis of light, the AOPs are differentiated into two main types: non-photochemical and photochemical (Figure 2.3).

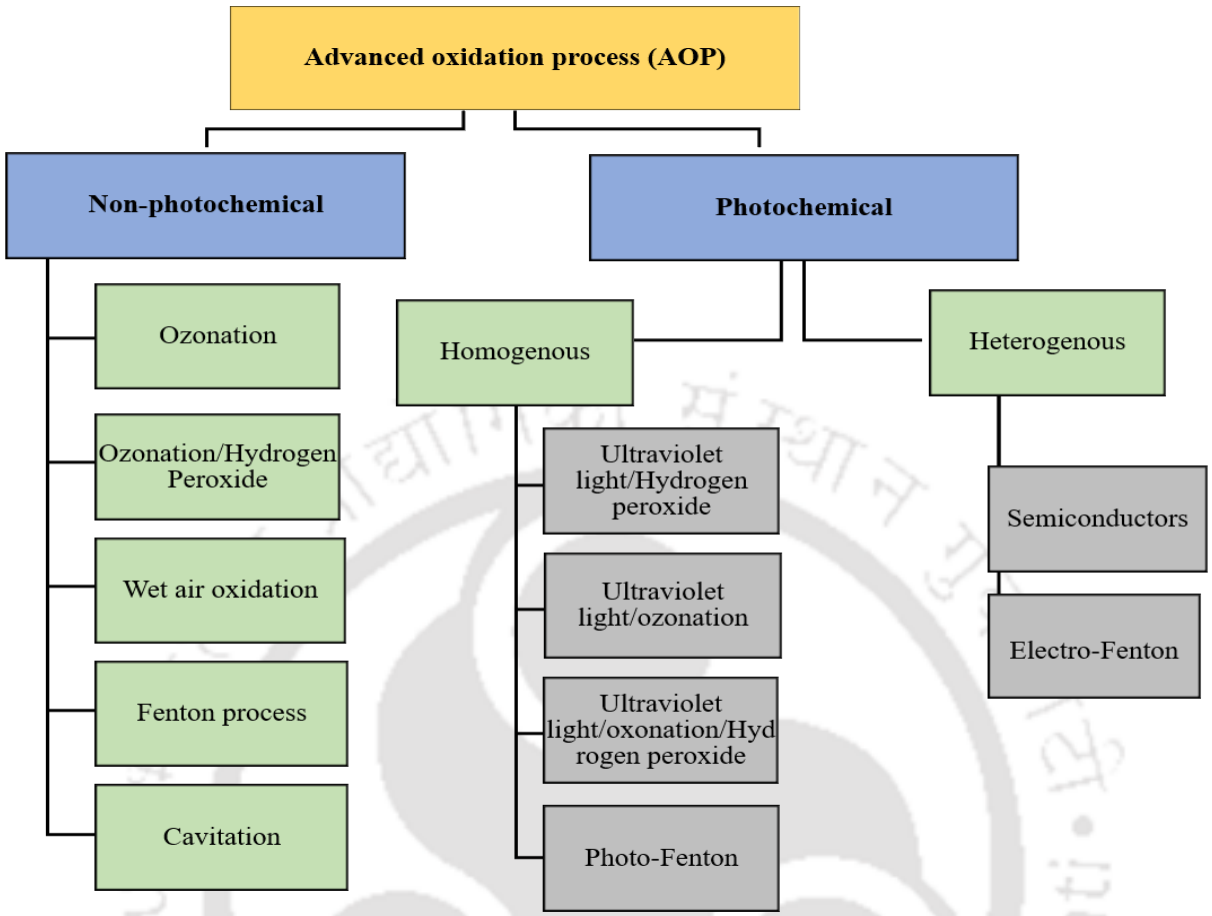

Fig. 2.3: Classifications of AOPs.

Non-photochemical AOPs include ozonation, ozonation with hydrogen peroxide (O_3/H_2O_2), wet air oxidation, Fenton process, and Cavitation, while the photochemical system includes homogenous and heterogeneous AOPs. Homogenous AOPs are photolysis, UV with the combination of hydrogen peroxide (UV/H_2O_2), UV with the combination of ozone (UV/O_3), UV with the combination of ozone and hydrogen peroxide ($UV/O_3/H_2O_2$) and photo-Fenton process. The heterogeneous process includes semiconductors and electro-Fenton-based AOPs.

2.4.1.3.2. Non-photochemical AOPs

These methods are performed in the absence of light and classified as (a) Ozonation; (b) Ozonation with hydrogen peroxide (O_3/H_2O_2); (c) Wet air oxidation; (d) Fenton process; (e) Cavitation; and (f) Electrochemical Oxidation. Most of these methods use O_3 for •OH radicals production while Fenton process uses Fe^{+2} ions as a catalyst. Out of them O_3, O_3/H_2O_2 and Fenton process is widely applied processes for the industrial wastewater treatment. These processes are widely applied for the decolorization of spent wash and reduction of COD level. A brief explanation and examples of these methods for distillery effluent treatment are discussed below.

(a) Ozonation

Ozonation is well known as a very powerful oxidizing method for industrial wastewater treatment. Once ozone dissolves in water, it reacts with organic and inorganic compounds present in two different ways, named as indirect reaction with •OH radicals by the help of intermediates and direct molecular reaction. Both types of ozonation reactions occur simultaneously [30]. Ozonation shows a higher efficiency of wastewater treatment at higher pH levels (above 9) [31]. In an acidic condition, the protons (H^+) combine with O_3 to generate O_2 and H_2O (Eq. 2.1), which prevents a direct interaction of O_3 with the contaminants and lowers the degradation rate of pollutants [32].

$$O_3 + 2H^+ + 2e^- \rightarrow O_2 + H_2O \quad (2.1)$$

In an alkaline pH, the impact of OH^- is favorable for the mineralization of pollutants, where O_3 immediately attacks OH^- to form •OH radical. The accelerated decomposition of ozone generates more hydroxyl radicals, responsible for the improved colour and COD removal effectiveness. as shown in the following equations (Eq. 2.2 and 2.3) [33-35]

$$O_3 + OH^- \rightarrow O_2^{\bullet -} + OH_2^{\bullet} \quad (2.2)$$

$$O_3 + OH_2^{\bullet} \rightarrow 2O_2 + \bullet OH \quad (2.3)$$

Therefore an increase of the amount of •OH free radicals and consequently, the efficiency of the treatment should be improved when ozonation occurs in alkaline pH. The reaction mechanism of the ozonation process is given below (Eq. 2.4). Three molecules of ozone are utilized for the generation of two •OH radicals [29].

$$3O_3 + OH^- + H^+ \rightarrow 2\bullet OH + 4O_2 \quad (2.4)$$

Benton *et al.* applied the ozonation process as post-treatment for anaerobically digested distillery spent wash. The highest colour removal of 80 % and total organic carbon (TOC) reduction of 18 % were achieved at an intermediate flow rate of 45 mg O_3 L^{-1} min^{-1} [36]. In another study, Siles *et al.* applied combined chemical–biological treatments (ozonation pre-treatment followed by bio-methanization) for the treatment of spent wash. Pre-ozonation reduced more than 50% phenols, which resulted in three-fold higher methane (biogas) generation (41 %) during bio-methanization because of the improved biodegradability of pre-treated effluent [37]. Recently, Sameena *et al*. observed COD and colour reduction of 28 % and 30 %, respectively of anaerobically digested (bio-methanated) spent wash, which was utilized for the bio composting. Ozone pre-treatment enhanced the biodegradation rate during composting as compared to untreated spent wash [38].

(b) Ozonation with hydrogen-peroxide (O_3/H_2O_2)

The combination of ozone with hydrogen peroxide resulted in the significant removal of contaminants from wastewater. Due to the high cost of ozone production, the combination of O_3/H_2O_2 is also economically feasible. The combined use of O_3/H_2O_2 accelerates the conversion of O_3 to •OH and enhances the rate of oxidization of pollutants, reducing the reaction time.

O_3 molecules have the ability to oxidize different pollutants by breaking the different bonds (C=C bonds) as well as aromatic rings, which enhances in the presence of H_2O_2 due to the high generation of •OH radicals. H_2O_2 molecules dissociate into hydroperoxide ion formation. In an aqueous solution, the ozone reacts with water molecules and produces 2 •OH radicals (Eq. 2.4) [39]. Two molecules of O_3 react with one molecule of H_2O_2 and produce two $\bullet OH$ radicals (Eq. 2.5).

$$H_2O_2 + 2O_3 \rightarrow 2\bullet OH + 3O_2 \quad (2.5)$$

During the combined O_3/H_2O_2 process, H_2O_2 partially decomposes in water and generates a conjugate base of H_2O_2 in the form of hydroperoxide anion (HO_2^-), which interacts with O_3 to produce •OH and also promotes the radical chain reaction (Eq. 2.6, 2.7 and 2.8) [40, 41].

$$H_2O_2 \rightarrow H^+ + HO_2^- \quad (2.6)$$

$$O_3 + HO_2^- \rightarrow \bullet OH + 2O_2^- + O_2 \quad (2.7)$$

$$2O_3 + H_2O_2 \rightarrow 2\bullet OH + 3O_2 \quad (2.8)$$

Rosenfeldt *et al.* estimated the efficiency of •OH radicals formation during ozonation and the advanced oxidation processes (O_3/H_2O_2). They experimented with O_3 and the addition of H_2O_2 (1:2 or 1:1 on a molar basis H_2O_2:O_3 ratio) and determined the $OH^\bullet$ radicals production per unit consumption of O_3. They resulted in more •OH radicals exposure in O_3/H_2O_2 combined process compared to O_3 alone and also stated 35 % greater energy consumption over the O_3 only process [42]. The combination of ozone with other oxidizing agents such as hydrogen peroxide under UV light is used for the treatment of wide range of toxic organic pollutants [43]. Tizaoui *et al.* reported that comparing to using ozone or hydrogen peroxide alone, ozone with small amount of hydrogen peroxide demonstrated to improve the treatment process. Also, Tizaoui *et al.* estimated the cost of O_3, H_2O_2 and O_3/H_2O_2 for per kg of COD removed and found to be 2.7, 3.2 and 2.3 USD, respectively

[44]. Hadavifar *et al.* found that the combination of H_2O_2 and O_3 are much more efficient than their individual applications on distillery wastewater and observed almost complete colour removal (98.4 %) and COD reduction [45]. Kolte *et al.* performed an experiment on anaerobically digested spent wash with the ozone at a flow rate of 0.3 $m^3 h^{-1}$ and found 62 % colour and 47 % COD removals [46].

(c) Wet air oxidation

Wet air oxidation (WAO), also known as hydrothermal treatment is a well-established pre-treatment technique for the decontamination of distillery effluents. The WAO process involves the oxidization of organic and inorganic substances in the liquid medium [47]. Oxidation of organic contaminants occurs at elevated temperature (120-350 °C) and high pressure (1-60 bar) using O_2 containing gas. Mainly two steps are involved in WAO process as shown in Figure 2.4 i.e. destruction of higher organic molecules into lower molecular organic compounds (acids) and complete mineralization of these organic compounds into H_2O and CO_2 [48].

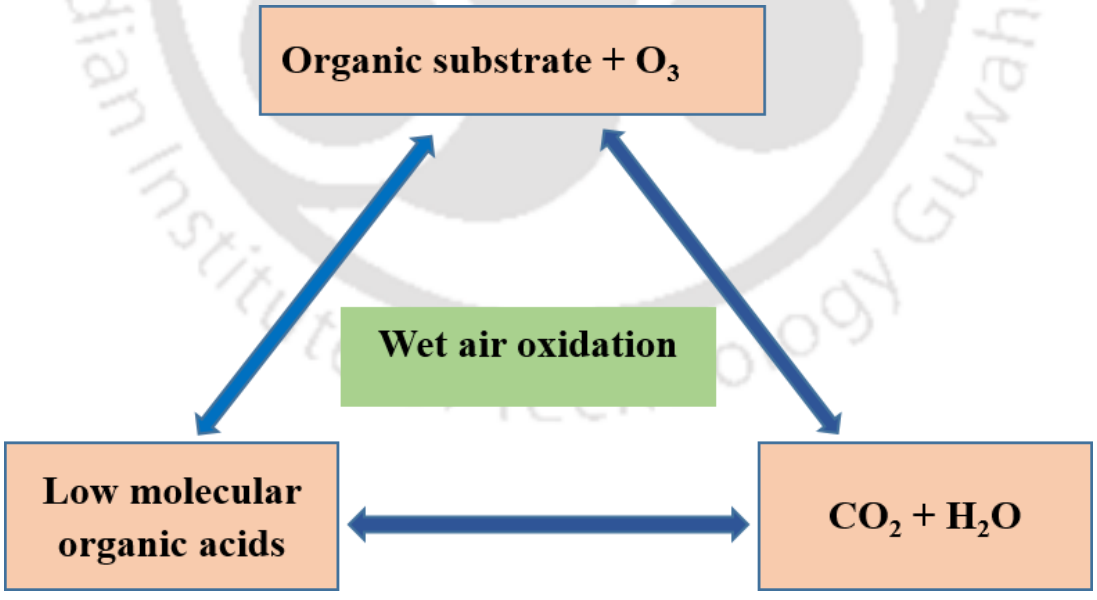

Fig. 2.4: Mechanism of wet air oxidation (WAO) process.

Recently, WAO has successfully applied and found great potential in the decontamination process of distillery wastewater. Dominguez *et al.* employed the WAO method for the treatment of real winery wastewater and found to be 80 % COD and 85 % of TOC removal in 4 hours [49]. In a catalytic WAO experiment ferrous sulphate was used as a catalyst for the bio-methanated distillery wastewater as shown in Figure 2.5. The process condition was the temperature in a range of 150 to 225 °C, oxygen partial pressure from 0.69 to 2.07 MPa and the catalyst loading (16 to 48 mg L^{-1}). 91 % COD reduction was achieved along with the improved quality of biogas (69 % methane) [50]. Chandra *et al.* reported 64% biogas (Methane) generation along with 55 % COD reduction and 98% melanoidin degradation as pre-treatment of bio-methanated spent wash [51].

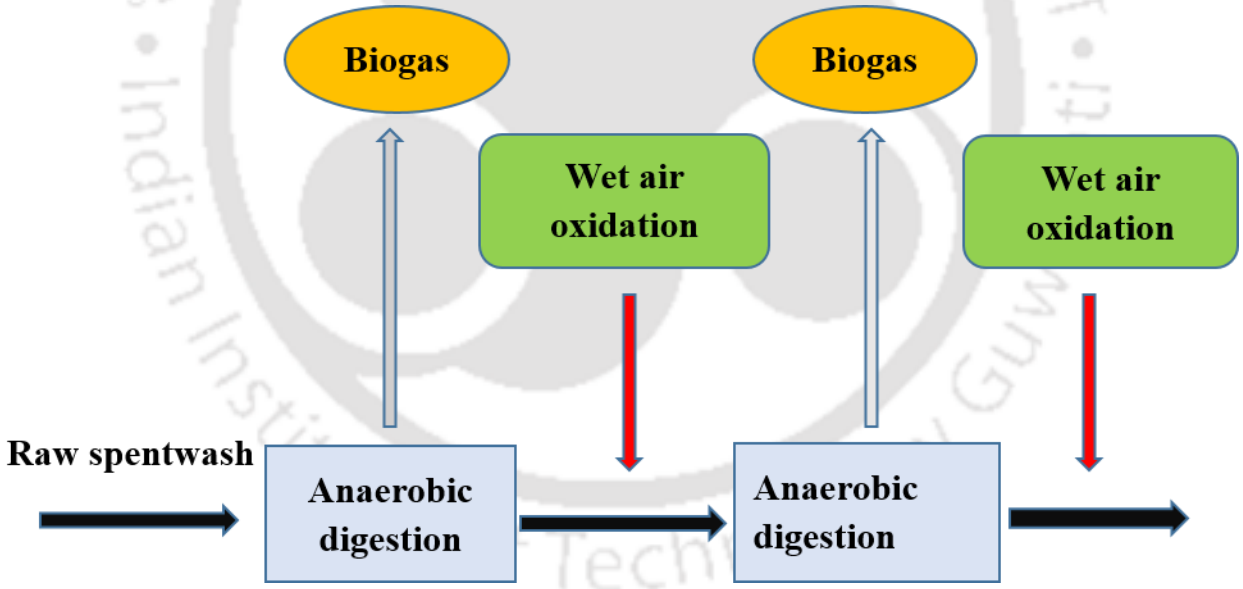

Fig. 2.5: WAO of biomethanated distillery wastewater.

(d) Fenton process

The Fenton process was first proposed by H.J.H. Fenton in 1894 as expressed by equation 2.9 [52].

$$Fe^{+2} + H_2O_2 \rightarrow Fe^{+3} + OH^- + \ \bullet OH \qquad (2.9)$$

The reaction of Fe^{+2} ion and H_2O_2 is very fast and ferrous ion oxidizes into ferric ion in a very short time (within few minutes) in the presence of excess H_2O_2. The application of Fe^{+2}/H_2O_2 process for the treatment of wastewater is much effective because of (i) Fe has highly abounded and non-toxic element (ii) H_2O_2 is environmentally benign and easy to handle, and (iii) It is cost-effective, degrades a wide range of organic compounds and easy to apply. Heredia *et al.* employed the Fenton process for wine-based pre-treated distillery wastewater and achieved 80 % COD reduction [53].

(e) Cavitation

The cavitation process is considered as pre-treatment process for the bio-methanated distillery wastewater. This method is described as the generation and collapse of microbubbles or cavities formation in milliseconds to microseconds time intervals, which generates a significant magnitude of energy in different small regions in the reactor [54]. When the cavity or bubbles collapse and it creates hot spots which have transient pressure and temperature up to 1000 atm and 10000 K, respectively [55]. Under this condition releasing highly reactive •OH free radicals are dissociated from water molecules, which diffuse in the liquid medium and react with organic contaminants present in wastewater and mineralize them. Padole *et al*. pre-treated the bio-methanated distillery wastewater by applying hydrodynamic cavitation under the optimized condition and observed the reduction of COD, TOC and colour up to 32 %, 31 % and 48 %, respectively [56]. In a similar study, Pardkar *et al.* treated the biomethanated spent wash by hydrodynamic cavitation and 36 % COD reduction was achieved [57].

(f) Electrochemical Oxidation

The electrochemical process is an effective and easy technique for the decontamination of various types of water and wastewater [58, 59]. This process offers a high removal efficiency of organic

pollutants in a compact reactor. The efficiency depends on solution pH, supporting electrolyte type and electrode, applied current and initial concentration of pollutants in wastewater [60]. Prasad *et al.* treated the distillery spent wash (10 times diluted) by electrochemical degradation and reported 83 % colour and 40 % COD removals at pH 5.5, applying 3h electrolysis time and 14.29 mA cm^{-2} current density [61]. In a similar study, 94 % colour removal of diluted distillery spent wash (18 %) were reported through the electrochemical process at a current density of 31 mA cm^{-2} for 4 hours [62].

2.4.1.3.3. Photochemical AOPs

Conventional H_2O_2 and O_3 methods do not fully oxidize the organic contaminants into CO_2 and H_2O. In some reactions, the complete degradation of organic compounds does not occur and the intermediate products formed through oxidation remains in the solution. These intermediates may be (more/less) toxic compared to the original compounds. So their complete oxidative destruction is required by supplementing the reaction with applying UV or solar radiation. These UV/solar radiation acts as catalyst in the reaction and encouraging the recalcitrant contaminants to decompose them by appropriate break down (Figure 2.6). The photochemical AOPs are classified into two types based on the number on phases i.e. homogenous and heterogeneous photochemical AOPs.

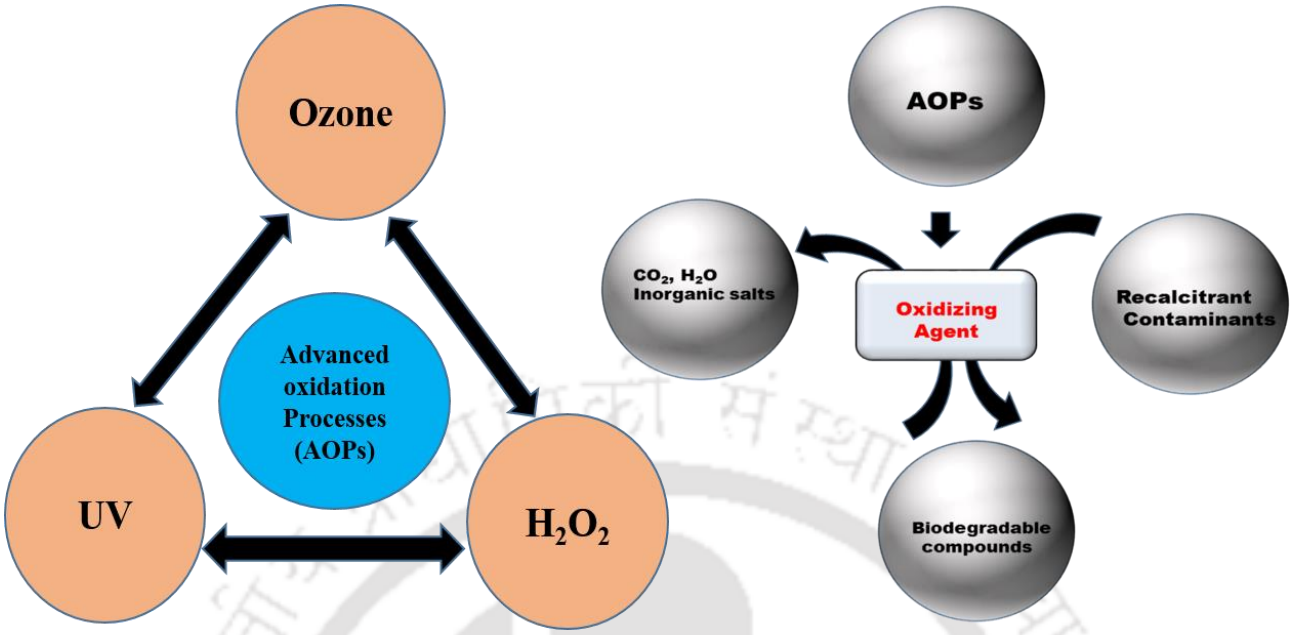

Fig. 2.6: Advanced oxidation process and the degradation processes of organic pollutants.

2.4.1.3.4. Homogenous photochemical AOPs

These methods are classified as (a) photolysis; (b) UV with hydrogen peroxide (UV/H_2O_2); (c) UV with ozone (UV/O_3); (d) UV with ozone and hydrogen peroxide (UV/O_3/H_2O_2); and (e) Photo-Fenton process. The photolysis process usually involves the use of a photo-oxidation reaction. The photon stimulates the electron of organic compounds from their ground state to an excited state, which further stimulates the oxygen molecules. The reaction rate of photolysis depends on the concentration of dissolved molecular oxygen, quantum yield and photon generation rate [63]. The reaction mechanism of the UV/H_2O_2 process is as follows (Eq. 2.10) [29]:

$$H_2O_2 + h\nu \rightarrow \ 2\bullet OH \tag{2.10}$$

Photolysis of O_3 with UV light in water solution produces H_2O_2 as an intermediate compound which further decomposes in •OH free radicals (Eq. 2.11 and 2.12 [64]).

$$O_3 + H_2O \xrightarrow{h\nu} H_2O_2 + O_2 \tag{2.11}$$

$$H_2O_2 \xrightarrow{h\nu} 2{\bullet}OH \quad (2.12)$$

O_3 has a very fast absorption rate of UV light and consequently produces a large number of •OH free radicals. In comparison to the UV/H_2O_2 process, the UV/O_3 process produces more •OH free radicals and enhances the treatment efficiency of wastewater. Further, a combination of the above three processes (UV/O_3/H_2O_2) appears to be most effective. In another approach, when Fe^{+2} and H_2O_2 are added in the presence of solar or UV radiations, the process is called as Fenton like system or photo-Fenton process, which improves the rate of decontamination than a non-photochemical Fenton process.

Lucas *et al.* performed the ozonation process for treatment of winery-based wastewater (Initial COD 4650 mg L^{-1}) and investigated the effectiveness of photolysis, O_3, O_3/UV and O_3/UV/H_2O_2 combined processes. Direct photolytic treatment was insignificant in COD removal while O_3 removed COD by 12 %, O_3/UV removed COD by 21 % and O_3/UV/H_2O_2 removed COD by 35 % at the optimized condition of pH 4, O_3 flow rate 100 mg min^{-1} for 3 hours [65]. In a similar study, Asaithambi *et al.* investigated AOPs with a different combination of UV, O_3, H_2O_2 and Fenton process for the treatment of distillery effluent containing initial COD of 1500 mg L^{-1}. The observed treatment efficiencies of various processes are listed in Table 2.2 [66]. These studies concluded that individual processes perform less efficiently as compared to their combinations. O_3/UV/Fe^{2+}/H_2O_2 process resulted in 100 % COD and colour removals at the optimized condition of pH 3, 100 mM of H_2O_2, 0.25 mM of Fe^{+2} and 240 min of reaction time consuming the least energy. As Asaithambi *et al.* have mentioned in the following table (table 2.2), "At the optimized conditions of pH 3, 100 mM of H_2O_2, 0.25 mM of Fe^{+2} and 240 min of reaction time, the electrical energy determination (kWh/m^3order^1) has been shown as 0.097 for UV/H_2O_2/Fe^{2+} and 0.01 for O_3/UV/H_2O_2/Fe^{2+}. Since the duration and colour removal (%)

are almost the same, the electrical energy consumption in $O_3/UV/H_2O_2/Fe^{2+}$ processes should be higher than in the $UV/H_2O_2/Fe^{2+}$ process."

Table 2.2: Performances of various AOPs along with energy requirements [Adopted from [66]]

Various AOPs process	Color removal (%)	COD removal (%)	Electrical energy determination (kWh/m^3 order^1)
O_3	39.62	29.17	0.64
O_3/UV	50.92	41.67	1.19
O_3/Fe^2	53.95	48	0.64
$O_3/UV/Fe^{2+}$	57.71	59	0.76
H_2O_2/Fe^{2+}	55.97	53.85	–
UV/H_2O_2	73.72	66.67	0.27
$O_3/UV/H_2O_2$	81.72	92	1.04
$UV/H_2O_2/Fe^{2+}$	100	99.99	0.097
$O_3/UV/Fe^{2+}/H_2O_2$	100	100	0.01

2.4.1.3.5. Heterogeneous photochemical AOPs

These processes are classified as (a) photocatalysis and (b) electro-Fenton process. Photocatalysis is a catalysis-based reaction occurs on a solid surface (semiconductor). In an aqueous suspension, energy equal or higher than the bandgap of the photocatalyst induces the charge separation process, which leads to the formation of the valence band hole (h^-) and conduction band (e^-) (Eq. 2.13). This electron-hole reacts with water to generate hydroxyl radicals by transferring the electrons (Eq. 2.14-2.16). Oxygen molecules present in water react with these electrons and contribute to the oxidation reactions [64].

$$TiO_2 + hv \rightarrow h^+ + e^- \quad (2.13)$$

$$e^- + O_2 \rightarrow O_2^{-\cdot} \quad (2.14)$$

$$H_2O + h^+ \rightarrow \bullet OH + H^+ \quad (2.15)$$

$$h^+ + OH^- \rightarrow \bullet OH \quad (2.16)$$

Semiconductor oxide photocatalysts (TiO_2, ZnO, CdS, ZnS, Fe_2O_3,) are proven to be outstanding catalysts for the mineralization of organic contaminants. Among them, TiO_2 and its alloys have received great attention because of their potential oxidizing activity, long-standing photostability, non-toxicity and cost-effectiveness. The combination of electrochemical oxidation with different photochemical process enhances the removal efficiency of pollutants [67]. This heterogeneous photocatalysis system is very robust and caused a quick degradation of melanoidin pigments into their intermediate products [68].

David *et al.* studied various combinations (pure kaolin, pure ZnO, ZnO/kaolin, light/ZnO, and light/ZnO/kaolin) for spent wash treatment (10 times diluted). Kaolin immobilized nano ZnO photocatalyst achieved the highest color removal (91 %) along with 35 % COD removal at pH 11 within 3 hours due to better surface adsorption and photocatalysis [69]. In another study photocatalytic color and COD removal of the distillery effluent was performed in the presence of solar light. TiO_2, H_2O_2 and their combination was examined for the treatment of diluted spent wash. Colour removal was observed 45 %, 70 % and 84 % in the presence of TiO_2, H_2O_2 and TiO_2/H_2O_2 along with solar radiation [70]. Table 2.3 shows the comparison study of photocatalytic degradation of various distillery effluents.

In the electro-Fenton process, the H_2O_2 and Fe^{+2} are generated electrochemically (concurrently or separately in the reaction). H_2O_2 are electro-generated by the reduction of dissolved oxygen and the ferrous ion (Fe^{+2}) generated by the reduction of ferric ion (Fe^{+3}) (Eq. 2.17-2.18) [71].

$$O_2 + 2H^+ + 2e^- \rightarrow H_2O_2 \quad (2.17)$$

$$Fe^{+3} + e^- \rightarrow Fe^{+2} \quad (2.18)$$

Davarnejad *et al.* reported that modified electro-Fenton process for treatment of spent wash (diluted) and removes the COD 69.29 % (unmodified electro-Fenton process removes only 51 % COD) at pH 2.84, a current density of 52 mA and reaction time of 70 min [72]. In a laboratory-scale experiment the Fenton, electro-Fenton and electrocoagulation process was examined on raw spent wash (initial COD 98400 mg L^{-1}), the colour removal efficiency was achieved 66 % by Fenton process (pH 3, 4 hours of treatment time), 44 % by electro-Fenton process (pH 3, current 4 A for 3 hours of electrolysis time) and 79 % by electrocoagulation process at the optimized condition (pH 7, 5 A current for 2 hours) [73].

Table 2.3. Literature review of photocatalytic degradation of distillery effluents.

Effluent type	Catalyst	Source of light	Time	% Degradation	Ref.
Vinasse wastewater	Nb_2O_5–TiO_2	Sunlight	5 days	80	[74]
Molasses wastewater	$PbWO_4$	HPMVL	2 hrs	90	[75]
Distillery spentwash	Ti electrode	Electro chemical	3 hrs	40	[76]
Molasses wastewater	TiO_2/$PbWO_4$	HPMVL	2 hrs	92	[77]
Vinasse wastewater	TiO_2 Anatase	Sunlight	24 hrs	40	[78]
Vinasse wastewater	TiO_2 P25	UV lamp	40 hrs	80	[79]
Distillery effluent	TiO_2	Sunlight	4 hrs	79	[80]
Distillery wastewater	TiO_2	UV lamp	25 days	85	[81]
Molasses wastewater	TiO_2/Zeolite	UV lamp	5.8 hrs	25	[82]
Distillery spentwash	Ag/TiO_2	Sunlight	4 hrs	74	[83]
Vinasse wastewater	TiO_2	UV lamp	48 hrs	22	[84]
Vinasse wastewater	TiO_2	Sunlight	3 days	86	[85]
Vinasse wastewater	TiO_2	UV lamp	3 hrs	95	[86]
Distillery wastewater	ZnO/kaolin	Visible light	3 hrs	71	[87]

2.4.2. Biological/microbial treatment

Several microorganisms such as bacteria, fungi, algae, etc., have also been used to break down complex, toxic, and recalcitrant compounds. Biological treatment approaches are eco-friendly and cost-effective. Thus, these organisms have also been applied to degrade the melanoidin pigment and treat distillery effluent.

2.4.2.1. Treatment of distillery effluent through bacterial

Different bacterial cultures have the ability to decolorize and bioremediate the distillery spentwash. In recent years, the treatment by pure bacterial culture has been frequently reported. *Bacillus sp*. was reported to decolorize distillery spentwash under the aerobic condition up to 35.5 % in 20 days at 55 °C [88]. Kumar *et al*. reported 84 % of COD removal (without aeration) in 4-5 days by a bacterial strain isolated from sludge [89]. Pseudomonas was isolated by Dahiya *et al.* from a reactor liquid and could decolorize the distillery wastewater up to 76 % in non-sterile conditions and up to 90 % in a sterile condition. The difference in the % decolorization could be due to the change in stability of melanoidin concerning pH and temperature. During the sterilization of the melanoidin compound at a higher temperature, the melanoidin pigments break into the low molecular weight compound [90]. Ohmomo *et al.* used calcium alginate immobilized *Lactobacillus hilgardi* cells to decolorize melanoidin pigments, resulting in 40 % decolorization. A limited amount of oxygen was continuously supplied by aeration for achieving the optimum decolorization[91]. Jain *et al.* isolated three bacterial strains *B. megaterium, B.cereus* and *B. fragairae* from the activated sludge of a distillery effluent, which removed color in the range of 38-58 % and COD in the range of 55-68 %, respectively [92]. Sirianuntapiboon *et al*. used waste fruit juice and vegetable samples to isolate an acetogenic strain, which showed the decolorization of spentwash 73-76 % in 5 days by providing the glucose and nitrogen source as a supplement. [93]. Patel *et al*. reported 26, 81 and 96 % decolorization of distillery spentwash through bio-flocculation by *Synechocystis sp., Lyngbya sp*. and *Oscillateria sp.,* respectively [94]. Ghosh *et al.* isolated some bacterial strain from the soil at the effluent discharge site, capable of degrading the recalcitrant compounds from anaerobically digested spentwash [95]. *Pseudomonas, Enterobacter, Stenotrophomonas,* and *Acinetobacter* were identified, all of which could degrade distillery effluent and a maximum of 44 % COD reduction was achieved either single

or collective use of the identified strains [96]. A detailed and comparative study of melanoidin treatment by various bacteria are listed in Table 2.4.

2.4.2.2. Treatment of distillery effluent through fungi

In recent studies, various ascomycetes and basidiomycetes fungi have been studied in the decolorization of distillery wastewater. The organic substances were consumed by the fungi and had the capability to purify the effluent substances i.e., spentwash, and also reduce the COD and BOD. In comparison to bacteria, fungi have less sensitivity to variations in environmental factors such as temperature, pH, nutrients, aeration, etc. [97]. The most studied fungi *Aspergillus sp*., for example, *A. niger, A. fumigatus, A. niveus, A. fumigatus* showed about 69-75 % decolorization of spentwash and 70-90 % COD reduction [98]. The *Coriolus sp. no. 20* from class basidiomycetes was the first strain used to remove color from the spentwash sample [99]. Ohmomo *et al*. obtained 80 % decolorization under optimum conditions in darkness used strain *Coriolusversicolour* Ps4a for spentwash decolorization. Fungi P.*decumbens* and *P. lignorum* belong to the ascomycetes group, resulting in 50 % color and COD reduction and 70 % phenol removal from distillery spentwash. Sirianuntapiboon *et al*. studied the strain *Rhizoctonia sp. D-90* which decolorized molasses and synthetic melanoidin pigments by 87.5 % and 84.5 %, respectively, under optimal conditions [100]. Malandra *et al.* studied color removal from spentwash by fungi *Aspergillus niger* and they found that 83 % of color was removed by biologically and 17 % by adsorption on the mycelium [101]. The anaerobically treated distillery has the capability to decolorize by the *Trametes versicolor*, it was found that the reduction in COD was 75 % and decolorization was 80 % [102]. Pant *et al.* recently isolated three fungal strains: *Penicillium pinophilum TERI DB*, *Pleurotusflorida EM 1303* and *Alternariagaisen TERI DB6*; these cultures showed the decolorization efficiency 50, 47 and 86 % of

spentwash [103]. Fungus *Coriolushirsutus* showed an Inhibitory effect on melanoidin decolorization by at the same time organic nitrogen and glucose were also required as a supplemented for increasing decolorization [104]. In another study, nitrogen was reported as the supplement and increased the activity of fungi *C. versicolour sp.* no. 20 [99]. Raghukumar *et al.* isolated a marine fungus *Flavodonavus*, and this fungus showed the decolorizing activity of spentwash up to 80 % [105]. *Aspergillus niveus* was used by Angayarkanni *et al*. for the decolorization of spentwash, and sucrose was used as the carbon source for the growth of strain in the effluent [98]. The decolorization efficiency in this study was due to alkaline condition (pH 9.0) and the melanoidin pigment which were more soluble in the acidic condition. In the acidic condition, the melanoidin pigments might be precipitated and removed easily [106]. In another study, a decolorization study of an aerobically treated spentwash and anaerobically treated (UASB) was performed by fungi, *Aspergillus* species isolated from the soil sample and 75 % decolorization was achieved. After the decolorization experiment, it was suggested that decolorization by fungi species was due to the breakdown of melanoidin pigments. The longer time duration for aeration period causes the adsorption of melanoidin pigments which result of endogenous respiration and death of cells, hence it reduces the decolorization efficiency after a long time [107]. A detailed and comparative study of various fungi involved in melanoidin treatment are listed in Table 2.4.

2.4.2.3. Treatment of distillery effluent through Yeast

A yeast called *Citeromyces* is the most studied organism for treating melanoidin-containing wastewater, and it has been shown to remove a lot of colour and organic matter [100]. Malandra *et al*. isolated a yeast that was able to reduce COD in synthetic wastewater by 95 % and 46 % in 24 hours [101]. Hansenula *et al.* isolated two yeast strains that were used to remove TOC from

wastewater of beet molasses spirits. They removed 25.9 % and 28.5 % of TOC from the wastewater without dilution, respectively [108]. Similarly, Phanerochaete *et al.* found removing color from MSW with white-rot fungi [109]. Another fungus, the basidiomycete *Coriolus sp*. No. 20 used glucose oxidase and showed 60 % of the colour removal [105]. A comparative study of melanoidin treatment through yeast are listed in Table 2.4.

Table 2.4. A detailed list of bacteria, fungi, and yeast tried for decolorization of distilled effluent.

Species	% Decolorization	% BOD decrease	% COD decrease	Type of sample	Parameters [Temp. (°C), pH, Time (Days), Conc.]	Ref.
Bacterial species						
Acetobacteraceti	76.4	58.5	35.5	Synthetic	Temp. = 30, pH = 6, Time = 5, Conc. = 1 %	[93]
Bacillus spp.	50.56	56.19	63.39	Synthetic	Temp. = 37, pH = 7, Time = 2, Conc.= 10 %	[110]
Pediococcus acidilactici B-25	79	94	85	Real	Temp. = 37, pH = 7, Time = 3, Conc. = 1 %	[111]
Pseudomonas aeruginosa	67		51	Synthetic	Temp. = 37, pH = 6, Time = 5, Conc. = 1 %	[112]
P. aeruginosa	67		50	Synthetic	Temp. = 37, pH = 7, Time = 5, Conc. = 4 %	[113]
P. aeruginosa	69	59.4	60.7	Synthetic	Temp. = 37, pH = 7.5, Time = 15, Conc. = 12.5 %	[114]
Pseudomonas putida	60		44.4	Real	Temp. = 37, pH = 7, Time = 5, Conc. = 30 %	[115]
Xanthomonas fragariae	75		81	Real	Temp. = 39, pH = 7, Time = 32, Conc. = 5 %	[92]
Fungal species						
Aspergillus niger UM2	80			Synthetic	Temp. = 39, pH = 5.5, Time = 27,	[97]
Aspergillus niveus	56	94	97.14	Synthetic	Temp. = 30, pH = 5.5, Time=5, Conc. = 0.5 %	[98]
Citeromyces sp. WR-43-6	68.91			Synthetic	Temp. = 30, pH = 6,	[100]

				Time = 8, Conc. = 2 %	
Coriolus versicolor sp no. 20	52	52	Real	Temp. = 30, pH = 7,	[99]
				Time = 9, Conc. = 10 %	
Flavodonflavus	80		Synthetic	Temp. = 35, pH = 5,	[105]
				Time = 8, Conc. = 10 %	
P. chrysosporium	56.81	54.21	Synthetic	Temp. = 30, pH = 5,	[116]
				Time = 6 Conc. = 5 %	
Penicillium sp.	30	52.1	Synthetic	Temp. = 30, pH = 5.5,	[117]
				Time = 7, Conc. = 2 %	
Phanerochaete chrysosporium	80		Real	Temp. = 30, pH = 6,	[118]
JAG-40				Time = 40, Conc. = 5 %	
Phanerochaete	55	48	Synthetic	Temp. =35, pH =5,	[119]
Chrysosporium				Time =8, Conc. = 2 %	
Pleurotus	37		Synthetic	Temp. = 30	[120]
florida					
Williopsissaturnus		43	Synthetic	-	[101]
strain CBS 5761					
Yeast species					
Candida tropicalis RG-9	75		Synthetic	Temp. = 30, pH = 6,	[121]
				Time = 12, Conc. = 1 %	
Citeromyces sp.	75		Synthetic	Temp. = 35, pH = 5,	[93]
				Time = 24, Conc. = 2 %	
Vyanobacteria	62		Real	Temp. = 35, pH = 5.5,	[122]
oscillotoriaboryana				Time = 7, Conc. = 5 %	

2.4.2.4. Treatment of distillery effluent through mixed consortium

During the last few years, several efforts have been applied to investigate all possibilities for the technology of aerobic wastewater treatment using cell immobilization [123]. Early experiments for wastewater treatment were restricted to using single bacterial cultures immobilized on solid surfaces to degrade particular organic or toxic compounds. After some time, the immobilized consortia of selected two or more culture strains were applied. After that, the activated sludge has been immobilized on many carriers and used to treat wastewater [124]. In a recent study decolorization of molasses-based spentwash without applying any additional nitrogen or carbon source using soil as an inoculum for mixed consortium source, 69 % decolorization was obtained using 12.5 % (v/v) melanoidin containing wastewater and 10 % (w/v) soil after 7 days incubation time [125].

2.4.2.5. Treatment of distillery effluent through phytoremediation approach

Treatment of distillery effluent by phytoremediation is a low-cost developing technique for treating melanoidin pigments, including removal of color, organic and inorganic pollutants of distillery effluents. [15, 125]. Kumar *et al.* used bacterium *Bacillus thuringiensis* to break down melanoidin components of the distillery effluent, followed by *Spirodelapolyrrhiza* to reduce organic and inorganic pollutants in a two-stage process [110]. A similar two-step treatment process used *B. thuringiensis* and *Typhaangustata* in a constructed wetland, reduced color, COD and 98-99 % of BOD after 7 days. In a recent study, a macrophyte named *Potamogeton pectinatus* was used for the removal of color and bio-accumulating the heavy metals from distillery wastewater [126]. In a constructed wetland *Typhalati pholia* used for the treatment of distillery effluent resulted in 47 % BOD and 78 % COD reduction in a period of 10 days, respectively [18]. Valderrama *et al.* reported 52 % color removal using a combined treatment

of two macrophytes *Lemnaminuscula* and *Chlorella vulgaris*, from distillery effluent. The microalgal treatment methods removed organic, inorganic matters and nutrients from wastewater and generate oxygen. The macrophyte present in wastewater consumes organic matter as nutrients and removes pollutants. These macrophytes have a very high potential for cleaning the wastewater and by using these plants in constructing a low-cost treatment technique is still at an experimental stage. In the future, phytoremediation approach can be considered as a potentially very important area of wastewater treatment and also in environmental management [15, 127].

2.4.2.6. Treatment of distillery effluent through cyanobacteria

Cyanobacteria are widely used in the industries for the color removal, and they are considered an ideal source for the breakdown of melanoidin pigment and reduction of the COD and BOD levels [15]. Kalavathi *et al*. reported a marine cyanobacterium for the treatment of distillery effluent and this bacterium strain could utilize the melanoidin pigments as a nutrient source for carbon and nitrogen. First, the microalgal treatment method removed the organic pollutants and further treatment with marine macrophytes removed the color, inorganic pollutants and precipitated the microalgae [122]. Saha *et al.* reported that a marine cyanobacteria *Oscillatoria willei*, when grown under low nitrogen content, showed increased oxidative stress with increased anti-oxidative enzymes such as laccase and superoxide dismutase, phenol oxidase, lignin peroxidase, catalase, ascorbate peroxidase, and peroxidase. They concluded that these enzymes are responsible for treating distillery effluent and decolorizingze the spentwash up to 52 % in 7 days using cyanobacterium *O. willei* [128]. Sankaran *et al.* have given the phytoremediation mechanism of distillery effluent. The coupling of the microalgal treatment process produces bioenergy, representing an important milestone with pollutant and nutrient

removal from distillery wastewater [129]. Travieso *et al*. used a laboratory-scale microalgal pond for the treatment of spentwash using *Chlorella vulgaris SR/2* in a previously digested AFBR. This *Chlorella vulgaris Sr/2* removed TSS 53.4 %, VSS 78.8 %, TS 60.6 %, BOD 88.0 % and COD 83.2 % from the effluent [130]. More recently, Solovchenko *et al.* reported phytoremediation of distillery spentwash with a novel strain *Chlorella sorokiniana* which was isolated from the sea. These algal strains showed the reduction of phosphate 77 %, nitrate 95 %, sulphate 35 % and COD 92.55 within 4 days [131]. Another marine cyanobacterium *Oscillatoria boryana* showed the decolorization efficiency of melanoidin pigment and crude pigment in the distillery effluents spentwash about 75 % and 60 %, at 0.1 % and 5 % concentration respectively, in 30 days [122].

2.4.2.7. Treatment of distillery effluent through actinomycetes

Until 1992, hardly known about the decolorization efficiency by applying actinomycetes for melanoidin-containing wastewater. However, Murata *et al.* found the strain of *Streptomyces werraensis* TT14, after screening about 75 actinomycetes. At the optimized pH 5.5 and 40°C for 4 days, the strain showed 64 % decolorization activity [132].

2.4.3. Treatment of distillery effluent using miscellaneous reactors

Some conventionally used reactors like single and biphasic fixed-film reactor, high rate upflow anaerobic sludge blanket reactors (UASB), continuous stirred tank reactors (CSTR) etc. have become more commercialized for the treatment of different types of wastewaters including distillery wastewater in recent few years [133]. The UASB reactors have a high rate of anaerobic wastewater treatment capacity, which is mainly applied for the treatment of distillery wastewater in worldwide. The efficiency and function of UASB reactors depend on various

factors such as temperature, concentration, pH, organic loading rate and the composition of wastewater, etc. Distillery wastewater treatment has been testified in both single system and as well as in a biphasic system, which results in an effective reduction in COD and BOD [134]. Tansengco *et al.* reported the COD and BOD reduction 60 % and 86 % with methane gas production throughout the treatment of distillery wastewater in ASBR at the 8 h reaction time [135]. In a recent study, Wolmarans *et al.* reported 90 % COD removal from DWW using UASB reactor [136]. Yu *et al.* reported 82 % COD removal using laboratory condition of DWW by up-flow anaerobic filter, ranging the temperature from 19 to 27 °C and HRT of 8 h from DWW [137]. High organic content makes anaerobic treatment more appealing than aerobic treatment for molasses-containing wastewater than other types of waste treatment. Anaerobic digestion is a complex ecosystem in which different microorganisms work together. There is a lot of methane and carbon dioxide production in the process [138]. Molasses wastewater treatment with an anaerobic process is a very promising new technology with many advantages over traditional aerobic treatment. It doesn't make a lot of sludge, uses less energy, and can be used with a lot of organic material; additionally, biogas generation can be used for energy needs [139]. Further, low nutrient needs and stable sludge production are two more benefits [140]. Anaerobic microbes have a slow growth rate, which means longer hydraulic retention times (HRT). Several high rate reactors have been used to treat wastewater at shorter HRTs to solve these problems [141].

In this regard, the treatment of molasses-containing wastewater by anaerobic lagoons is the best choice. Rao *et al.* did the first research in distillery waste management by using anaerobic lagoons resulting in a BOD removal rate of 92 % [142]. However, lagoon systems require significant space, smell bad, and there's a chance of groundwater pollution [143]. Continuous stirred tank reactors (CSTR) are the closed reactor's most straightforward digesters with the gas collection. Treatment of molasses wastewater in a CSTR has been reported in both single

and biphasic operations, with COD reductions of up to 90 % in 10–15 days [144]. An anaerobic sequencing batch reactor (ASBR) was also investigated for winery wastewater treatment. The reactor operates at an OLR of 8.6 kg COD m^{-3} d^{1} with a soluble COD removal efficiency of more than 98 % and an HRT of 2.2 days [145]. Banerjee and Biswas made a semi-continuous batch digester for biomethanation of distillery waste at different temperatures. At a BOD loading rate of 2.74 kg m^{3} of achieving 86 % of BOD reduction and 73.23 % methane production at 50 °C [146]. Table 2.5 shows how anaerobic reactors work for lab experiments and profitable operations that clean up waste from alcohol-based distilleries.

Table 2.5. List of reactors used for decolorization of distillery effluent.

Reactors							
Reactor type	**SW Conc. (%)**	**Initial BOD (g L^{-1})**	**% BOD removal**	**Initial COD (g L^{-1})**	**% COD removal**	**HRT (Days)**	**Ref.**
Anaerobic contact filter	10	58	-	120	73 to 98	4	[147]
Anaerobic filter and UASB	10-30	24-27	-	49-53	90	1.3	[148]
Anaerobic granular sludge reactor	5	-	-	-	80 - 90	1	[149]
Diphasic (upflow) fixed film reactor	-	45-60	-	70-98	67.1	4	[150]
Downflow fluidized bed reactor	-	-	-	-	85	1.3 to 3.3	[151]
Granular bed anaerobic baffled reactor (GRABBR)	10-25	9-30	90	17-58	82 to 92	4	[152]
Thermophilic UASB reactor	-	-	-	-	87	0.3	[153]
UASB	-	-	-	-	75	-	[154]
UASB	-	-	-	45-50	93	1 to 1.5	[136]
Upflow anaerobic fixed film bioreactor	-	50-60	56	110-190	64	8	[155]
UASB	-	-	-	-	90 - 95	-	[156]
UASB	-	-	80	-	39 to 67	-	[157]

2.4.4. **Treatment of distillery effluent through activated sludge process**

The activated sludge process is the most common way to deal with wastewater. Research is focused on improving the reactor configuration and performance. For example, an aerobic sequencing batch reactor (SBR) was said to be an excellent way to deal with waste from small wineries [158]. Due to the higher efficiency of aerobics systems, many researchers have been treating them with pure cultures even though the treatment of molasses containing distillery wastewater is treated by conventional activated sludge, which reduces higher COD load and energy consumption.

Heterotrophic microorganisms break down carbonaceous materials through the aerobic pathway, depending on the availability of organic materials and the presence of inorganic materials that help them grow. This process is called bio-composting. Composting is very good at turning wet materials into something that can be used. This makes the organic materials more stable and kills the pathogenic organisms after significantly drying the wet substrates. In the process of composting, organic wastes that are at least 40 % moisture content are broken down by thermophilic organisms to make durable, hummus-like materials [159].

2.4.5. **Potential enzymatic treatment of distillery wastewater**

Even though the enzymatic degradation of melanoidins is not entirely known, it seems to be very important for melanoidin degradation. The white-rot fungi have a complex enzymatic system that is extracellular and non-specific. Under lack of nutrients, they can break down ligninolytic compounds, melanoidins, and polyaromatic compounds that other microorganisms can't break easily [59]. Many enzymes from plants and microorganisms from all over the world have been found to be important in a wide range of waste treatment applications. Several studies have shown that basidiomycetes can break down melanoidins, humic acids, and other

compounds with the help of at least one laccase enzyme from fungi in the family *Trametes (Coriolus) [160]*. Ohmomo *et al.* used *C. versicolour* Ps4a, which removed 80 % of the colour from molasses wastewater in the dark under the optimized conditions [161]. Sugar-dependent and sugar-independent intracellular enzymes were used to remove the colour. Few of these enzymes didn't need sugar or oxygen to work and could change the colour of melanoidin containing wastewater up to 20 % in the dark [161]. These enzymes produce H_2O_2, part of a complex enzymatic system that fungi use to break down melanoidin. Miyata *et al.* conducted detailed enzyme studies on melanoidin decolorization. They found the melanoidin removal by involvement of peroxidases and extracellular H_2O_2 produced by glucose-oxidase, in the presence of small amount of fungal laccase *C. hirsutus* [104]. Similarly, after inoculating with the fungus *Trametes sp.* I-62, Mansur *et al.* saw a maximum decolourization of about 60 % on day 8 [162].

2.4.6. **Effect of environmental factors on the treatment process**

Many environmental factors affect the activity of enzymes in the process of microbial decomposition of industrial waste. These environmental factors include the source of carbon, nitrogen, potassium, pH, temperature, air, and inoculum [93, 110]. Hayase *et al.* applied H_2O_2 at pH 3 to 13 and at optimized pH of 10, achieved 94 % of melanoidin degradation [163]. Mohana *et al.* found that at pH 7.0, the most decolorization happened and reported that melanoidin is less soluble in acidic pH than in alkaline pH. They stated that if the pH is more or less than pH 7.0, the decolorization activity and the growth of microbes both decreased, which is why they found the most decolorization at pH 7.0 [112]. In another study. Color removal (80 %) and COD removal (75 %) were the best when the pH was 5 [59]. They also found that the temperature rises from 20°C to 37°C, which led to a rise in decolorization from

35 % to 67 %. When the temperature rose above 40°C, the ability of microbes to remove melanoidin was lost. The strain D90 grew best and removed the most colour at 30°C, while *Coriolus versicolor* grew best at 35°C and *Phanerochaete chrysosporium* grew best at 40°C and effectively removed the colour [164, 165]. Having a carbon source is essential for mold growth and eliminating melanoidins from the soil. The researchers who looked at the effect of different carbon and nitrogen sources on the MDA of *Aspergillus fumigatus* G-2-6 found that glucose was the best carbon source for the maximum degradation of melanoidins [166]. There were a lot of different nitrogen sources, including yeast extract, peptone, beef extract, and tryptone; these all reduce the level of decolorization. It has also been found that the decolorization of melanoidins increases with the size of the inoculums. The maximum decolorization was reached at 15 % (v/v) inoculum size (about 11×10^6 CFU mL^{-1}), and further increases in inoculum size did not improve the decolorization of melanoidins [112]. Dahiya *et al.* found that 5 % (w/v) dry weight *Phanerochaete chrysosporium* JAG-40 mycelial suspension in melanoidin medium with glucose and peptone was best for maximum decolorization [90].

2.4.7. **Production of alternative metabolites**

To increase its value, valuable and/or beneficial substances can be extracted from raw material. Value-added products such as eco-friendly biopolymer, polyhydroxyalkanoates (PHAs), fermentative hydrogen production and biosurfactants; can be extracted depending upon the raw material. The concentration of bioactive compounds in fermented for ethanol production is influenced by various factors such as genetic and environmental factors and exposure of substrates to stress [167]. As a result, selecting the best settings for the recuperation process is critical. Liquid-liquid extractions and solid-phase extractions are the most popular substrate

recovery procedures [168]. Various organic solvents such as acetone, ethyl acetate, methanol, ethanol, propanol, and their multiple combinations are employed to recover value-added products. Green chemistry-compliant recovery methods are increasingly in demand because of their environmental benefits. Therefore, new green procedures and solvents are being studied to retrieve valuable chemicals [167, 169]. However, there are several limitations to using supercritical fluids, such as a limited range of molecular solubility, high costs of equipment, and cleaner effluent generation. In other words, this technology has extensive exposure and lots of challenges. Alternatively, it may be possible to use biomass-derived solvents such as ethyl lactate, glycerol, or 2-methyl tetrahydrofuran as an alternative option. These solvents are renewable, non-toxic, and inexpensive in nature; however, their application possibilities are limited [170]. According to the above assertion, researching and creating environmentally friendly solvents to improve extraction efficiency is difficult. Bioethanol, a bio-solvent produced through alcoholic fermentation of sugar or starch-containing food wastes, is commonly utilized in traditional solvent extraction [171]. Reduced energy consumption and the application of nontoxic solvents should be characterized as environmentally friendly extraction along with high-efficiency substance recovery, which would appear to be a potential approach toward long-term manufacturing.

Table 2.6. Comparisons study of different treatment methods of distillery wastewater.

Treatment technology		Advantages	Disadvantages
Biological treatment method	Anaerobic Aerobic Bacterial Fungal	Eco-friendly Cost-effective	High dilution requires Time-consuming Very slow process Required large space
Treatment using other organisms	Yeast Microalgae Cyanobacteria	Used photosynthesis for energy No use to add nutrients Biogas or biodiesel are produced By-products are used as a fertilizer	The growth rate is very slow Light-dependent process
Physico-chemical treatment method	Adsorption Coagulation/ Flocculation Photocatalysis Oxidation process	Simultaneous adsorption and degradation of many pollutants Widely accepted Simple and cost-effective Significant color removal Removal of other contaminants Used low-cost chemicals Enhances filtration process Oxidized the broad range of organic compounds These methods can be applied over AOP, so it can be used either in the pretreatment process or in the final treatment process Separates many kinds of organic pollutants and particles from wastewater	pH-sensitive Temperature-sensitive Use of chemicals Sludge generated High energy lost Must be fully oxidized The commercially available adsorbent is very costly

2.5. **Conclusions**

In general, these hazardous by-products/wastes of distillery effluent have an unfavorable effect on the environment when discharged into the environment without treatment [79]. Removing these organic-inorganic pollutants and color from this distilleries wastewater is essential from the environmental and aesthetic point of view [18]. Conventional methods like oxidation, coagulation, membrane filtration, precipitation, adsorption, and biological treatments are employed to decolorize the wastewater and reduce the residual organic load. A conclusive table

along with the advantages and disadvantages of physiochemical and biological treatment methods for distillery effluent treatment are listed in Table 2.5. But these methods or techniques are generally not viable or lead to incomplete treatment of the organic and inorganic compounds present in it [172]. So, the distilleries need a robust method with the incorporation of new techniques along with the existing approaches to solve these issues.

Chapter 3

Melanoidin removal by biosorption using low cost and biogenic adsorbents

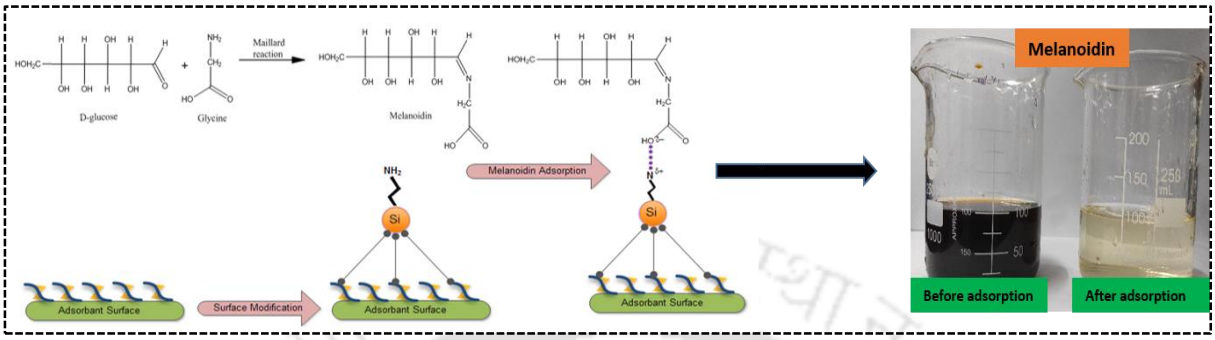

(Enhanced melanoidin removal by amine-modified Phyllanthus emblica leaf powder. ***Rahul Verma****, L.M. Kundu, and L.M. Pandey (2021),* ***Bioresource Technology****, 339, 125572)*

In this chapter, melanoidin was removed through adsorption using amine surface-modified *Phyllanthus emblica*, *Citrus limon* and *Tamarindus indica* leaf powder as a low-cost natural adsorbent. The amine-modified adsorbents were prepared by forming self-assembled monolayers (SAMs). The experimental conditions (pH, temperature and adsorbent dose) were optimized using the Response Surface Methodology-Central Composite Design (RSM-CCD) to maximize the adsorption capacity. The modified leaf-powder was characterized using various analytical techniques such as FTIR, EDX, FESEM, TGA, etc. The design tool plotted the 3D response under the optimized condition of temperature, pH, and adsorbent dose on melanoidin.

3.1. Introduction

As discussed in chapter 2, various physical, chemical and biological methods have been applied to treat distillery wastewater. The biological techniques such as bacterial, fungal, and algal treatment methods have also been applied to remove the melanoidin compounds before

discharging them into the environment [9]. However, the treatment efficacies of these methods are quite low due to the poor biodegradability of melanoidin [10]. Thus various alternatives to conventional methods such as the use of activated carbon, electrochemical degradation, integrated biochemical adsorption, oxidation, coagulation, membrane filtration, Fenton and photo-Fenton process have been applied for melanoidin removal [11]. The drawbacks of these methods include higher operational and maintenance costs, a requirement of a large number of chemicals, generation of by-products (secondary waste) in large amounts and various harmful effects on the ecosystem.

Among different physical methods, adsorption is the most explored process because of its simplicity, effectiveness, and economic viability [173]. In this direction, several methods have been used to treat melanoidin by applying natural materials as adsorbents over conventional materials such as activated charcoal, bagasse, slag, clays, and various plants and wood-based adsorbents promising as cheap, effective and eco-friendly [174, 175]. Different kinds of plant and agro-waste biomass have been investigated for melanoidin adsorption. Arulmathi *et al*. used activated carbon prepared from *Piper nigrum* to decolorize the distillery spentwash. The maximum removal was 75 % at the optimized condition of pH 7.5 after 195 min of contact time [176]. Similarly, Wongcharee and Aravinthan applied mesoporous magnetic nano-sorbent derived by macadamia nutshell for melanoidin adsorption and the maximum adsorption capacity was achieved 14.7 mg g^{-1} at the temperature of 41.7 °C, pH of 6.3 and 240 min of contact time [175]. Ahmed *et al.* utilized fly ash as an adsorbent for melanoidin and achieved 281 mg g^{-1} of maximum adsorption capacity with 84 % of melanoidin removal at pH 6 and 120 min of contact time [174]. However, a lower adsorption capacity of bio-sorbents limits their practical applications and thus researchers are exploring this aspect.

Surface properties of the adsorbents regulate the interfacial interactions among adsorbent, solvent and adsorbate and thus can be tuned by surface modifications. The plant leaf-based

adsorbents of different trees contain various organic and inorganic compounds such as lignin, pectin, cellulose, hemicellulose, and various functional groups such as amino, nitro hydroxyl, carbonyl and carboxyl [177]. It has been reported that multiple intermolecular forces, including van der Waals, hydrogen bonding and electrostatic regulate the adsorption process. Hence, activating adsorbent materials by treating different chemical methods such as acid, base, inorganic and organic salts and self-assembled monolayers (SAMs) significantly improve the effectiveness and adsorption capacity [178]. SAMs are formed spontaneously on surfaces through van der Waals interactions, ionic interactions and covalent bonding, which impart stability in an aqueous environment. Different SAMs like CH_3, NH_2 and COOH has been reported to alter the hydrophobicity and charge [179-182].

In the present chapter, *Phyllanthus emblica*, *Citrus limon* and *Tamarindus indica* leaves were investigated for the removal of synthetic melanoidin. *Phyllanthus emblica*, *Citrus limon* and *Tamarindus indica* are common medicinal plants widely distributed in tropical and subtropical areas of Asia, Africa, Australia, and South America. The surfaces of leaf powder were modified by forming self-assembled monolayers (SAMs) to enhance the surface adsorption capacity. The experimental conditions (pH, Temperature and adsorbent doses) for maximum adsorption capacity were optimized by employing the Response Surface Methodology-Central composite design (RSM-CCD) method. The novel amine-modified leaves powder was characterized by several techniques such as Fourier-transform infrared spectroscopy (FTIR), Differential Scanning Calorimetry/ Thermo Gravimetric (DSC/TG), Brunauer–Emmett–Teller (BET) surface area analyzer, Energy dispersive spectrum (EDX), Field Emission Scanning Electron Microscope (FESEM) and Dynamic Light Scattering (DLS). Equilibrium isotherms were studied by Langmuir, Freundlich and Temkin model to investigate the maximum adsorption capacity of modified adsorbent while kinetic studies for adsorption were also tested by pseudo-first-order, pseudo-second-order, intra-particle diffusion, and Elovich models to investigate the

effect of change of Physico-chemical properties on the adsorption process. Thermodynamic and reusability were also studied to find the role of temperature and efficiency of bio-adsorbent. The effectiveness of the modified leave powder of these plants was also evaluated for decolorizing the actual spentwash.

3.2. Material and methods

3.2.1. Materials

3-aminopropyl-triethoxysilane (APTES) (APTES, Cat. No. 440140) was purchased from Sigma Aldrich, India and used for the formation of amine self-assembled monolayers (SAMs). Glucose (Cat. No. GRM077) and Glycine (Cat. No. MB013) were obtained from HiMedia Laboratories, India for the synthesis of melanoidin. Ferrous ammonium sulfate (Cat. No. GRM302), potassium dichromate (Cat. No. GRM1033), mercuric sulphate (Cat No. GRM1088) and silver sulphate (Cat. No. GRM1412) were purchased from HiMedia Laboratories, India and used for the analysis of chemical oxygen demand (COD). Ethyl alcohol (Cat. No. 64–17-5) was purchased from Merck, India and sulfuric acid (Cat. No. 7664–93-9) was procured from Finar Limited, India.

3.2.2. Sample collection and preparation of the adsorbent

Phyllanthus emblica, Citrus limon and *Tamarindus indica* leaves were collected from the rural areas of Pratapgarh district, Uttar Pradesh, India. The collected leaves were washed several times with deionized water to remove the dust particles and impurities from the surfaces and dried under sunlight for 48 h and stored in a hot air oven at 50 °C. The dried leaves were grounded with the help of a grinder to form the fine powder. The powder was sieved using a

sieving machine having a pore size of 300 μm to separate the large particles and fibers. These fine leaf powders were stored in a closed container for further modification. The powder was kept overnight in a 10 % sulfuric acid solution in a ratio of 1:4 (w/v) to remove the cellulose content, chlorophyll pigments, etc., and increase the adsorption capacity. Further, it was washed thoroughly with deionized water until neutral pH was obtained. The acid-treated powder samples were oven-dried at 110 °C for 24 h until the constant weight was conquered [183, 184].

3.2.3. Surface modification of adsorbent

The surface of acid-treated powder was modified by forming self-assembled monolayers (SAMs) of amine (NH_2) according to our reported methods [179, 185]. Briefly, the activated PELP were dipped in 1 % (v/v) APTES silane solution prepared in anhydrous toluene under an inert N_2 atmosphere inside a closed glove bag for 24 h at room temperature (25 °C). After modification, samples were twice washed with absolute ethanol (99.9 %) and oven-dried at 70 °C.

3.2.4. Characterization of adsorbent

The presence of functional groups was analysed using Fourier-transform infrared (FTIR) after preparing potassium bromide (KBr) discs. The surface morphology and Elemental investigation of samples were examined by and Field Emission Scanning Electron Microscope (FESEM) (Zeiss-Sigma 300), and energy dispersive spectrum (EDX) (Zeiss-Sigma), respectively. The surface charge of samples in de-ionized water was analyzed using Dynamic Light Scattering (DLS) (Anton Paar, Litesizer 500). The specific surface area and porosity were investigated using Brunauer–Emmett–Teller (BET) analyzer (Quantachrome, Autosorb-IQ

MP). 90 mg of sample was stored in a glass crucible and kept for degassing at 150 °C for 4 h to achieve the constant weight. After degassing, the final weight was measured and analyzed for surface area analysis [186]. The thermal stability of modified powder was investigated using Thermo Gravimetric analysis (TGA) (Netzsch, STA449F3A00) in a temperature range of 0 to 600 °C with an increment of 10 °C/min.

3.2.5. Preparation of melanoidin

Synthetic melanoidin pigments were prepared using amino acids and sugars. 0.05 M glycine (18.75 g) and 0.05 M of Glucose (45 g) were dissolved in 100 mL of distilled water. The solution was kept at 125 °C in the oven for 2 h [187]. The chemical reaction is stated as Eq. (3.1). Prepared melanoidin was then transferred into a mortar pestle and ground into a very fine powder. The prepared melanoidin was stored in a closed airtight container.

$$Amino\ acid + Sugar \xrightarrow[(High\ temperature\ (120-150℃))]{Maillard\ reaction} Melanoidin \quad (3.1)$$

3.2.6. Optimization of the experimental conditions by response surface methodology (RSM)

Optimization of environmental conditions for the maximum decolourization was carried out by applying RSM technique. RSM is an empirical technique that involves mathematical and statistical calculations to evaluate the actual and experimental data. Minitab statistical software and Central composite design (CCD) were applied to design the experimental set-ups. In this chapter, three independent variables such as temperature (A), pH (B) and adsorbent doses (C) were varied in the range of 25–55 °C, 3–11 and 0.2–2.0 % w/v, respectively. Decolourization (%) of the melanoidin solution was considered as a response. The software suggested a total of

20 experimental conditions by applying these independent variables as listed in Table (3.2) to predict the most suitable conditions for obtaining maximum removal (decolourization) on the adsorbent. The obtained experimental data was applied in Analysis of variance (ANOVA) software to get the regression analysis.

3.2.7. Adsorption studies

The batch adsorption experiments were performed at the suggested experimental conditions by RSM-CCD in 100 mL of 0.5 % w/v melanoidin solution in a 250 mL conical flask. All experimental setups were incubated in a shaker incubator (Scigenics Biotech-Orbitek) for 5 h and 180 rpm. After the adsorption, samples were collected and centrifuged at 10000 rpm for 10 min at 25 °C temperature using a centrifuge (Sigma 4–16 K) [188]. The optical density (OD) of the supernatant was measured at 475 nm to estimate the concentration of melanoidin [189]. The % removal of melanoidin was calculated by the following equation (Eq. 3.2).

$$\% \, Decolorization = \frac{(C_i - C_f)}{Ci} \times 100 \qquad (3.2)$$

where c_i and c_f are the concentrations of melanoidin solution before and after adsorption, respectively.

In addition, the closed reflux process followed by a titrimetric method analysed for chemical oxygen demand (COD) values of untreated and treated samples. The protocol for COD analysis of the samples was followed from the American Public Health Association (APHA) manual [190].

3.2.8. Equilibrium and kinetic studies of adsorption

The adsorption process of melanoidin on surface-modified *Phyllanthus emblica* leaf-powder (PELP), *Citrus limon* leaf-powder (CLLP) and *Tamarindus indica* leaf-powder (TILP) were examined at the optimized conditions predicted by RSM-CCD. The samples were collected at different time intervals till 300 min for the kinetic studies. The equilibrium adsorption studies were performed at optimized conditions by varying the adsorbate concentrations in the range of 0.1 to 1.0 % w/v. Adsorption kinetic models were tested by pseudo-first-order, pseudo-second-order, intra-particle diffusion, and Elovich models to investigate the rate parameters [191]. The four classical adsorption isotherm models such as Langmuir, Freundlich, Temkin and Dubinin–Radushkevich were employed to analyze the equilibrium behavior [192]. The adsorption experiments were also carried out at different temperatures (25, 35, 45 and 55 °C) to decipher the thermodynamics of the process. The expressions used for the kinetic and equilibrium models are listed in Table 3.1.

Table 3.1. Isotherm/kinetic/thermodynamic models, linear expression forms, and their plots.

Models	Linear expression	Plot
	Kinetic models	
Pseudo 1st order	$ln(q_e - q_t) = \ln(q_e) - k_1 t$	$t\ vs. ln(\ q_e - q_t)$
Pseudo 2nd order	$\frac{t}{q_t} = \frac{1}{k_2 q_e^2} + \frac{t}{q_e}$ $h = k_2 q_e^2$	$t\ \ vs.\ \ \frac{t}{q_t}$
Intra-particle diffusion	$q_t = k_p t^{1/2} + C$	$t^{1/2}\ vs.\ q_t$
Elovich models	$q_t = \frac{1}{\beta}\ln(\alpha\beta) + \frac{1}{\beta} lnt$	$lnt\ vs.\ q_t$
	Isotherms	
Langmuir	$\frac{C_e}{q_e} = \frac{C_e}{q_m} + \frac{1}{K_L q_m}$	$C_e\ vs.\ \frac{C_e}{q_e}$
Freundlich	$lnq_e = lnK_F + \frac{1}{n} lnC_e$	$lnC_e\ vs.\ lnq_e$
Temkin	$q_e = \frac{RT}{b_T} lnK_T + \frac{RT}{b_T} lnC_e$	$lnC_e\ vs.\ q_e$
Dubinin–Radushkevich	$lnq_e = lnq_m - K_{ad} \in^2$ $\in = RTln\left(1 + \frac{1}{C_e}\right)$	$lnq_e\ vs.\ \ \in^2$
Thermodynamic	$\Delta G = \Delta H - T\Delta S$ $\Delta G = -RTlnK_c$ $log\ K_c = \frac{\Delta S}{2.303R} - \frac{\Delta H}{2.303RT}$	$\frac{1}{T}\ vs.\ log\ K_c$

Here, q_t (mg g^{-1}) is the amount of melanoidin adsorbed per gram of adsorbent at a time interval of t. k_1 (min^{-1}) is the pseudo-first-order rate constant. k_2 (g mg^{-1} min^{-1}) refers to the pseudo-second-order rate constant and h (mg g^{-1} min^{-1}) is defined as the initial adsorption rate of pseudo-second-order and calculated as $h=k_e q_e^2$. k_p (mg g^{-1} $min^{-1/2}$) is the intra-particle diffusion rate constant, c is a constant. α (mg g^{-1} min^{-1}) and β (g mg^{-1}) are the initial adsorption rate and Elovich constant, respectively.

C_e (g L^{-1}) is defined as the equilibrium concentration of adsorbate and q_e (mg g^{-1}) is the amount of melanoidin adsorbed per gm of the adsorbent at the equilibrium. q_m (mg g^{-1}) refers to the maximum adsorption capacity of the adsorbent and K_L (L mg^{-1}) is the Langmuir isotherm constant. K_f (mg g^{-1}) is the Freundlich constant and n (L $g^{-1})^{1/n}$ denotes the adsorption intensity. b_T is defined as Temkin constant related to the heat of adsorption (J mol^{-1}) and K_T is Temkin isotherm equilibrium coefficient (L g^{-1}). K_{ad} and $\in$ are expressed as adsorption energy constant (mol^2 J^{-2}) correlated to the mean free energy and Polanyi potential related to the equilibrium constant in the D-R isotherm model, respectively. ΔG (J mol^{-1}), ΔH (J mol^{-1}), and ΔS (J mol^{-1} K^{-1}) refer to the change in Gibbs free energy, enthalpy and entropy, respectively, while K_c is expressed as q_e/C_e. R and T are the universal gas constant (8.314 J mol^{-1} K^{-1}) and temperature (K), respectively.

3.2.9. Regeneration and reusability study

Regeneration and reusability are essential factors of any adsorbent, which indicate their economics and feasibility for actual applications. Reusability study was investigated using 0.1 M NaOH solution [193, 194]. After the adsorption, the adsorbents were separated by centrifugation at 10000 rpm for 10 min. The pellet was placed in 30 mL of 0.1 M NaOH solution at 180 rpm and 25 °C for 120 min. Then, the adsorbent was separated from the NaOH solution and rinsed in distilled water several times to neutralize (pH 7). The washed adsorbent was dried in an oven at 70 °C for overnight. The dry weight of the adsorbent was noted and the dried adsorbent was reused for the next cycle of adsorption study under the same conditions.

3.2.10. Colour removal of the real sample (spentwash)

An industrial-based real spentwash sample was collected from DCM Shriram Ltd, a sugar cane molasses-based distillery plant in Hardoi, India. The spentwash samples were contained in a mouth-capped glass bottle and stored in a cool and dry place for further analysis. It was brown colour effluent with acidic pH (4.8) and very high COD (193 ± 1 g L^{-1}). 1 % v/v spentwash was used for the colour removal at the optimized conditions and % decolourization was analyzed as discussed in section 3.2.7.

3.3. Results and Discussion

3.3.1. Characterization of surface-modification

FTIR analysis of unmodified and modified powder was conducted to confirm the formation of amine SAMs as shown in Figure 3.1. The appearance of new characteristic peaks confirmed the presence of the amine group. Peak position at 1196 and 1585 cm^{-1} in PELP indicated the C–N stretching and N-H bending vibrations of the amine group and similarly the peak position at 1215 cm^{-1} in CLLP marked the C–N stretching of the amine group, respectively [42, 47]. While the peak at 1514, 1516 and 1515 cm^{-1} reflected the presence of stretching vibration of the nitro group (N-O) in PELP, CLLP and TILP, respectively [47]. This confirmed the successful surface modification with amine SAMs.

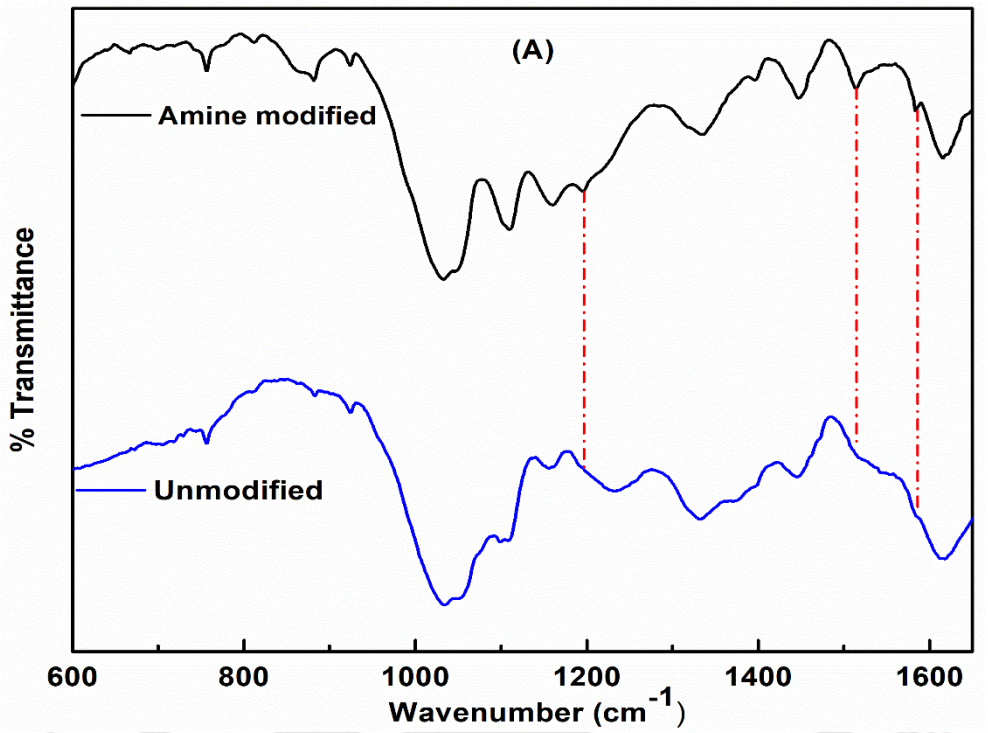

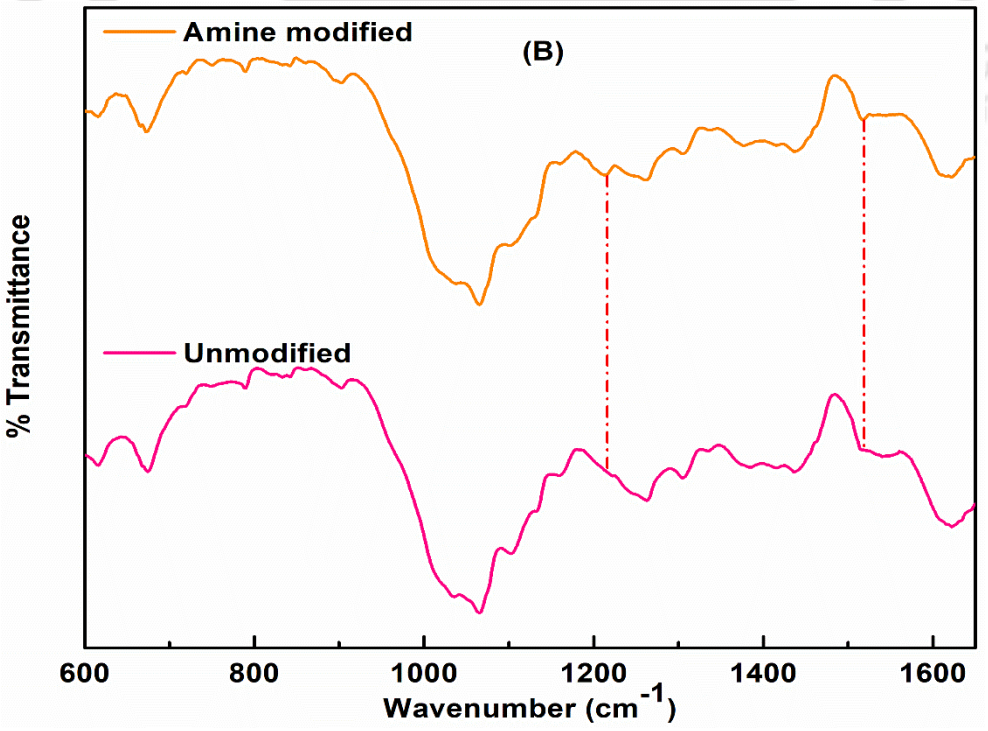

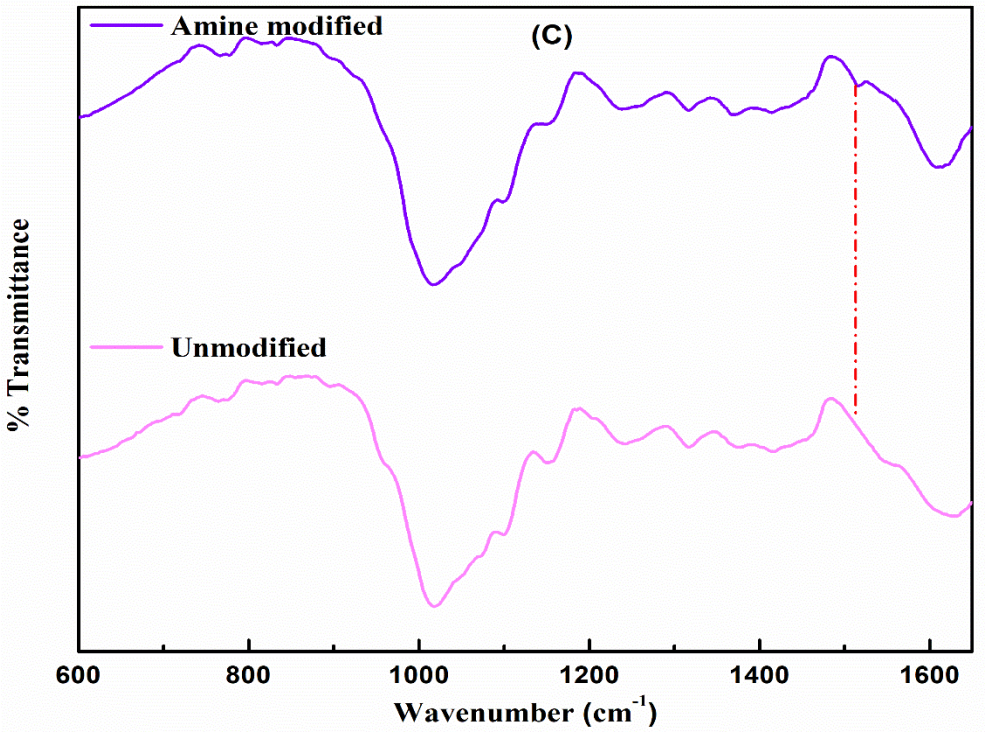

Fig. 3.1: FTIR spectra of unmodified and amine-modified (A) PELP (B) CLLP and (C) TILP.

3.3.2. Thermal stability, surface area and pore size analysis

The thermostability of modified powders was analyzed using TGA in the range of temperature 0 to 600 °C. The thermal behavior of modified PELP, CLLP and TILP can be classified into three phases as shown in Figure 3.2 (A, B and C). In PELP, the first phase was observed between the temperature 0-100 °C, indicating the slight weight loss (≤ 10 %) due to moisture removal. The second phase was between 100-180 °C and no substantial weight loss (≤ 2 %) was observed, indicating thermal stability up to 180 °C. The last phase was noted from 180-600 °C, in which a rapid weight loss was observed due to thermal degradation [19]. Similarly, in the case of CLLP and TILP, the first phase was observed between the temperature 0-260 and

0-120 °C, indicating the weight loss of ≤ 10 and ≤ 15 % due to the removal of moisture. In the second phase CLLP showed sudden weight loss of weight upto 300 °C while the TILP showed the thermostability upto temperature 220 °C. The last phase in both the plants showed thermal degradation. Using a BET analyzer, the surface area and pore size of PELP, CLLP, and TILP were determined and found to be 25.28, 21.79, 17.24 $m^2 g^{-1}$ and 83, 47, 19 nm, respectively.

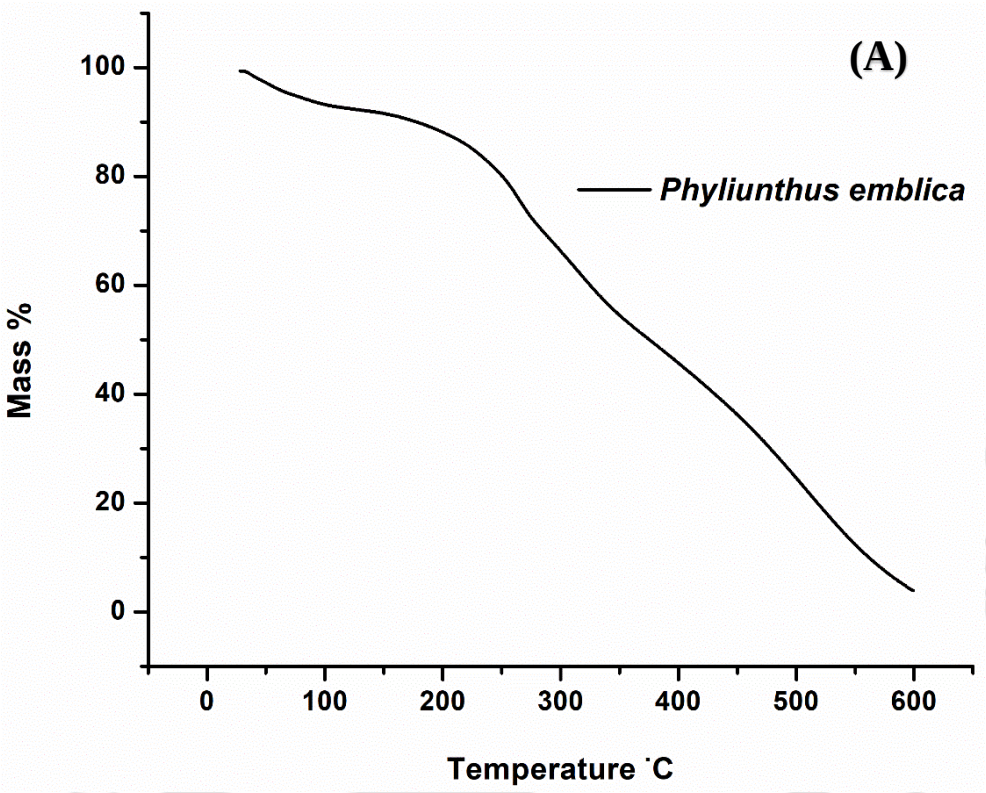

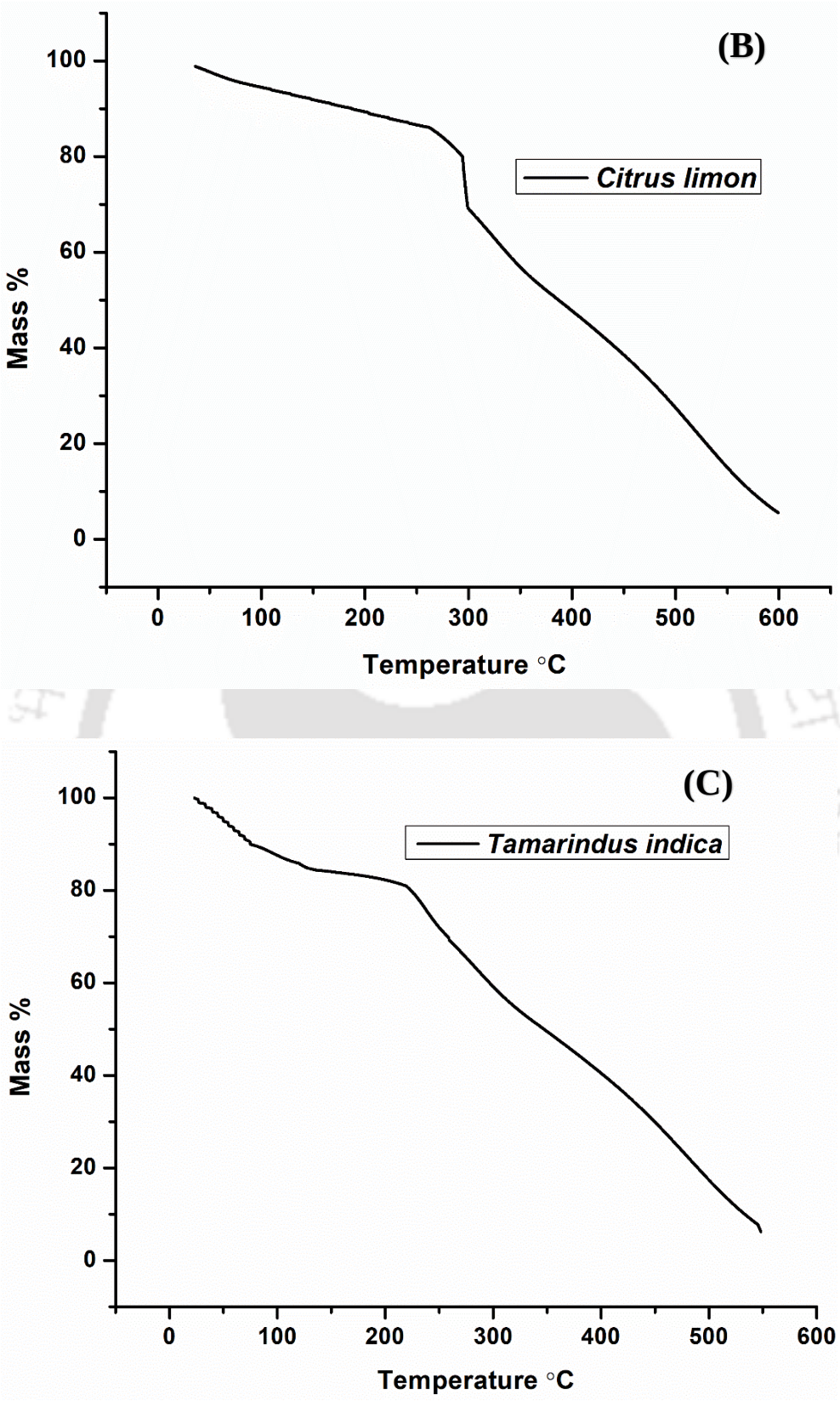

Fig. 3.2: Thermostability analysis of amine-modified (A) PELP (B) CLLP and (C)TILP.

3.3.3. Optimization of experimental conditions for the maximum removal of melanoidin

Three independent variables such as temperature (A), pH (B), and amine-modified adsorbent concentration (C) were selected to optimize the maximum adsorption of melanoidin using RSM-CCD [195, 196]. The lower/upper bounds of variables A (°C), B and C (% w/v) were 25/55, 3/11, and 0.2/2.0, respectively. The mini-tab software suggested a total of 20 experimental set-ups by applying these independent variables as listed in Table 3.2. The percentage decolourization was selected as the response. The obtained responses were fitted to a quadratic polynomial equation and predicted response values were compared with the experimental values as listed in Table 3.2. The obtained model equation for PELP, CLLP and are as follows;

$$\%\ Decolourization\ for\ PELP = 91.84 + 3.48A - 9.15B + 30.14C - 1.25AB - 1.75AC + 0.36BC - 12.77A^2 - 4.82B^2 - 15.60C^2 \quad (3.3)$$

$$\%\ Decolorization\ for\ CLLP = 60.94 - 10.72A - 9.02B + 26.23C + 7.73AB - 4.25AC - 1.01BC - 13.00A^2 - 6.06B^2 - 5.87C^2 \quad (3.4)$$

$$\%\ Decolorization\ for\ TILP = 25.10 - 3.52A - 3.13B + 9.45C + 2.81AB + 0.53AC - 4.52BC - 2.57A^2 - 5.47B^2 - 3.39C^2 \quad (3.5)$$

The regression study was performed by ANOVA analysis [197]. The higher correlation coefficient value (R^2) of experimented and predicted data indicates the closeness of experimented and predicted results (Table 3.3) [198]. The significance of the ANOVA model is evidenced by the lesser p-values and higher F-values (Table 3.3). The ANOVA analysis of independent variables A, B and C (Temperature, pH and Adsorbent concentration) and their interactions such as AB, AC, BC, A^2, B^2, C^2 are listed in Table 3.4. All model terms and their squares are found to be significant for PELP and CLLP and insignificant for TILP, respectively. The predicted optimized conditions (Temperature, pH and Adsorbent concentration) by mini-

tab software was found to be 44°C, 5.93 and 1.34 % for PELP, 26.7°C, 3.1 and 2.0 % for CLLP and 25°C, 3.5 and 2.0 % for TILP, respectively. PELP shows efficient results in terms of maximum adsorption (616 mg g^{-1}) of melanoidin compound in comparison of the modified CLLP (213 mg g^{-1}) and TILP (30 mg g^{-1}), respectively. The experimental response (melanoidin decolourization) was 99 ± 1 %, which agreed to the predicted value at the optimized conditions. The 3D response surface plots for maximum decolorization under the optimized conditions are shown in Figure 3.3.

Table 3.2.1. Experimental and predicted values of melanoidin decolourization at different experimental set-ups of independent variables for amine-modified PELP (Temperature, pH and adsorbent concentration) in RSM-CCD.

Serial No.	Independent Variable			Response (% decolorization)	
	Temp °C (A)	pH (B)	Adsorbent Conc. % w/v (c)	Actual Value	Predicted Value
1	25	3	0.2	34.14	31.55
2	55	3	0.2	37.03	44.49
3	25	11	0.2	15.05	15.04
4	55	11	0.2	21.26	22.99
5	25	3	2	94.69	94.59
6	55	3	2	98.91	100.56
7	25	11	2	85.35	79.52
8	55	11	2	76.26	80.49
9	14.8	7	1.1	44	49.86
10	65.2	7	1.1	69.73	61.56
11	40	0.3	1.1	96.62	93.59
12	40	13.7	1.1	62.12	62.84
13	40	7	0	0.18	0
14	40	7	2.61	97.58	98.41
15	40	7	1.1	93.59	91.84
16	40	7	1.1	92.15	91.84
17	40	7	1.1	90	91.84
18	40	7	1.1	92.29	91.84
19	40	7	1.1	94.34	91.84
20	40	7	1.1	88.26	91.84

Table 3.2.2. Experimental and predicted values of melanoidin decolourization at different experimental set-ups of independent variables for amine-modified CLLP (Temperature, pH and adsorbent concentration) in RSM-CCD.

Serial No.	Independent Variable			Response (% decolourization)	
	Temp °C (A)	pH (B)	Adsorbent Conc. % w/v (c)	Actual Value	Predicted Value
1	25	3	0.2	22.81	31.99
2	55	3	0.2	7.40	3.60
3	25	11	0.2	4.44	0.51
4	55	11	0.2	3.62	3.04
5	25	3	2.0	92.99	94.96
6	55	3	2.0	44.25	49.56
7	25	11	2.0	54.26	59.45
8	55	11	2.0	52.76	44.97
9	14	7	1.1	48.91	42.20
10	65	7	1.1	1.40	6.15
11	40	0.3	1.1	65.81	58.95
12	40	13.7	1.1	23.73	28.62
13	40	7	0	0.09	0.24
14	40	7	2.6	90.57	88.45
15	40	7	1.1	63.96	60.94
16	40	7	1.1	55.48	60.94
17	40	7	1.1	59.50	60.94
18	40	7	1.1	65.76	60.94
19	40	7	1.1	59.13	60.94
20	40	7	1.1	61.47	60.94

Table 3.2.3. Experimental and predicted values of melanoidin decolourization at different experimental set-ups of independent variables for amine-modified TILP (Temperature, pH and adsorbent concentration) in RSM-CCD.

Serial No.	Independent Variable			Response (% decolourization)	
	Temp °C (A)	pH (B)	Adsorbent Conc. % w/v (c)	Actual Value	Predicted Value
1	25	3	0.2	5.86	9.69
2	55	3	0.2	2.75	0
3	25	11	0.2	3.38	6.85
4	55	11	0.2	4.31	4.38
5	25	3	2	36.87	36.59
6	55	3	2	28.67	24.98
7	25	11	2	9.10	15.66
8	55	11	2	19.34	15.29
9	14.8	7	1.1	31.94	23.76
10	65.3	7	1.1	3.44	11.92
11	40	0.3	1.1	10.90	14.91
12	40	13.7	1.1	8.08	4.38
13	40	7	0	0.07	0
14	40	7	2.6	30.64	31.40
15	40	7	1.1	18.24	25.10
16	40	7	1.1	29.91	25.10
17	40	7	1.1	26.51	25.10
18	40	7	1.1	22.13	25.10
19	40	7	1.1	28.76	25.10
20	40	7	1.1	25.13	25.10

Table 3.3. Comparison of correlation coefficient value (R^2) and significance of the ANOVA model by the lesser p-value and higher F-value for amine-modified PELP, CLLP and TILP.

	PELP	CLLP	TILP
R^2	>0.99	0.97	0.85
P-value	<0.0001	<0.0001	0.0039
F-value	79.69	39.25	29.80
Lack of fit	<0.05	0.04	0.11
Significant/Insignificant	Significant	Significant	Insignificant

Table 3.4.1. ANOVA table of quadratic model for PELP.

Source	Sum of squares	df	Mean Square	F-value	p-value
Model	19160.87	9	2128.99	79.69	< 0.0001
A (Temp.)	165.28	1	165.28	6.19	0.03
B (pH)	1141.83	1	1141.83	42.74	< 0.0001
C (Ads.)	12402.88	1	12402.88	464.23	< 0.0001
AB	12.47	1	12.47	0.47	0.51
AC	24.35	1	24.35	0.91	0.36
BC	1.03	1	1.03	0.04	0.85
A^2	2350.58	1	2350.58	87.99	< 0.0001
B^2	334.21	1	334.20	12.51	0.0054
C	3505.34	1	3505.34	131.20	< 0.0001

Table 3.4.2. ANOVA table of quadratic model for CLLP.

Source	Sum of squares	df	Mean Square	F-value	p-value
Model	15721.34	9	1746.82	39.25	< 0.0001
A (Temp.)	1568.79	1	1568.79	35.25	0.0001
B (pH)	1110.32	1	1110.32	24.95	0.0005
C (Ads.)	9392.91	1	9392.91	211.05	< 0.0001
AB	477.87	1	477.87	10.74	0.01
AC	144.59	1	144.59	3.25	0.1
BC	8.14	1	8.14	0.18	0.68
A^2	2435.10	1	2435.10	54.72	< 0.0001
B^2	529.93	1	529.93	11.91	0.01
C	495.89	1	495.89	11.14	0.01

Table 3.4.3. ANOVA table of quadratic model for TILP.

Source	Sum of squares	df	Mean Square	F-value	p-value
Model	2347.14	9	260.79	6.37	0.0039
A (Temp.)	169.21	1	169.21	4.13	0.07
B (pH)	133.90	1	133.90	3.27	0.1
C (Ads.)	1220.26	1	1220.26	29.80	0.0003
AB	63.17	1	63.17	1.54	0.3
AC	2.23	1	2.23	0.054	0.8
BC	163.62	1	163.62	4.00	0.1
A^2	95.01	1	95.01	2.32	0.2
B^2	430.68	1	430.68	10.52	0.01
C	165.92	1	165.92	4.05	0.1

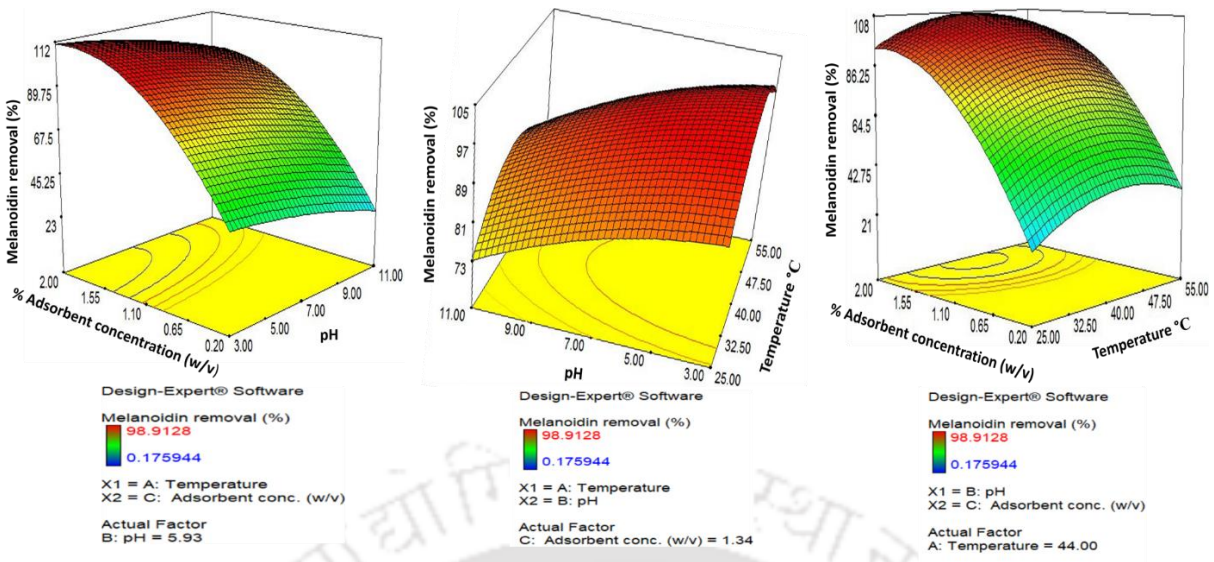

Fig. 3.3.(A): 3D response surface plots of amine-modified PELP for the melanoidin adsorption considering their independent parameters as temperature, pH and concentration of adsorbent.

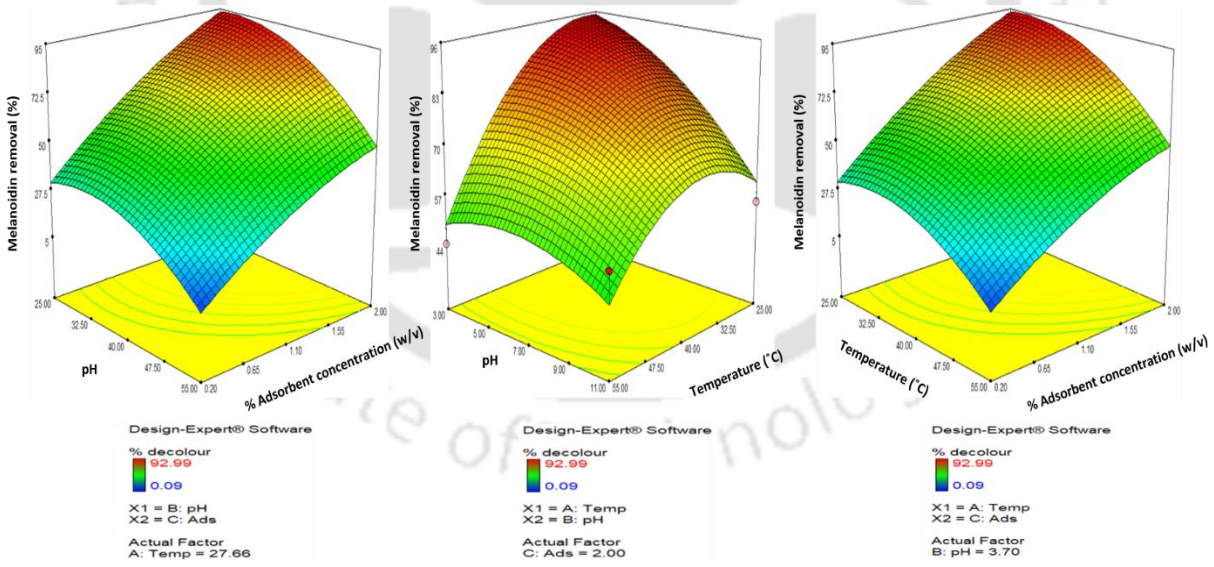

Fig. 3.3.(B): 3D response surface plots of amine-modified CLLP for the melanoidin adsorption considering their independent parameters as temperature, pH and concentration of adsorbent.

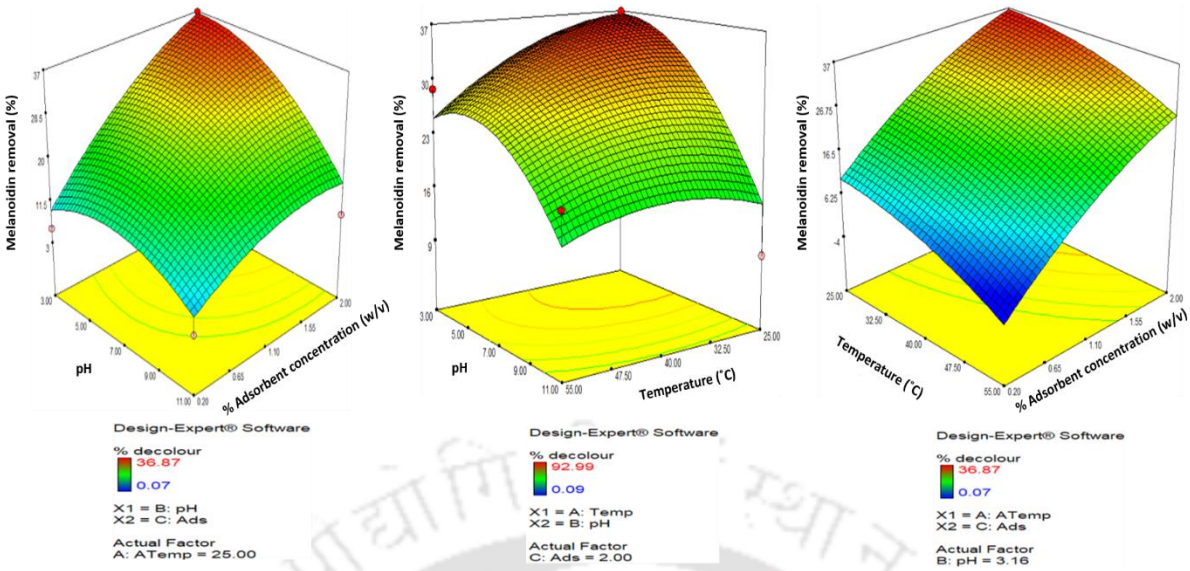

Fig. 3.3.(C): 3D response surface plots of amine-modified TILP for the melanoidin adsorption considering their independent parameters as temperature, pH and concentration of adsorbent.

3.3.4. Surface morphology analysis by FESEM

The surface morphology of the modified PELP was analysed using FESEM. The roughness of surfaces was masked due to the adsorption of melanoidin as shown in Figure 3.4. The adsorption of melanoidin compound on the surface of amine-modified adsorbents was due to the trapping of melanoidin particles on rough surfaces. Amine-treated PELP and CLLP show adequate morphological properties as adsorbents due to the presence of irregular pores and activated functional groups on its surface. As a result, the activated binding sites or reactive groups were occupied on the surfaces of modified PELP and CLLP. The differences of rough surfaces and occupied surfaces of modified and used PELP and CLLP can be clearly distinguished in Figure 3.4.a and b. After the adsorption of melanoidin, an increase in N and C contents were observed as listed in Table 3.10. This also indicated the adsorption of melanoidin

on modified PELP, CLLP and TILP. The images of these adsorbents were analyzed at very high resolution (2k) to study and compare their morphological properties.

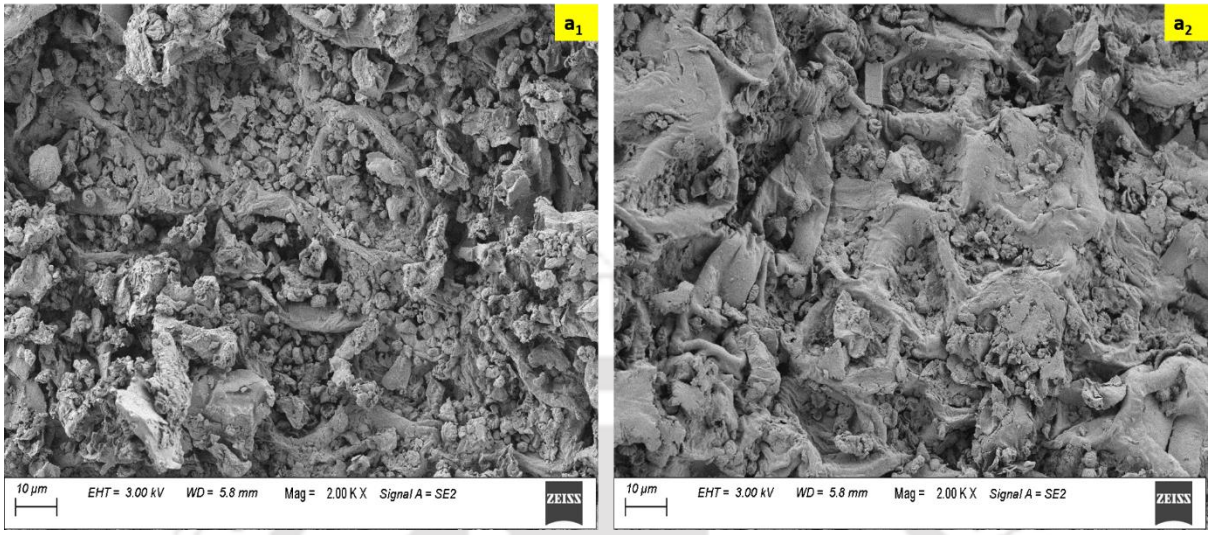

Fig. 3.4.(A): FESEM images of modified PELP (a_1) before and (a_2) after adsorption of melanoidin.

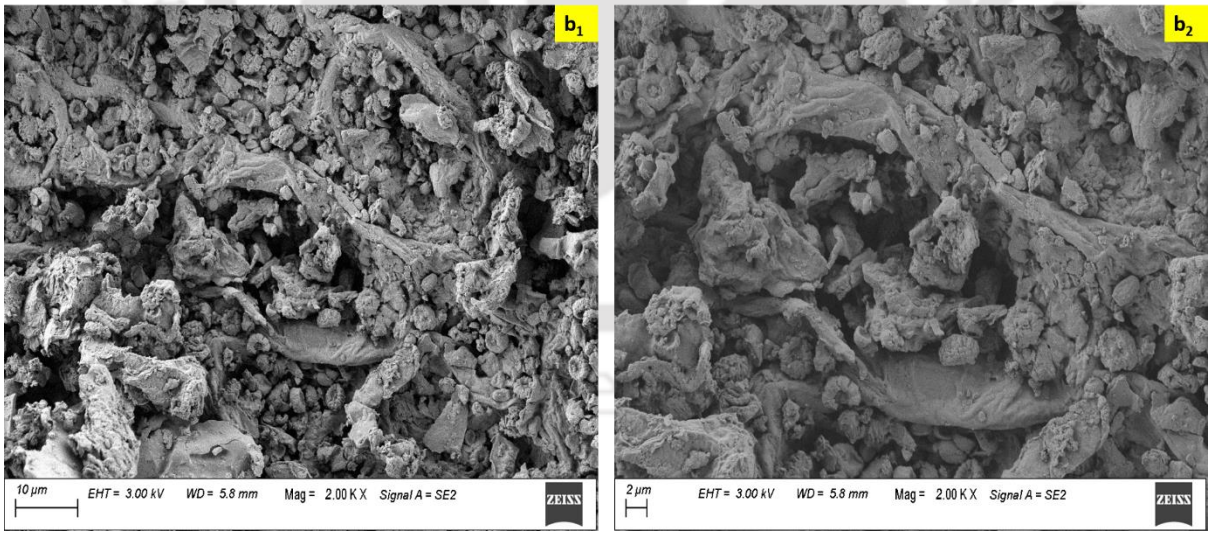

Fig. 3.4.(B): FESEM images of modified CLLP (b_1) before and (b_2) after adsorption of melanoidin.

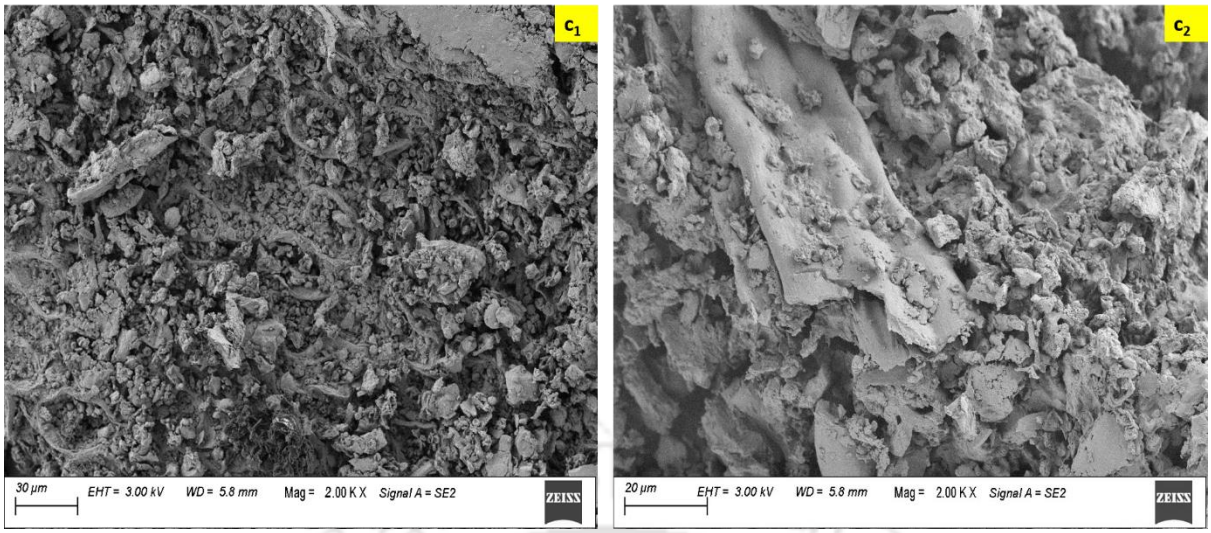

Fig. 3.4.(C): FESEM images of modified TILP (c_1) before and (c_2) after adsorption of melanoidin.

3.3.5. Adsorption equilibrium isotherms

Adsorption equilibrium is an important study to determine the adsorption capacity and adsorption process. Out of several reported adsorption isotherms; Langmuir, Freundlich, Temkin and Dubinin-Radushkevich (D-R) isotherms were applied to the experimental data for determining the adsorption equilibrium (Figure 3.5). Langmuir adsorption isotherm describes the quantitative adsorption on the outer surface of the adsorbent [199]. Homogenous monolayer adsorption on the surface takes place till the saturation stage. Further that no more adsorption occurs on the surface of the adsorbent. Freundlich isotherm model represents the heterogeneous adsorption on the surfaces of the adsorbent and describes the exponential distribution of adsorption sited concerning their bond energy [200]. This model states that the binding affinity exponentially decreases with occupying the binding sites of the adsorbent [193]. Temkin isotherm model assumes that there is an inverse relationship between the heat of adsorption of all molecules in a layer with surface coverage on adsorbent; i.e. the linear decrease in heat of

adsorption of all molecules in a layer occurs as a result of the increment of adsorbate on the surface of the adsorbent [201]. Adsorption is characterized by a uniform distribution of binding sites on the surfaces of the adsorbent. D–R Isotherm is a semiempirical equation and a popular model to develop the adsorption potential onto a porous surface by Gaussian energy distribution [202]. This model considers multilayer adsorption involving physical forces i.e., Van der Waals interactions.

The expressions used for the above equilibrium models are listed in Table 3.1. The experimental data were fitted to these models and estimated model parameters along with respective root mean square error (RMSE) are listed in Table 3.5. The Langmuir isotherm constant K_L (L g^{-1}) and q_m (mg g^{-1}) were estimated for amine-modified PELP (0.22 and 616), CLLP (0.08 and 213) and TILP (0.32 and 30), respectively. R_L value indicates the nature of adsorption feasibility i.e; irreversible (if $R_L = 0$), favourable (if $0< R_L<1$), linear (if $R_L =1$) and unfavourable (if $R_L>1$) [193]. R_L values varied in the range of 0.15 to 0.35, indicating the favorable adsorption process. The value of 1/n in the Freundlich isotherm between 0 to 1 reflects a favorable heterogenous adsorption process, while 1/n > 1 states a cooperative adsorption process [203]. In the present study, the 1/n value was found to be 0.53, 0.93 and 0.62 for amine-modified PELP, CLLP and TILP, respectively, and reflected a homogeneous adsorption process. The Temkin isotherm model estimated the heat of adsorption (b_T) as 17.40, 22.50 and 86.07 kJ mol^{-1} and adsorption energy constant (mol^2 J^{-2}) correlated to the mean free energy (K_{ad}) was predicted from D-R isotherm to be 0.81, 7.07 and 1.85 kJ mol^{-1} for amine-modified PELP, CLLP and TILP, respectively. These values indicated the presence of the physical adsorption process.

The R^2 values of the Langmuir, Freundlich, Temkin and D-R isotherms for amine-modified PELP are nearly same (listed in Table 3.5). Based on the RMSE values of Langmuir, Freundlich, Temkin and D-R isotherms, the D-R isotherm model better agreed with the

experimental data followed by Temkin, Langmuir and Freundlich isotherms of amine-modified PELP. Similarly, Temkin isotherm better agreed with the experimental data followed by Freundlich, D-R and Langmuir isotherms by amine-modified CLLP. The experimental data of amine-modified TILP better agreed with D-R isotherm followed by Temkin, Freundlich and Langmuir isotherms.

The higher R^2 values of the Langmuir, Freundlich, Temkin and D-R isotherms indicated the surface adsorption proportional to the available surface area/ binding sites. The maximum adsorption capacity, q_m (mg g^{-1}) of the amine-modified PELP was found to be 616, followed by 213 and 30 for CLLP and TILP, respectively. While the same for the unmodified PELP was found to be 243 mg g^{-1}. This indicated 2.5 folds enhanced adsorption capacity after surface modification with amine SAMs. A comparison of melanoidin removal between the present study and different reported adsorbents are listed in Table 3.6, which indicated excellent melanoidin adsorption capacity by amine-modified leaves powder.

Table 3.5. Comparison of Langmuir, Freundlich, Temkin and D-R isotherm models for the sorption of melanoidin on amine-modified PELP, CLLP and TILP.

	Parameters	PELP	CLLP	TILP
Langmuir	R^2	0.98	0.98	0.92
	q_m (mg g^{-1})	616.2	213.23	30.34
	K_L (L g^{-1})	0.22	0.08	0.32
	$R_L = 1/(1 + K_L C_0)$	0.15	0.31	0.35
	RMSE	0.0343	0.1312	0.0382
Freundlich	R^2	0.95	0.99	0.97
	1/n	0.53	0.93	0.62
	K_F (mg g^{-1}) (L $g^{-1})^{1/n}$	129.2	50.56	25.35
	RMSE	0.0458	0.0801	0.0259
Temkin	R^2	0.97	0.98	0.99
	B_T (kJ mol^{-1})	17.40	22.50	86.07
	K_T (L g^{-1})	1.66	1.45	2.26
	RMSE	0.0319	0.0304	0.0196
D–R	R^2	0.96	0.99	0.98
	K_{ad} mol^2 J^{-2}	7.58×10^{-7}	1.0×10^{-8}	2.0×10^{-7}
	$E = 1/\sqrt{2K_{ad}}$ (kJ mol^{-1})	0.81	07.07	1.58
	q_m (mg g^{-1})	406.1	252.30	69.27
	RMSE	0.0265	0.1004	0.0110

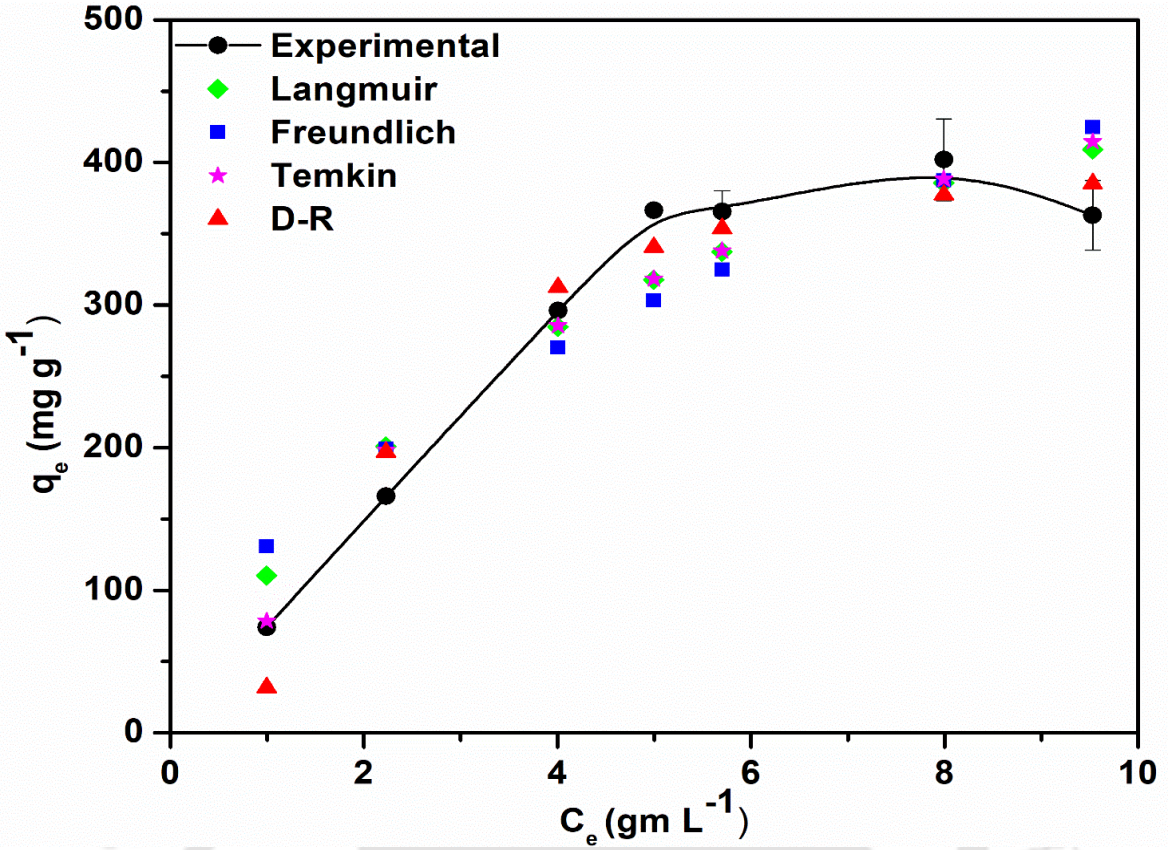

Fig. 3.5: Fitting and comparison of Langmuir, Freundlich, Temkin and D-R isotherm models of melanoidin adsorption with experimental data of amine-modified PELP.

Table 3.6. Different adsorbents used for melanoidin removal and their maximum adsorption capacity.

Adsorbents	Substrate	Adsorption conditions	q_m (mg g^{-1})	% removal	Ref.
Coal fly ash	Distillery spent wash	25 °C, pH 6, 120 min	281	85	[174]
Bagasse fly ash	Distillery spent wash	27 °C, 140 min	125	76	[204]
Bagasse fly ash	Synthetic melanoidins	25 °C, pH 3, 240 min	125	64	[184]
Activated bagasse fly	Distillery spent wash	25 °C, pH 8, 240 min	92	62	[183]
Magnetic carbon nanocomposites	Synthetic melanoidins	40 °C, pH 3, 30 min	315	80	[205]
Chitin nanofibers	Synthetic melanoidin	60 °C, pH 4, 60 min	353	89	[206]
Activated carbon	Synthetic melanoidin	27 °C, pH 3, 8 days	232	-	[207]
Coal fly ash	Synthetic melanoidin	50 °C, pH6, 24 hr	53	86	[208]
Amine-modified TELP	Synthetic melanoidin	25 °C, pH 3.5, 300 min	30	20.3 ± 2	Present study
Amine-modified CLLP	Synthetic melanoidin	27 °C, pH 3.1, 300 min	213	85.6 ± 2	Present study
Amine-modified PELP	Synthetic melanoidin	44 °C, pH 5.9, 300 min	616	98.5 ± 1	Present study

3.3.6. Kinetic studies of melanoidin adsorption on modified leaves powder

The adsorption kinetics for melanoidin removal by amine-modified leaves powder was carried out as a function of contact time at the optimized conditions. Rapid adsorption at initial contact time followed by slower adsorption by intra-particle diffusion analysis to reach equilibrium/saturation in 300 min were observed by intra-particle diffusion analysis. Experimental data were fitted into pseudo-first-order, pseudo-second-order, intra-particle diffusion, and Elovich models to investigate the order of reaction and rate constant. The expressions used for the above equilibrium models are listed in Table 3.1. The experimental data were fitted to these models and estimated model parameters are listed in Table 3.7.

The experimental data were better fitted to the pseudo 2nd order kinetic model (RMSE = 0.0014) for amine-modified *Phyllanthus emblica*, pseudo 2^{nd} model (RMSE = 0.0357) for amine-modified *Citrus limon* and pseudo 1st and 2nd order kinetic models (RMSE = 0.0047) for amine-modified *Tamarindus indica* leaves powder, respectively (Figure 3.6) (Table 3.7).

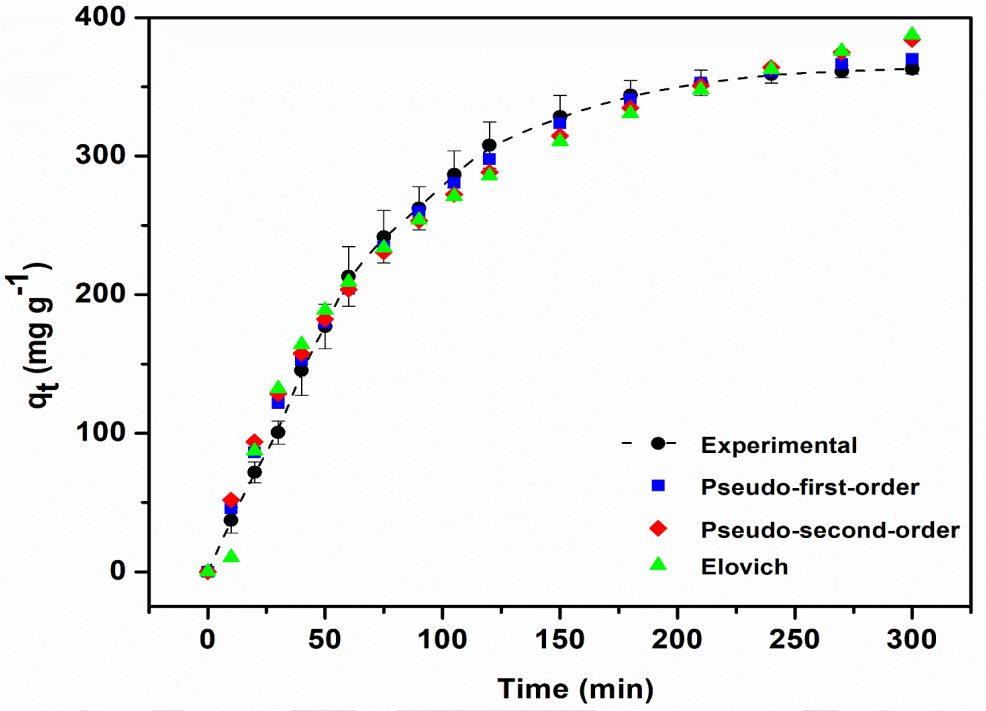

Fig.3.6: Kinetic model fitting of experimental data for the melanoidin adsorption and comparison with Pseudo-first-order, Pseudo-second-order and Elovich isotherm models and their parameters.

The adsoption process can be distinguished as a multi-process system, which proceeds by following boundary layer diffusion, adsorption on active binding sites of adsorbent and finally intra-particle diffusion [203, 209]. The intra-particle diffusion rate constant k_p was separated as $k_{initial}$ (from 0 to 150 min for rapid adsorption) and K_{intra} (from 150 to 300 min for slow adsorption), respectively (Table 3.8). Thus, the total adsorbed amount is the sum of surface adsorption (0-150 min) and intra-particle diffusion (150-300 min) (Figure 3.7).

Summarily, this adsorption process is comprised of at least two distinguished steps. The initial 150 min faster adsorption followed by slower adsorption until 300 min. The adsorption kinetics followed pseudo 1st order. The rapid adsorption occurs due to the availability of binding sites on the surfaces of modified leaves, while the slower adsorption happens possibly due to intra-

particle diffusion of melanoidin into the interior structure of modified leaves. At the optimized conditions, a complete decolourization of melanoidin was observed in 300 min (98 ± 1 %) in the presence of modified PELP followed by CLLP (92 ± 2 %) and TILP (28 ± 1 %), while only 66 ± 3, 44 ± 1 and 21 ± 1 % decolourization was achieved with unmodified PELP, CLLP and TILP, respectively (Figure 3.8). Simultaneously, decolourization also resulted in the reduction of COD values. Overall, 93 ± 1, 86 ± 2 and 21 ± 2 % of COD reduction was achieved using the modified PELP, CLLP and TILP in 300 min, respectively.

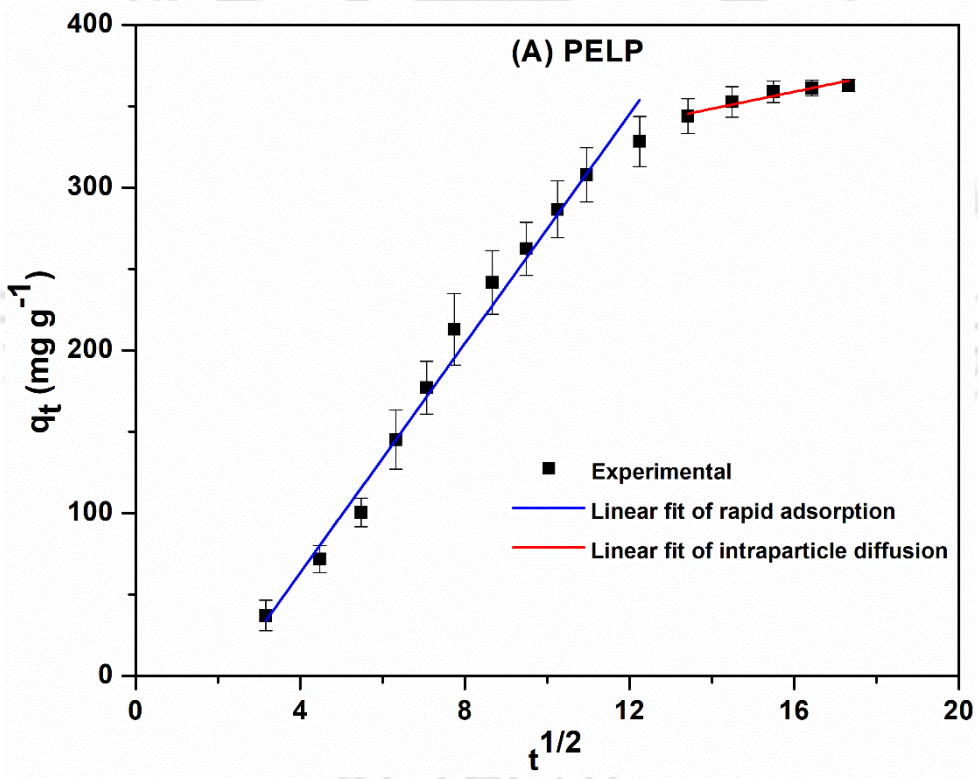

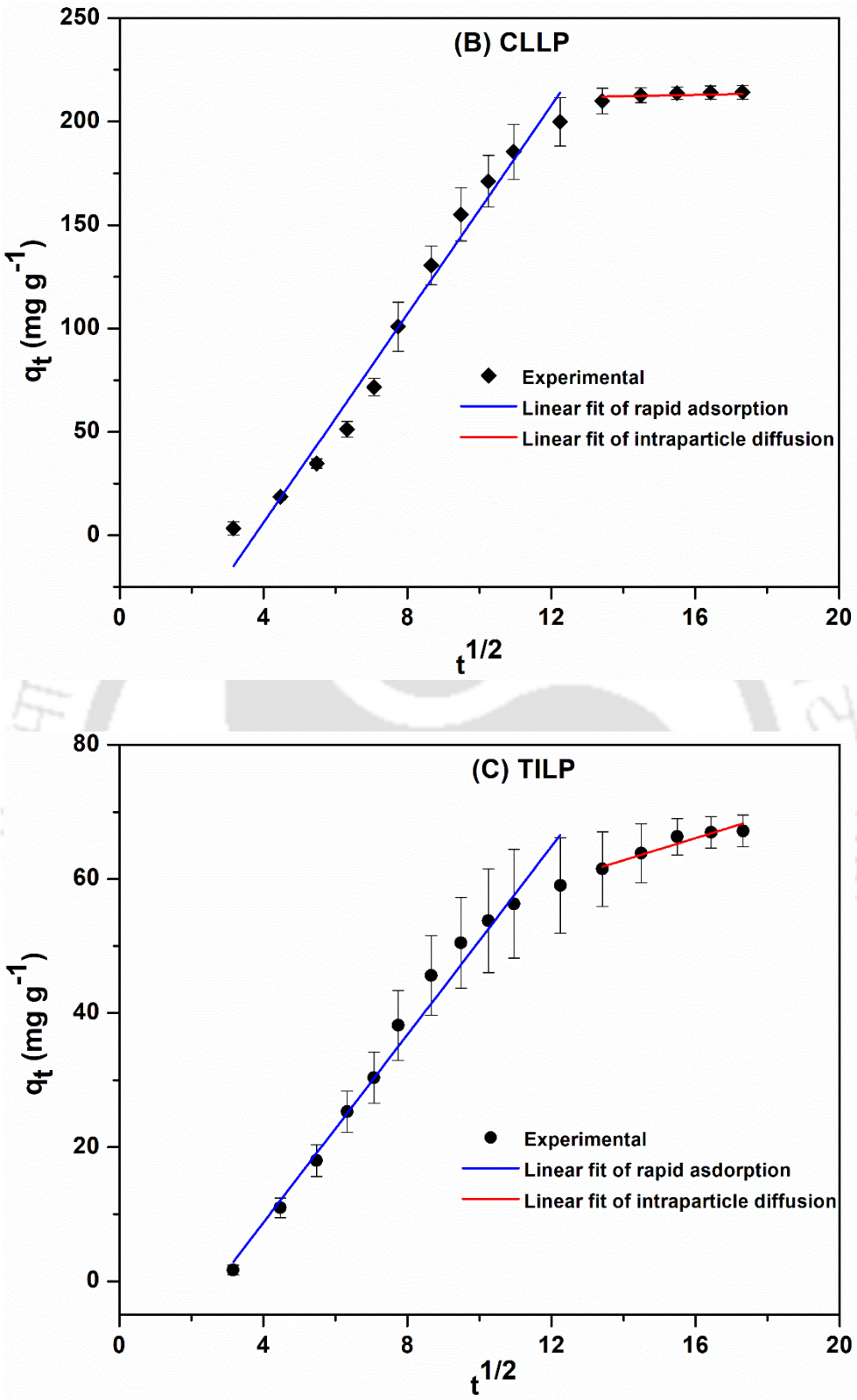

Fig. 3.7: Fitting of intraparticle diffusion kinetic model to experimental data of the melanoidin adsorption on modified (A) PELP (B) CLLP and (C) TILP, indicating two processes: the rapid adsorption (blue line) and intraparticle diffusion (red line).

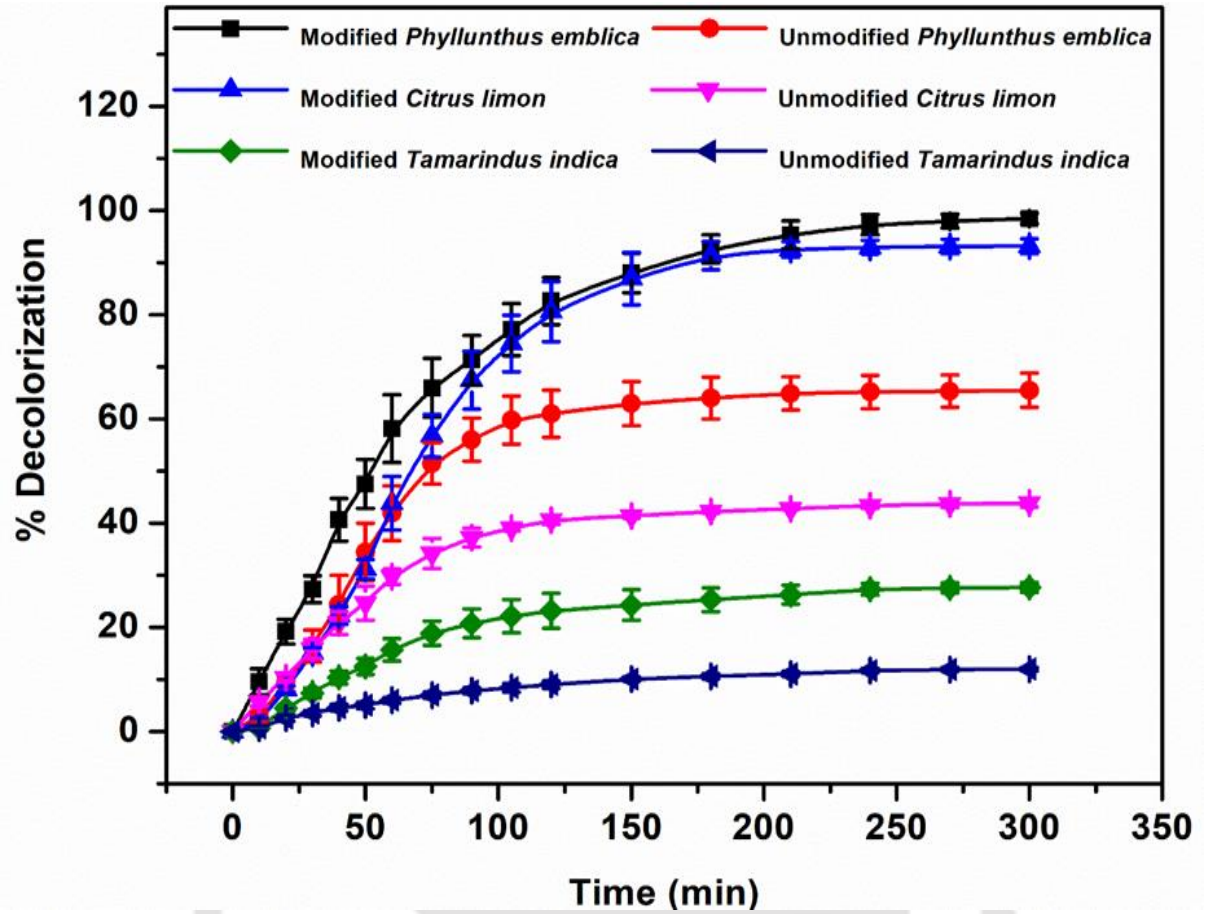

Fig. 3.8: Decolorization of melanoidin at optimized condition by PELP, CLLP and TILP before and after amine-modification at their respective RSM optimized conditions.

Table 3.7. Comparison of kinetic studies of melanoidin adsorption on modified PELP, CLLP and TILP.

Kinetic models	Constant	PELP	CLLP	TILP
Pseudo-first-order	R^2	0.99	0.96	0.99
	k_1 (min^{-1})	1.29×10^{-2}	2.75×10^{-2}	1.47×10^{-2}
	q_e (mg g^{-1})	378.1	471.6	71.2
	RMSE	0.0083	0.2460	0.0047
Pseudo-second-order	R^2	0.98	0.99	0.99
	q_e (mg g^{-1})	493.3	252.90	81.29
	k_2 (g $mg^{-1}min^{-1}$)	2.38×10^{-5}	8.89×10^{-5}	20.29×10^{-5}
	h (mg $g^{-1}min^{-1}$)	5.79	54.9	1.41
	RMSE	0.0014	0.0357	0.0047
Elovich	R^2	0.97	0.98	0.98
	α (mg g^{-1} min^{-1})	12.17	4.67	0.12
	β (g mg^{-1})	9.0×10^{-2}	9.25×10^{-3}	1.19×10^{-2}
	RMSE	0.0017	0.4955	0.1566

Table 3.8. Comparison of intraparticle diffusion analysis of amine-modified PELP, CLLP and TILP.

	Constant	PELP	CLLP	TILP
Rapid adsorption	$R^2_{initial}$	0.98	0.98	0.97
	$K_{initial}$ (mg g^{-1} min^{-1})	32.4	24.6	62.9
	$c_{initial}$ (mg g^{-1})	-58.5	-90.1	3514.0
	% Contribution $_{initial}$	95	71	87
Slow adsorption	R^2_{intra}	0.91	0.71	0.99
	k_{intra} (mg g^{-1} $min^{-1/2}$)	3.5	2.5	33.7
	c_{intra} (mg g^{-1})	303.5	174.0	7311.7
	% Contribution $_{intra}$	5	29	13

3.3.7. Thermodynamic analysis of melanoidin adsorption

The thermodynamic studies investigate the role of temperature / thermal energy on adsorption kinetics. This study outlines the driving forces applied by the system to regulate the entropy and energy to enhance the adsorption capacity. The adsorption experiments were performed in batch at 298, 308, 318 and 328 K of temperatures for 300 min at the optimized conditions. The thermodynamic parameters such as changes in ΔS, ΔH and ΔG were investigated by applying the expressions listed in Table 3.1. The plot between 1/T vs. log K_c is shown in Figure 3.9. The estimated thermodynamic parameters are listed in Table 3.9. The negative value of ΔG at all the experimental temperatures indicated spontaneous adsorption of melanoidin on amine-modified leaves [210]. A decrease in ΔG value with an increase in temperature (from 298 to 328 K), suggested that the adsorption capacity of modified leaves was also augmented (Table 3.9). In fact, the positive value ΔH indicated the endothermic nature of the melanoidin adsorption process. The positive value of ΔS also revealed the enhancement of melanoidin adsorption capacity on the surface binding sites.

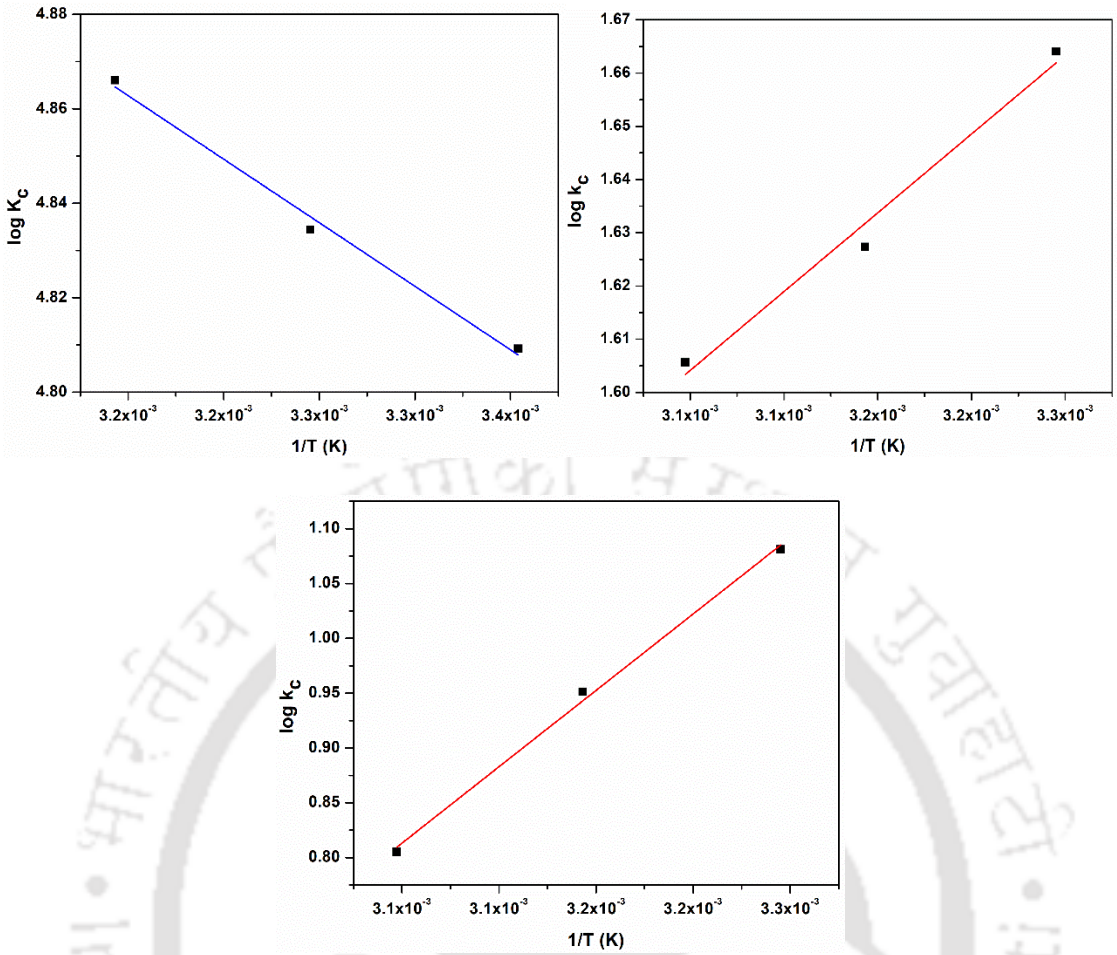

Fig. 3.9: Thermodynamic analysis of melanoidin adsorption on amine-modified (A) PELP (B) CLLP and (C) TILP.

Table 3.9. Thermodynamic parameters for melanoidin adsorption on amine-modified leaves.

Adsorbents	Constants	Temperature (K)			
		298.15	308.15	318.15	328.15
PELP	ΔG (kJ mol^{-1})	-10.33	-10.82	-11.37	-11.61
	ΔH (kJ mol^{-1})		5.15		
	ΔS (J mol^{-1} K^{-1})		51.90		
	R^2		0.99		
CLLP	ΔG (kJ mol^{-1})	-9.6	-9.8	-9.9	-10.1
	ΔH (kJ mol^{-1})		-5.67		
	ΔS (J mol^{-1} K^{-1})		13.43		
	R^2		0.98		
TILP	ΔG (kJ mol^{-1})	-6.63	-6.38	-5.79	-5.06
	ΔH (kJ mol^{-1})		-2.67		
	ΔS (J mol^{-1} K^{-1})		-65.81		
	R^2		0.99		

3.3.8. Reusability study

Reusability of any bio-adsorbent is a significant phenomenon to establish the system on an industrial scale as well as economically feasible. In the present study, the amine-modified PELP and CLLP resulted in > 75 and > 70 % removal efficiency up to four successive cycles while TILP was inefficient in reusability, as shown in Figure 3.10. The removal efficiency decreased to 52 and 48 % after the fifth adsorption and desorption cycle by PELP and CLLP, respectively. A slight decrease in removal efficiency up to the 4th cycle also accounts for the loss of adsorbent quantity during consecutive recycling. These results showed very effective adsorption and desorption of melanoidin by the prepared adsorbent. The repetitive use of adsorbent demonstrates the economic feasibility. These eco-friendly bio adsorbents reduce sludge handling and further can be utilized as a bio-compost.

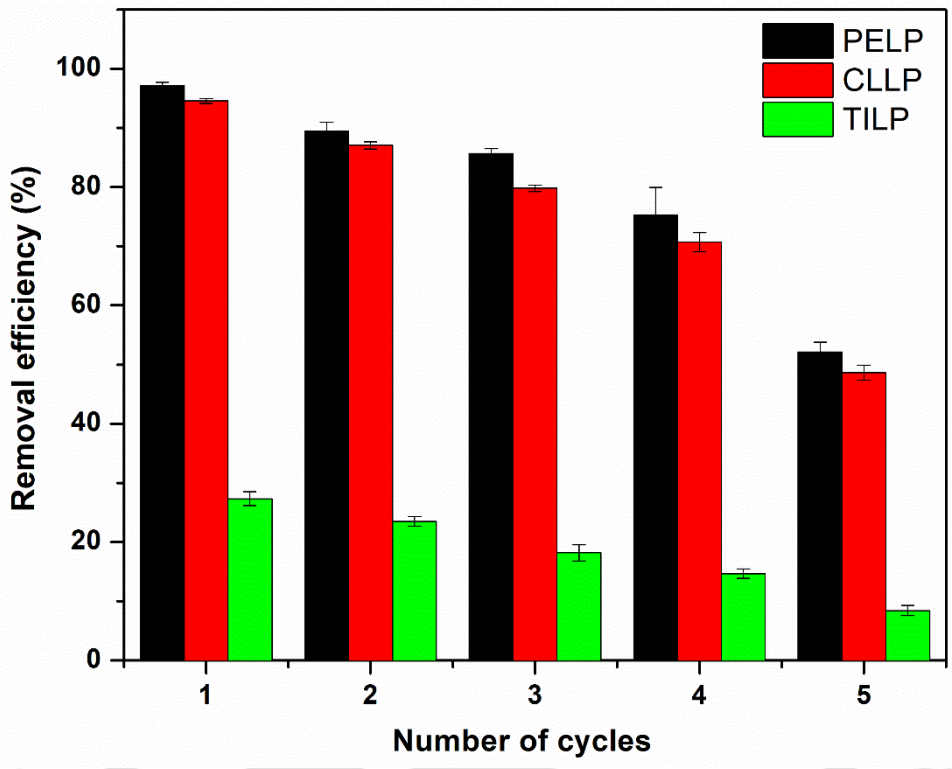

Fig. 3.10: Adsorption-desorption efficiency of modified PELP, CLLP and TILP up to 5th consecutive cycles.

3.3.9 Adsorption mechanism

The adsorption mechanism of melanoidin over modified PELP, CLLP and TILP was investigated by FTIR, EDX and Zeta potential analysis.

3.3.9.1. Adsorption mechanism through FTIR

FTIR spectra of melanoidin and modified PELP before and after adsorption are shown in Figure 3.11. The appearance of different peaks after the adsorption at 1220, 1373 and 1730 cm^{-1} corresponded to C-N stretching, C-H bending and C=O stretching of melanoidin in PELP, respectively. Similarly, the presence of extra peaks at the 1025 and 1230 cm^{-1} in TILP and the

presence of a peak at 1215 cm^{-1} in CLLP corresponded to C-N stretching of the amine group. These peaks are marked in green colour. This agreed to the presence/adsorption of melanoidin on the surface. In addition, blue shifts from 756 to 757 cm^{-1} and 1033 to 1036 cm^{-1} in modified PELP, 1101 to 1105 cm^{-1} in CLLP and 1306 to 1313 cm^{-1} in TILP indicated the involvement of bonding between amine-modified powders and melanoidin [194]. Further, new peaks at 1055 and 1671 cm^{-1} specified the presence of C-N stretching of amine groups and C=O stretching of amide groups in PELP while the presence of new peaks at 1065 and 1259 cm^{-1} corresponds the presence of C-N stretching and 1441 cm^{-1} specified the presence of C-H bending, respectively (denoted by the purple line) [211].

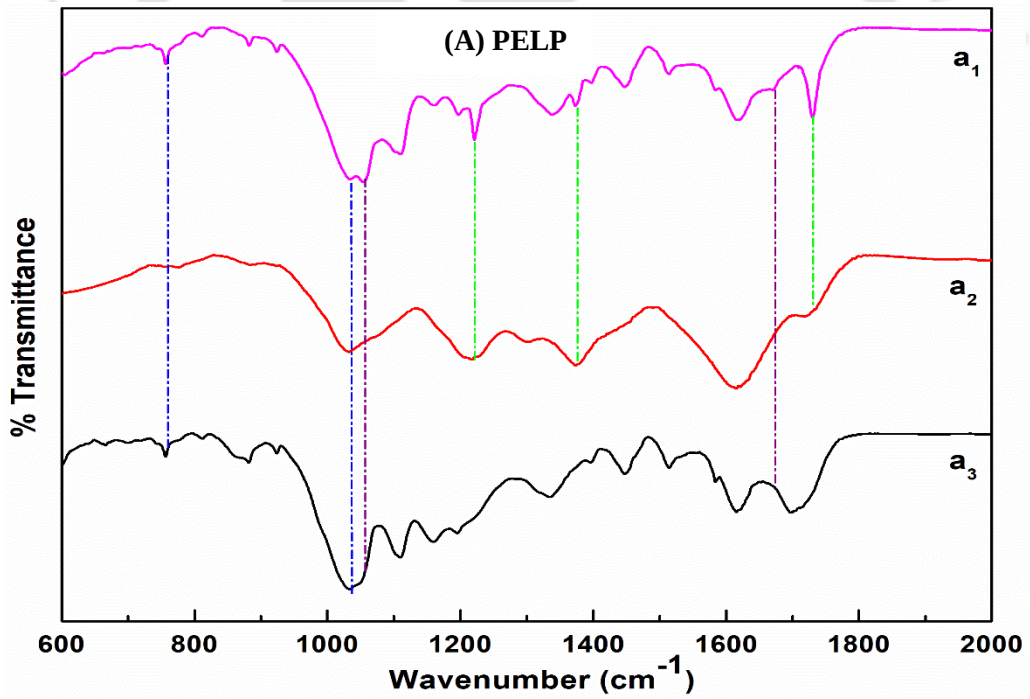

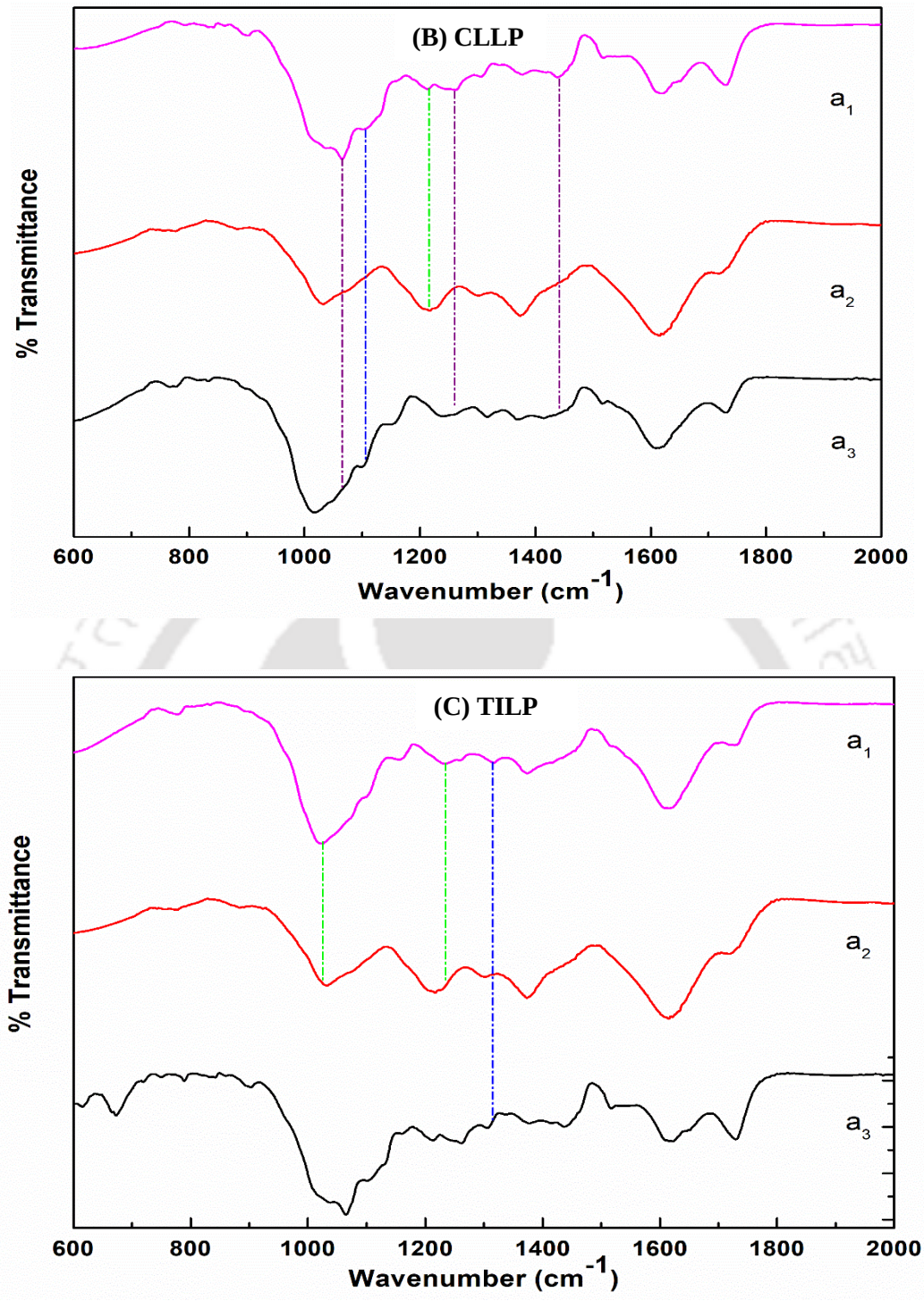

Fig. 3.11: Analysis of adsorption mechanism through FTIR spectra indicating (a_1) (modified adsorbent post adsorption), (a_2) melanoidin and (a_3) modified adsorbent before adsorption of (A) PELP (B) CLLP and (C) TILP.

3.3.9.2. Adsorption mechanism through zeta potential analysis

Zeta potential (Ψ_d) values of the adsorbent and adsorbate were measured at different pH as shown in Figure 10 (b). The point of zero charge (pzc) was estimated using the following expression: $\Psi_d = \mathrm{RT/z_i F}\ \ln c_i/c_i^{pzc}$ [212]. Here z_i, R, T, F and c_i refer valency, gas constant, temperature, Faraday's constant and molar concentration of H^+, respectively. The pzc of melanoidin and anime-modified PELP were found to be 6.9 and 3.8, respectively. This indicated a positive change on melanoidin and a negative charge on modified PELP at a pH value of 5.9, which resulted in electrostatic attraction between them. The zeta potential of melanoidin at working pH (5.93) was +6.55 mV while the charge on the modified PELP was showing -35.7. It is noted that unmodified PELP was negatively charged (-12.95 mV) at pH value of 5.93, which become positively charged (+6.55 mV) after the formation of amine SAMs (Figure 3.11(a)). From the graph, it is clearly observed that the differences between the zeta potential of melanoidin and modified adsorbent are maximum at the optimized pH value of 5.93. The difference in zeta potential between them suggested the involvement of electrostatic interaction in the adsorption process [213, 214]. In the case of CLLP and TILP, the pzc of melanoidin and anime-modified CLLP and TILP was found to be 4.3, 6.3 and 4.5, 6.2, respectively. This indicated the positive change in melanoidin and amine-modified CLLP and TILP leaves at their respective working pH value of 3.1 and 3.5, respectively. The same charge on melanoidin and amine-modified adsorbent (CLLP and TILP) is inherent in the electrostatic interaction in the adsorption process (Figure 3.12(b and c)).

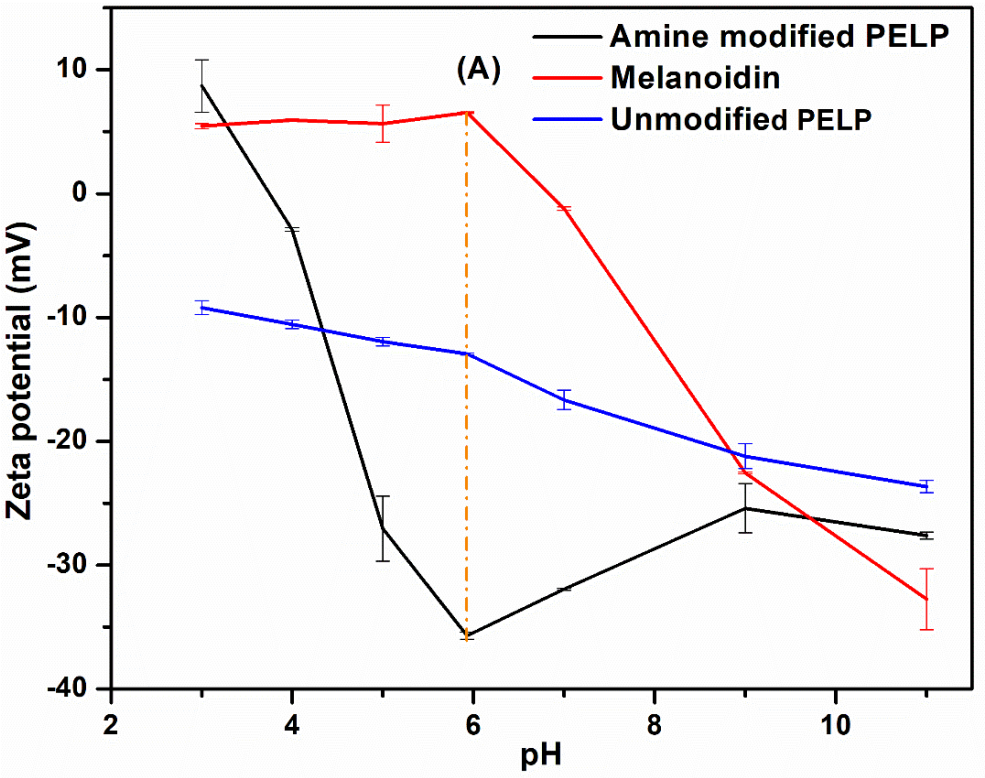
(A)
Amine modified PELP
Melanoidin
Unmodified PELP
Zeta potential (mV)
pH
10
0
-10
-20
-30
-40
2
4
6
8
10

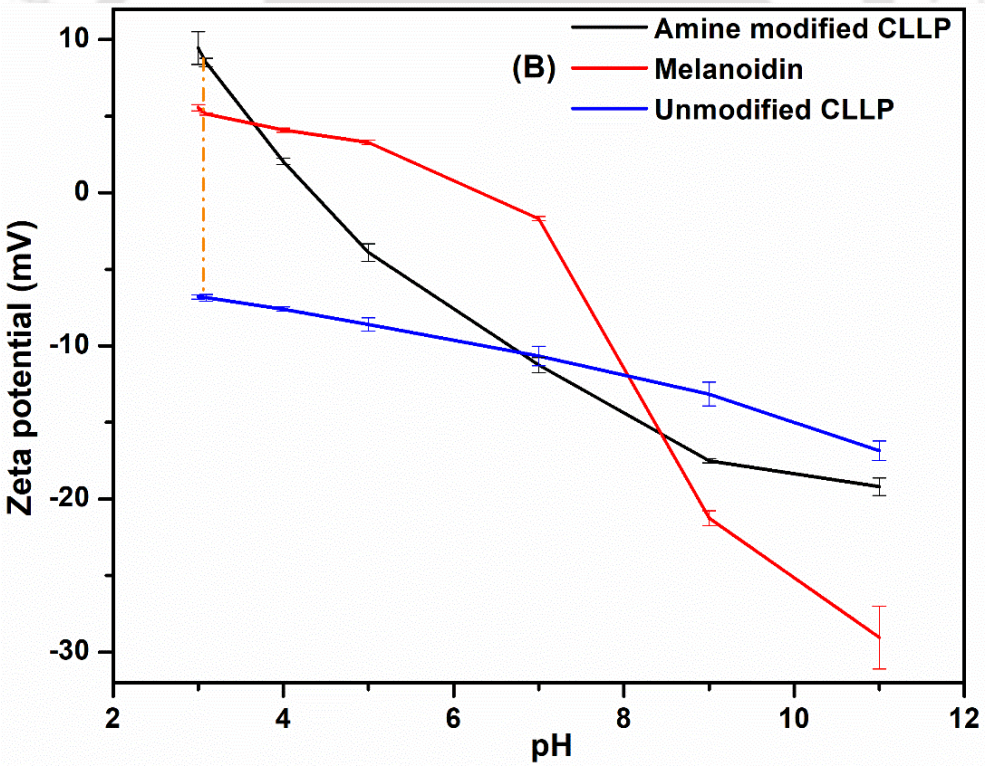
(B)
Amine modified CLLP
Melanoidin
Unmodified CLLP
Zeta potential (mV)
pH
10
0
-10
-20
-30
2
4
6
8
10
12

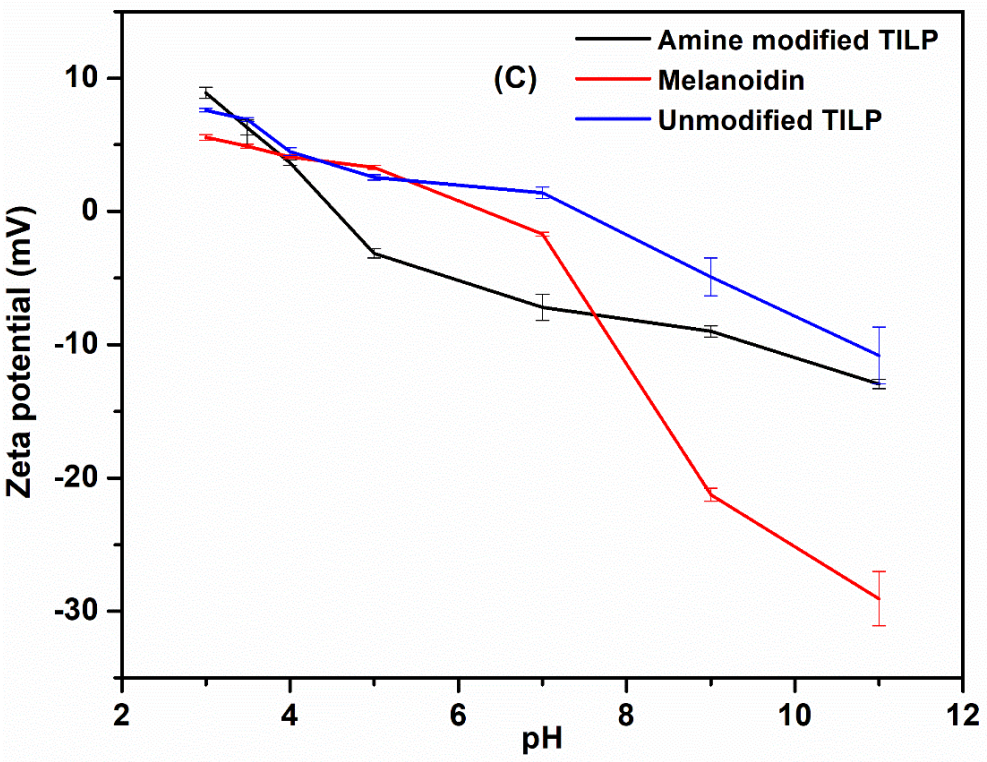

Fig. 3.12: Zeta potential values of melanoidin, unmodified and modified (A) PELP (B) CLLP and (C) TILP at different pH.

3.3.9.3 Adsorption mechanism through EDX

EDX analysis of modified PELP after the adsorption of melanoidin also resulted in increased contents of N and C elements, as listed in Table 3.10. These findings confirm the complexation/bonding between melanoidin and adsorbent [186, 194].

Table 3.10. Elemental analysis (wt %) of amine-modified PELP, CLLP and TILP before and after adsorption of melanoidin.

Elements	PELP		CLLP		TILP	
	Before adsorption	After adsorption	Before adsorption	After adsorption	Before adsorption	After adsorption
C	90.4 ± 1.3	91.1 ± 1.9	83.2 ± 2.1	85.2 ± 1.9	88.0 ± 2.0	88.0 ± 2.2
N	5.0 ± 1.3	6.9 ± 1.0	8.4 ± 1.4	8.6 ± 1.3	5.0 ± 1.3	7.3 ± 1.4
S	4.6 ± 0.2	1.9 ± 1.4	8.2 ± 1.8	6.2 ± 1.6	6.0 ± 1.6	4.3 ± 1.4

3.3.10. Application of amine-modified PELP, CLLP and TILP in real spentwash sample

To demonstrate the usefulness of the present study on an industrial scale to the treatment of melanoidin compound, the same adsorption study was performed with a real spentwash sample collected from a molasses-based distillery. The experiment was performed at the optimized conditions with 1 % v/v spentwash. The decrease in COD of the solution along with efficient decolourization is listed in Table 3.11. This study clearly highlights the potential of amine-modified PELP, CLLP and TILP for melanoidin removal from industrial wastewater (Figure 3.12).

Table 3.11. Comparison study of COD and colour reduction of melanoidin and real spentwash samples by amine-modified PELP, CLLP and TILP.

	Parameters	PELP	CLLP	TILP
Melanoidin	**Initial COD (mg L^{-1})**		28576 ± 452	
	Final COD (mg L^{-1})	2016 ± 10	4000 ± 450	22560 ± 450
	% COD Reduction	94 ± 0.1	85.6 ± 2	20.3 ± 2
	% Colour Reduction	98.50 ± 1	93.2 ± 2	27.7 ± 1
Spentwash	**Initial COD (mg L^{-1})**		1920 ± 26	
	Final COD (mg L^{-1})	312 ± 31	400 ± 18	1576 ± 16
	% COD Reduction	84 ± 2	79 ± 1	18 ± 1
	% Colour Reduction	91 ± 3	84.5 ± 1	21 ± 1

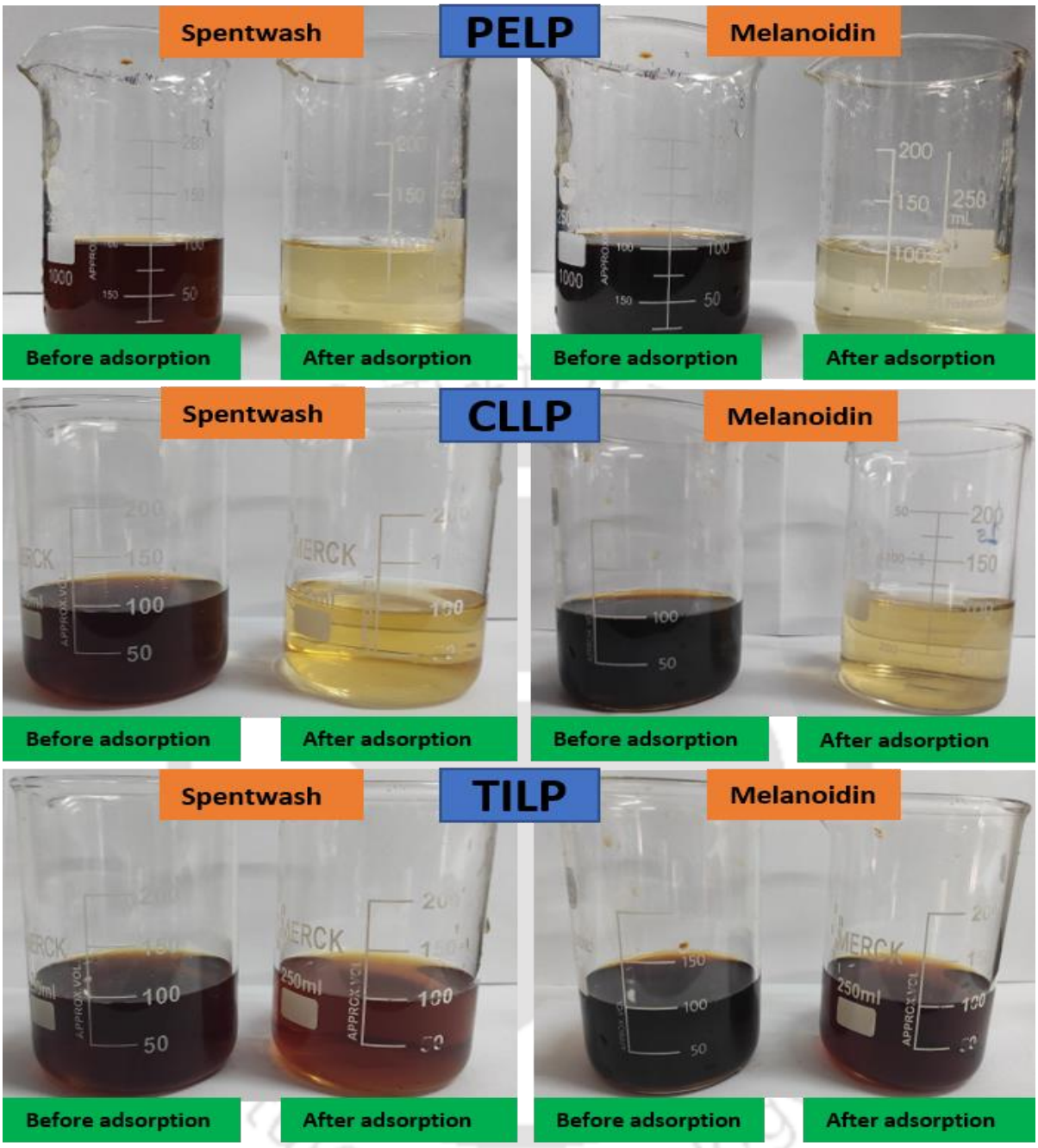

Fig. 3.13: The difference in the colour of samples before and after the adsorption of spentwash and melanoidin by amine-modified PELP, CLLP and TILP at optimized conditions.

3.4. Conclusions

In the present study, we have successfully explored the amine-modified adsorbents prepared by forming self-assembled monolayers (SAMs) for melanoidin removal as a cheap, effective and eco-friendly adsorbent prepared by the widespread Indian plants *Phyllanthus emblica* and *Citrus limon* leaf. The RSM-CCD was applied to optimize experimental parameters (temperature, pH and % adsorbent doses) and was found to be 44 °C, 5.93 and 1.34 % for PELP and 27 °C, 3.1 and 2.0 % for CLLP, respectively, in terms of maximum adsorption of melanoidin compound. The adsorption isotherm was well described by Langmuir, Freundlich, Temkin and D-R Isotherm models. Langmuir (R^2 = 0.98) and Temkin (R^2 = 0.97) isotherm models agreed better with the PELP experimental data while Freundlich (R^2 = 0.99) and D-R Isotherm (R^2 = 0.99) models agreed better with the CLLP experimental data. Pseudo first-order kinetic model was fitted better with PELP, while Pseudo-second-order kinetic model was fitted better with CLLP of experimental data of melanoidin removal. Initial 150 min was dominated as rapid adsorption and attained equilibrium followed by intraparticle diffusion. The adsorption process was described as spontaneous and exothermic in the respects of negative and positive values of ΔG and ΔH, respectively. The maximum adsorption capacity of novel adsorbents was estimated to be 616 and 213 mg g^{-1} for PELP and CLLP, respectively. Reusability up to 5th consecutive adsorption/desorption cycles suggested modified adsorbent's good stability and efficiency. The FTIR and Zeta potential analysis explains the chemo-adsorption of melanoidin onto the surface of modified PELP. Overall the modified adsorbent (PELP and CLLP) can be suggested as a suitable adsorbent for melanoidin removal applications and can be applied on an industrial scale in distilleries as cheap, effective and environment friendly.

Chapter 4

Treatment of melanoidin and real spentwash samples using advanced oxidation processes

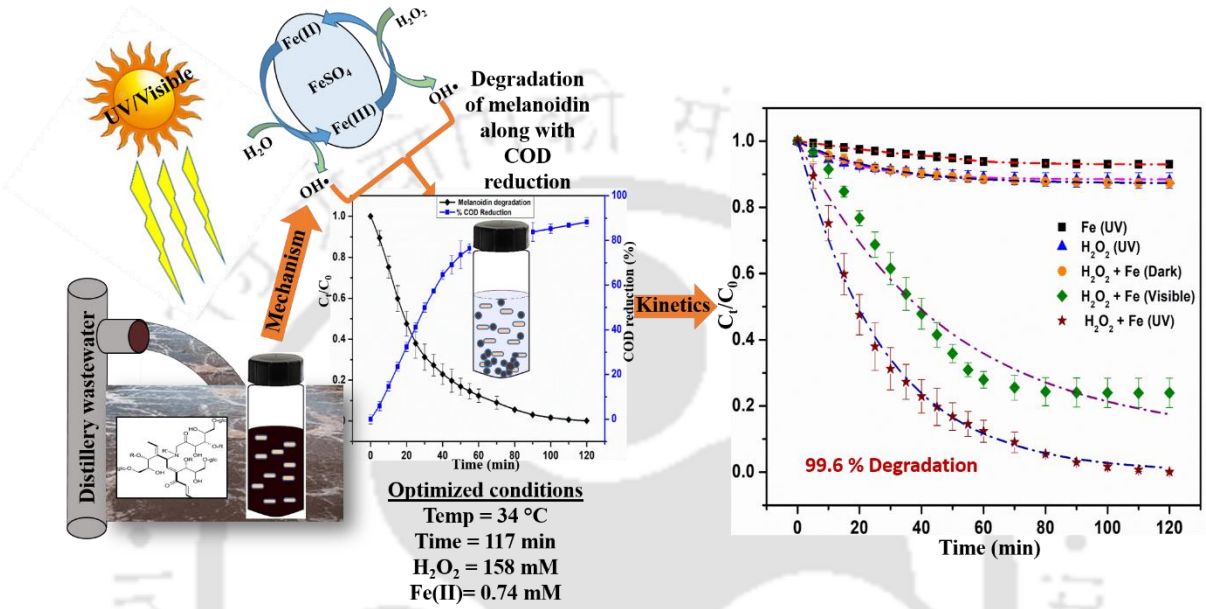

The photochemical degradation of melanoidin has been investigated in this chapter by the photo-Fenton process. The experimental parameters such as temperature, time, H_2O_2 and Fe(II) concentrations were optimized. At the optimized condition, degradation of melanoidin solution was observed associated with COD reduction**.** The individual and combined role of Fe(II)/H_2O_2/UV/Visible/Dark were also investigated in different combinations of Fe(II)/H_2O_2/UV, Fe(II)/H_2O_2/Visible, Fe(II)/H_2O_2/Dark, H_2O_2/UV, Fe(II)/UV and only under UV radiation. The experimental data were fitted for kinetics and thermodynamic analysis. The degradation efficiency of the real spent wash samples was also studied at the optimized conditions. It was found that the optimized photo-Fenton condition effectively removes the color of the real spentwash sample.

4.1. Introduction

As discussed in previous chapters, the distilleries are one of the most polluting industries on the planet, as it generates a significant amount of wastewater every year. Extensive amounts of organic and inorganic pollutants, in addition to toxic heavy metals and their oxides, are detected in distillery effluent wastewater. This has significant ramifications on the ecosystem as well as human health. There are two forms of wastewater generated by the distillery business; the first is spentwash, which is generated after the distillation of fermented broth to separate alcohol [215, 216]. Washing fermenters, cooling water, boilers and other similar activities contribute to the second form of wastewater. There are considerable quantities of COD and BOD load present in spentwash [217]. Untreated sewage has been shown to have hazardous and carcinogenic effects on humans and plants and as a consequence, it is a threat to the ecosystem [5, 218, 219].

In order to successfully remove melanoidin from water while also decreasing the levels of COD and BOD in the water, several physiochemical (adsorption, coagulation-flocculation, oxidation, membrane filtration etc.) and biological (bacterial, fungal, and algal) treatment processes have been applied [5, 174, 220-223]. However, due to the high organic loadings and the presence of melanoidin chemicals in the water, the efficacy of the above treatment procedures is severely hampered [3, 12].

Advanced oxidation processes (AOPs) have been discovered in the recent few decades to rapidly degrade pigments like melanoidin into their intermediates, depending on the treatment period and concentration utilized [12, 224-227]. This decolorizes the wastewater. AOPs generate extremely potent oxidants such as hydroxyl (•OH) radicals which are produced by ozone (O_3), hydrogen peroxide (H_2O_2), photocatalysis, the Fenton process, and ultraviolet radiation [6, 228]. These free radicals oxidize and terminate organic and inorganic molecules,

causing them to degenerate and decay. These approaches are widely recognized as being quite effective for the treatment of various kinds of wastewater [65, 66, 228-231].

4.2. Material and methods

4.2.1. Materials

The list of major chemicals used has been stated in section 3.2.1. Chemicals for Fenton reagents such as Ferrous Sulphate Heptahydrate (Cat. No. 7782-63-0) was acquired from Sisco Research Laboratories in India, with a hydrogen peroxide solution 30 percent w/v (Cat No. 7722-84-1) was purchased from Finar Limited, India. To analyse the total iron (Fe), the standard Fe salt (Cat. No. 84425) were purchased from SRL Limited, India and to analyse Fe(II) and Fe(III), Ferrous ammonium sulphate hexahydrate (Cat.No. GRM1026) and ferrous chloride anhydrous (Cat. No. GRM1178) were purchased from HiMedia Laboratories, India, respectively.

Further, a 15 W (6 Nos) mercury lamp (254 nm) for the Fenton reactor was purchased from OSRAM light groups.

4.2.2. Preparation of Melanoidin

Please refer to section 3.2.5.

4.2.3. Design of Photo-reactor

All the batch experiment was performed inside a house-built closed wooden reactor (24-inch × 18-inch × 15-inch). The reactor contained 6 nos of low-pressure mercury vapor lamp (254 nm) for UV irradiation source (15 W each) procured locally from OSRAM light groups. The mercury vapor lamp was placed in the set of 3 opposite and parallel to the other side as shown in Figure 4.1. All the experiments were performed under this UV-irradiation reactor, having an average UV light intensity of 59 mW/cm^2. A heating magnetic stirrer was placed at the centre

of the reactor box for providing the proper mixing and maintaining the temperature of the reaction mixture. The inner wall of the reactor was covered with an aluminum sheet for adequate reflection of the UV light.

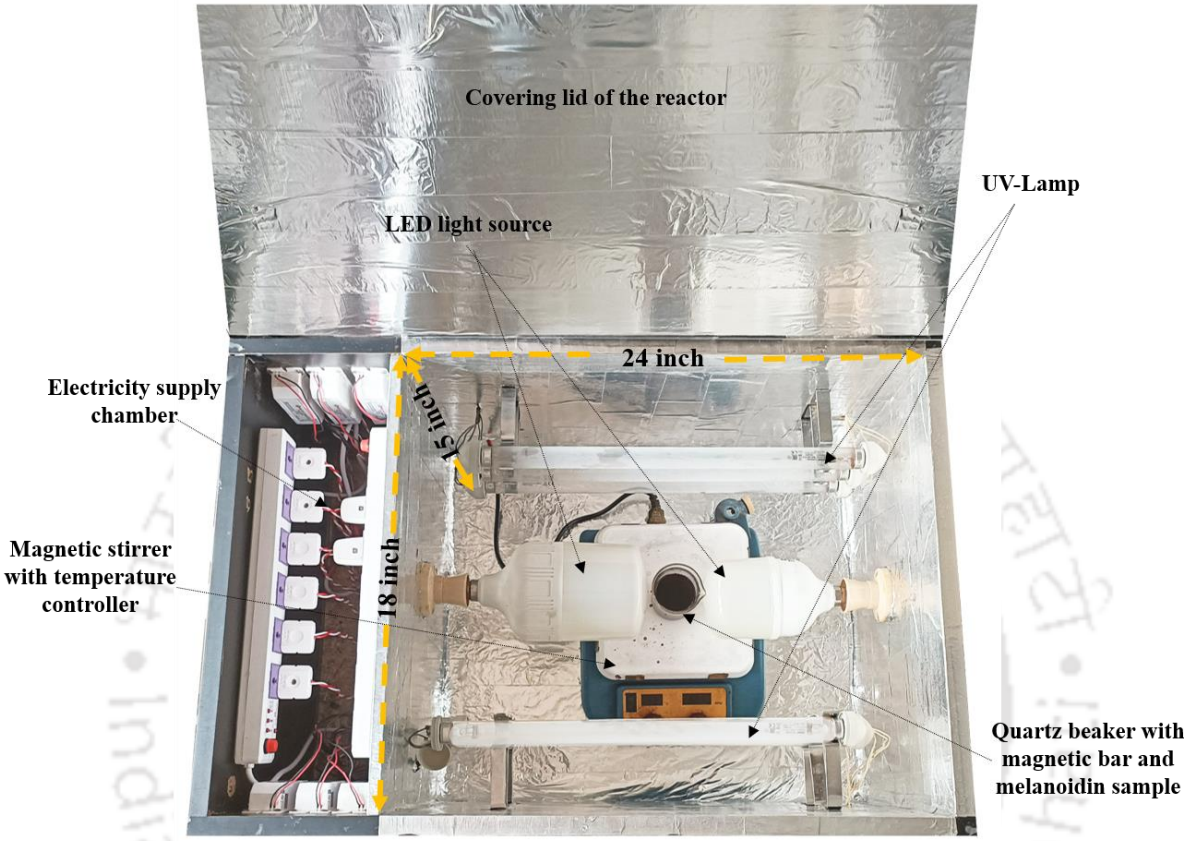

Fig. 4.1: Photo-Fenton reactor equipped with UV light source.

4.2.4. Optimization of the experimental conditions by response surface methodology (RSM)

The RSM-CCD was applied for the optimization of the key process parameters. Please refer to section 3.2.6 and 3.3.3 for the detailed methodology. The four independent variables, temperature (A), time (B), H_2O_2 concentration (C) and Fe(II) concentration (D) were varied at the temperatures ranging from 25 to 55 °C, time ranging from 30 to 200 minutes, H_2O_2 concentration concentrations ranging from 10 to 200 mM and Fe(II) concentration ranging from 0.1 to 1.0 mM, respectively in the present work. Melanoidin degradation (%) was used as

a response of the reaction. To forecast the best conditions for the maximal removal (% degradation) by the Fenton process, the software generated 30 experimental sets indicated in Table 4.2. The ANOVA program was used to perform regression analysis based on the experimental data [232, 233].

4.2.5. Melanoidin degradation studies

The batch experiments for melanoidin degradation (%) were carried out under the RSM-CCD recommended experimental conditions in a 100 mL of 1.0 % w/v initial melanoidin concentration in a 150 mL of quartz beaker. All the batch experimental setups were performed in the reactor chamber, providing 500 rpm of mixing speed using a stirrer. The samples were collected and centrifuged at 10000 rpm for 10 minutes at 25 °C temperature using a centrifuge (Sigma 4-16K). The melanoidin content was determined by measuring the optical density of the supernatant at a wavelength of 475 nm [14]. All the experiments were performed in triplicates. The following calculation was used to compute the percentage degradation/elimination of melanoidin (Eq. 4.1).

$$\%\, Degradation = \frac{(C_i - C_f)}{C_i} \times 100 \qquad (4.1)$$

Where C_i is the initial concentration of melanoidin solution and C_f is the concentrations of melanoidin solution after degradation.

In addition, a titrimetric approach was used to determine the chemical oxygen demand (COD) values of both untreated and treated samples in the closed reflux process. The reagents and protocol for the COD analysis were prepared in accordance with the American Public Health Association (APHA) manual's standard examination techniques for water and wastewater [234].

The melanoidin degradation by the Fenton process was further analysed by HPLC (Agilent Technologies, Model: 1260 Infinity Ⅱ) equipped with a reverse phase C-18 column (having

the dimension of 250 × 4.6 mm, with a particle size diameter of 5 µm) along with a UV detector. The 20 µl samples collected at different time interval were injected, after filtering through a 0.2 µm syringe filter followed by a progression of 100 % ultrapure Mili-Q water with a flow rate of 0.5 mL min^{-1} as mobile phase, at 25 °C for 20 min in isocratic mode. The wavelength of the UV detector for the monitoring of degradation of melanoidin was set at 290 nm [96, 235, 236].

To understand the mechanism of the photo-Fenton process, the concentrations of total iron (Fe), Fe(II) and Fe(III) in the samples at different time intervals were calculated using Atomic Absorption spectrophotometer (AAS) (Make: Varian, Netherlands, Model-AA240).

4.2.6. Kinetic and thermodynamic studies

The kinetics of melanoidin degradation was carried out under optimum conditions predicted by RSM-CCD, with samples taken at various time intervals up to 120 minutes. In order to explore the rate parameter of the degradation, the first-order kinetic model was tested. The degradation studies were also conducted at three different temperatures (35, 45 and 55 °C) to decipher the thermodynamics of the process. The expressions that were employed in the kinetic and thermodynamic models are listed in the following Table 4.1 [5].

Table 4.1. Expressions of the kinetic and thermodynamic models used to fit the experimental data.

Models	Equations
Kinetic model	
First-order	$C_t = C_1 \times e^{-kt} + C_2$ $C_1 + C_2 = C_0$
Thermodynamic model	
Thermodynamic	$\Delta G = \Delta H - T\Delta S$ $\Delta G = -RTlnK_c$ $ln\ K_c = \frac{\Delta S}{R} - \frac{\Delta H}{RT}$

Where, C_0 is the initial concentration of melanoidin at time t = 0, C_t is the concentration of melanoidin at any time t. K_c is expressed as C_{Ae}/C_{Se} [237] where C_{Ae} and C_{Se} refer to the amounts of degraded melanoidin and residual concentration in solution at equilibrium, respectively. R and T are the universal gas constant (8.314 J mol^{-1} K^{-1}) and temperature (K).

4.2.7. Colour removal of the real sample (spentwash)

Please refer to the section 3.2.10

4.3. Results and Discussion

4.3.1. Optimization of experimental conditions for the maximum degradation of melanoidin

To optimise the maximal degradation of melanoidin using RSM-CCD, four independent variables were chosen: (A) temperature, (B) time, (C) H_2O_2 concentration, and (D) Fe(II) concentration. The variables' lower and upper bounds were set to (A) 25/55 °C, (B) 30/200 min, (C) 10/200 mM, and (D) 0.1/1.0 mM, respectively. The mini-tab software proposed a total

of 30 experimental setups based on these four variables (Table 4.2). The melanoidin degradation (%) was selected as the response. Table 4.2 compares the actual response values with the expected values obtained from fitting the data to a quadratic polynomial equation. The model equation for the degradation of melanoidin is as follows (Eq. 4.2):

$$\%\, Degradation\ of\ melanoidin = 87.79 + 7.97A + 19.54B + 35.28C + 34.06D - 1.96AB + 3.66AC + 5.00AD + 6.37BC + 10.09BD + 26.30CD - 0.98A^2 - 10.05B^2 - 6.23C^2 - 14.80D^2 \quad (4.2)$$

To acquire the results of the regression study, the experimental data were subjected to an ANOVA analysis. The experimental and predicted data had an R^2 value of 0.85. The ANOVA model's higher F-value (5.93) and lower p-value (< 0.01) demonstrated its relevance. Table 4.3 lists the independent variables A, B, C, and D (temperature, time, H_2O_2 concentration, and Fe(II) concentration) and their interactions including AB, AC, AD, BC, BD, CD, A^2, B^2, C^2 and D^2 of the ANOVA analysis. This study found that model terms B, C, D, CD and D^2 were significant (p-value < 0.05). Minitab program projected optimal conditions for melanoidin breakdown at 34 °C, 117 min, H_2O_2 concentration of 158 mM, and Fe(II) concentration of 0.74 mM, respectively. Figure 4.2 shows 3D response surface plots for maximal melanoidin degradation under optimal conditions. The experimental response (% melanoidin degradation) at the optimal conditions showed almost complete degradation (99.0 ± 1 %) and 88.0 ± 2 % of COD reduction, which agreed to the closeness of the predicted value (Figure 4.3).

The degradation of melanoidin at RSM optimized conditions was also quantified by HPLC analysis by comparing the chromatograms of standard melanoidin samples of known concentrations (Figure S4 A). The reduction in the peak area at different time interval was compared to control samples to analyse the degradation efficiency of melanoidin. The melanoidin peak was eluted at the retention time of 5.2 minutes (Figure S4 (B and C)). The exponential decrease in peak area and intensity justify the degradation of melanoidin over the

time. The degradation (%) measured using UV-Visible Spectrophotometer was comparable with that determined using HPLC as shown in Figure 4.4. The HPLC analysis also estimated 98 ± 1 % of melanoidin degradation within 120 minutes by the photo-Fenton treatment.

Table 4.2. The experimental set-ups of four independent variables along with actual and predicted response values.

Serial No.	Independent variable				Response (% degradation)	
	Temp. °C (A)	Time min (B)	H_2O_2 mM (C)	Fe(II) mM (D)	Actual Value	Predicted Value
1	25.00	200.00	10.00	0.10	21.54	18.43
2	25.00	30.00	200.00	1.00	78.97	96.78
3	70.00	115.00	105.00	0.55	96.36	99.81
4	40.00	30.00	295.00	0.55	99.60	91.11
5	55.00	200.00	200.00	0.10	35.66	51.14
6	40.00	115.00	105.00	0.55	98.84	87.79
7	40.00	285.00	105.00	0.55	98.70	86.69
8	25.00	30.00	10.00	1.00	17.85	6.32
9	25.00	200.00	200.00	0.10	29.89	41.79
10	40.00	115.00	105.00	0.55	96.83	87.79
11	25.00	200.00	10.00	1.00	32.72	44.15
12	55.00	30.00	10.00	1.00	26.54	16.21
13	55.00	30.00	200.00	0.55	92.13	93.50
14	40.00	115.00	105.00	0.00	6.87	24.05
15	55.00	115.00	105.00	0.55	99.94	94.78
16	40.00	115.00	105.00	1.45	99.92	96.72
17	40.00	115.00	105.00	0.55	97.19	87.79
18	10.00	115.00	105.00	0.55	65.20	67.93
19	55.00	30.00	10.00	0.10	17.54	10.88
20	40.00	115.00	0.00	0.55	3.97	41.18
21	40.00	0.00	105.00	0.55	1.38	42.96
22	55.00	200.00	10.00	0.10	27.14	13.12
23	40.00	115.00	105.00	0.55	96.00	87.79
24	25.00	30.00	200.00	0.10	23.20	6.24
25	40.00	115.00	105.00	0.55	96.07	87.79
26	25.00	30.00	10.00	0.10	8.79	8.34
27	40.00	115.00	105.00	0.55	95.49	87.79

28	25.00	200.00	105.00	0.55	98.41	90.30
29	55.00	200.00	10.00	1.00	46.31	58.83
30	55.00	30.00	200.00	0.10	29.73	23.43

Table 4.3. ANOVA table of quadratic model for melanoidin degradation.

Source	Sum of squares	df	Mean Square	F-value	p-value
Model	35938.43	14	2567.03	5.93	< 0.01
A (Temp.)	1386.89	1	1386.89	3.20	0.09
B (Time)	5600.51	1	5600.51	12.94	< 0.01
C (H_2O_2)	15261.37	1	15261.37	35.27	< 0.01
D (Fe(II))	15183.10	1	15183.10	35.08	< 0.01
AB	54.54	1	54.54	0.13	0.73
AC	163.04	1	163.04	0.38	0.55
AD	274.71	1	274.71	0.63	0.44
BC	391.49	1	391.49	0.90	0.36
BD	997.36	1	997.36	2.30	0.15
CD	6250.50	1	6250.50	14.44	< 0.01
A^2	26.74	1	26.74	0.062	0.81
B^2	1675.83	1	1675.83	3.87	0.07
C^2	460.04	1	460.04	1.06	0.32
D^2	3878.23	1	3878.23	8.96	< 0.01
Residual	6491.41	15	432.76		
Lack of Fit	6484.22	10	648.42	451.04	< 0.01
Pure Error	7.19	5	1.44		
Cor Total	42429.84	29			

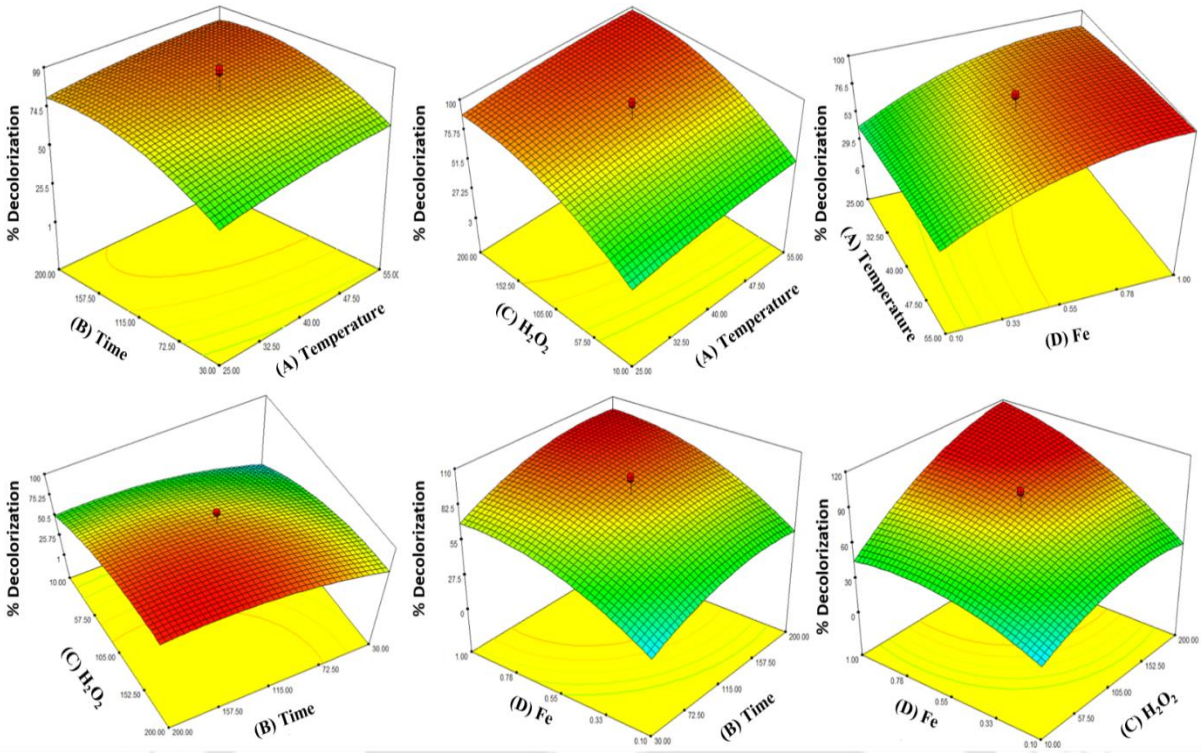

Fig. 4.2: 3D response surface plots with their respective independent variables such as (A) Temperature in °C, (B) Time in min, (C) H_2O_2 concentration in mM and (D) Fe(II) concentration in mM for the maximum degradation of melanoidin.

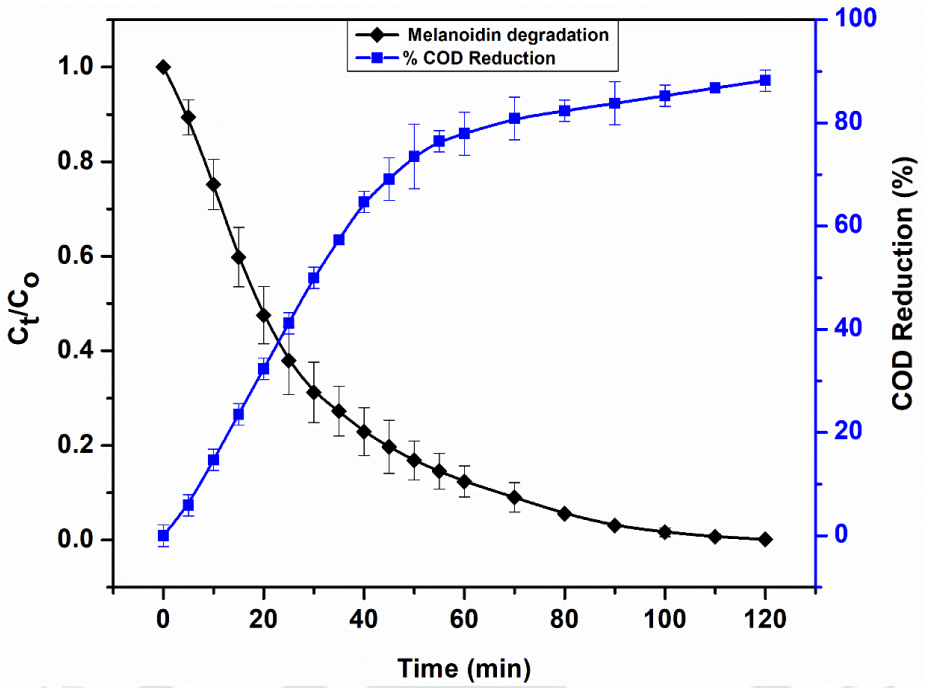

Fig. 4.3: Degradation of melanoidin and COD reduction at RSM optimized conditions of temperature 34°C, time 117 min, 158 mM of H_2O_2 concentration and 0.74 mM of Fe(II) concentration.

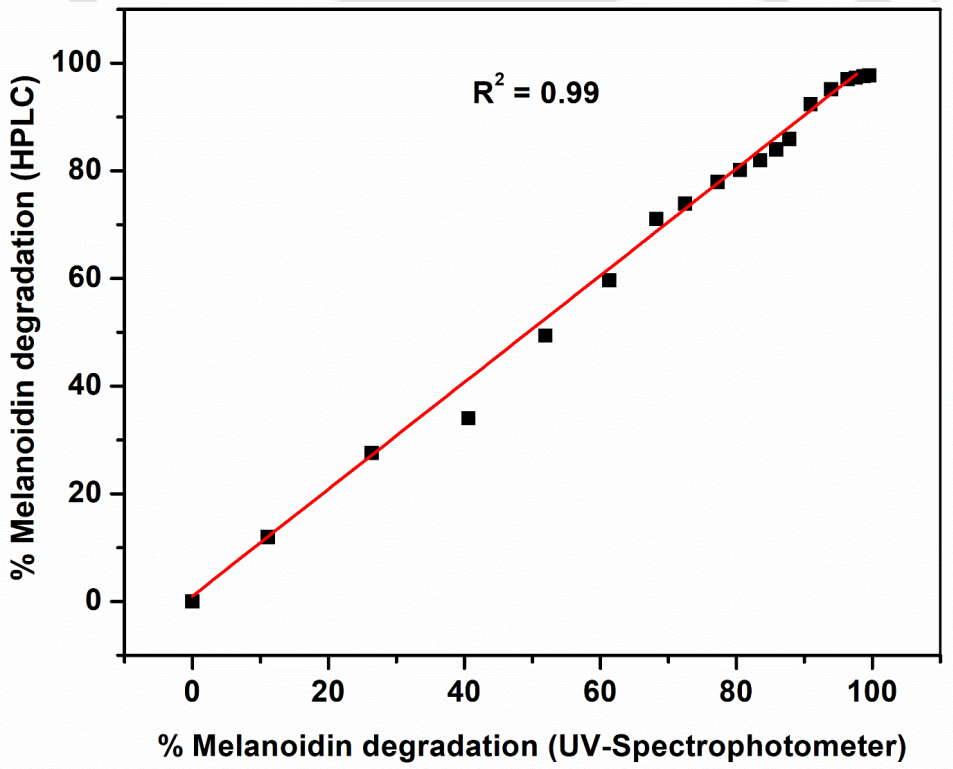

Fig. 4.4: Comparison of melanoidin degradation (%) estimated through HPLC and UV-Spectrophotometer methods.

4.3.2. Effect of pH on photo-Fenton reaction for melanoidin degradation

The previous chapter shows that pH plays a main parameter for the adsorption of melanoidin. Similarly, the role of pH in the Fenton process for melanoidin degradation was also investigated. The experiment was carried out under the RSM optimized conditions by ranging the pH of the solution from 3 to 11 with the initial melanoidin concentration of 1 % (w/v). As observed by Figure 4.5, a slight decrease in melanoidin degradation efficiencies was obtained by increasing solution pH to the alkaline values of 9 and 11. This corresponds to the reduction in the rate of generation of •OH free radicals during the process of melanoidin degradation. In the alkaline medium, the •OH radicals may have been scavenged after a significant level of H_2O_2; as a result, the phenomena of melanoidin degradation efficiencies decrease with an increase in pH. Similar trends of effects of pH on melanoidin degradation were also reported by various literature studies [66, 238, 239].

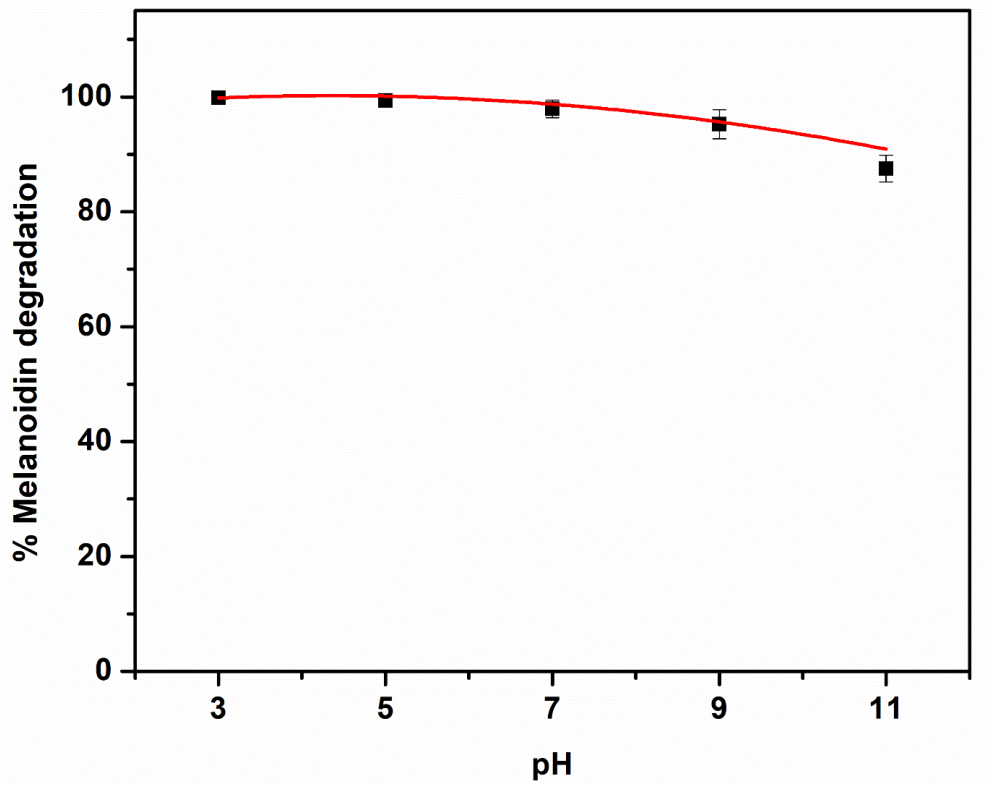

Fig. 4.5: Consequence of solution pH on melanoidin degradation at photo-Fenton optimized condition.

4.3.3. Kinetic study on melanoidin degradation

As depicted in Figure 4.6, the effects of various physicochemical conditions of the Fenton process have been investigated on melanoidin degradation. In the absence of H_2O_2, only 7 ± 1 % of melanoidin degradation was found. The poor degradation efficiency may be due to the generation of a significantly less amount of •OH free radicals in the absence of H_2O_2. Similarly, only 12 ± 2 % of melanoidin degradation was found in the absence of Fe(II) ions. The poor degradation efficiency occurred due to the lack of Fe(II) catalyst. As mentioned in equation 4.2, the Fenton reaction cannot be completed without the Fe(II) catalyst. The degradation efficiency of melanoidin by the Fenton process was also performed without solar irradiation (dark), visible and UV light irradiation. The degradation efficiencies of melanoidin were achieved as 13 ± 1, 76 ± 2 and 99 ± 1 % under dark, visible and UV light irradiation, respectively.

The degradation kinetics of melanoidin by the photo-Fenton process was carried out as a function of contact time at the optimized conditions. As discussed in the above section (sec. 4.3.3), the degradation rate of melanoidin compounds depends on the availability of H_2O_2 concentration and variations in the total iron (Fe), Fe(II), and Fe(III) concentrations in the reaction. The kinetics studies may adequately explain the degradation response in terms of melanoidin concentration during the period of exponential utilization of H_2O_2. The experimental data at RSM optimized conditions including various control experiments were applied in the equation $\boldsymbol{C_t = C_1 \times e^{-kt} + C_2}$ to estimate the model parameters. The plot of time (t) vs. relative concentration of melanoidin (C_t/C_o) with respect to time is shown in Figure 4.6 [240, 241]. The experimental data are shown as symbols while fitted data are plotted as dotted lines. The correlation coefficient value (R^2) of 0.99 indicated the fitness of the first-order kinetic model. The fitted parameters are listed in Table 4.4. The reaction rate constants (k) under UV light at the optimized condition (UV light photo-Fenton) were found to be 0.04

± 0.01 min^{-1}, which decreased to 0.02 ± 0.01 min^{-1} for the visible light photo-Fenton. The degradation rate in visible light is slower than UV light irradiation because the difference in •OH free radicals produced by the Fenton reaction under higher energy UV light that the lower energy visible light. Thus the degradation of organic pollutants (melanoidin) is slower in visible light rather than UV light [241].

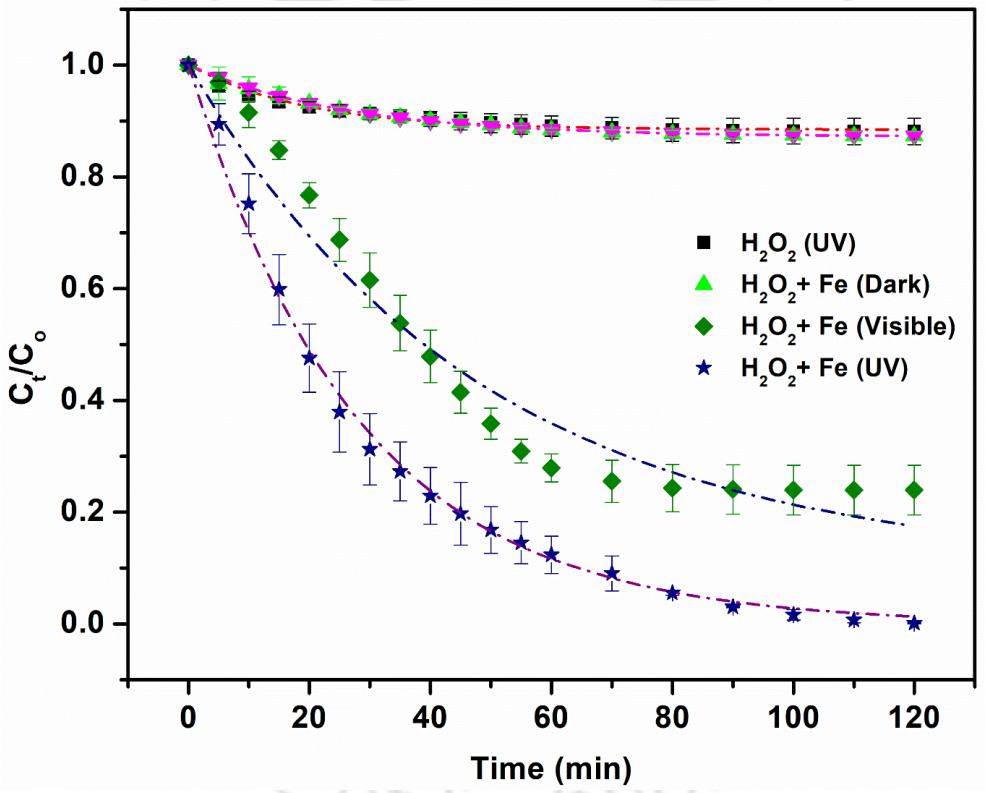

Fig. 4.6: The fitting of first-order kinetic models of experimental data obtained at the optimized conditions of temperature 34°C, time 117 min, H_2O_2 concentration of 158 mM and Fe(II) concentration of 0.74 mM under UV and visible lights. The control experiments were performed in the dark and in the absence of Fe(II). The experimental data are shown as symbols while the dotted lines refer the fitted data.

Table 4.4. The kinetic parameters were obtained by fitting the experimental data to the first-order kinetic model at different conditions of the photo-Fenton process.

S. No	Experimental conditions	C_1 (g L^{-1})	K (min^{-1})	C_2 (g L^{-1})	% Degradation	R^2
1	H_2O_2 (UV)	1.24 ± 0.24	0.05 ± 0.01	9.50 ± 0.24	12 ± 2	0.98
2	H_2O_2 + Fe(II) (Dark)	1.37 ± 0.15	0.04 ± 0.01	9.37 ± 0.15	13 ± 1	0.94
3	H_2O_2 + Fe(II) (Visible)	9.65 ± 0.39	0.02 ± 0.01	1.09 ± 0.39	76 ± 5	0.97
4	H_2O_2 + Fe(II) (UV)	10.74 ± 0.29	0.04 ± 0.01	0.02 ± 0.03	99 ± 1	0.99

4.3.4. Thermodynamic analysis of melanoidin degradation at RSM optimized conditions

In addition, the effect of temperature on the rate of melanoidin degradation under RSM optimal situations was examined. The thermodynamic analysis investigated the ΔS, ΔH and ΔG of the melanoidin degradation process. The examinations of melanoidin degradation were carried out in batches for 120 minutes under optimal conditions at 308, 318, and 328 K temperatures. The thermodynamic expressions listed in Table 4.1 were used to estimate ΔS, ΔH and ΔG. Plot of 1/T vs. $\ln K_c$ was used to determine the thermodynamic parameters (Figure 4.7). Table 4.5 lists the estimated thermodynamic parameters. At all three experimental temperatures, the negative value of ΔG value suggests the spontaneous degradation of melanoidin [210]. The impulsive increase in ΔG value with an increase in temperature (from 298 to 328 K) indicated a decrease in the degradation efficiency of melanoidin (Table 4.5). The negative values of ΔH reflected the exothermic nature of melanoidin degradation and hence lower degradation is observed at a higher temperature. The negative values ΔS indicated the decrease in randomness at the interface due to a decline in the solution concentration.

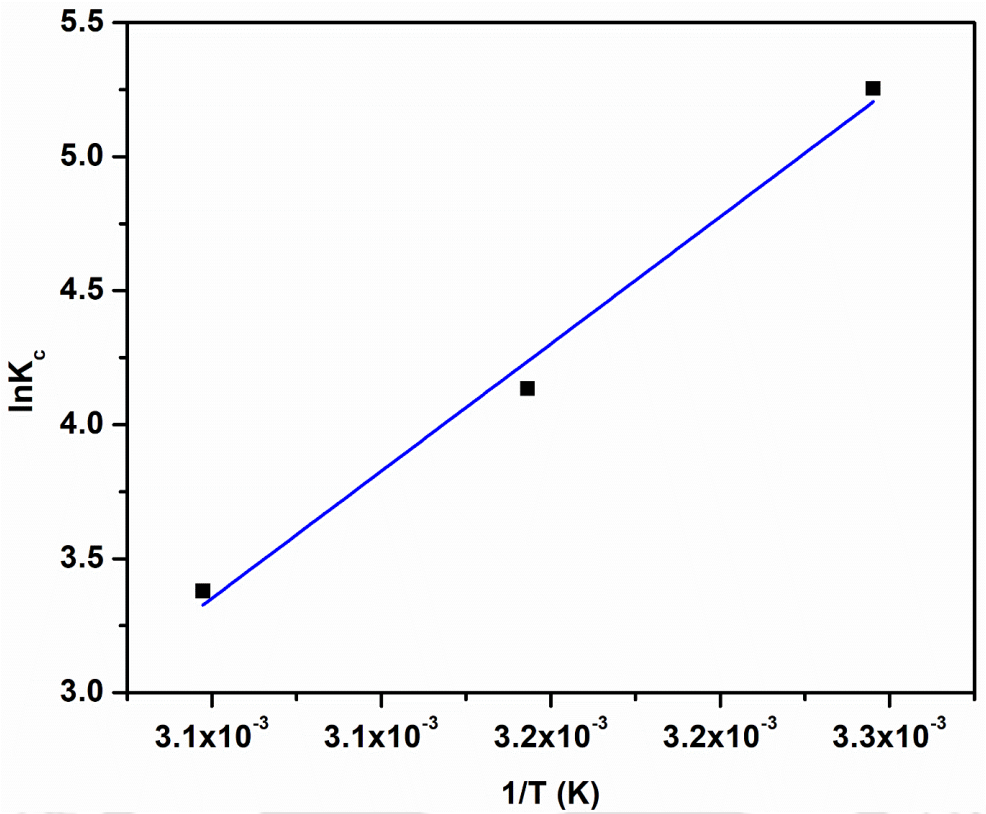

Fig. 4.7: Thermodynamic investigation of melanoidin degradation at RSM optimized conditions.

Table 4.5. Thermodynamic investigation of melanoidin degradation and its characteristics under RSM optimized conditions.

Temperature (K)	ΔG (kJ mol^{-1})	ΔH (kJ mol^{-1})	ΔS (J mol^{-1} K^{-1})	R^2
308.15	-13.46			
318.15	-10.94	-78.91	-212.80	0.99
328.15	-9.2			

4.3.5. Mechanism of melanoidin degradation by the photo-Fenton process

The photo-Fenton process generates extremely potent oxidants such as •OH radicals [228]. These •OH free radicals oxidize and terminate organic and inorganic molecules, causing them

to degenerate and decay. Thus have a lot of potential for treating extremely polluted distillery wastewater.

In 1894, H.J.H. Fenton proposed the Fenton method for the first time, as expressed by Eq. (4.3 and 4.4) [242].

$$Fe(II) + H_2O_2 \rightarrow Fe(III) + OH^- + \bullet OH \quad (4.3)$$

$$\mathrm{Fe(III)} + H_2O + h\vartheta \rightarrow Fe(II) + H^+ + \bullet OH \quad (4.4)$$

$$(Fe(III) + 3OH^- \rightarrow F_e(OH)_3 \quad (4.5)$$

$$H_2O_2 \overset{h\nu}{\rightarrow} 2\bullet OH \quad (4.6)$$

$$\boldsymbol{Organic\ pollutants + \bullet OH \rightarrow Degradate\ products} \quad (4.7)$$

When Fe(II) and H_2O_2 are combined in the presence of sun or ultraviolet radiation, the process is referred to as a photo-Fenton method, and it significantly enhances the decontamination as compared to a non-photochemical Fenton process. Equations 4.4 and 4.6 describe the role of light irradiation (4.6) [64]. Fe(II) interacts with H_2O_2 and generates Fe(III) ions (Eq. 4.3), which participate in the photo-Fenton process (Eq. 4.4). A part of Fe(III) precipitates in the form of $Fe(OH)_3$ (Eq. 4.5) [243, 244].

The utilization of total iron Fe, Fe(II) and Fe(III) concentrations were measured as a function of time as shown in Figure 4.8. At the beginning of the photo-Fenton reaction, the iron was present as Fe(II) from ferrous sulphate heptahydrate. Fast interaction between Fe(II) ions and excess hydrogen peroxide (H_2O_2) results in the formation of ferric (Fe(III)) ions within minutes (Eq. 4.3). The Fe(II) concentration rapidly decreased from 0.74 to 0.03 mM and the concentration of Fe(III) reached to 0.73 mM. Further, the Fe(III) was gradually converted into Fe(II) (Eq. 4.4), which was rapidly consumed during the Fenton reaction [245, 246]. This resulted in a slight increase in the concentration of Fe(II) during the photo-Fenton process.

Due to the limitation of H_2O_2 availability in the reaction, the rate of reaction (Eq. 4.3 and 4.5) gradually starts to decrease and resulted in the reduction in the ratio of Fe(II) consumption and Fe(III) generation (Figure 4.8). In fact, the pH of the reaction system decreases slightly during the early degradation phase due to the presence of a higher concentration of H_2O_2 and subsequently increased slightly during the final degradation because of the depletion/utilization of H_2O_2 as shown in Figure 4.8. The series of catalytic cycles between Fe(II) and Fe(III) for producing radicals impact the availability of H_2O_2 concentration in the reaction [240]. Figure 4.8 also illustrates that the concentration of total iron (Fe) also decreased in the Fenton reaction due to the diversion of a part of Fe(III) for the formation of ferric oxyhydroxides through equation 4.5.

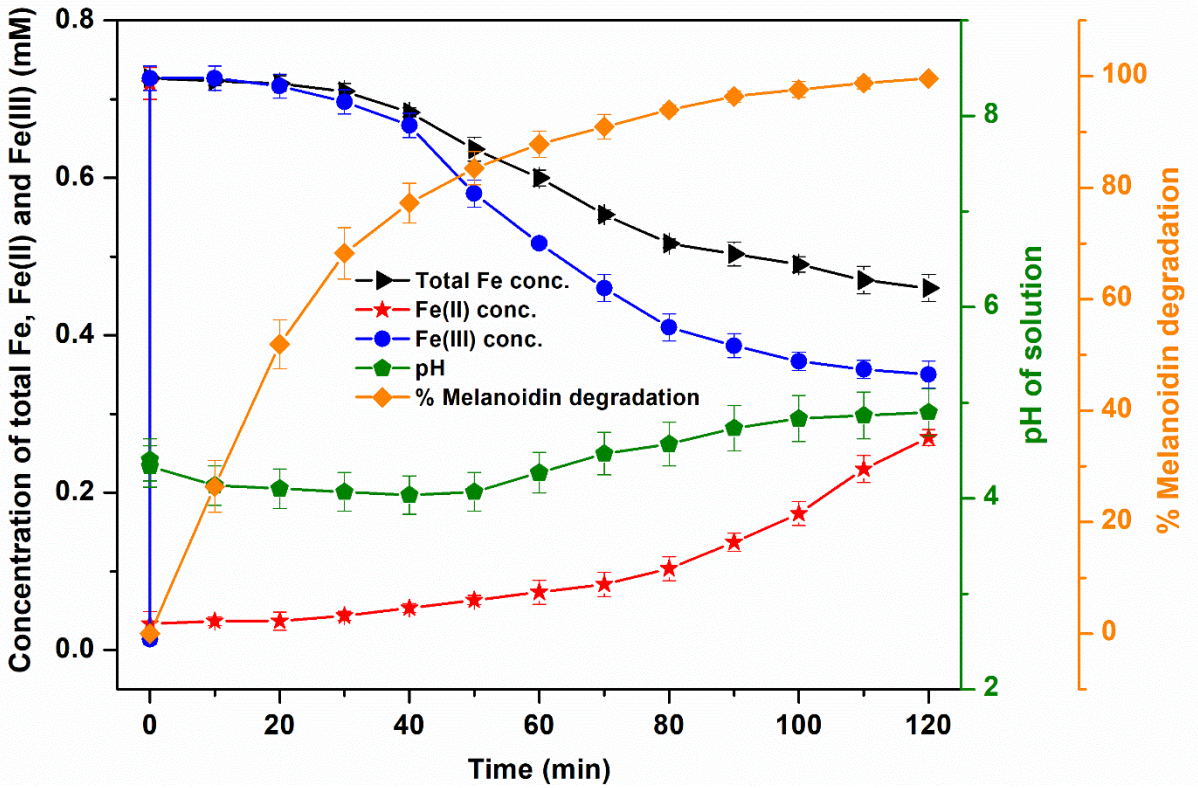

Fig. 4.8: Change in concentrations of Fe, Fe(II), Fe(III) ions and pH of the solution during the melanoidin degradation process ($Fe(II)_{t=0}$ = 0.74 mM, $pH_{t=0}$ = 4.4).

4.3.6. Treatment of real spentwash samples by the photo-Fenton process

A similar degradation investigation was carried out with real spent wash samples collected from a molasses-based distillery to evaluate the applicability of the photo-Fenton process for practical applications. The experiment was carried out under optimized conditions of temperature 34°C, time 117 min, H_2O_2 concentration of 158 mM and Fe(II) concentration of 0.74 mM. The concentration of spentwash was varied from 1 to 10 % v/v. Almost complete degradation of sepntwash was observed up to 5 % of real spentwash including with 87 ± 2 % of COD reduction, and further degradation efficiency was gradually decreased with an increase in the concentration from 5 to 10 % (Figure 4.9). Table 4.6 lists the various forms of melanoidin-containing wastewaters treated by the photo-Fenton process. In the present study, the melanoidin degradation and COD reduction efficiencies were improved several times compared to the literature. The higher H_2O_2/Fe(II), COD/H_2O_2 and COD/Fe(II) ratio evidently highlights the photo-Fenton process's potential at the optimized conditions for the effective treatment of melanoidin-containing wastewater from visible and UV-light irradiations, respectively (see Table 4.9).

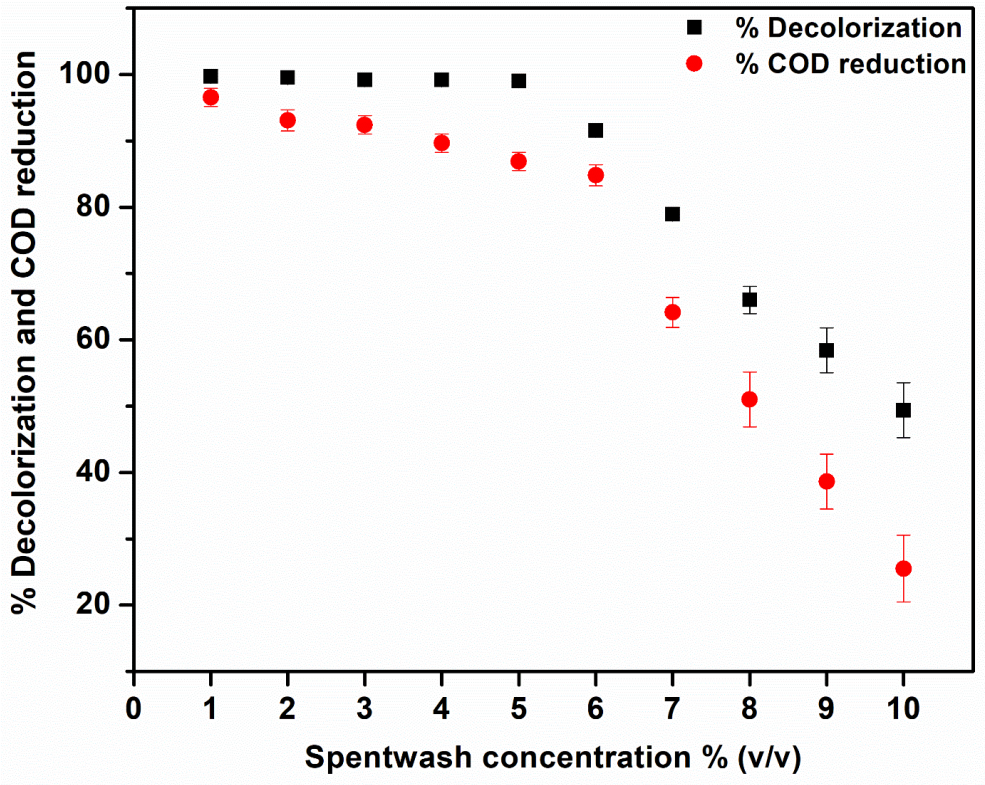

Fig. 4.9: Performance of optimized photo-Fenton conditions on actual spentwash samples.

Table 4.6. Comparison of the current study and experimental circumstances with several types of wastewater treated by the photo-fenton procedure.

Source of wastewater	Experimental condition	Light Source	Initial COD	% Decolorization	% COD reduction	H_2O_2/Fe(II) molar ratio	COD/H_2O_2 ratio	COD/Fe(II) ratio	Ref.
Melanoidin containing	H_2O_2 = 2.0 mM Fe(II) = 0.71 mM pH = 8.7 Time = 30 min	Visible	4500	92	25	2.82	66.18	113.18	[247]
Synthetic melanoidin	H_2O_2 = 173 mM Fe(II) = 10.71 mM pH = 3 Time = 90 min	Visible	8000	77.1	74.4	16.15	1.36	13.34	[248]
Synthetic melanoidin	H_2O_2 = 240 mM Fe(II) = 9.82 mM pH = 3 Time = 90 min	Visible	8000	84.7	76.2	24.44	0.98	14.55	[249]
Distillery spentwash	H_2O_2 = 1.8 M Fe(II) = 22 mM pH = 3.8 Time = 60 min	Visible	100000	N/A	48	81.82	1.63	81.17	[250]
Distillery spentwash	H_2O_2 = 282 mM Fe(II) = 0.13 mM	Visible	400	N/A	54	2169	0.04	54.95	[251]

	pH = 3 Time = 60 min H_2O_2 = 49 mM								
Distillery Spentwash	Fe(II) = 89 mM pH = 5.5 Time = 80 min	Visible	40700	N/A	47	0.55	24.43	8.17	[252]
	H_2O_2 = 120 mM								
Distillery effluent	Fe(II) = 0.40 mM pH = 2.0 Time = 180 min	Visible	1500	52	49	300	0.37	66.96	[253]
	H_2O_2 = 500 mM								
Distillery effluent	Fe(II) = 50 mM pH = 3 Time = 60 min	Visible	19000	N/A	44	10	1.12	6.79	[254]
	H_2O_2 = 16 mM								
Distillery effluent	Fe(II) = 4.3 mM pH = 2.84 Time = 70 min	Visible	60000	N/A	66	3.72	110.29	249.17	[72]
	H_2O_2 = 158 mM								
Distillery spentwash	**Fe(II) = 0.74 mM pH = 4.8 Time = 117 min**	**Visible**	**11600**	**77 ± 1**	**66 ± 2**	**213.51**	2.16	279.92	**Present study**

Synthetic melanoidin	**H_2O_2 = 158 mM Fe(II) = 0.74 mM pH = 4.2 Time = 117 min**	**Visible**	**54400**	**76 ± 4**	**63 ± 2**	**213.51**	10.13	1312.74	**Present study**
Distillery spentwash	H_2O_2 = 206 mM Fe(II) = 4.6 mM pH = 3 Time = 180 min	UV	12550	N/A	80	44.78	1.79	48.72	[255]
Distillery spentwash	H_2O_2 = 49 mM Fe(II) = 89.3 mM pH = 5.5 Time = 80 min	UV	40700	N/A	73	0.55	24.43	8.14	[252]
Distillery effluent	H_2O_2 = 7.4 mM Fe(II) = 0.05 mM pH = 3 Time = 120 min	UV	120	75	70	148	0.48	42.86	[256]
Distillery effluent	H_2O_2 = 29.4 mM Fe(II) = 0.36 mM pH = 3 Time = 240 min	UV	10300	75		81.6	10.30	510.91	[257]
Distillery effluent	H_2O_2 = 120 mM Fe(II) = 0.40 mM pH = 4.5	UV	1500	100	95	300	0.37	66.96	[253]

Distillery effluent	Time = 180 min H_2O_2 = 98 mM Fe(II) = 107 mM pH = 3 Time = 240 min	UV	825	N/A	36	0.92	0.25	0.14	[258]
Distillery spentwash	**H_2O_2 = 158 mM Fe(II) = 0.74 mM pH = 4.8 Time = 117 min**	**UV**	**11600**	**92 ± 1**	**85 ± 2**	**213.51**	2.16	279.92	**Present study**
Synthetic melanoidin	**H_2O_2 = 158 mM Fe(II) = 0.74 mM pH = 4.2 Time = 117 min**	**UV**	**54400**	**99 ± 1**	**88 ± 2**	**213.51**	10.13	1312.74	**Present study**

4.4. Conclusions

In the present study, photochemical degradation of melanoidin has been investigated by the photo-Fenton process. The experimental parameters such as temperature, time, H_2O_2 and Fe(II) concentrations were optimized. At the optimized condition (34°C, 117 min, 158 mM of H_2O_2 and 0.74 mM of Fe(II)), the 99 ± 1 % degradation of 1 % w/v of melanoidin solution was observed along with 88.2 ± 2 % of COD reduction. The treatment of distillery effluent was investigated in this inquiry employing a variety of Fenton processes such as Fe(II)/H_2O_2/UV, Fe(II)/H_2O_2/Visible, Fe(II)/H_2O_2/Dark, H_2O_2/UV, Fe(II)/UV and only in UV and resulted in 99 ± 1 %, 76 ± 5 %, 13 ± 1 %, 12 ± 1 %, 7 ± 1 % and ≥1 % of melanoidin degradations, respectively. Fitting of the First-order kinetics and thermodynamic analysis was also performed. The degradation experiment was performed at different pH and observed that the degradation is more effective on acidic pH than basic pH. The HPLC was also investigated for the quantification of melanoidin degradation. The degradation efficiency at optimized conditions was investigated in an industrial-scale spentwash sample to validate the usefulness of the present study. It was found that the optimized photo-Fenton state ultimately removal (100 %) of the colour from 1 to 5 % v/v of real spentwash.

Chapter 5

Photocatalytic degradation of the melanoidin under UV/Visible light illumination

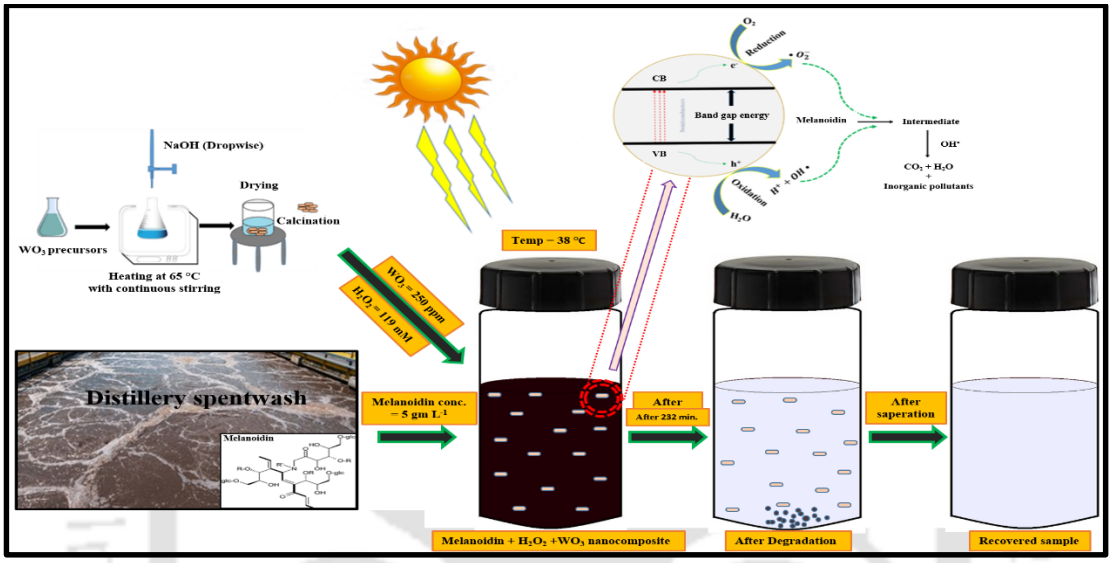

In the 21st century, nanomaterials are widely used in all prospective fields. Decontamination of environmental pollutants by applying nanoparticles is one of the great interests to researchers. In this prospect, we have investigated the nanomaterials for effective photodegradation of melanoidin and distillery spentwash. Various nanomaterials such as ZnO, TiO_2, Fe doped ZnO (FZO) and WO_3 were tested for the photocatalytic degradation of the melanoidin under different light conditions. The synthesized WO_3 and FZO nanoparticles were investigated under visible light and UV light illumination, respectively, for the degradation of melanoidin. These nanomaterials were found to efficiently degrade the melanoidin (> 98 %) under optimized conditions. These photocatalysts also displayed complete degradation of real spentwash and excellent reusability for multiple cycles.

5.1. Introduction

During the COVID pandemic, the use of disinfectants has increased significantly, which are mainly formulated using ethanol. Bioethanol is majorly produced by microbial fermentation of molasses and a considerable amount of effluent (spentwash or vinasse) is generated [259]. India ranks second (followed by Brazil) for ethanol production [260]. Currently, India has more than 300 distilleries producing above 4.27×10^9 liters of ethanol per year and subsequently generating 53.1×10^9 liters of waste effluent [3]. Spentwash is distinguished by its dark brown colour due to the presence of melanoidin compounds [216, 261].

The spentwash contains a high amount (load) of COD and is acidic in nature [262]. Melanoidin has the potential to pollute aquatic habitats due to its dark colour and poor biodegradability. The sunlight is blocked by the deep brown colour of the substance, which results in the inhibition of photosynthesis [3, 5, 263]. Consequently, the Ministry of Environment, Forests, and Climate Change (MOEF), Government of India has designated these businesses as belonging to the "red category" of polluting industries. In order to treat the melanoidin-containing wastewater, a variety of wastewater treatment methods have been developed, including biological treatment, physiochemical treatment and an advanced oxidation process [15, 218, 264-267].

Semiconductor photocatalysts have gained the interest of researchers in the domains of electrochemistry, catalysis, and photochemistry for a long time due to their chemical stability and photocatalytic activity [66, 268, 269]. A few of the most common semiconductor photocatalysts are titanium oxide (TiO_2), zinc oxide (ZnO), Cadmium sulfide (CdS), Zinc sulfide (ZnS), ferric oxide (Fe_2O_3) etc. The photocatalysts have wide-bandgap energy, enormous exciting binding energy, and diverse activity [270-274]. Consequently, these semiconductor photocatalysts have received widespread interest in environmental applications for prospective uses in photocatalytic

degradation of various organic and inorganic pollutants [275]. Various factors including size, shape, defects and surface morphology affect photocatalytic activity [276, 277]. The photocatalytic activity of nanostructured semiconductors is significantly improved as compared to the bulk material [278]. Photocatalysts typically react with water molecules when they are introduced to light irradiations. The hole (h^+) in the catalyst valence band (VB) combines with the water molecule to generate •OH radicals. These generated •OH radicals have a high redox potential, and as a result possess a tendency to oxidize a variety of organic/inorganic contaminants [6, 224].

In this regard, the production of semiconductor nanoparticles has been a significant focus of research for various purposes. The recent advances in nanotechnology have enabled to design of visible light as well as UV light active photocatalysts by tuning the material properties [279, 280]. However, these semiconductors are not extensively explored for the degradation of melanoidin, spentwash or other dyes [96, 281-283]. The acid-treated zeolite was applied with Fenton catalyst to enhance the rate of degradation and resulted in excellent decolourization (90 %) and COD reduction (60 %) up to two consecutive cycles under UV-light irradiation [239]. A similar study was also performed by Benton *et al.* by applying activated carbon (30 %) with TiO_2–ZnO nanohybrid photocatalyst synthesized via reflux method in a ratio of 3:1 and resulted in 97 % degradation of synthetic melanoidin (initial COD load of 3000 mg L^{-1}) at the optimized conditions under UV-light irradiation [283].

Visible light photocatalysts were also explored for the degragation of dyes. Li *et al.* reported complete degradation of Rhodamine B (RhB) and 69.2 % of Orange (II) by multiple-metal oxide photocatalyst Ag_2ZnGeO_4 under visible light illumination [284]. Rahman *et al.* synthesized WO_3 nanomaterials in bulk by applying argon/oxygen plasma beam inside a novel plasma chemical reactor and applied for photocatalytic degradation of Rh-B dye. Almost complete degradation of

20 ppm dye solution in 150 min under visible light was reported [278]. Vineetha *et al*. reported that distillery spentwash treatment by photodegradation resulted in 79 % of colour reduction using the catalyst TiO_2 at the optimum conditions under solar radiation [269]. In a recent study, ZnO was immobilised by kaolin by co-precipitation method and applied as a photocatalyst for spentwash treatment. 91 % decolourization was observed at the optimized conditions of pH 7, catalyst dose of 2.5 g L^{-1}, and reaction time of 240 min under visible light illumination [87]. In a similar study, 1 % vanadium-doped TiO_2 nanoparticles were synthesized applying a sol-gel method and resulted in 65 % of spentwash decolourization in 300 min under solar light irradiation [285].

Thus nanomaterial photocatalysts like WO_3 particles can be employed as an efficient and cost-effective substance for distillery wastewater treatment. Further, the generation of hydroxyl radicals was boosted by adding H_2O_2 which improved photocatalytic processes (by generating •OH free radicals) and enhanced the melanoidin degradation rate [163, 286, 287]. Similarly, the iron-doped ZnO was investigated as a potential substrate for melanoidin degradation. In this regard, the present study used a chemical co-precipitation approach to synthesize photocatalytic nanomaterials [214, 288]. We investigated the photocatalytic efficacy of synthesized nanomaterials under UV and sunlight irradiation for the breakdown of molasses. The significance of the present study is that synthesized semiconductors (WO_3 and iron-doped Zinc oxide (FZO)) were principally first time investigated for the melanoidin degradation and also compared the degradation efficiencies with few most common semiconductors photocatalysts (TiO_2 and ZnO).

5.2. Materials and methods

5.2.1. Materials

The major chemicals and reagents used were of analytical grade, and the aqueous solution was prepared in ultrapure Mili-Q water. Titanium dioxide (TiO_2 - Cat. No. GRM3065), Zinc oxide (ZnO - Cat. No GRM3978) and Hydrochloric Acid (HCl - Cat. No. TC536M) were purchased from HiMedia Laboratories, India. Sodium tungstate dihydrate ($Na_2WO_4.2H_2O$ - Cat. No. 223336), Tungsten (VI) oxide (WO_3 - Cat. No 550086) were purchased from Sigma Aldrich Limited, India and Hydrogen peroxide (H_2O_2 - Cat. No. 70776L2M50) was purchased from Finar Limited, India. $Na_2WO_4.2H_2O$ and HCl were used for synthesis for the tungsten oxide. Glucose ($C_6H_{12}O_6$ - Cat. No. GRM077) and Glycine ($C_2H_5NO_2$ - Cat. No. MB013) were also obtained from HiMedia Laboratories, India for the synthesis of the melanoidin pigments.

5.2.2. Preparation of Melanoidin

Please refer to section 3.2.5 for the preparation of synthetic melanoidin.

The synthesis of melanoidin was characterized by HPLC. The HPLC chromatogram shows the main characteristic peak at the retention time of 5.2 minutes, which corresponded to the reported data [236, 289]. This confirmed the synthesis of melanoidin.

5.2.3. Synthesis of WO_3 and FZO nanoparticles

WO_3 nanoparticles were synthesized via the co-precipitation method with slight modifications [290, 291]. 0.1 M $Na_2WO_4.2H_2O$ (1.65 g in 50 mL of Mili-Q water) were continuously stirred at 80 °C for 2 h. After that 50 mL of 1N HCl solution was mixed dropwise in the solution and further kept for continuous stirring for the next 2 h. The solution was allowed to settle down for 24 h. The

pellets were separated and calcined at different temperatures for 4 h to form the crystalline structure for better photocatalytic activity [292, 293]. The iron dopped zinc oxide (15 % Fe) nanoparticles were also synthesized via the co-precipitation method. In brief, 0.15 molar $Zn(NO_3)_3.6H_2O$ solution was mixed with 1 molar of anhydrous $FeCl_3$ in 100 mL of Mili-Q water at 65 °C. The prepared solution was dropwise titrated in a 65 °C preheated 100 mL of 2 M NaOH. After complete titration of this solution, the synthesis reaction was followed by continuous stirring for 3 h. The residue was extracted out and washed several times with ultrapure Mili-Q water to neutralize the pH. The prepared samples were oven-dried at 80 °C for overnight, followed by the calcination process at 650 °C [294].

5.2.4. Characterization of WO_3 and FZO Nanoparticles

The powder UV–visible spectra of synthesized WO_3 and FZO nano-powder was recorded for band-gap analysis using UV-VIS Spectrophotometer (Shimadzu, Japan - UV-2600 with ISR 2600 attachment). A small amount of $BaSO_4$ powder was spread out into a thin layer and used as the standard (control). X-ray diffraction (XRD) analysis was performed using an X-ray diffractometer to determine the crystalline phase (Rigaku - SmartLab 9kw). The synthesized WO_3 and FZO nanoparticles were characterized using Fourier-transform infrared (FTIR) spectroscopy (Perkin–Elmer - Spectrum 2) in the range of 4000–400 cm^{-1} after preparing potassium bromide (KBr) discs. Raman analysis of synthesized nanomaterials was also performed to analyze the functional groups. A Raman microspectroscopy (Horiba Jobin Vyon - LabRam HR) device with a Peltier-cooled CCD detector was used for this analysis. In this device, the excitation source was a laser line with a wavelength of 633 nm.

The surface morphology of samples was visualized using a Field Emission Scanning Electron Microscope (FESEM) (Zeiss - Sigma 300) and elemental analysis was investigated by energy dispersive spectrum (EDX) (Zeiss - Sigma). The structure of synthesized nanoparticles was monitored using Field-Emission Transmission Electron Microscope (FETEM) analysis (JEOL-2100F). The surface charge of synthesized nanoparticles in de-ionized water was analyzed by zeta potential measurement using Dynamic Light Scattering (DLS) (Anton Paar - Litesizer 500). The specific surface area was investigated using Brunauer–Emmett–Teller (BET) analyzer (Quantachrome - Autosorb-IQ MP).

5.2.5. Photocatalytic degradation experiment

Photocatalytic degradation experiments were performed inside a house-built closed wooden reactor chamber (24-inch × 18-inch × 15-inch) that contains an 80W-LED lamp as a visible light source emitting an average light intensity of 400 mW/cm^2 (Figure S5.1). Also, the reactor comprises with mercury vapor lamp (254 nm) for UV irradiation, which emits an average of 59 mW/cm^2 of the UV light intensity, as discussed in the previous chapter. The chamber contains one magnetic stirrer for continuous shaking and maintaining the temperature of the reaction mixture. All photocatalytic degradation experiments were performed in a 150 mL quartz beaker. Initially, the melanoidin solution was prepared followed by the addition of the photocatalyst. This suspension was continuously stirred in the dark for 30 min and allowed to obtain adsorption-desorption equilibrium between the melanoidin solutions and photocatalyst. After this, the lights were illuminated along with the addition of the optimized H_2O_2 concentration in the suspension solution to enhance the production of •OH radicals and promote photocatalytic activity [295]. 1 mL sample was collected after specific intervals of time and centrifuged at 10000 rpm for 10 min

at 25 °C temperature using a centrifuge (Sigma 4–16 K) [5]. The optical density of the supernatant was immediately recorded at a wavelength of 475 nm using a spectrophotometer (Shimadzu - UV-1900) to analyze the concentration of the residual melanoidin [296]. All the experiments were performed in triplicates. The % degradation of the melanoidin was calculated by the following equation 5.1.

$$\% \, Degradation = \frac{C_i - C_f}{C_i} \times 100 \quad (5.1)$$

where C_i and C_f are the concentrations of the melanoidin solution before and after photocatalytic degradation, respectively.

HPLC analysis was also used to examine the breakdown of the melanoidin by the synthesized photocatalysts WO_3 and FZO using an HPLC system (Agilent Technologies - 1260 Infinity II) equipped with a reverse phase C-18 column (with 250 × 4.6 mm diameter and particle size diameter of 5 mm) and an ultraviolet detector. Syringe filtered (0.2 µm pore size) 20 µl of samples were injected into the system to determine the residual concentration and analyze the degradation efficiency. Mili-Q water was injected at a flow rate of 0.5 mL min^{-1} as a mobile phase. The experiment was conducted in isocratic mode at 25 °C for 20 min. The UV detector's wavelength was set at 290 nm to monitor the concentration of the melanoidin [96, 235, 236, 296].

5.2.6. Optimization of the experimental conditions by response surface methodology (RSM)

The RSM algorithm has been used to optimize the experimental factors in order to maximize the degradation capability. Minitab statistical tool and Central Composite Design (CCD) were used to create the experimental matrix [31, 216, 297]. The four independent variables were selected as listed in Table 5.1. The response of the reaction was measured in terms of the melanoidin degradation (%) and COD reduction (%). The RSM-CCD application designed 30 trial conditions

listed in Table S5.1 and the batch studies for the % melanoidin degradation and % COD reduction were conducted. Based on the experimental data, the ANOVA algorithm was used for the regression analysis [297-299].

Table 5.1. Independent Variables and their ranges were scrutinized in the RSM-CCD design.

Factors (Independent Variables)	Unit	Coded name	Lower limit	Upper limit
Temperature	°C	A	25	55
Time	Minutes	B	30	300
H_2O_2 concentration	mM	C	10	200
WO_3 concentration	ppm	D	100	300

5.2.7. Kinetic and thermodynamic study

The first-order kinetic degradation model was examined to estimate the rate parameters for the degradation of melanoidin. The kinetic study was performed at the optimized conditions and samples were collected at the different time intervals to analyze % degradation and COD reduction. A set of degradation experiments at three different temperatures (35, 45, and 55 °C) were also conducted to understand the thermodynamics of the process. The following Table 5.2 lists the equations used in the kinetic and thermodynamic models.

Table 5.2. Plots for graphical representations of the kinetic and thermodynamic models.

Models	Equations
First-order Kinetic model	$C_t = C_1 \times e^{-kt} + C_2$ Where $C_1 + C_2 = C_0$
Thermodynamic model	$\Delta G = \Delta H - T\Delta S$ $\Delta G = -RTlnK_c$ $ln\, K_c = \frac{\Delta S}{R} - \frac{\Delta H}{RT}$

Where, C_0 is the initial concentration of melanoidin at time t = zero and C_t is the concentration of melanoidin at any time t. K_c is expressed as C_{Ae}/C_{Se} [237] where C_{Ae} and C_{Se} refer to the amounts of degraded melanoidin and residual concentration in solution at equilibrium, respectively. R and T are the universal gas constant (8.314 J mol^{-1} K^{-1}) and temperature (K).

5.2.8. Reusability study of photocatalyst

The phorocatalyst's reusability is an essential element indicating the viability of its economical and practical operations. After the photocatalytic experiments, the supernatant and pellet were separated by centrifugation at 10000 rpm for 10 min. The nanoparticle-containing pellets were washed several times with ultrapure Mili-Q water to clean and desorb adsorbate. The washed nanoparticles were dried in an oven at 80 °C for overnight. The dry weight of the photocatalyst was measured and then proceeded for the next loop of photocatalytic degradation under the above conditions to investigate the reusability [300].

5.2.9. Application of photocatalyst in real-life industrial spentwash sample

The real spentwash sample was collected from DCM Shriram Ltd, a distillery factory based on sugar cane molasses in Hardoi, India. The brown-colored collected spentwash sample was acidic in nature (pH 4.8) and had a very high COD load (193 ± 1 g L^{-1}). This spentwash in varying concentrations of 1-10 % v/v was explored for decolourization and COD removal at the optimized conditions. The reusability of photocatalysts was also investigated on this industrial-grade spentwash sample.

5.2.10. Analysis of the antibacterial property of the synthesized WO_3 and FZO nanoparticle in real wastewater sample (Spentwash sample)

For practical applications, the antimicrobial activity of treated samples was investigated using the plate count test method by comparing the microbial pollution of untreated spentwash, and treated spentwash samples at optimized conditions. The untreated (10^8 times diluted) and treated samples were pleated in nutrient agar plates and incubated at 37°C for overnight [186]. The number of visible colonies was multiplied by the dilution factor and reported as cell forming unit per milliliter (CFU/mL) [301].

$$CFU/mL = \frac{Number\ of\ colonies \times Dilution\ factor}{Volume\ of\ culture\ plated\ in\ mL} \quad (5.2)$$

5.3. Results and Discussion

5.3.1. Bandgap calculation of the nanoparticles

The absorbance broadband of the synthesized WO_3 and FZO nanoparticles along with reference WO_3, TiO_2 and ZnO nanoparticles was analyzed at the wavelength range of 200 to 700 nm as shown in Figure 5.1 (A). The bandgap of these nanoparticles was determined by Tauc's method (Eq. 5.3) based on the UV–vis absorbance spectrum.

$$\propto = \frac{B(h\upsilon - E_g)^n}{h\upsilon} \tag{5.3}$$

Where α is the absorption coefficient, $h\upsilon$ denotes photon energy, B represents a constant, E_g indicates optical bandgap energy and n is the absorption coefficient constant. The plot between $(\alpha h\upsilon)^2$ vs. $h\upsilon$ demonstrates the bandgap energy (Figure 5.1 (B)). The bandgap energy of synthesized WO_3 and FZO nanoparticles were found to be 2.44 eV and 2.88 eV, respectively, which are almost equal to the reported values [291, 302, 303]. Also, the commercial WO_3. TiO_2 and ZnO nanoparticles showed the bandgap energy of 2.34 eV, 3.22 eV and 3.01 eV, which are similar bandgap energy as reported in various literature and standards [304-307]. The lower value of bandgap energy of WO_3 indicated that it reasonably extends into the visible range, while FZO with higher bandgap energy extends towards UV light.

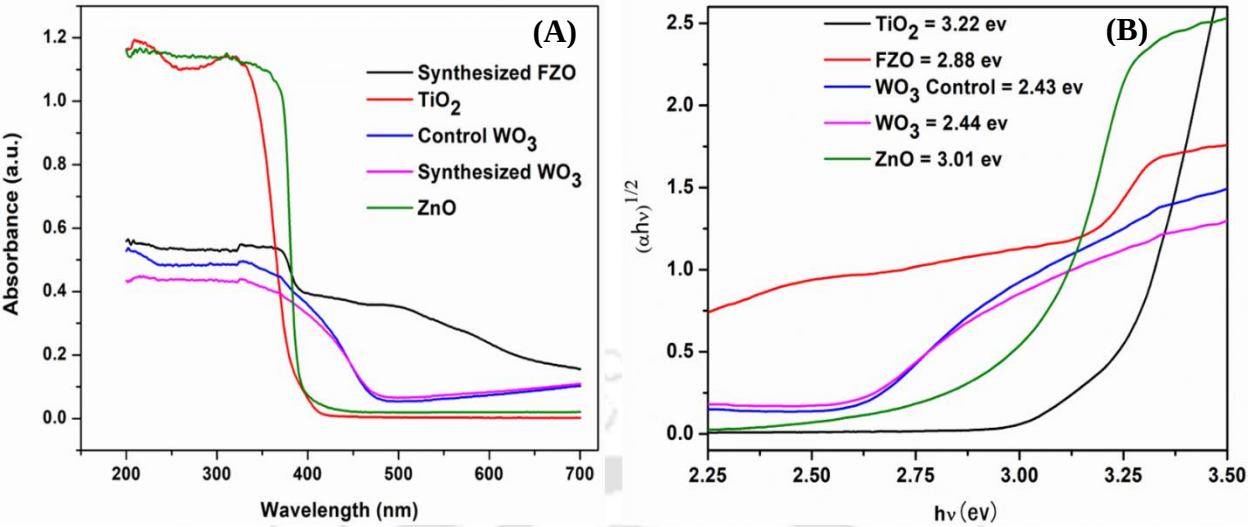

Fig. 5.1: (A) UV–vis diffused reflectance spectra and (B) Bandgap calculation by the Tauc's plot of synthesized WO_3 and FZO nanoparticles along with the commercial WO_3, TiO_2 and ZnO nanoparticles.

5.3.2. Characterization of synthesized photocatalysts

5.3.2.A. Characterization of synthesized WO_3 photocatalyst

5.3.2.A.1. Phase analysis through X-ray diffractometer

The synthesized WO_3 samples were analyzed using the powder X-ray diffractometer in the 2θ range of 20^o-80^o. The samples calcined at 300℃, 500℃, 700℃ and 900℃ showed different peak patterns. The characteristic peaks were obtained for the 2θ values of 23.09^o, 23.61^o, 24.30^o, 28.98^o, and 41.80^o. The peaks obtained with the calcined samples were matched with the monoclinic phased tungsten oxide (WO_3) (ICDD file 01-083-0950) [308]. The peak obtained at 25.7^o value of 2θ can be observed to disappear after the calcination due to water removal for the tungstite sample. The commercial WO_3 showed the peaks for the 2θ values of 25.7^o, 33.34^o, 34.21^o, 52.57^o and 57.43^o. The obtained peaks matched to the tungstite ($WO_3.H_2O$) as per the International Centre for Diffraction Data (ICDD) file 01-084-0886. The diffraction pattern of the

synthesized samples was compared with that of commercially purchased tungsten oxide (reference sample). All the calcined samples have shown similar peak patterns concerning the commercial sample (Figure 5.2).

The crystallite size was calculated using the Debye-Scherrer's formula given as follows (Eq. 5.4),

$$D = \frac{0.9\times\lambda}{\beta\times cos\theta} \tag{5.4}$$

Where, λ is the X-ray wavelength, θ is the Braggs's angle (in degrees) and β is the full width at half maximum. The average crystallite size for the non-calcinated tungstite sample was measured as 31.8 nm. While for the calcined samples, the crystallite size was observed as 31.7 nm, 33.50 nm, 34.50 nm, and 38.60 nm at 300℃, 500℃, 700℃ and 900℃, respectively. The crystallite size of the reference sample was calculated as 34.10 nm, matching the sample calcined at 700℃. Due to the higher temperature calcination, the increased surface energy has resulted in the coalescence of the smaller particles; hence increase in the crystallite size was observed [309, 310].

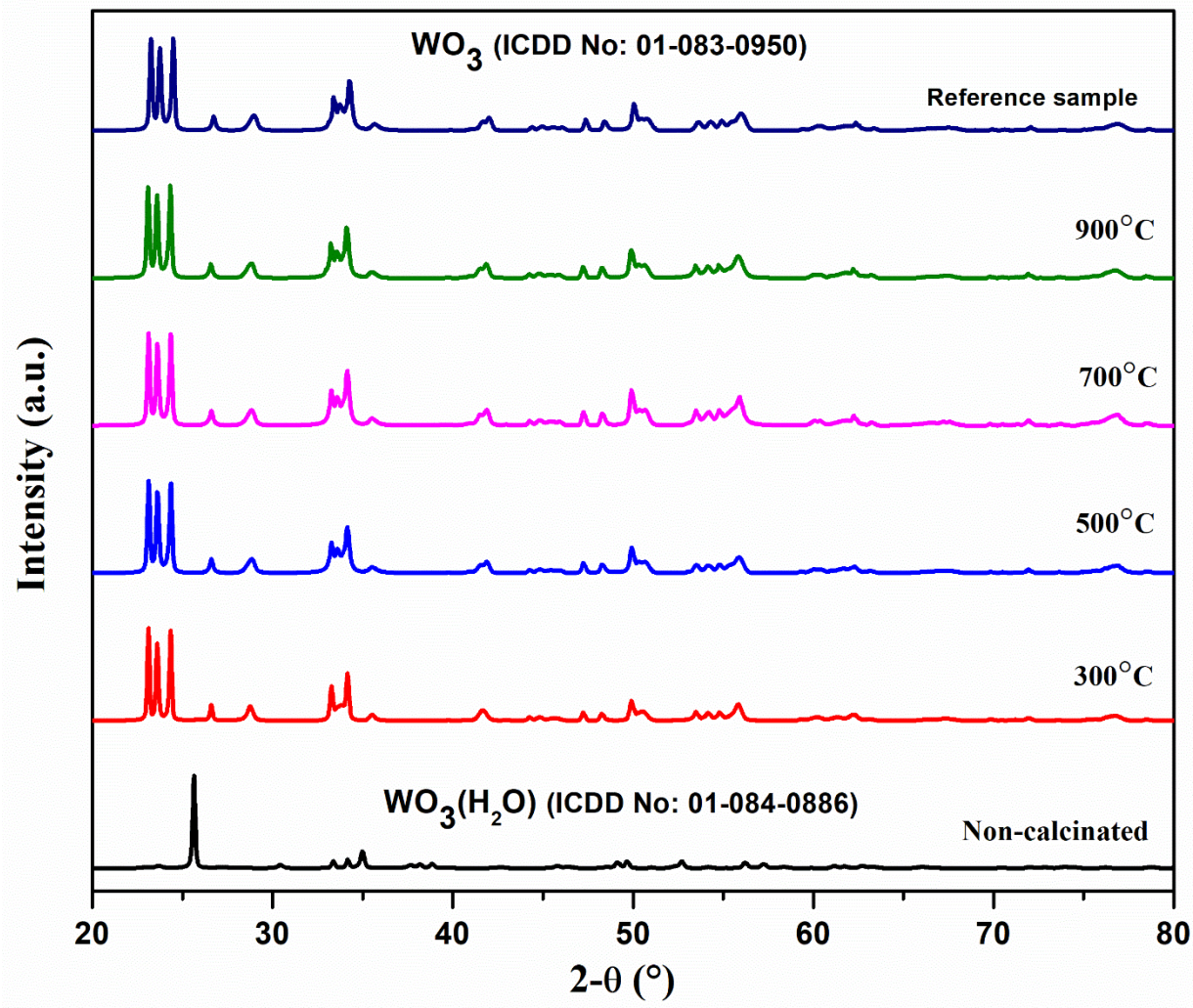

Fig. 5.2: XRD spectra of synthesized WO_3 nanoparticles calcinated at different temperatures along with the reference WO_3 sample.

5.3.2.A.2. Functional group analysis using FTIR and Raman spectroscopy

The FTIR analysis of synthesized WO_3 nanoparticles (300, 500, 700, 900 ℃) and reference WO_3 was conducted to reveal their functional similarity. The similar FTIR spectra for commercial and synthesized WO_3 nanoparticles confirm identical compounds [311]. The peaks at 726 cm^{-1} correspond to W-O stretching vibration [312]. Interestingly, the peak intensities of WO_3 gradually increased with an increase in calcination temperature from 300 to 700 ℃ due to the increase in stretching mode of vibrations, while at 900 ℃ calcination temperature, the peak intensity relatively decreased. At higher temperatures, the reduction in peak intensities occurs due to the deformation of particles and causes a decrease in the intensity of vibrations [313]. Raman analysis of synthesized nanomaterials was also performed to analyze the functional moieties. Similar Raman peaks were recorded for reference and synthesized WO_3 nanoparticles corresponding to the peak positions of 270, 325, 717 and 806 cm^{-1} (Figure 5.4). The characteristic peak position at 270 cm^{-1} corresponded to lattice vibration of WO_3 particles while peak positions at 325, 717 and 806 cm^{-1} corresponded to the O-W-O stretching, W_2O_6 stretching and W-O-W anti-symmetric stretching, respectively [314, 315].

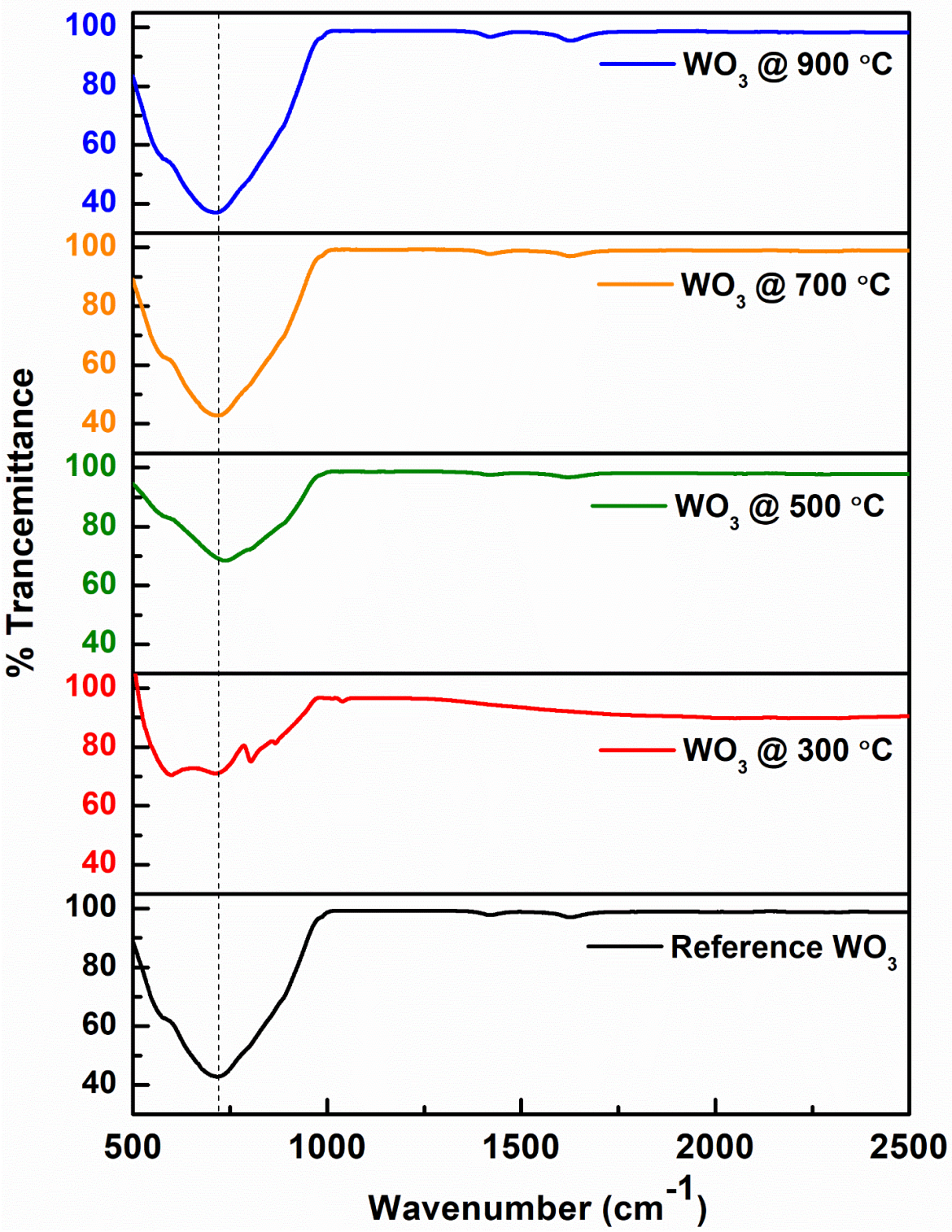

Fig. 5.3: FTIR spectra of reference WO_3 and synthesized WO_3 nanoparticles at different calcined temperatures.

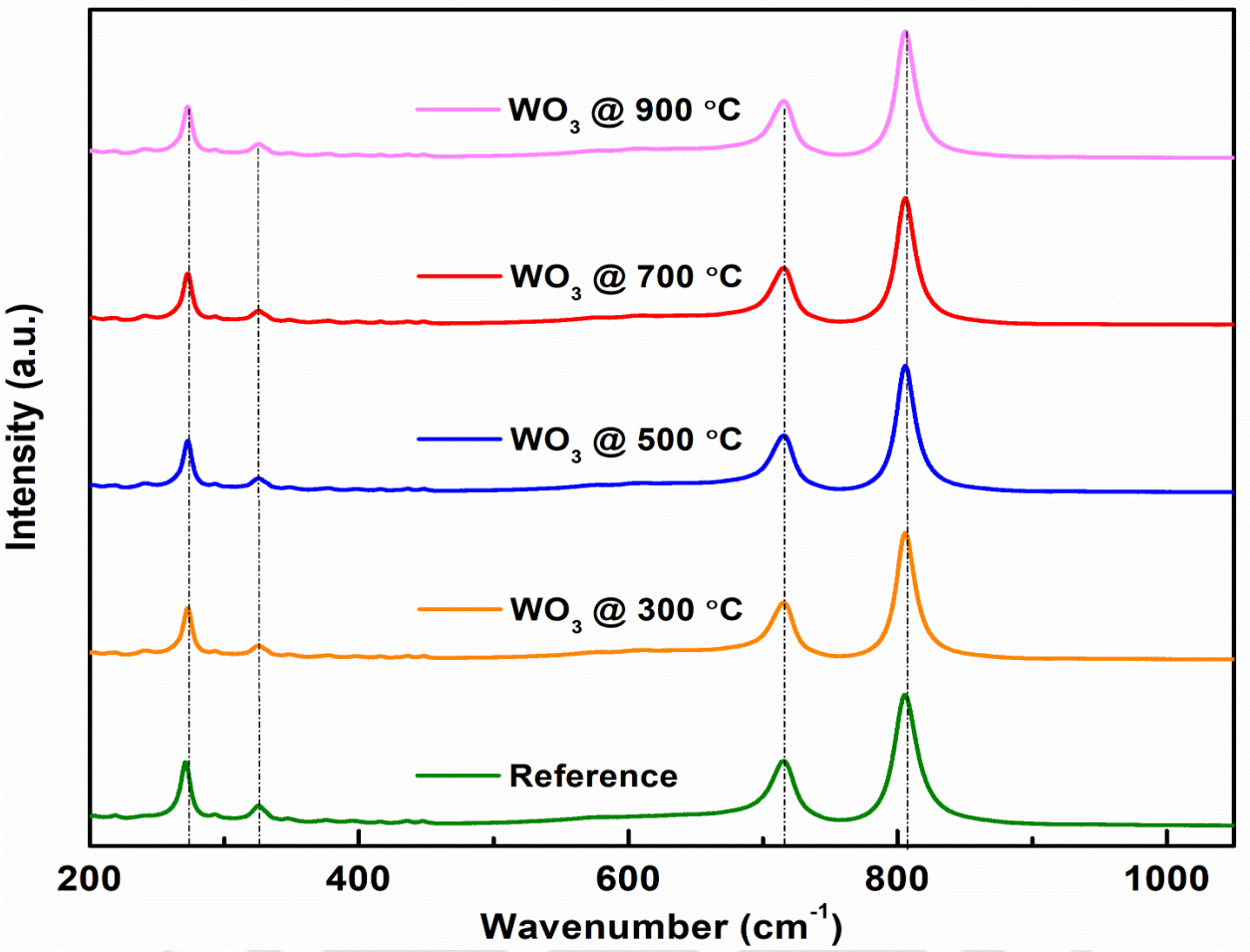

Fig. 5.4: Raman spectra of synthesized WO_3 nanoparticles calcined at different temperatures.

5.3.2.A.3. Morphological and Elemental Analysis through FETEM, BET, FESEM and EDX

Figure 5.6 shows FESEM images of the synthesized WO_3 nanoparticles revealing approximately spherical nanoparticles accompanied by sheet-like structures. The FESEM micrograph of the synthesized WO_3 displayed aggregated nanoparticles. The average particle sizes were found to be 58, 62, 63 and 66 nm for the WO_3 samples calcined at 300, 500, 700 and 900 °C, respectively. The average hydrodynamic diameter of WO_3@700 ℃ was also measured using DLS and found to be 92 ± 16 nm. This value is overestimated due to the formation of the hydration layer. In FESEM analysis, WO_3 nanoparticles calcined at 700 ℃ resulted in similar morphology as compared to reference WO_3 nanoparticles [313].

The FETEM analysis of the synthesized WO_3@700 ℃ sample showed a spherical shape with an average diameter of 45 ± 2 nm (Figure 5.5 A and B) [316, 317]. The high-resolution TEM images revealed the crystalline nature of the samples with clear lattice fringes of 0.184 ± 0.03, which was in good correlation with the d-spacing (0.188 nm) obtained through XRD analysis (Figure 5.5 C) applied in following Bragg's (Eq. 5.5).

$$n\lambda = 2d\ Sin\theta \tag{5.5}$$

Where λ is wavelength of incident X-ray (Å), θ is peak position (in radians), n denoted the order of diffraction and d is the interplaner spacing or d-spacing (Å).

The SAED pattern of the synthesized WO_3-700 ℃ nanoparticle confirmed the crystalline planes of the nanoparticle (Figure 5.5 D). Furthermore, TEM and SAED studies revealed that the synthesized sample has high crystallinity. The surface area of WO_3 determined using a BET analyzer was found to be 5.56 $m^2\ g^{-1}$ [316].

The elemental analysis of synthesized WO_3 nanoparticles was done using an energy dispersive spectrum (EDX). The elements identified in reference WO_3 sample were W and O with atomic %

of 74.5 and 25.5, respectively (Figure 5.7 A). The synthesized WO_3-700 resulted in 75.7 and 24.3 atomic % of W and O, respectively, which are almost similar to the reference sample (Figure 5.7 B).

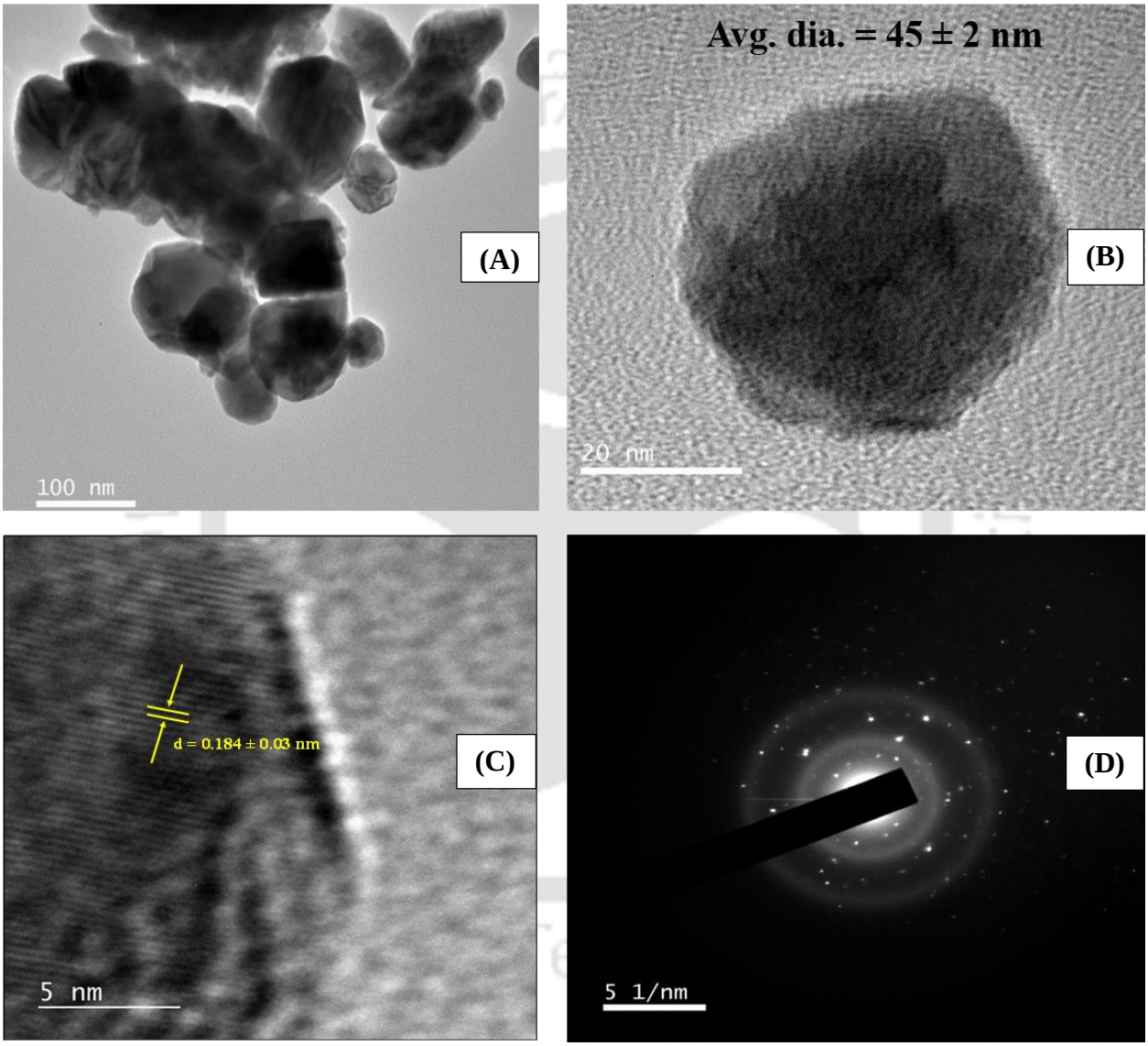

Fig. 5.5: FETEM micrographs of (A) synthesized WO_3@700 °C nanoparticles (B) a synthesized single WO_3@700 °C nanoparticle (C) atomic crystal planes and (D) SAED pattern.

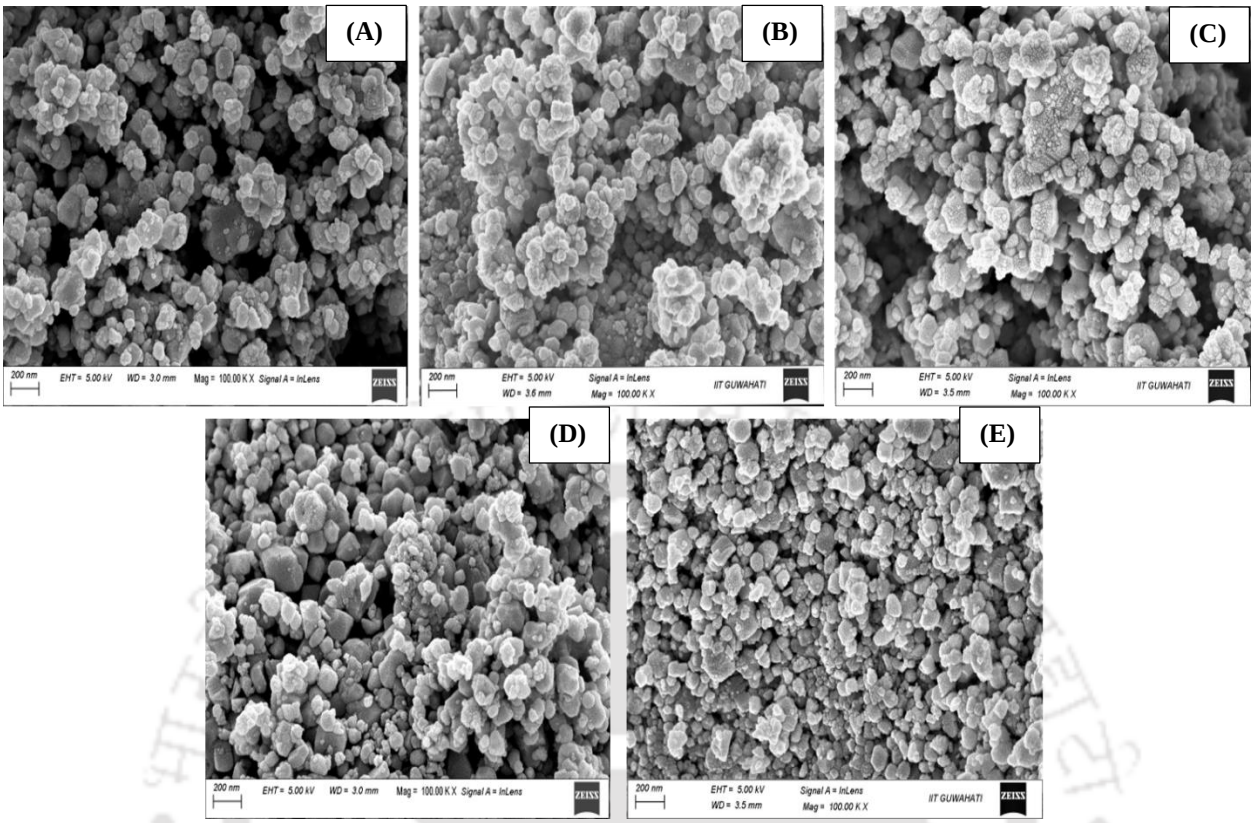

Fig. 5.6: FESEM images of (A) Reference WO_3 and synthesized WO_3 calcinated at (B) 300 ℃, (C) 500 ℃, (D) 700 ℃ and (E) 900 ℃.

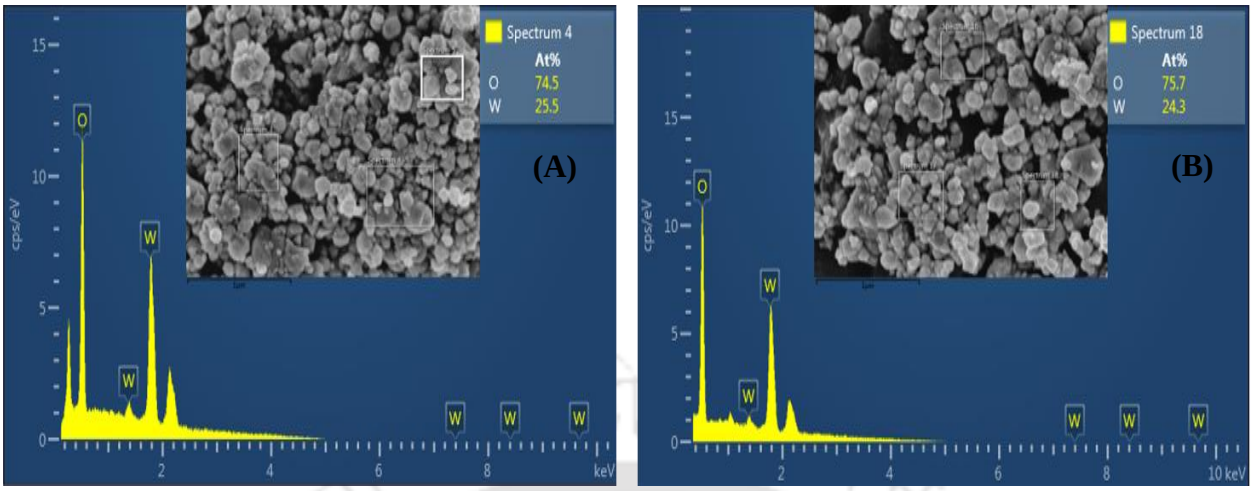

Fig. 5.7: Energy-dispersive X-ray spectroscopy of (A) Reference WO_3 sample and (B) Synthesized WO_3@700 ℃ sample.

5.3.2.A.4. Colloidal stability of the synthesized WO_3 nanoparticles

The colloidal stability of the synthesized WO_3 nanoparticles was analysed by measuring the surface charges using DLS at various pH levels. As depicted in Figure 5.8, photocatalyst WO_3 had negative zeta charges. The surface charge at the working pH value of 5.0 was found to be -21 ± 1 mV, which indicated the good colloidal stability of the synthesized WO_3 nanoparticles [318]. Further, an increase in the pH values resulted in a decline in the surface charge (Figure 5.8).

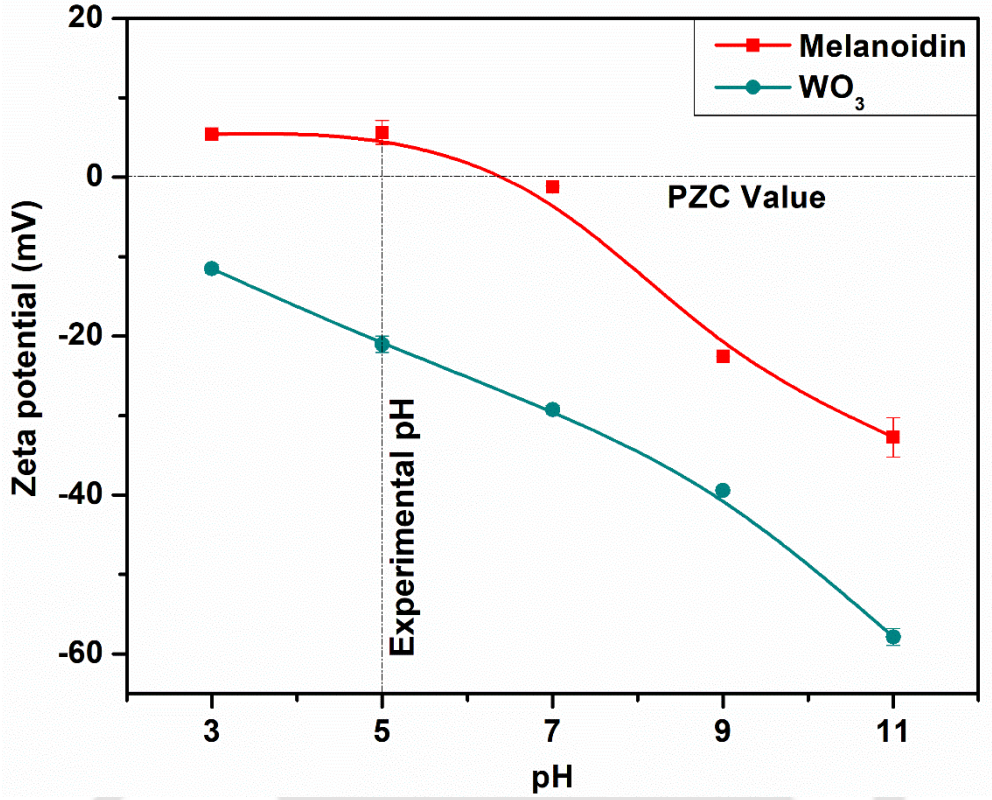

Fig. 5.8: Zeta potential values of WO_3 photocatalysts and melanoidin at different pH values. The surface charge of WO_3 photocatalysts was found to be -21 ± 1 mV confirming its colloidal stability. The point of zero charge (pzc) of melanoidin was estimated as 6.9.

5.3.2.B. Characterizations of synthesized FZO photocatalyst

5.3.2.B.1. Phase analysis using X-ray diffractometer

The synthesized Fe doped ZnO nanomaterials were also analyzed using XRD to confirm the formation of the desired nano-assembly. The diffraction patterns of the FZO, Fe_3O_4 and ZnO are as shown in Figure 5.19. The hexagonal wurtzite structure was confirmed by diffraction pattern, which is the most stable form of ZnO [319]. The peaks obtained at 31.81° (0 1 0), 34.37° (0 0 2), 36.32° (0 1 1), 47.54° (1 0 2), 56.61° (1 1 0), 62.95° (1 0 3), and 68.01° (1 1 2) were corresponsive to ZnO with slight redshifts (ICDD No. 01-070-8072). The small peaks at 2θ values of 30.06° and

35.51° were observed belonging to Fe_3O_4 (ICDD No. 01-084-9337). This indicated that Fe^{3+} precursors were integrated into the ZnO lattice at 65℃, which prevented the oxidation and valency transition of Fe [294, 319, 320]. The average crystalline size for the FZO nanomaterials was calculated to be 20.45 nm.

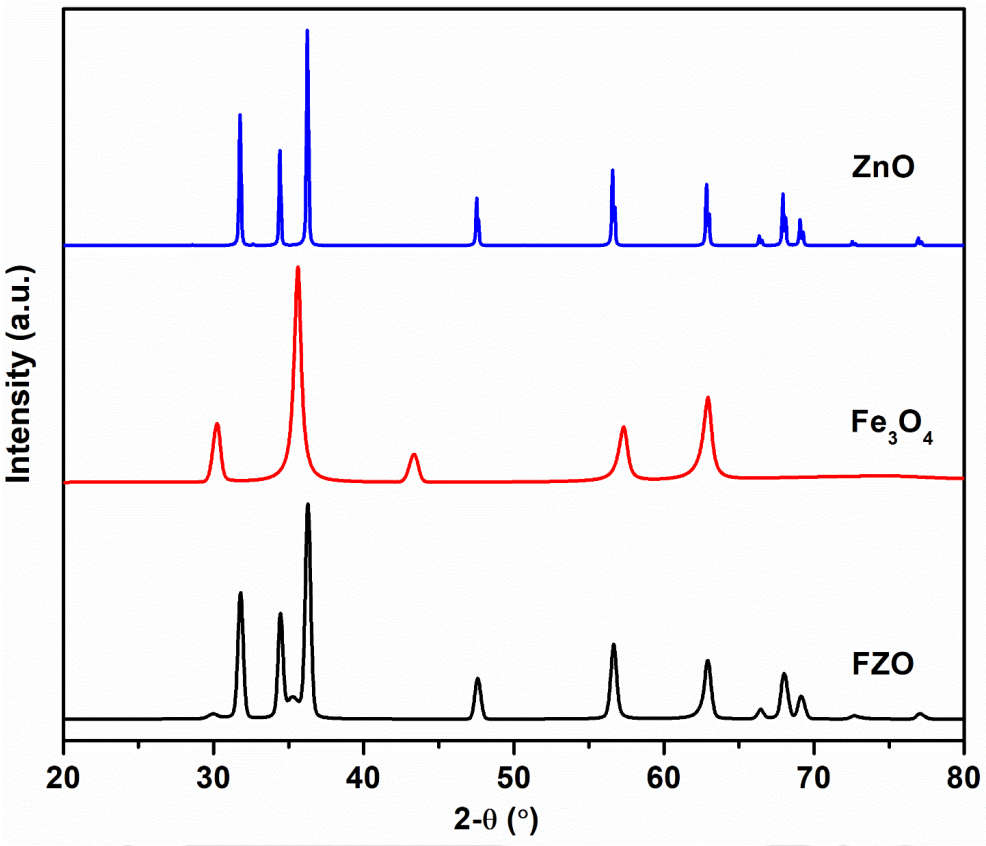

Fig. 5.9: XRD spectra of synthesized FZO nanoparticles confirm the formation of the desired nano-assembly.

5.3.2.B.2. Functional group analysis using FTIR and Raman spectroscopy

FTIR analysis of the synthesized FZO nanomaterials is shown in Figure 5.10. Peaks at the position of 455 and 517 cm^{-1} in the synthesized FZO nanoparticles correspond to the stretching vibration of Zn–O, which confirmed the formation of Fe doped ZnO nanoparticles [319, 321-324]. The Raman analysis of the FZO nanoparticles was done as explained in the previous section. The broad

Raman peaks were recorded at peak positions of 331, 435 and 650 cm^{-1} for synthesized FZO nanoparticles (Figure 5.11). The peak positions for the synthesized nanoparticles were also documented by various works corresponding to FZO [304, 319, 325-327].

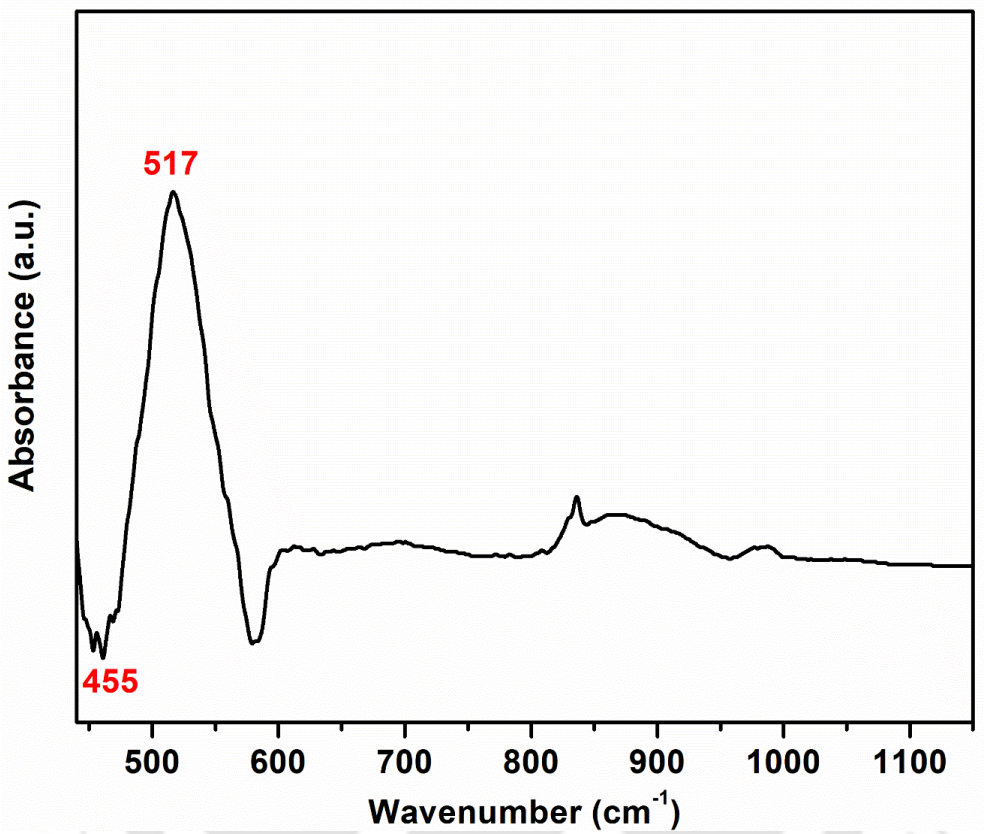

Fig. 5.10: FTIR spectra of synthesized FZO nanoparticles.

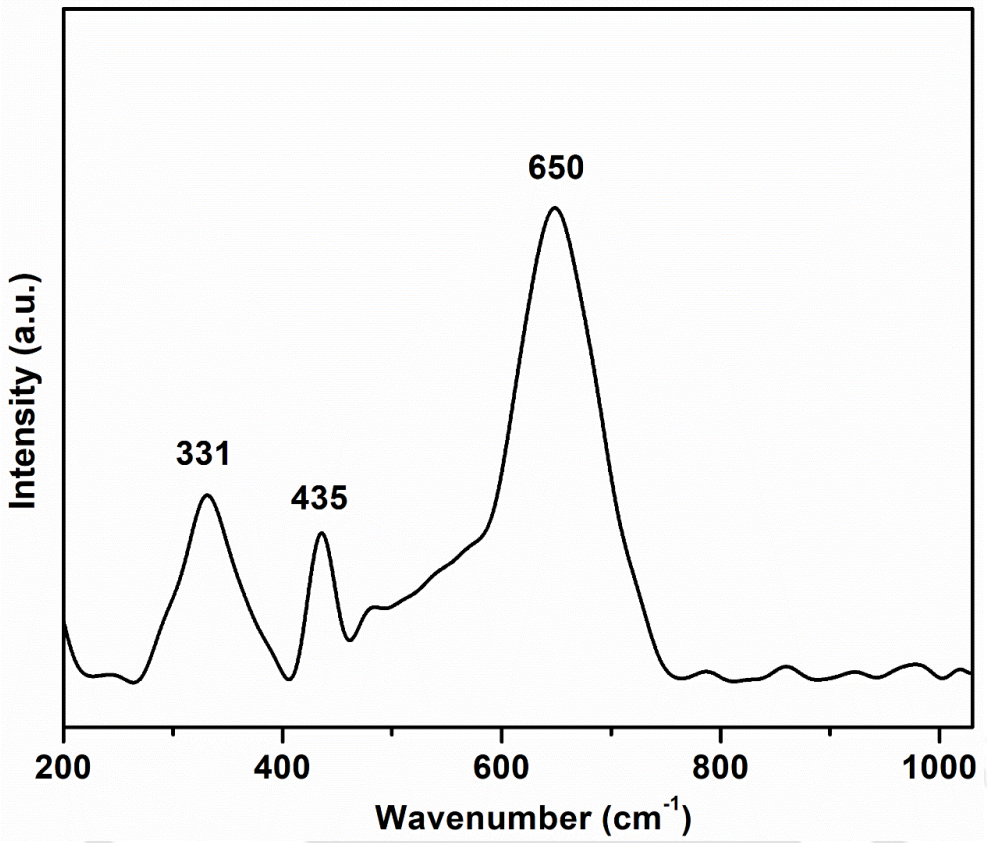

Fig. 5.11: Raman spectra of synthesized FZO nanoparticles.

5.3.2.B.3. Morphological and Elemental analysis of synthesized FZO photocatalyst

The FETEM analysis of the synthesized FZO samples showed rod-shaped morphology with an average diameter of 40 ± 3 nm [316, 317] and an average length of 103 ± 14 nm (Figure 5.12 A and B). The high-resolution TEM images revealed a highly crystalline sample with lattice fringes of 0.301 ± 0.03 nm. The fringe width correlated with the d-spacing obtained through XRD analysis (0.3 nm) (Figure 5.12 C). The SAED pattern further supported the higher crystallinity of the synthesized FZO nanoparticles (Figure 5.12 D). The BET analysis calculated the surface area of the nanoparticles to be 13.64 $m^2 g^{-1}$ [316].

Figure 5.13 shows a FESEM image of the synthesized FZO nanoparticles revealing approximately rod shape geometry of the nanoparticles along with aggregates. The average diameter and length

were estimated to 55 ± 9 nm and 135 ± 20 nm, respectively, which agreed to the FETEM data. The average hydrodynamic size of FZO was also measured using DLS and found to be 131 ± 5 nm, which corresponded to the larger dimension of the nanorods. The elemental analysis of the prepared FZO nanomaterial through EDX confirmed the presence of Zn (43.4 at %) and O (51.8 at %) as major elements and Fe (4.5 at %) as a trace element (Figure 5.14). These elemental descriptions validated the synthesis of FZO nanoparticles.

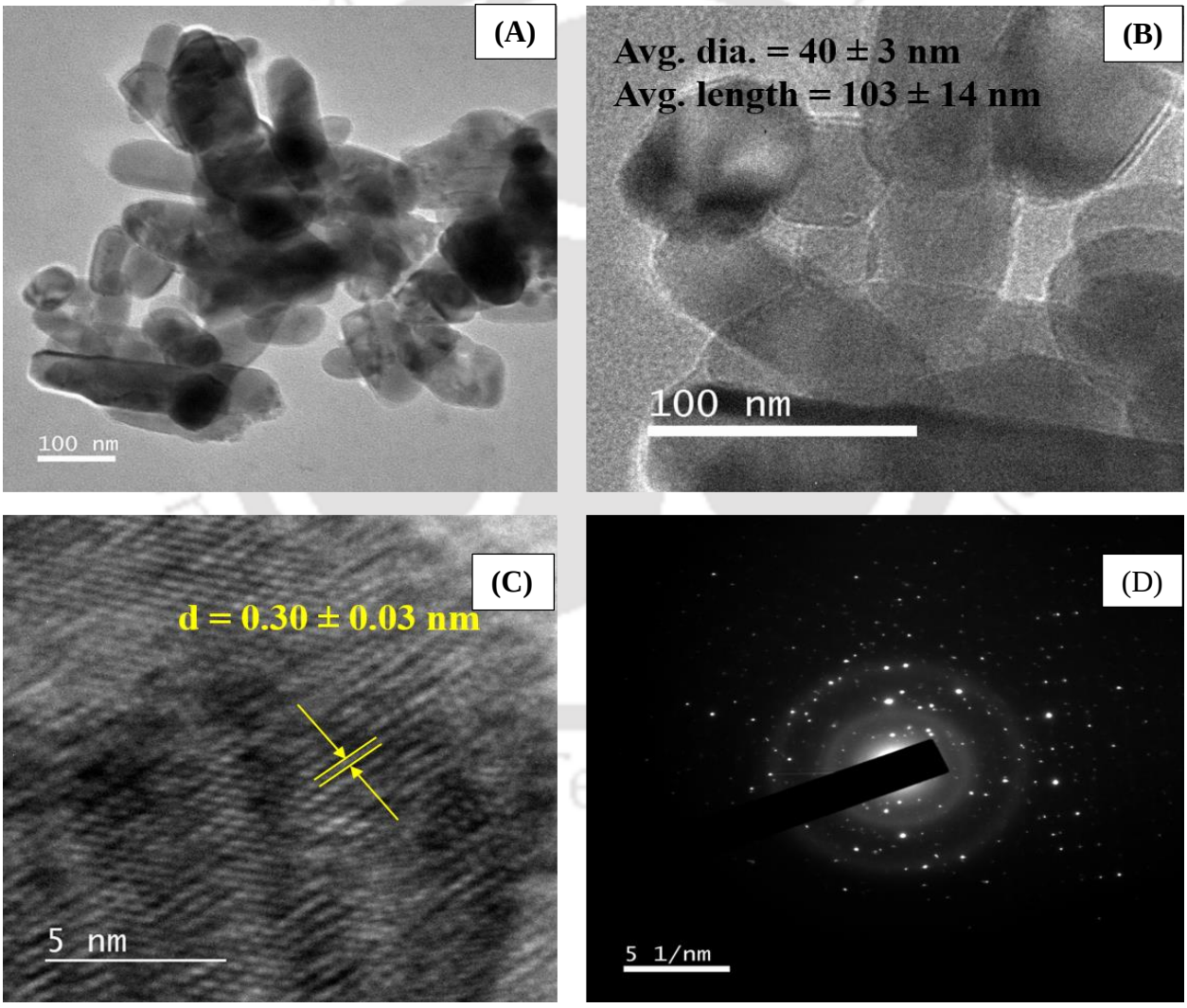

Fig. 5.12: FETEM images of (A-B) synthesized FZO nanoparticles, (C) Atomic crystal planes and (D) SAED pattern.

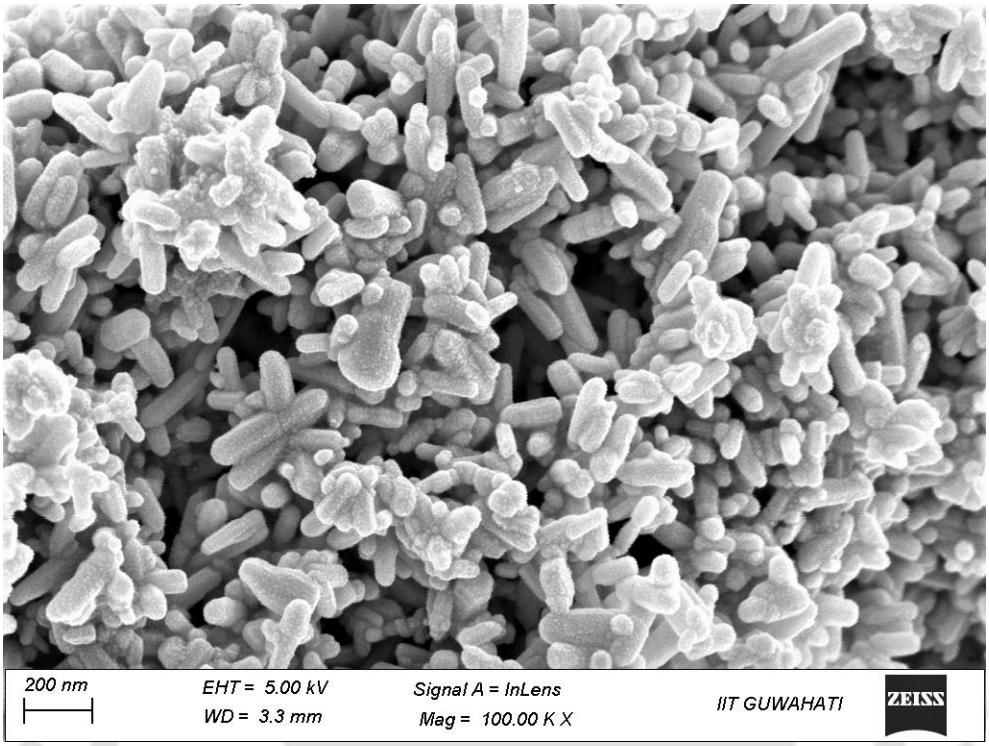

Fig. 5.13: FESEM image of synthesized FZO nanoparticles.

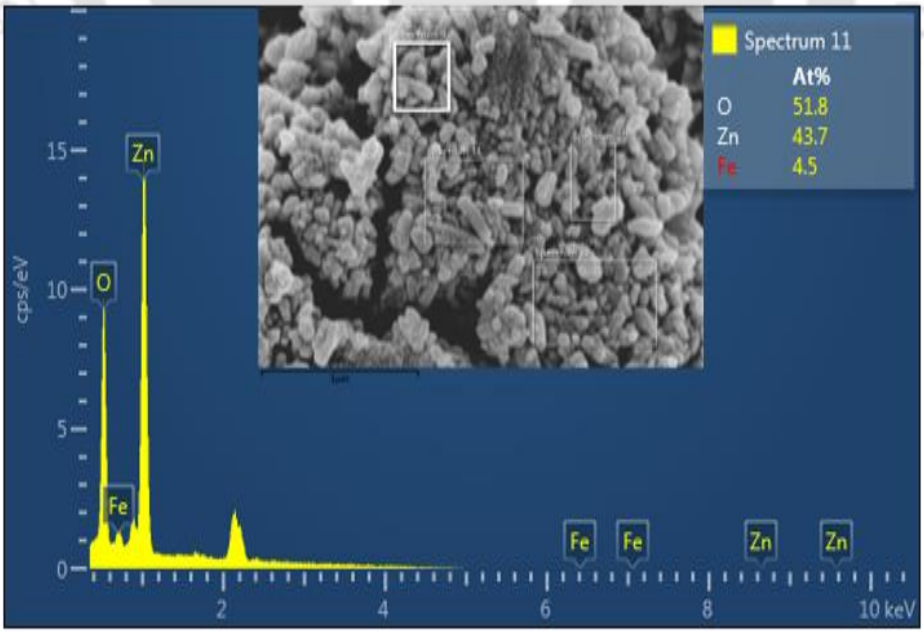

Fig. 5.14: Energy-dispersive X-ray spectroscopy of synthesized FZO sample

5.3.2.B.4. Colloidal stability of FZO nanomaterials

The colloidal stability of the synthesized FZO nanomaterials was analysed by measuring the surface charges using DLS at various pH levels. As depicted in Figure 5.15, photocatalyst FZO had positive zeta charges below the pH of 9.0. The surface charge was maximum at the pH value of 3.0 (37 ± 2 mV) and was found to decrease with the increase in pH value from 3 to 11 (Figure 5.15). The surface charge at the working pH value of 4.0 was estimated to be 30 mV, which indicated the good colloidal stability of the synthesized FZO nanomaterials.

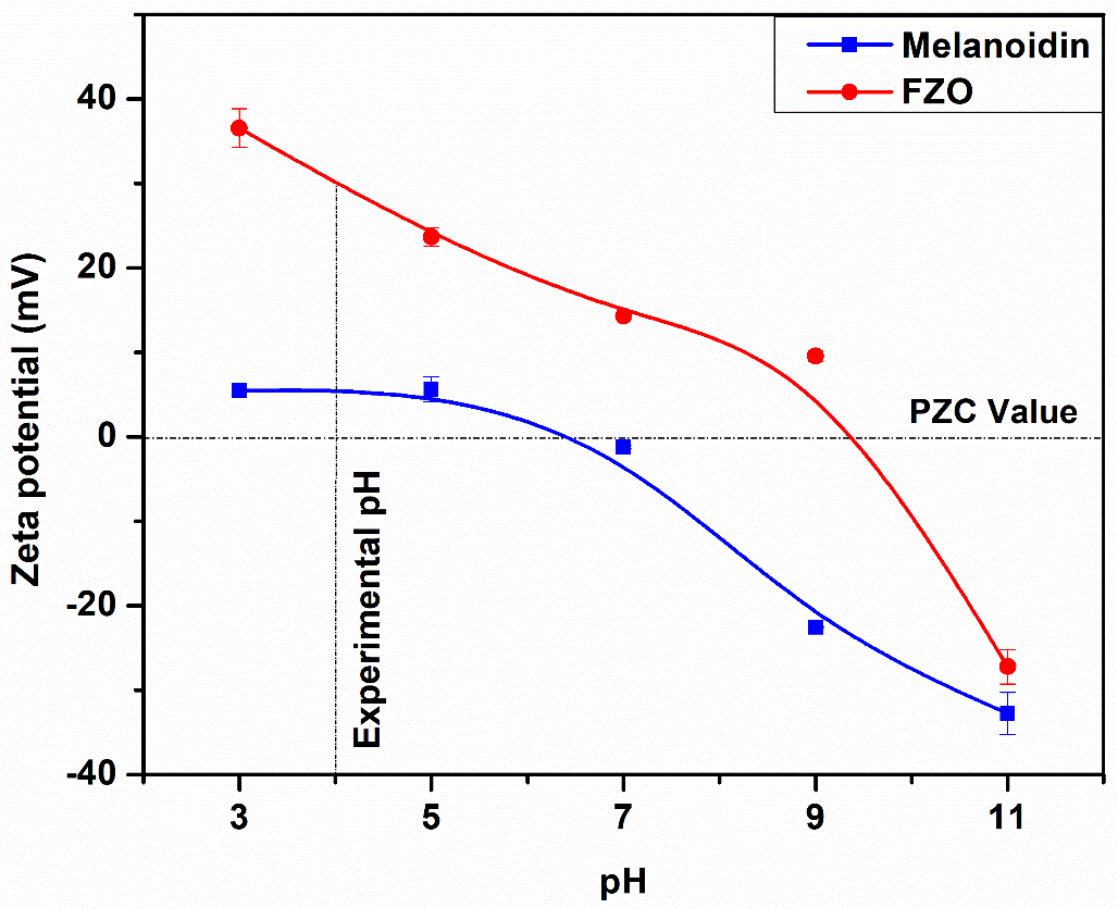

Fig. 5.15: Zeta potential values of FZO photocatalysts and melanoidin at different pH values. The surface charge of FZO photocatalysts was found to be 24 ± 1 mV confirming its colloidal stability at the pH value of 5.0.

5.3.3. Degradation study of the melanoidin under visible light using WO_3 as photocatalyst

5.3.3.1. Effect of initial melanoidin concentrations and calcination temperature of WO_3

The initial experiments were performed using 200 ppm WO_3 photocatalyst calcined at different temperatures and 100 mM of H_2O_2 in a solution of 0.1, 0.2 and 0.5 % of melanoidin concentrations. Degradation of melanoidin was observed up to 300 min. The calcined WO_3@700 was found to be most effective followed by WO_3 calcined at 900, 500 and 300 °C as shown in Figure 5.16. The degradation efficiency was found to be 96 $\pm$ 1 % for 0.5 % of initial melanoidin solution after 300 min in the presence of WO_3@700. A similar experiment was also performed using the reference WO_3 purchased commercially for comparison. The reference WO_3 resulted in 93 $\pm$ 2 % of degradation efficiency of 0.5 % of initial melanoidin solution after 300 min. This suggested the better degradation performance of the synthesized WO_3 calcined at 700 C. Further investigations were performed using WO_3@700 as a photocatalyst. Other environmental parameters such as temperature (°C), time (min), H_2O_2 concentration (mM) and WO_3@700 °C concentration (ppm) were further optimized by RSM-CCD to determine the optimized condition for the maximum degradation of melanoidin.

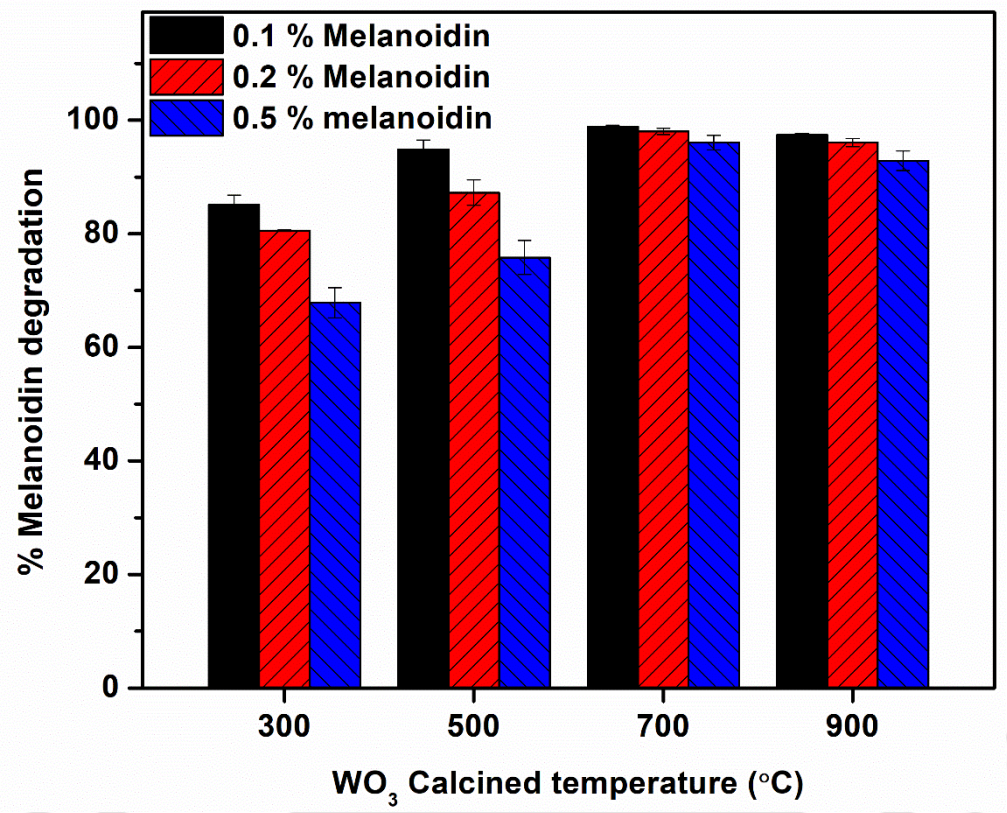

Fig. 5.16: Effect of initial melanoidin concentrations and calcination temperature of WO_3 on melanoidin degradation (%).

5.3.3.2. Optimization of Experimental parameters by RSM-CCD to enhance the melanoidin degradation

Four independent factors such as temperature, time, H_2O_2, and WO_3 concentration were optimized to maximize the melanoidin degradation using RSM-CCD [328]. The lower and upper limits of temperature, time, H_2O_2 concentration and WO_3 concentration were 25/55 °C, 30/300 minutes, 10/200 mM, and 100/300 ppm, respectively. The mini-tab software suggested 30 experimental set-ups based on these independent variables as listed in Table S5.1. The % melanoidin degradation and % COD reduction were consided as responses. A quadratic polynomial equation fitted to the

experimental data to predict the expected responses. The model equations for the melanoidin degradation and COD reduction are given by equations 5.6 and 5.7, respectively.

$$\%\, Melanoidin\ degradation = 92.58 + 5.53A + 8.92B + 8.28C + 11.25D + 0.54AB + 0.058AC + 0.036AD - 0.64BC - 1.64\, BD + 2.22CD - 2.20A^2 - 7.12B^2 - 1.78C^2 - 5.82D^2 \quad (5.6)$$

$$\%\, COD\ reduction\ = 82.67 + 3.05A + 10.48B + 8.86C + 12.28D + 1.28AB - 0.71AC + 0.43AD - 0.43BC - 1.57\, BD + 3.00CD - 1.60A^2 - 7.02B^2 - 2.02C^2 - 5.74D^2 \quad (5.7)$$

ANOVA analysis was performed for the regression analysis [197]. There was a strong correlation between the experimental and predicted data, as evidenced by the R^2 value of 0.90 and 0.92 for the % melanoidin degradation and % COD reduction, respectively [329]. The relevance of the ANOVA model was proved by the higher F-values (9.62 and 11.55) and lower p-values (< 0.0001) [5]. The independent variables A, B, C and D and their various intersections for the melanoidin degradation and COD reduction are listed in Table S5.2 and Table S5.3, respectively. The independent variables B, C, D and their interactions B^2 and D^2 were found to be statically significant for melanoidin degradation and COD reduction with p-values ≤ 0.01. Figure S5.2 and S5.3 illustrate 3-D response surface plots for optimal melanoidin degradation and COD reduction. The Minitab algorithm predicted the ideal situation for the maximum melanoidin degradation and COD reduction as the temperature of 38 °C, time of 231 min, H_2O_2 concentration of 119 mM and WO_3 concentration of 250 ppm. The predicted melanoidin degradation and COD reduction at the optimized conditions were 100 % and 93 %, respectively. The experimental results under optimized conditions resulted in approximately complete degradation (99 ± 1 %) and 93 ± 1 % of

COD reduction (Figure 5.17), which corresponded to the predicted values and confirmed the suitability of the model equations.

HPLC analysis was also performed to determine the melanoidin concentrations to confirm the UV-spectrophotometer data. The residual melanoidin concentrations were evaluated from the peak area of HPLC chromatograms. As per the HPLC analysis, photocatalyst WO_3 resulted in 97 % of melanoidin breakdown at the RSM optimized conditions (Figure S5.4). The degradation efficiency of melanoidin by UV-spectrophotometer and HPLC analysis were linearly related with R^2 value of 0.98 (Figure 5.18). Hence, the subsequent analysis of the residual melanoidin concentrations was performed using UV-spectrophotometer.

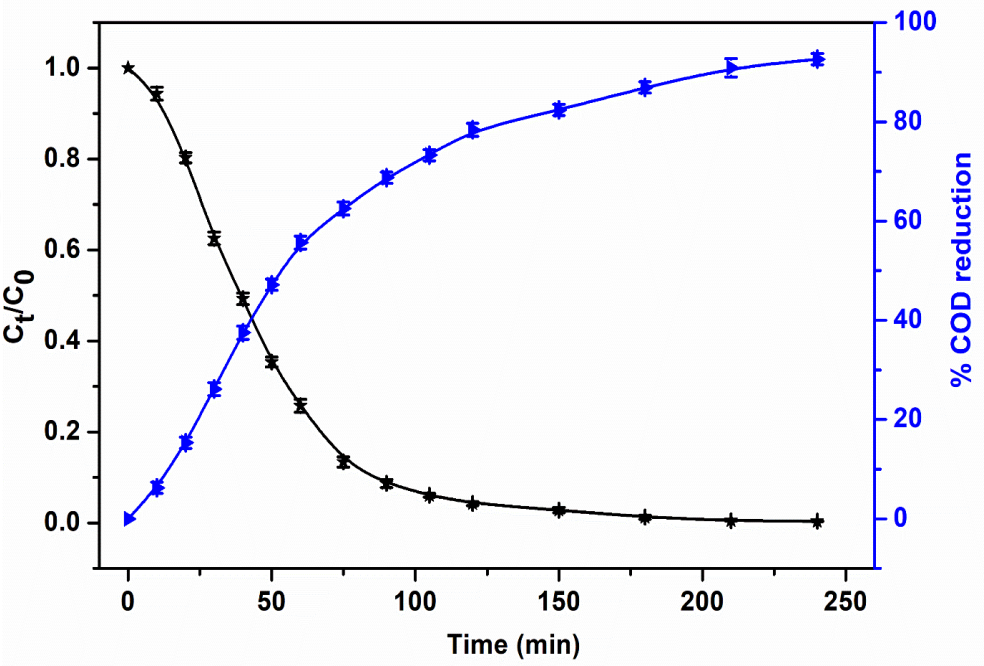

Fig. 5.17: Degradation of the melanoidin and COD reduction at RSM optimized conditions of temp. 38 °C, time of 231 min, H_2O_2 concentration of 119 mM and WO_3 concentration of 250 ppm. (C_0 is the initial concentration of melanoidin and C_t is the concentration at any time t).

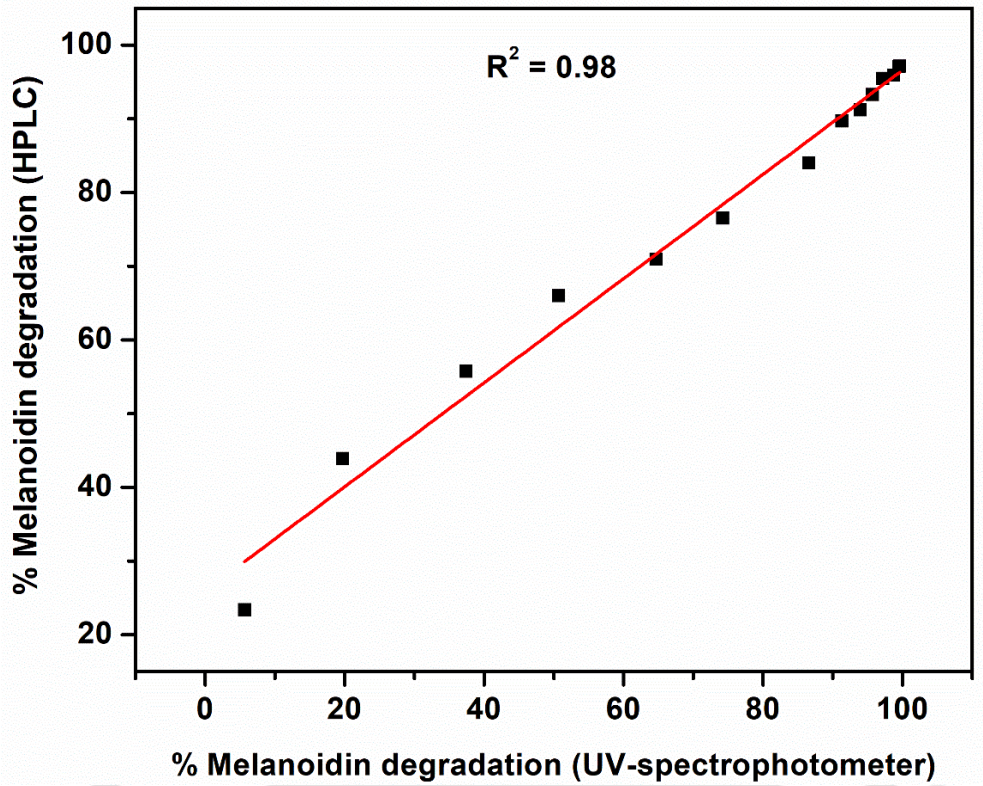

Fig. 5.18: Comparison of melanoidin degradation using HPLC analysis and UV-Spectrophotometer.

5.3.3.3. Role of pH on photocatalytic degradation of the melanoidin

In previous chapters, pH has been shown to be an essential factor in the adsorption/degradation of melanoidin. Similarly, the pH effect on the melanoidin degradation in the photocatalytic process was also examined. The pH of the solution was varied from 3 to 11 with a constant melanoidin concentration of 0.5 % (w/v) for WO_3 photocatalytic degradation at the optimized conditions. The melanoidin degradation efficiency decreased from 99 ± 1 % to 67 ± 1 % for WO_3 photocatalysts as the pH of the solution was increased from 3 to 11 as shown in Figure 5.19. The photocatalysts resulted in a high degradation rate in an acidic medium. This corresponds to a decrease in the rate of production of •OH free radicals during the melanoidin degradation with increasing the solution

pH. The •OH radicals in the alkaline medium may have been scavenged due to the excess amount of H_2O_2 present in alkaline pH [330, 331]. As a result, the phenomenon of melanoidin breakdown efficiency decreases with increasing the pH value. According to several literature findings, a complementary relationship between the effects of pH on melanoidin degradation has also been observed [330, 331].

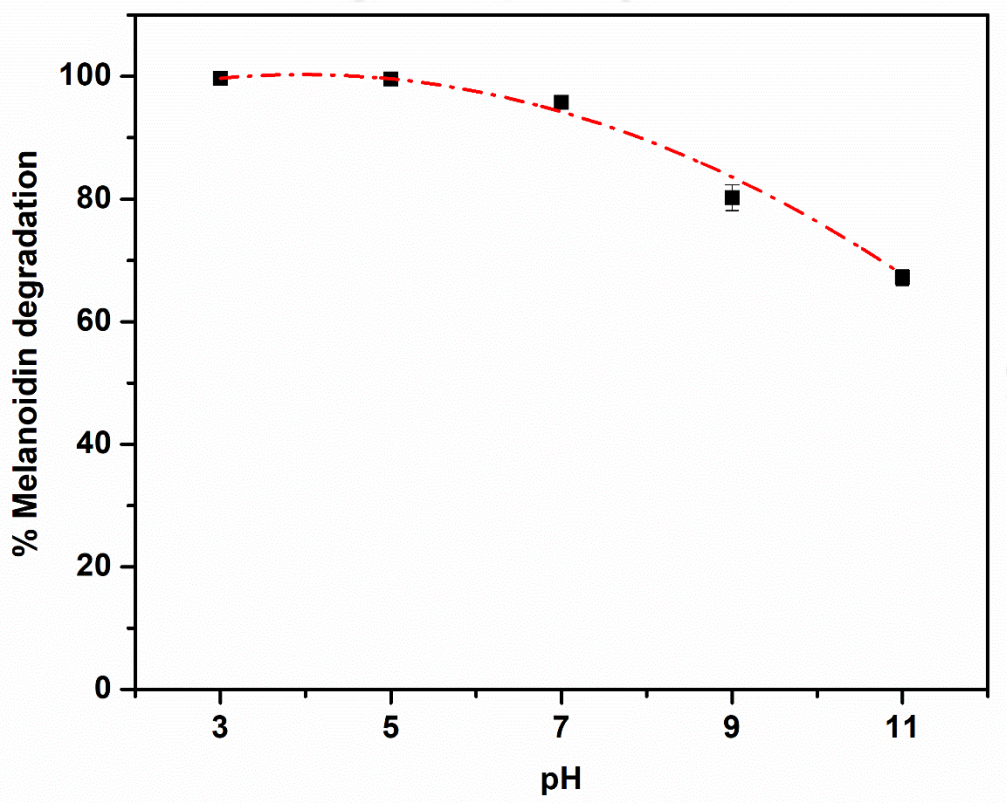

Fig. 5.19: Effects of solution pH on the melanoidin degradation using WO_3 photocatalyst at the optimized conditions.

Further, the surface charge of the melanoidin and WO_3 photocatalysts were investigated using DLS at various pH levels. The following model equation was used to calculate the point of zero charges (*pzc*) (Eq. 5.8).

$$\Psi_d = RT/Z_i F \ln C_i/C_i^{pzc} \quad (5.8)$$

where Ψ_d, R, T, Z_i, F and C_i refer to Zeta potential, gas constant, temperature, valency, Faraday's constant and molar concentration of H^+ ions, respectively [212]. The *pzc* value of the melanoidin was found to be 6.9. As depicted in Figure 5.8, photocatalyst WO_3 had a negative zeta charge while melanoidin occupied a positive zeta charge at the working pH value of 5.0. This reveals the electrostatic interaction. WO_3 and melanoidin solution had the greatest zeta potential difference (25.89 mV) at the working pH of 5.0. The positive charge on melanoidin and negative charge on WO_3 resulted in e^- transfer to the phase interface. The charge-charge interaction was amplified and improved the dispersion stability of particles and resulting in active site accumulation between the melanoidin and WO_3 nanoparticles. This enhanced the rate of melanoidin degradation at the working pH of 5.0 [332, 333].

5.3.3.4. Kinetic and thermodynamic study

The degradation kinetics of melanoidin by the WO_3 photocatalyst was carried out as a function of contact time at the optimized conditions. The plot of time (t) vs. relative concentration of melanoidin (C_t/C_o) is shown in Figure 5.20. The experimental data at RSM optimized conditions, including various control experiments, were applied in the equation $C_t = C_1 \times e^{-kt} + C_2$ (Table 5.2) to estimate the model parameters [240, 241]. The fitted data are shown as dotted lines in Figure 5.20. The correlation coefficient value (R^2) of 0.98 indicated that the first-order kinetic model is better defined to the experimental data. The rate of reaction constants, melanoidin degradation efficiency and correlation coefficient values of various experiments are listed in Table 5.3. The reaction rate constants (k) were found to be 2×10^{-2} min^{-1}.

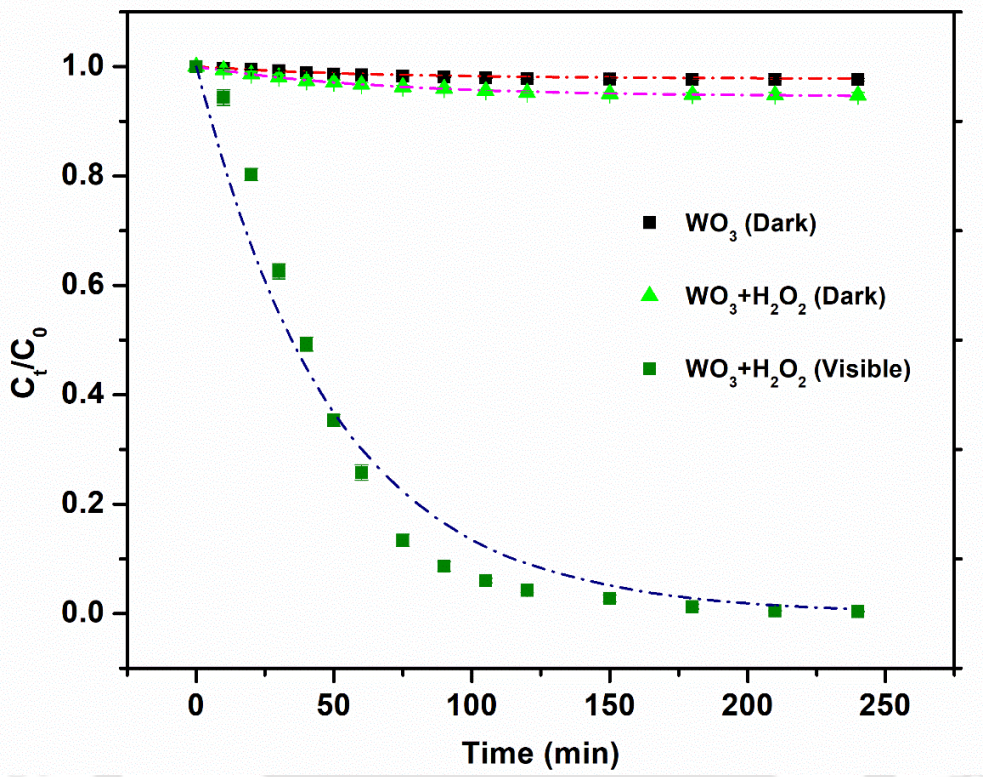

Fig. 5.20: Degradation kinetics of melanoidin at optimized conditions of temperature 38 °C, time 231 min, H_2O_2 concentration 119 mM and WO_3 concentration of 250 ppm along with control experiments under dark. The experimental data are presented as symbols, while fitted data are depicted as dotted lines.

The melanoidin degradation at the optimum conditions was also investigated at different temperatures. The melanoidin degradation was studied at 308, 318, and 328 K. Entropy and enthalpy were examined as potential moderators of the melanoidin degradation rate. The thermodynamic parameters were determined by plotting 1/T vs. ln Kc (Figure 5.21) [334]. Table 5.2 lists the equations used to scrutinize the thermodynamic parameters (ΔS, ΔH and ΔG). The thermodynamic parameters estimated for the degradation of melanoidin by WO_3 photocatalyst under visible light are listed in Table 5.4. The negative value of ΔG suggests the spontaneous

degradation of the melanoidin at all experimental temperatures [189, 193]. As the temperature increased from 298 to 328 K, the degrading efficiency of the melanoidin had also increased. The positive value of ΔH specified the endothermic nature of the melanoidin degradation indicating the enhancement of the melanoidin degradation capacity by increasing temperature. This also resulted in an increase in the entropy as reflected by the positive value of ΔS.

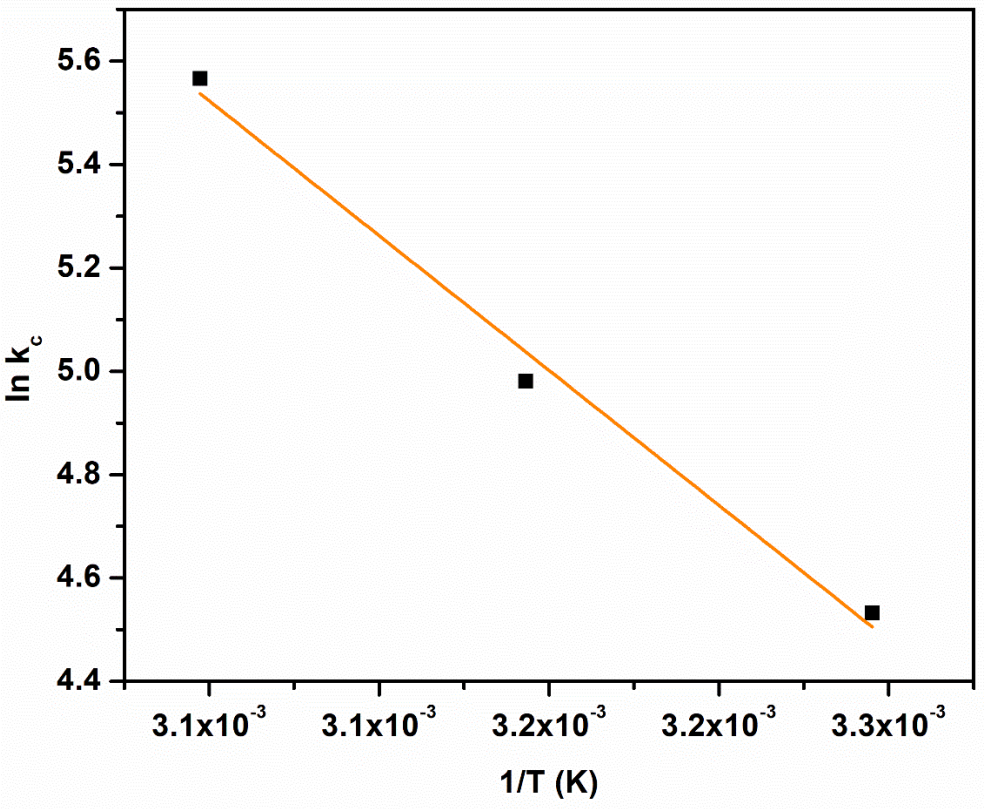

Fig. 5.21: Thermodynamic analysis of melanoidin degradation using WO_3 photocatalyst at the optimized conditions.

Table 5.3. Kinetic parameters of melanoidin degradation using WO_3 photocatalyst at the optimized conditions along with control experiments in the dark.

S No.	Experimental conditions	C_1 (g L^{-1})	K (min^{-1})	C_2 (g L^{-1})	% Degradation	R^2
1	WO_3 in dark	0.14 ± 0.02	0.02	5.24 ± 0.24	2 ± 0.2	0.99
2	WO_3+H_2O_2 (Dark)	0.29 ± 0.01	0.02	5.08 ± 0.01	5 ± 1	0.99
3	WO_3+H_2O_2 (Visible)	5.18	0.02	0	99 ± 1	0.98

Table 5.4. Thermodynamic parameters during melanoidin degradation using WO_3 photocatalyst at the optimized conditions.

Temperature (K)	ΔG (kJ mol^{-1})	ΔH (kJ mol^{-1})	ΔS (J mol^{-1} K^{-1})	R^2
308.15	-11.61			
318.15	-13.17	43.36	178.18	0.99
328.15	-15.19			

5.3.4. Photocatalytic degradation of melanoidin under UV light using FZO as photocatalyst

5.3.4.1. Optimization of Experimental parameters by RSM-CCD to enhance the melanoidin degradation using FZO photocatalyst

Using RSM-CCD, H_2O_2 (mM) and FZO (ppm) concentration were optimised (following the Fenton optimized conditions of temperature = 33.85, time = 116.49 min, melanoidin concentration = 1 % w/v) to maximise the melanoidin degradation. Lower and upper limits were set as 10/200 mM for H_2O_2 and 100/300 ppm for FZO. The mini-tab program predicted 13 experimental configurations as listed in Table S5.4. The melanoidin degradation (%) was considered as the response. The model equations for the melanoidin degradation is projected as equation 5.9.

$$\%\, Melanoidin\ degradation = 82.93 + 24.66A + 12.93B + 9.32AB - 12.82A^2 - 9.80B^2 \quad (5.9)$$

Table S5.4 shows the predicted response values from a quadratic polynomial model. The R^2 value of 0.95 evidenced the strong correlation between the experimental and predicted data. The ANOVA analysis indicated the higher F-value (22.60) and lower p-value (< 0.01) for the melanoidin degradation, which evidenced the relevance of the model [5]. The independent variables A and B as H_2O_2 and FZO concentrations and their interactions (A^2 and B^2) for the melanoidin degradation were found to be significant with p-values ≤ 0.02 as listed in Table S5.5. Figure S5.5 illustrates the 3-D response surface plots for the maximum melanoidin degradation at the RSM optimized condition. The Minitab software predicted 163 mM of H_2O_2 and 261 ppm of FZO concentrations for maximum degradation at photo-Fenton optimized conditions of the temperature of 34°C, time of 117 min and 1 % (w/v) of the initial melanoidin concentration. The experimental response (% melanoidin degradation) at optimized condition demonstrated

practically the total melanoidin degradation of 98 ± 1 %, which agreed to the predicted value. Correspondingly, the COD reduction was also found to be 85 ± 2 % as shown in Figure 5.22. The HPLC analysis of the residual melanoidin also resulted in 97 % of melanoidin degradation (Figure S5.6). In fact, the melanoidin degradation analyzed by UV-spectrophotometer and HPLC analysis were linearly related with the R^2 value of 0.99 (Figure 5.23).

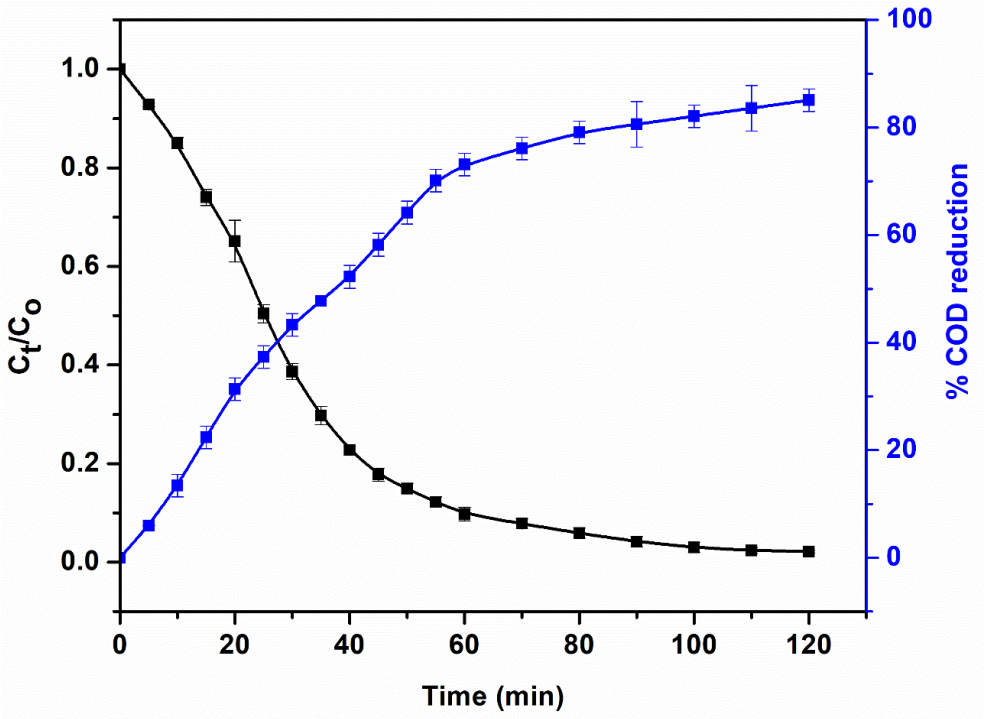

Fig. 5.22: Degradation of the melanoidin and COD reduction at optimized conditions of temperature 34°C, time 117 min, 163 mM of H_2O_2, and 261 ppm of FZO concentration. C_0 is the initial concentration of melanoidin and C_t is the residual melanoidin at any time t.

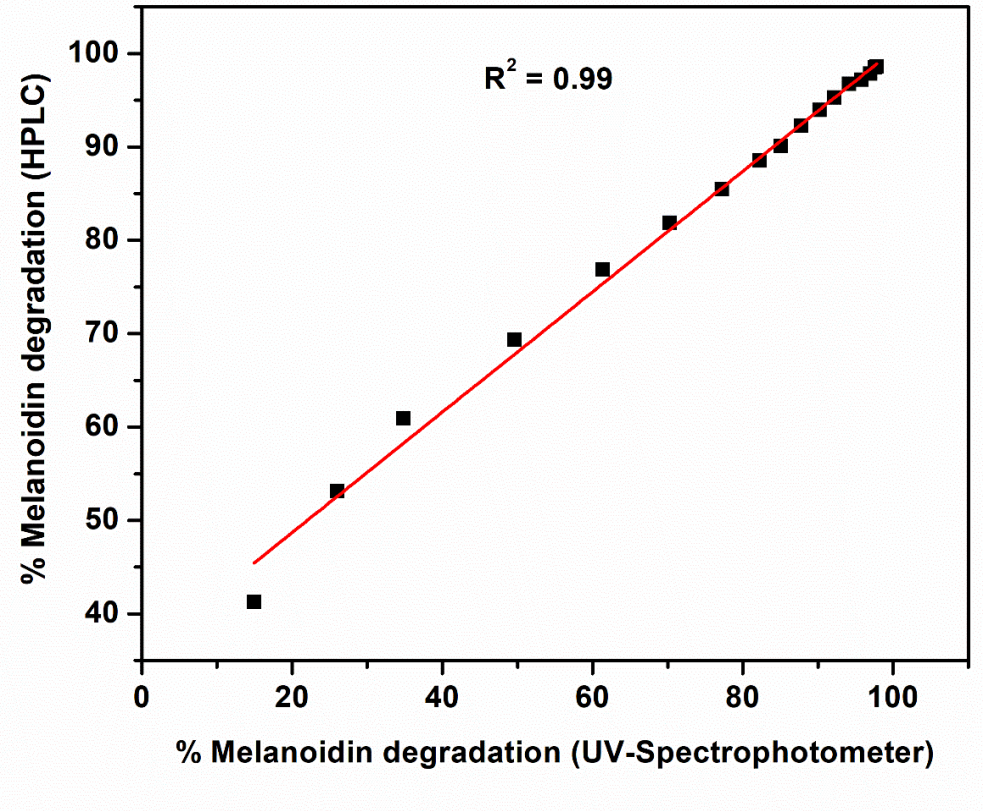

Fig. 5.23: Comparison of melanoidin degradation using HPLC and UC-Spectrophotometer analysis at optimized conditions of temperature 34°C, time 117 min, 163 mM of H_2O_2, and 261 ppm of FZO concentration.

5.3.4.2. Role of pH on photocatalytic degradation of the melanoidin

The pH of the solution was varied from 3 to 11 with a starting melanoidin concentration of 1 % (w/v) for photocatalytic degradation using FZO at the optimum conditions. The melanoidin degradation efficiency decreased from 98 ± 1 % to 58 ± 1 % as the pH of the solution was increased from 3 to 11, as shown by Figure 5.24. As discussed in the previous section (5.3.3.3) the photocatalysts resulted in a high degradation efficiency in an acidic medium [330, 331].

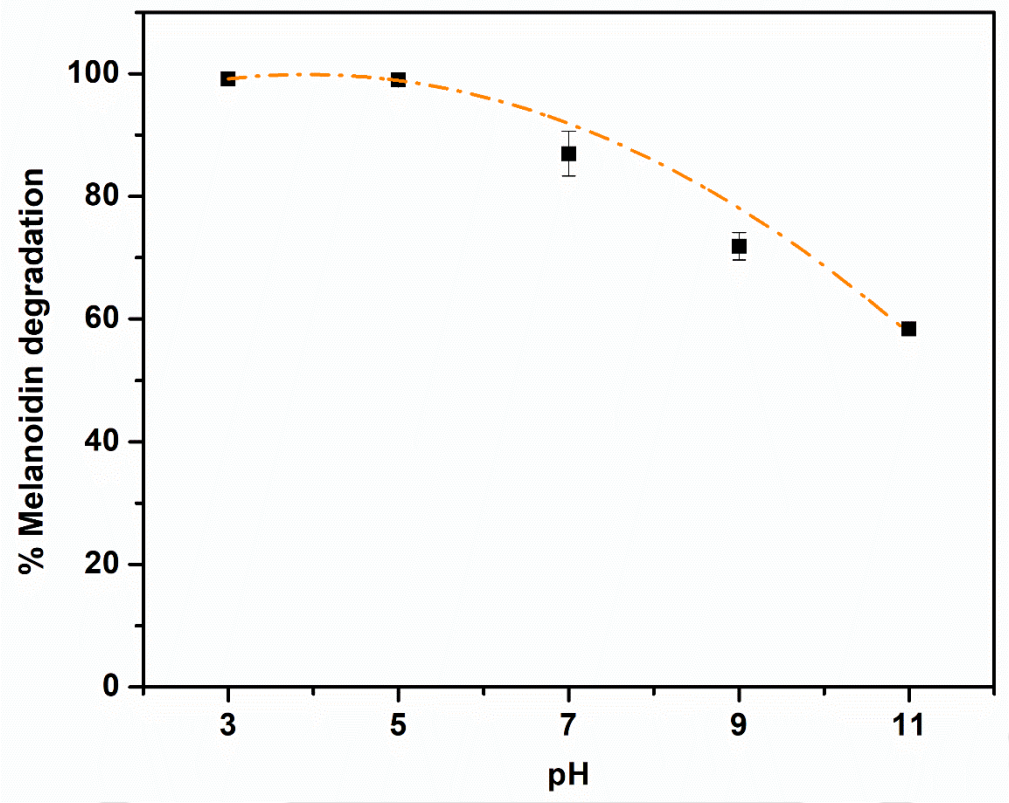

Fig. 5.24: Effect of solution pH on photocatalytic degradation of melanoidin using FZO at the optimized conditions.

The surface charge analysis of FZO nanoparticles resulted in a positive surface charge at the working pH of 4.0. The pzc values of the synthesized FZO was found to be 9.8, while the same for the melanoidin was 6.9. Thus at the working pH of 4.0, both the melanoidin and synthesized FZO nanoparticles had a positive zeta charge on their surfaces. This reveals that there is no electrostatic interaction occurring between nanoparticles and melanoidin compounds during the degradation process. The change of zeta potential with the change in the pH was observed as given in Figure 5.15. FZO and melanoidin solution had the zeta potential difference of 25.04 mV at the working pH of 4.0. The positive charge on melanoidin and FZO surfaces resulted in the excess generation of e^- which participated in redox reaction and oxidized the melanoidin compound to

enhance the degradation. The charge-charge repulsion caused the dispersion of particles and resulted in the increased impact of applied illuminance intensity [335, 336].

5.3.4.3. Kinetic and thermodynamic study

The experimental kinetic data of the melanoidin degradation were well fitted to the first-order kinetic model with the correlation coefficient value (R^2) of 0.99. The fitted data are shown as dotted lines in Figure 5.25. The rate of reaction constants, melanoidin degradation efficiency and correlation coefficient values at optimized conditions along with various control experiments are listed in Table 5.5. The reaction rate constant (k) for the photocatalytic degradation of melanoidin using FZO was found to be 3×10^{-2} min^{-1} in the UV irradiation, which was three folds higher as compared to that in the visible light. This agreed with the better photocatalytic activity of FZO in UV light due to its higher bandgap energy.

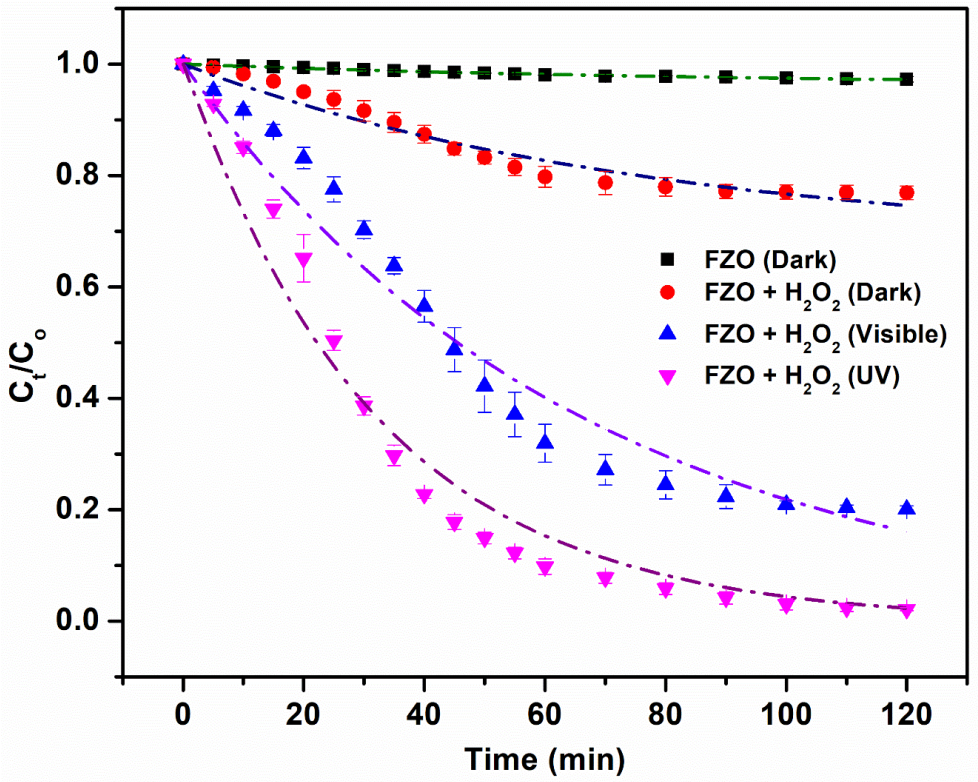

Fig. 5.25: The photocatalytic degradation kinetics of melanoidin using FZO under UV irradiation at optimized conditions of temperature 34°C, time 117 min, H_2O_2 concentration of 163 mM and FZO concentration of 261 ppm. The control experiments were performed in dark and under visible light. The experimental data are shown as symbols, while fitted data are represented as dotted lines.

The thermodynamic parameters during the photocatalytic degradation of melanoidin using FZO were determined by plotting $\ln k_c$ vs 1/T as shown in Figure 5.26. The estimated thermodynamic parameters for the photocatalytic degradation of melanoidin using FZO are listed in Table 5.6. The negative value of ΔG suggested the spontaneous degradation of the melanoidin at all experimental temperatures [189, 193]. The positive value of ΔH indicated the endothermic nature of the

degradation process. Thus the degradation efficiency was enhanced at a higher temperature. Correspondingly the increased randomness is reflected by the positive value of ΔS.

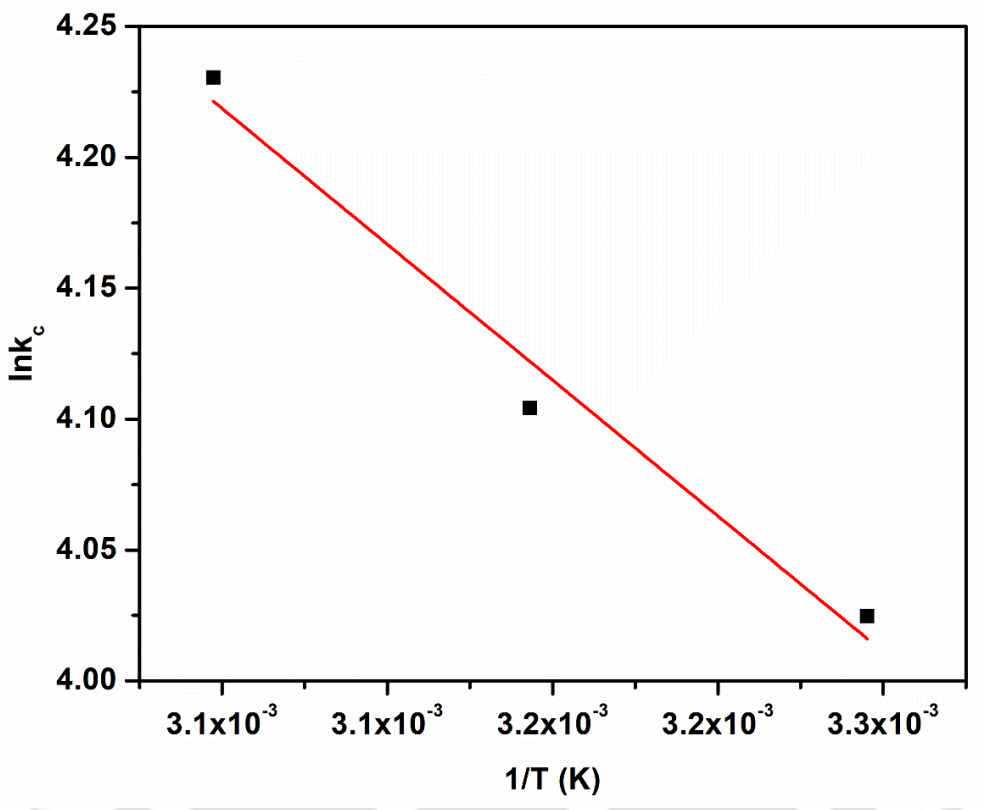

Fig. 5.26: Thermodynamic analysis during photocatalytic degradation of melanoidin using FZO at optimized conditions.

Table 5.5. The kinetic parameters for photocatalytic degradation of melanoidin using FZO at optimized conditions along with control experiments.

S No.	Experimental conditions	C_1 (g L^{-1})	K (min^{-1})	C_2 (g L^{-1})	% Degradation	R^2
1	FZO in dark	0.48 ± 0.24	1.0×10^{-2}	10.50 ± 0.24	3 ± 1	0.99
2	FZO+H_2O_2 (Dark)	3.58 ± 0.08	1.0×10^{-2}	7.40 ± 0.08	23 ± 1	0.96
3	FZO+H_2O_2 (Visible)	10.98	1.0×10^{-2}	0	80 ± 1	0.97
4	FZO+H_2O_2 (UV)	10.98	3.0×10^{-2}	0	98 ± 1	0.98

Table 5.6. Thermodynamic parameters for photocatalytic degradation of melanoidin using FZO at optimized conditions.

Temperature (K)	ΔG (kJ mol^{-1})	ΔH (kJ mol^{-1})	ΔS (J mol^{-1} K^{-1})	R^2
308.15	-10.31			
318.15	-10.86	8.63	61.39	0.98
328.15	-11.54			

5.3.5. Reusability study

The ability to re-use a photocatalyst is crucial for industrializing the process and making it economically viable. The reusability studies of synthesized photocatalysts (WO_3 and FZO) at the respective optimized conditions were performed. The synthesized WO_3 nanoparticles were found to attain a melanoidin degradation and COD reduction efficiency of greater than 81 and 75 %, respectively, up to eight consecutive cycles (Figure 5.27 A). While FZO retained above 81 and 68

% of melanoidin degradation and COD reduction, respectively, up to five consecutive cycles (Figure 5.27 B). However, after the eighth and fifth cycles of the melanoidin degradation by WO_3 and FZO, the removal efficiency dropped due to the significant loss of catalysts quantity during recycling. The repetitive usage of the synthesized photocatalysts demonstrated their practical and economic feasibility.

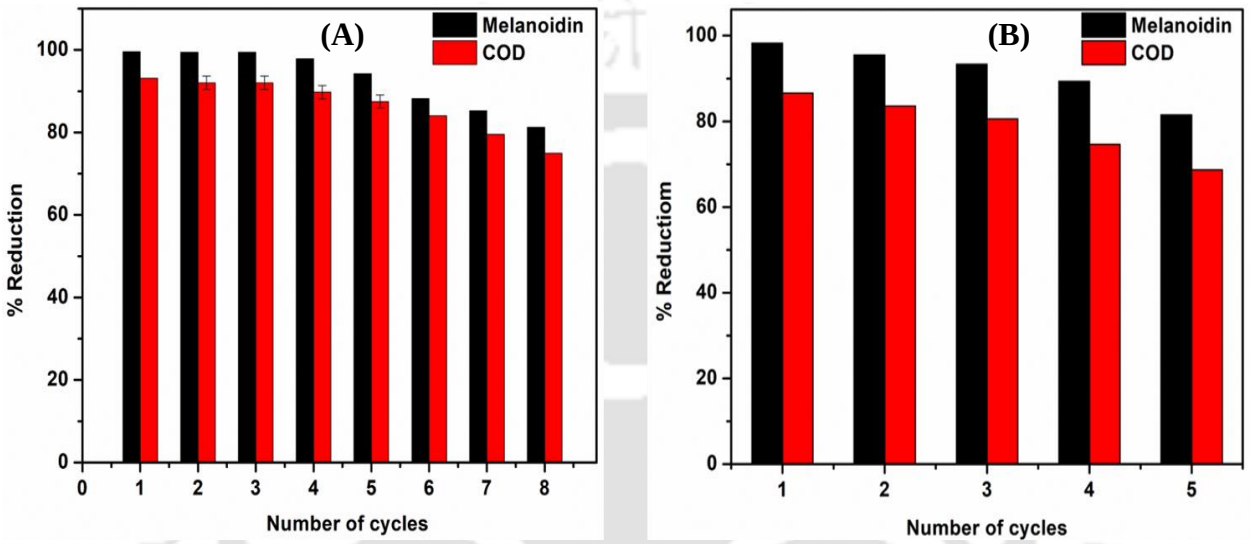

Fig. 5.27: Reusability study of synthesized (A) WO_3 nanoparticles up to 8th consecutive cycles and (B) FZO nanoparticles up to 5th consecutive cycles for the photocatalytic degradation of melanoidin and COD reduction at the respective optimized conditions.

5.3.6. Proposed mechanism of photocatalytic degradation of melanoidin

The mechanism of photocatalytic degradation of melanoidin succeeded by following several segments. A schematic representation of the photocatalytic degradation of melanoidin is given in Figure 5.28. In initial, the photo-excited (visible/UV) WO_3/FZO catalysts generated an electron (e^-) and hole pairs (h^+) at the conduction band and valance band, respectively (Eq. 5.10) [337]. These generated e^- and h^+ migrated to the surface of WO_3/FZO catalysts and participated in a redox reaction with melanoidin. Subsequently, hydrogen peroxide (H_2O_2) breaks into 2•OH molecules

in the presence of light (Eq. 5.11), and water molecules dissociated into ions (Eq. 5.12) [338]. The oxygen (O_2) molecules acted as an acceptor and generate superoxide radical (O_2^-) (Eq. 5.13). The h^+ also reacted with water molecules and OH^- to generate the $\bullet OH$ radicals (Eq. 5.14 and 5.15) [339]. The •OH radicals oxidized the melanoidin compounds on the surface of WO_3/FZO particles and break the melanoidin compounds into intermediate compounds (RCOO•) [340, 341]. These intermediate compounds again reacted with •OH resulting in the complete degradation of melanoidin in the form of CO_2, H_2O and inorganic ions (Eq. 5.16) [338, 339].

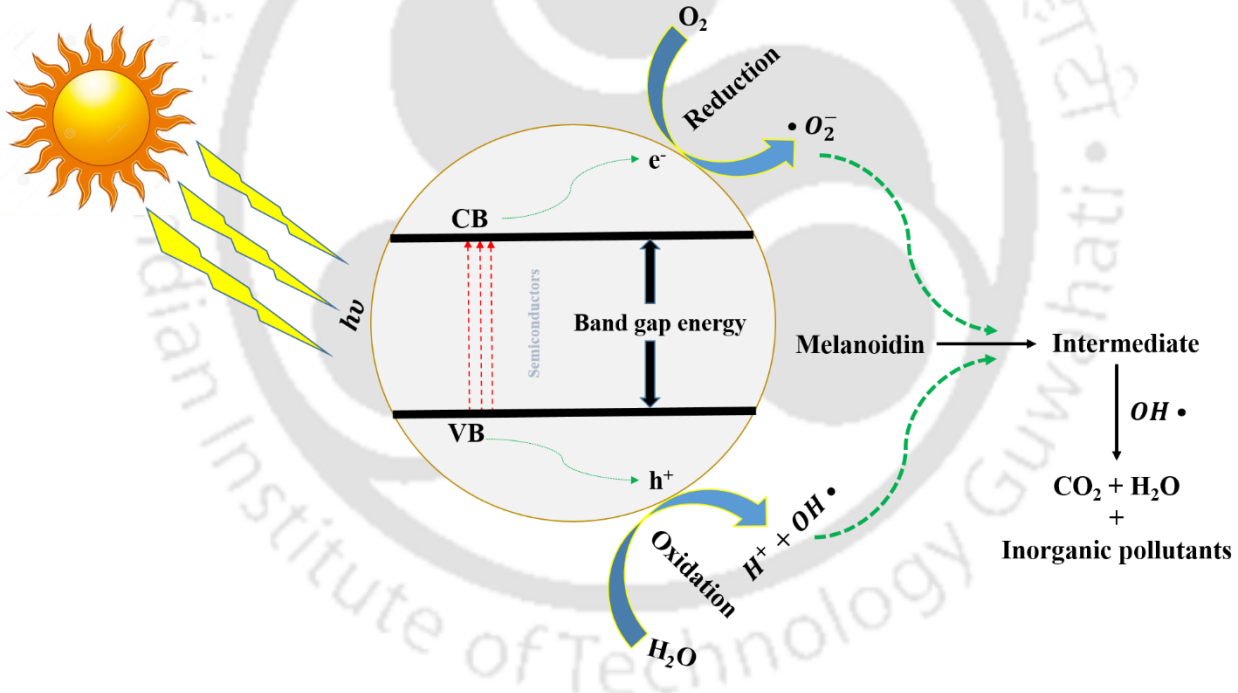

Fig. 5.28: Schematic diagram of the photocatalytic mechanism for melanoidin degradation.

$$Semiconductore + h\upsilon \rightarrow e^- + h^+ \quad (5.10)$$

$$H_2O_2 + h\upsilon \rightarrow 2\bullet OH \quad (5.11)$$

$$H_2O \rightarrow OH^- + H^+ \quad (5.12)$$

$$O_2 + e^- \rightarrow \bullet O_2^- + H^+ \quad (5.13)$$

$$h^+ + H_2O \rightarrow \bullet OH + H^+ \quad (5.14)$$

$$h^+ + OH^- \rightarrow \bullet OH \quad (5.15)$$

$$R - H + \bullet OH \rightarrow RCOO\bullet + \bullet OH \rightarrow CO_2 + H_2O + inorganic\ ions \quad (5.16)$$

5.3.7. Application of photocatalysts for the real (industrial-grade) spentwash samples

The applicability of the photocatalytic degradation efficiencies of WO_3 and FZO nanoparticles for the melanoidin were evaluated for real spentwash samples collected from a molasses-based distillery located in Hardoi, Uttar Pradesh, India. The spentwash concentrations were varied from 1 to 5 % v/v. WO_3 under visible light resulted in almost complete decolourization of spentwash up to 2 % at the RSM optimized condition. Further increase in the concentration of spentwash from 3 to 5 % (v/v) reduced the decolourization efficiencies as 97 ± 2, 92 ± 1 and 73 ± 1 % for 3, 4 and 5 % spentwash, respectively. Similarly, the COD reduction for 1 to 5 % v/v spentwash samples were also found to be 89 ± 2, 87 ± 1, 86 ± 1, 78 ± 2 and 66 ± 1 %, respectively (Figure 5.29 A). FZO photocatalyst under UV light was also examined for the decolourization of spentwash at the RSM optimized conditions. The FZO resulted in almost complete decolourization of spentwash up to 3 % v/v of spentwash and a further increase in the concentration of spentwash from 4 to 5 % (v/v) decreased the decolourization efficiencies as 95 ±1 and 84 ± 1 %, respectively. The COD reductions were also measured to be 96 ± 2, 93 ± 2, 84 ± 2, 80 ± 4 and 73 ± 2 % for 1 to 5 % v/v of spentwash concentrations, respectively (Figure 5.29 B).

A comparison between the results of this present investigation and those of other relevant studies based on the melanoidin degradation and COD removal efficiencies in various forms of melanoidin-containing wastewaters is presented in Table 5.7. The developed combinations of WO_3/H_2O_2/Visible and FZO/H_2O_2/UV could be selected as one of the most competitive systems

among the other systems based on the % decolourization, % COD, lower H_2O_2/COD ratio and multiple cycles of reusability. Compared to other photocatalytic systems for melanoidin and COD removal, the synthesized WO_3 and FZO photocatalyst exhibited better oxidation efficiency presumably due to the formation of sufficient active catalysis binding sites. The organic content (melanoidin) was oxidized and low molecular organic/inorganic compounds were agglomerated and settled down during the oxidation reaction, which was easily separated from the solution. This resulted in efficient decolourization of spentwash and significant reduction of COD.

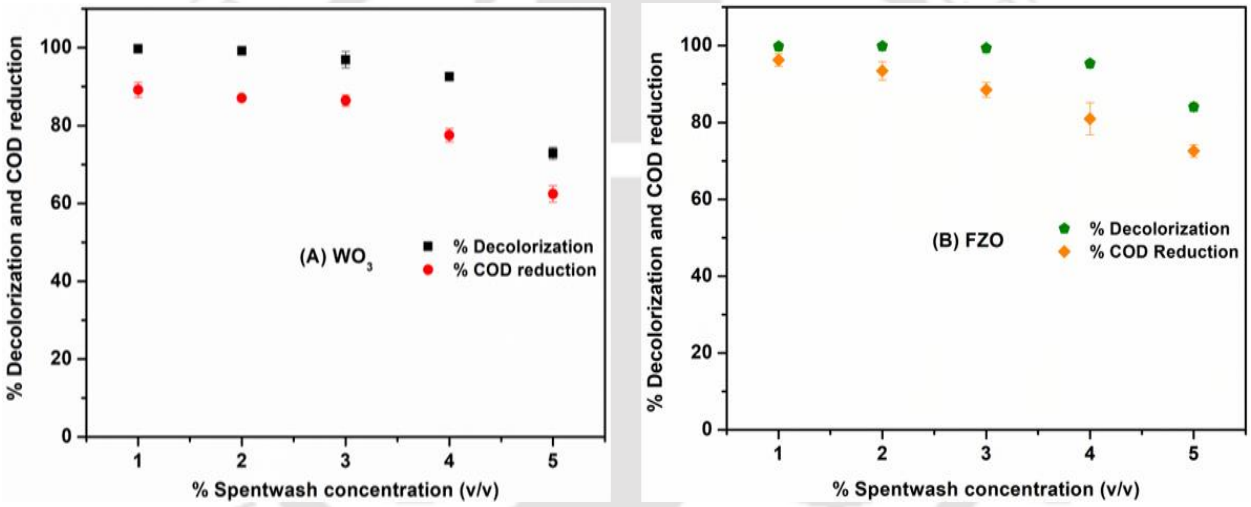

Fig. 5.29: Application of the developed combinations of WO_3/H_2O_2/Visible and FZO/H_2O_2/UV at the respective RSM optimized conditions of the decolourization of a real spentwash sample.

Table 5.7. Comparison of relavent studies for decolourization and COD reduction of melanoidin containing wastewater.

Methods/Catalyst	Wastewater Source	Light source	Initial COD (mg L^{-1})	% Decolorization	% COD Reduction	H_2O_2/ COD	Re-usability	Ref.
Fe-doped Activated carbon	Synthetic melanoidin	Visible	8000	84.7	72.6	1.02	5 cycles	[249]
AAC–CH–Fe)	Synthetic melanoidin	Visible	8000	77.1	74.4	0.02	N/A	[248]
Vanadium-doped TiO_2	Distillery spentwash	Visible	N/A	65	N/A	N/A	N/A	[285]
Fe_2O_3-graphite composite	Distillery effluent	Visible	N/A	N/A	66.15	N/A	N/A	[72]
TiO_2/H_2O_2	Distillery effluent	Visible	500	79	N/A	20.40	N/A	[342]
WO_3/H_2O_2	**Synthetic melanoidin**	**Visible**	**28160**	**99.6**	**93**	**0.14**	**8 cycles**	**Present study**
WO_3/H_2O_2	**Distillery spentwash**	**Visible**	**9840**	**73**	**66**	**0.41**	**6 cycles**	**Present study**
UV/H_2O_2 AOP	Synthetic melanoidin	UV	N/A	99	N/A	N/A	N/A	[287]
TiO_2–ZnO-Activated Carbon	Synthetic melanoidin	UV	3000	97	N/A	N/A	N/A	[283]
UV/H_2O_2/TiO_2/Zeolite	Synthetic melanoidin	UV	5000	97	N/A	0.01	N/A	[281]
Natural zeolite-Fe/H_2O_2	Distillery effluent	UV	1000	90	60	2	2 cycles	[239]
Fe-doped ZnO/H_2O_2	**Synthetic melanoidin**	**UV**	**53600**	**98**	**85**	**0.10**	**5 cycles**	**Present study**
Fe-doped ZnO/H_2O_2	**Distillery spentwash**	**UV**	**9840**	**84**	**73**	**0.56**	**4 cycles**	**Present study**

5.3.8. Antibacterial property of the synthesized WO_3 and FZO nanoparticles in real wastewater sample

After treatment with synthesized WO_3 and FZO nanoparticles, the bacterial count in spentwash sample decreased from 9.08×10^{11} CFU/ml to 0, as shown in Figure 5.30. This result demonstrated the synergistic effects of synthesized WO_3 and FZO nanoparticles as excellent photocatalysts and antimicrobial activity [278, 294]. Hence, the synthesized WO_3 and FZO nanoparticles can be promised as a powerful nanomaterial for distillery wastewater treatment.

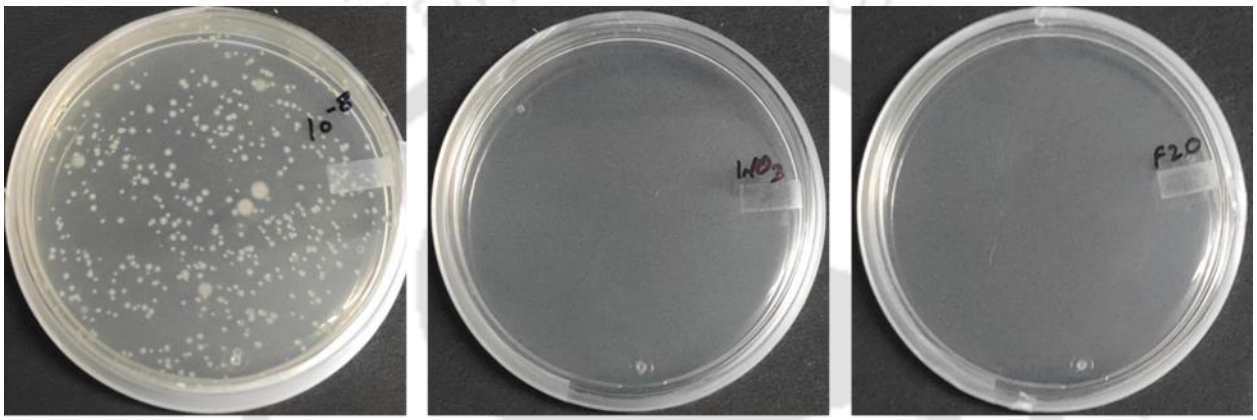

Untreated spentwash (10^8 times diluted) | WO^3 treated spentwash | FZO treated spentwash

Fig. 5.30: Antibacterial activity of WO_3 and FZO nanoparticles on real wastewater sample (spentwash) for removal of microbes.

5.4. Conclusions

In the present study, photochemical degradation of melanoidin has been investigated by WO_3 and Fe doped ZnO nanoparticles. The experimental parameters such as temperature, time, H_2O_2 and WO_3/FZO concentrations were optimized using RSM-CCD. At the optimized conditions (Temp 38°C, Time 231 min, H_2O_2 concentration of 119 mM and WO_3 concentration of 250 ppm) WO_3 photocatalyst resulted in almost complete (99.6 ± 0.1 %) degradation of 0.5 % w/v of melanoidin solution along with 92.6 ± 1 % of COD reduction under visible light illumination. Similarly, at the

optimized conditions (Temp 34°C, Time 117 min, H_2O_2 concentration of 163 mM and FZO concentration of 261 ppm) FZO photocatalyst showed 98 ± 1 % degradation of 1.0 % w/v of melanoidin concentration along with 85.1 ± 2.0 % of COD reduction under UV light irradiation. The first-order kinetic model better described the degradation process. The degradation study was conducted at various pH levels, and it was observed that the degradation of melanoidin in acidic pH is more efficient than basic pH. The degradation process was found to be as spontaneous and endothermic. The synthesized photocatalysts were resulting 1.5 to 2 times higher melanoidin degradation efficiency than commercially available very common photocatalysts (TiO_2 and ZnO). The findings of the present investigations were validated on a real industrial spentwash sample and it was found that the synthesized photocatalysts efficiently removed the colour up to 5 % v/v of real spentwash. The repetitive use of catalysts up to the 8th and 5th cycles of WO_3 and FZO nanoparticles, respectvely, for melanoidin degradation demonstrated the practical and economic feasibility.

Chapter 6

Exploring molasses as a sole nutrient for the production of alternative metabolite biosurfactants

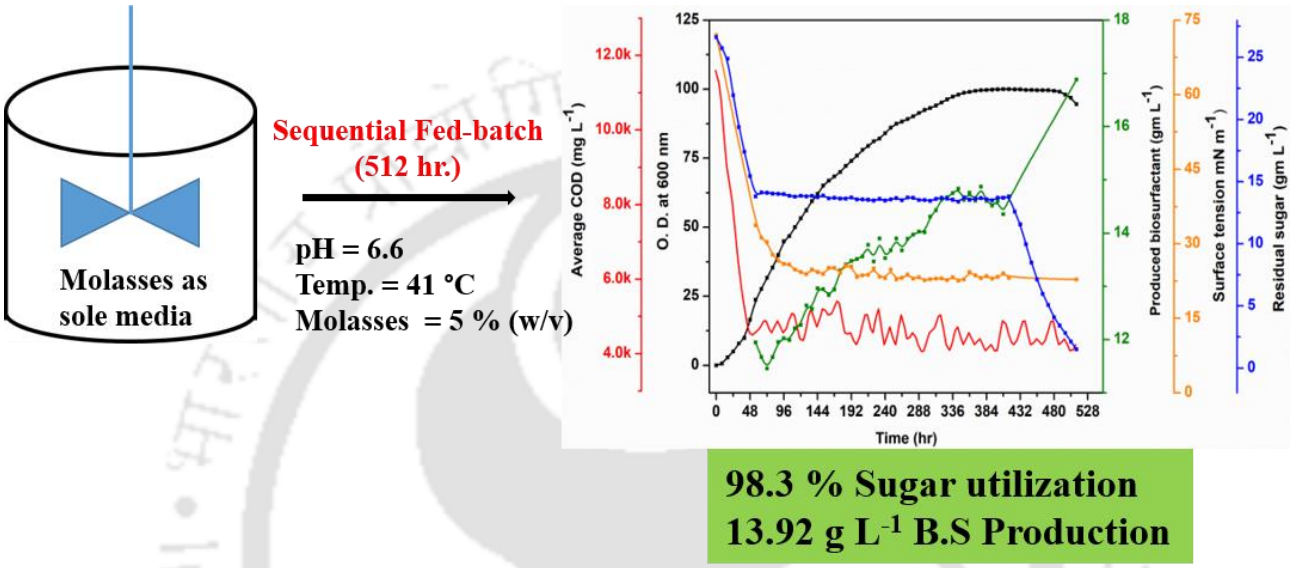

(Experimental investigation of molasses as a sole nutrient for the production of an alternative metabolite biosurfactant. ***Rahul Verma****, S. Sharma, L.M. Kundu and L.M. Pandey (2020).* ***Journal of Water Process Engineering****, 38, 101632.)*

(Enhanced Production of Biosurfactant by Bacillus subtilis RSL2 in Semicontinuous Bioreactor Utilizing Molasses as A Sole Substrate. ***Rahul Verma****, S. Sharma, L.M. Kundu, S.K. Maiti and L.M. Pandey (2022).* ***Journal of Biotechnology****, 362, 24-35.)*

This chapter explores sugarcane molasses as the sole nutrient source (media) for biosurfactant production using an isolated inherent microbe, *Bacillus subtilis* RSL-2. The experimental conditions (pH, temperature and molasses %) were optimized using the Response Surface Methodology-Central composite design (RSM-CCD) method for the maximum biosurfactant production, considering molasses as the sole nutrient. This study puts forward the potential waste to strategic wealth applications through microbial fermentation of molasses.

At the optimized condition, remarkable biosurfactant concentration and surface tension were obtained. The key finding of this study is the enhanced biosurfactant concentration by many folds using only molasses. The produced biosurfactant was identified to be lipopeptide in nature, characterized by FTIR, NMR, LCMS and MALDI-TOF. The produced biosurfactant has higher thermostability, low CMC value and negative zeta potential. These properties of the biosurfactant endorsed its applicability in medicinal, environmental and food industry applications. The produced biosurfactant showed excellent surface activities, thermal and colloidal stability. The present study endorsed the suitability of molasses as a suitable substrate (media) for the remarkable production of biosurfactants.

6.1. Introduction

Biosurfactant has become the demand of the decade due to its versatility. Biosurfactants are amphiphilic molecules of biological origin with the potentiality of lowering the interfacial tension/energy without any harmful ill-effects to flora and fauna. Such distinct features have led various researchers across the globe to overtake the commercial chemical surfactants [343]. Several biosurfactants are widely used in food, cosmetics, medicines, petroleum and environmental sectors

[297-299, 344]. Microbial biosurfactants are gaining attention due to lower critical micelle concentration (CMC), stability and biodegradability [299]. However, the higher production, extraction and separation costs of biosurfactants restrict the practical applicability. Various researches are being undertaken to utilize waste or low-cost substrate, strains with high production yield, and easy extraction processes [345-347].

Microbial biodegradation is the most eco-friendly and economical effluent remediation tool for controlling environmental pollutants. Various genera of fungi and bacteria such as *Aspergillus, Fusarium, Stenotrophomonas, Bjerkandera,* and *Bacillus* have been reported to utilize these organometallic compounds as a source of energy for their metabolic activity [348-350]. In this direction, molasses are low-cost and renewable substrates produced as a bulk by-product of sugarcane industries. Its nutritional composition, enriched in carbohydrates, vitamins and minerals, makes it highly suitable for microbial consumption without any pre-treatment expenditures. Molasses are being utilized for ethanol fermentation, producing highly polluted spent wash, featuring high COD and BOD [351]. Various research works are being carried out to use molasses as a low-cost substrate to produce alternative metabolites like biosurfactants [352-356], a highly commercial value product. Most of the studies utilized molasses as a carbon (C) source in minimal salt media. However, the utilization of molasses as the sole nutrient source for biosurfactant production is yet to be extensively explored. Among various potential molasses degraders, *Bacillus* sp. have shown tremendous activity in degrading molasses and producing value-added products such as biosurfactants [357-360]. These bacteria produce biosurfactants as surface-active metabolites during the degradation of molasses-rich effluents, thus accelerating its solubility and bioavailability for microbial utilization [361, 362].

Various bioremediation strategies have been developed for improving the bacterial molasses biodegradation ability. Optimization of bacterial growth conditions such as temperature, pH, and

substrate concentrations are the major driving factor for microbial biodegradation. Though effective during the early growth stage, these parameters' role becomes less pronounced during the late stage of bacterial growth due to the accumulation of by-products and deprivation of substrates.

In the present study, we have explored the molasses as the sole nutrient source (media) for the biosurfactant production using an isolated inherent microbe *Bacillus subtilis* RSL-2 [363]. The experimental conditions (pH, temperature and molasses %) were optimized using the Response surface methodology-Central composite design (RSM-CCD) method for the maximum biosurfactant production. The produced biosurfactant's physical, chemical and interfacial properties are analysed using various analytical techniques. A few studies explored the suitability of a semicontinuous mode of operation as a solution to sustain bacterial growth for the long term with an intermittent fill-and-draw strategy [364, 365]. This study also employed the semicontinuous mode of operation with a fill-and-draw strategy to intermittent replenishment of substrate and harvesting of product for improving biomass growth, substrate utilization and product yield. The produced biosurfactant has been characterized using various analytical techniques like FTIR, NMR and MALDI. The colloidal and interfacial properties of the produced biosurfactant have also been analyzed to highlight the potential applications.

6.2. Materials and methods

6.2.1. Materials

Bushnell Haas (BH) media (M350), Sucrose (GRM601-500G) 3,5-Dinitrosalicylic (DNS) reagent (GRM1582), Toluene (108883), Hexadecane (544763), Sodium hydroxide (NaOH) pellets (GRM467), Hydrochloric (HCl) acid (AS004) and Nutrient broth (NB) media, (MB002) were purchased from HiMedia Laboratories, India. COD reagents such as Ferrous ammonium sulfate (Cat.

No. GRM302), Potassium dichromate (Cat. No. GRM1033), Mercuric sulfate (Cat No. GRM1088), and Silver sulfate (Cat. No. GRM1412) were also purchased from HiMedia Laboratories, India. Paraffin oil (11079LM500), Methanol (70930LC250) and Ethyl acetate (70680LC250) were purchased from Finar Limited, India. Sinapinic acid (CAS no. 530-59-6) and Trifluoracetic acid (TFA, CAS no. 76-05-1) were procured from Sigma-Aldrich, India. n-Hexane (110543) was purchased from SRM, India. Silicone oil (GRM704-100G) were purchased from HiMedia Laboratories, India, and used as an antifoam agent 0.1 % (w/v) for this study. All chemicals and reagents for this investigation were of analytical grade.

6.2.2. Sample collection and media preparation

As discussed in previous chapters, the industrial-based Sugar cane molasses sample was collected from DCM Shriram Ltd, a sugar cane molasses-based distillery manufacturing plant in Hardoi, India. The molasses sample was contained in a mouth-capped glass bottle and stored in a cool and dry place for further analysis. For the experimental work, the desired concentrations of molasses (1–5 % *w/v*) were prepared in distilled water. Molasses contain a high sugar content (30–50 %) along with other nitrogen (N), phosphorous (P) and minor elements. Along with sugar, N and P are utilized by microbes for the biosynthesis of biomass and product (biosurfactant). The minor elements act as cofactors for various cellular metabolic pathways. Hence molasses solution was used as a sole nutrient (media) without supplementing any chemicals. Diluted molasses samples were centrifuged (Thermo-Fischer, Legend XTR) at 10,000 rpm for 10 min to remove solid residues. The pH of the sample was adjusted with 1 N NaOH and HCl solutions and autoclaved at 15 psi, 121 °C for 20 min [363].

6.2.3. Production of biosurfactant

The bacteria (*Bacillus subtilis* RSL-2) was isolated by our group from a sludge sample of Guwahati Refinery [363]. The isolated bacteria were incubated in Bushnell-Haas (BH) media for 24 h at 37 °C, 180 rpm in a shaker incubator. 5 % (*v/v*) of this seed culture (Optical density, OD = 1) was inoculated in molasses media and incubated at 37 °C, 180 rpm for 8 days [366]. The growth profile of bacteria was observed at every 12 h by measuring the OD at 600 nm wavelength.

6.2.4. Determination of biomass concentration

Biomass concentration was determined by estimating the dry cell weight after removing the fermentation broth by centrifuging at 10,000 rpm, 4 °C for 15 min. The supernatant was collected for the extraction of biosurfactant and the pellet was dried in a hot air oven at 80 °C to obtain a constant biomass weight [345]**.**

6.2.5. Extraction of produced biosurfactant

The concentration of overall biosurfactant produced by bacterial during biodegradation of molasses was estimated using acid precipitation followed by solvent extraction technique [367]. Upon completion of the incubation period, the culture was centrifuged to separate cell-free supernatant. This supernatant was acidified to pH 2.0 using 6.0 M HCl and left overnight at 4°C. Next, the acidified solution was solvent-extracted using ethyl acetate and Methanol (4:1, v/v). Afterward, the organic phase containing biosurfactant was separated using a separating funnel and concentrated using a rotary evaporator (Rotavapor® R-300, Buchi), and extracted crude biosurfactant was quantified gravimetrically. Thus, the obtained crude biosurfactant was stored in a cool, dry, and dark place for further analysis.

6.2.6. Estimation of residual sugar in molasses

The total reducing sugar from the samples collected at different time intervals was opted by a colorimetric technique using the 3,5-dinitrosalicylic acid (DNS) method [368, 369]. 45 g of Sodium potassium tartrate reagent was dissolved in 75 mL of distilled water. 1.5 g of DNS was dissolved in 30 mL of 2 M NaOH solution. Both reagents were mixed and a total volume of 150 mL with distilled water was maintained. The concentration of residual sugar was assessed at a regular time interval of 8 h. First, 100 µL of a sample was mixed with 3 mL of acidic water (pH=2). Then 300 µL of DNS reagent was added and the mixture was heated in a water bath at 90 °C for 5 min. The absorbance was measured at 540 nm after cooling at room temperature using a multiplate reader (Infinite 200 pro Tecan) [370]. Different known concentrations of sucrose were used for the preparation of the standard curve.

6.2.7. Optimization of culture condition by response surface methodology

Response surface methodology (RSM) was utilized to optimize the culture conditions for the maximum production of biosurfactants. It is an empirical technique applied for the optimization of multiple experimental parameters such as pH, temperature, molasses concentration [195, 196, 371]. It is a statistical and mathematical tool and evaluates the actual experimental data. Minitab statistical software was used to design all experimental conditions. Central composite design (CCD) was applied to design the different experimental conditions with variable ranges [372]. In this study, three independent variables were used as pH (4–8), temperature (25–45 °C) and, molasses concentration (1–5 %) for the maximum biosurfactant production. Biosurfactant production and surface tension (ST) values were the dependent variables (responses). A total of 20 experimental conditions were

suggested with the interaction of these variables to predict the output (optimized conditions). Analysis of variance (ANOVA) was applied to analyse the experimental data for the regression analysis [297-299, 345].

6.2.8. Determination of bacterial growth kinetics

At a regular interval, the specific growth rate (μ) was determined using equation 6.1;

$$\mu = \frac{1}{x}\frac{dx}{dt} \tag{6.1}$$

Where, 'x' stands for the biomass concentration and 't' represents the time of incubation [373]. Also, the specific biosurfactant production rate, (q_p), and specific substrate (molasses) utilization rate, (q_s) were estimated using equation 6.2 and 6.3 [373]. Here m_S stands for the maintenance coefficient which describes the specific rate of substrate utilized for cellular maintenance and is assumed to be negligible during the bacterial growth.

$$q_p = \mu\frac{Y_{p/s}}{Y_{x/s}} \tag{6.2}$$

$$q_s = \frac{\mu}{Y_{x/s}} + \frac{q_p}{Y_{p/s}} + m_s \tag{6.3}$$

Additionally, the coefficient of yield for biosurfactant ($Y_{P/S}$), and biomass ($Y_{X/S}$) were calculated using equations 6.4 and 6.5, respectively [373].

$$Y_{P/S} = \frac{\Delta P}{\Delta S} \quad (6.4)$$

$$Y_{X/S} = \frac{\Delta X}{\Delta S} \quad (6.5)$$

6.2.9. Batch bioreactor study using molasses as a sole nutrient

The bacterial growth and biosurfactant production ability using molasses as the sole nutrient source was previously optimized in a shake-flask study [216] at pH 6.6, temperature 41°C, and 5 % (w/v) of molasses. These conditions were applied for the bioreactor study using a 4 L reactor system (Minifors, Switzerland) at a working volume of 1.5 L. The aeration rate and stirring speed were constant throughout the reactor operation at 1 vvm and 250 rpm, respectively. The bacterial growth was determined by measuring the optical density of the culture medium at different time intervals. The bacterial cells were separated from samples by centrifugation at 10000 rpm for 10 min. Later, the cells were washed with distilled water twice and re-suspended in distilled water for the measurement of optical density (O.D) at 600 nm using a UV-Vis spectrophotometer (Cary 60, Agilent). The batch operation was continued until the culture entered to the death phase. Later, the cells were separated from the culture media using centrifugation (10000 rpm for 10 min at 4°C), washed with sterile water, and dried at 80°C to determine the dry cell biomass. Also, the cell-free supernatant was analyzed for residual sugar, reduction in surface tension, and biosurfactant concentration.

6.2.10. Semicontinuous fermentation based on a fill-and-draw strategy

A semicontinuous bioreactor study was performed to extend the exponential growth phase of bacteria targeting to (i) replenish the sugar, (ii) improve the sugar utilization ability of bacterial [374] and (iii) minimize the product inhibition. For this purpose, bacteria were grown in semicontinuous mode with

initial culture conditions similar to the batch bioreactor, i.e., 4 L bioreactor holding a working volume of 1.5 L, initial molasses concentration of 5 % (w/v) and 10 % (v/v) inoculum. As stated above, the bacterial growth was assessed at a regular interval of 8h by measuring O.D. The semicontinuous mode of operation was commenced at the 56^{th} hour of culture age, which was the starting period of the stationary phase in the batch culture. Then a fixed volume of culture was harvested and replenished with sterile molasses solution of a fixed concentration to maintain the working volume of the bioreactor set at 1.5 L. The process was performed at intermittent intervals of 8 h and continued until the culture O.D. was accomplished at the stationary phase. The operation was stopped at the beginning of the death phase i.e. no further growth in the O.D. of culture with the supplementation of fresh molasses. Finally, residual sugar, biosurfactant concentration and dry cell mass were estimated as mentioned in section 6.2.9.

6.3. Characterization of biosurfactant

6.3.1. Chemical characterization

The functional group analysis of the crude biosurfactant was performed using Fourier-transform infrared (FTIR) spectroscopy (Perkin-Elmer, Spectrum Two). 1 mg of crude biosurfactant was mixed with 100 mg of anhydrous potassium bromide (KBr) and pelletized using hydraulic press followed by recording spectra in the range of 400–4000 cm^{-1} by averaging 32 scans at a resolution of 4 cm^{-1} [216]. Proton (1H) nuclear magnetic resonance (NMR) was also recorded to 600MHz NMRSpectrometer (AVANCE III HD, Bruker). 200 µL of the crude biosurfactant was mixed with 600 µL of deuterium oxide (D_2O). Matrix-Assisted Laser Desorption/Ionization-Time of Flight (MALDI-TOF, AUTOFLEX SPEED, BRUKER) technique was used to estimate the molecular weight of the biosurfactant. 3 mg of sinapinic acid was dissolved in 100 µL of 30 % acetonitrile in

water containing 0.1 % TFA as a matrix solution. The biosurfactant was mixed with different matrix ratios (1:1 to 1:6, v/v) and analyzed using mass spectroscopy [366, 375].

6.3.2. Thermal stability of biosurfactant

The thermal stability of crude biosurfactant was analyzed using thermogravimetry (TG) (Netzsch, STA449F3A00). 10 mg of crude biosurfactant placed on the aluminium crucible and subjected to heating at the rate of 10 °C min^{-1} to a temperature range of 0 to 1000 °C under an argon atmosphere. A thermogram was prepared by plotting the weight loss of biosurfactant with the increase in temperature [376].

6.3.3. Critical micelle concentration (CMC) determination

The CMC of the crude biosurfactant was measured using a tensiometer (Dataphysics, DCAT 11EC) based Du Nouy ring method where the reduction of surface tension of water with the subsequent addition of different concertation of biosurfactant was determined [376]. The concentration of biosurfactant where it starts to form micellar structure causing no more change in the reduction of surface tension (ST) of water is deciphered as the CMC value for the crude biosurfactant.

6.3.4. Oil displacement test

The ability of biosurfactant to disperse hydrophobic surfaces was assessed using an oil displacement test. For this, 0.5 % (v/v) of oil was allowed to form a uniform layer on distilled water's surface in a Petri plate of 90 × 10 mm diameter. Further, 0.05 % (v/v) of biosurfactant (at CMC) was added to the uniform layer of oil, and the dispersion caused to the oil film was instantly recorded. The oil

displacement was calculated from the diameter of the halo zone formed after biosurfactant addition using distilled water as negative control [345].

6.3.5. Colloidal stability and hydrodynamic diameter

The colloidal stability of the produced biosurfactant was analyzed by measuring the zeta potential and hydrodynamic diameter of the biosurfactant solution using Litesizer (Anton Paar). The produced biosurfactant at CMC concentration was dissolved in distilled water at varying pH ranging from 3 to 11. An electrode cuvette was used to measure the zeta potential. The experiment was performed at 25°C, providing 30 seconds of equilibration time and an average of 200 scans. Similarly, the hydrodynamic diameter of the biosurfactant solution was measured at 25°C in a transparent glass cuvette. An average of 20 scans and an integration time of 10 seconds was employed with the backscattered angle of 175° [373].

6.3.6. Determination of Emulsification index (E24)

The emulsification activity was assessed accordingly by Cooper and Goldenberg's method. The emulsification index of the cell-free supernatant was determined in various organic solvents such as mustard oil, kerosene oil, paraffin oil, n-hexane, Toluene, and Hexadecane. Approximately 4 mL of cell-free supernatant was thoroughly mixed with an equal volume of aforementioned organic solvents using vortexes for 5 min and kept idle for 24 h at room temperature. The emulsion index was determined by the following equation (Eq. 6.6) [345];

$$Emulsification\ index\ (E24\ \%) = \frac{Height\ of\ the\ emulsified\ layer}{Total\ height\ of\ the\ liquid\ column} \times 100 \qquad (6.6)$$

6.3.7. Determination of wettability alteration

The wetting characteristics of produced biosurfactant on the hydrophobic surface were analyzed by measuring the contact angle using the Goniometer, Drop Shape Analysis System (Make: HOLMARC). The contact angle of cell-free supernatant and produced biosurfactant (at CMC) were measured on the hydrophobic surface of coverslips/paraffin sheet providing ambient of 25 ◦C of temperature and 1 atm of atmospheric pressure by following the described protocol. All the contact angle measurements of cell-free supernatant and produced biosurfactant solution were performed multiple times and the average values along with standard deviations are reported.

6.4. Results and discussion

6.4.1. Growth profile of *Bacillus subtilis* RSL-2 bacteria

The bacterial growth in molasses (5 % (*w/v*)) media was observed at every 12 h by recording the OD at 600 nm wavelength. A typical sigmoidal bacterial growth pattern was observed (Figure 6.1). The lag phase was found up to day one and after it entered the exponential phase up to 4 days and further reached to the stationary phase. After 6 days, the death phase was observed. The specific growth rate during the exponential phase was found to be 0.57 ± 0.2 day^{-1}, which corresponded to the reported data for *Bacillus subtilis* MG 495086 [366].

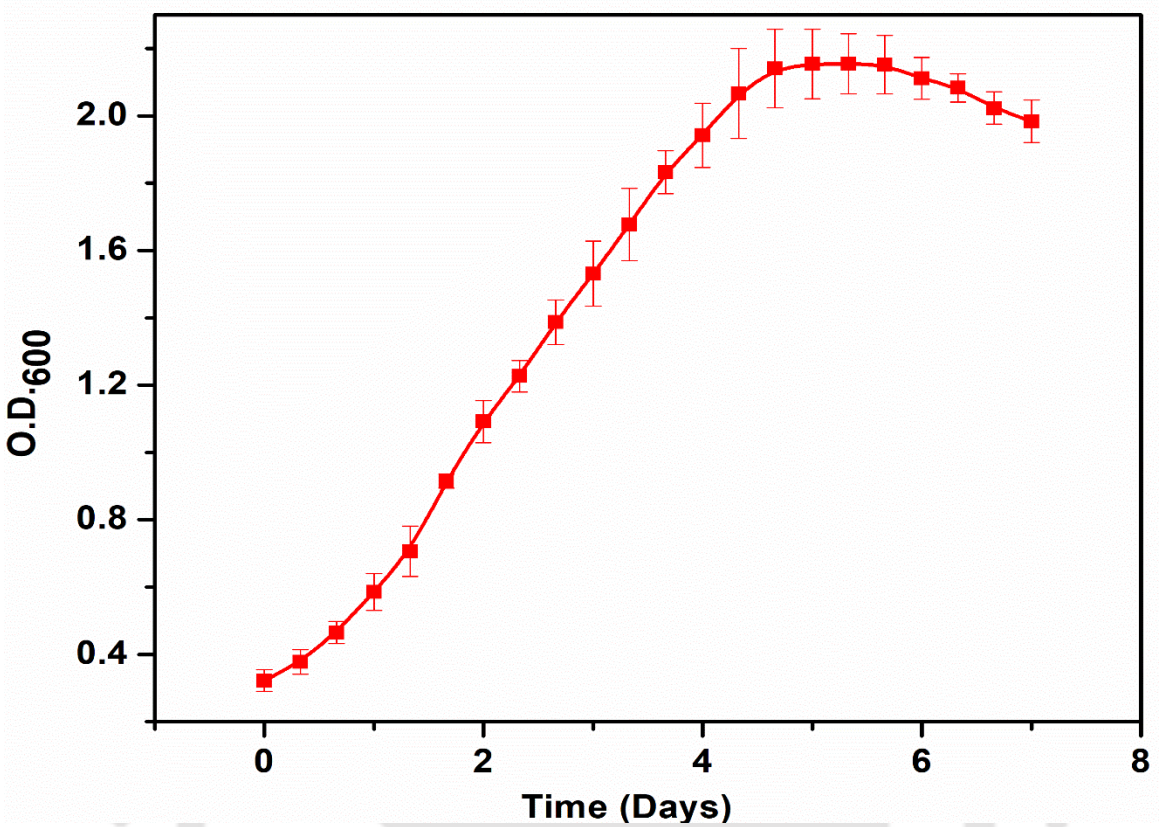

Fig. 6.1: Growth profile of *Bacillus subtilis* RSL-2 bacteria at 37 °C, 180 rpm and 1 % (*w/v*) molasses.

6.4.2. Optimization of culture conditions for the maximum production

Three independent variables such as pH (*A*); temperature (*B*); and molasses concentration (*C*) were selected to optimize the biosurfactant production using RSM-CCD. The lower/upper bounds of *A*, *B* (°C) and C (% *w/v*) were 4/8, 25/45 and 1/5, respectively. The mini-tab software designed 20 experimental set-ups as listed in Table 6.1. The responses including ST, biosurfactant concentration and dry-biomass were measured experimentally at the predicted conditions. The obtained experimental responses (ST, Biomass and BS conc.) were fitted to the model. The predicted response values are listed in Table 6.1, and found to be quite close to the experimental results. ANOVA was

applied for the regression analysis. The obtained correlation coefficient values were $R^2 > 0.96$, indicating the very similar results between the experimental and predicted values. The lesser p-value (<0.0001) and the higher F-value proved the significance of the model. The quadratic polynomial equations were obtained for each response factors as mentioned in Table 6.2. In addition, ANOVA analysis of independent variables (*A*, *B* and *C*) and their interactions (*AB*, *BC*, *AC*, A^2, B^2, C^2) are also tabulated in Table 6.2. The optimized conditions were predicted at pH of 6.6, temperature of 41 °C and 5 % (*w/v*) of molasses concentration. The 3D response surface plots are shown in Figure 6.2. Under the optimized conditions, the experimental responses i.e. biomass, biosurfactant concentration and ST, were obtained as 5.2 ± 0.2, 12.34 ± 0.1 and 24.09 ± 0.11 mN m^{-1}, respectively (Figure 6.3).

Table 6.1. Experimental and predicted values of ST, biosurfactant concentration and biomass with respect to independent variables (pH, temperature and molasses concentration) in RSM-CCD runs.

Independent variables				Experimental results (Responses)			Predicted results (Responses)		
S. No.	pH (A)	Temp °C (B)	Molasses % (w/v) (C)	ST (mN m^{-1})	BS conc. (g L^{-1})	Biomass conc. (g L^{-1})	ST (mN m^{-1})	BS conc. (g L^{-1})	Biomass conc. (g L^{-1})
1	8	25	1	39	4.4	3.1	39.17	4.91	3.16
2	6	35	6.4	25.39	9.1	5.9	25.55	8.71	5.09
3	6	35	3	24.46	4.9	6.3	24.59	4.45	6.54
4	6	35	3	24.49	4.1	7.8	24.59	4.45	6.54
5	6	51.8	3	37.18	5.7	4.7	36.89	5.94	5.27
6	6	18.2	3	34.15	2.2	3	34.35	1.56	2.76
7	6	35	3	24.52	4.3	6.3	24.59	4.45	6.54
8	8	45	1	30	5.5	5	29.96	5.22	4.00
9	8	45	5	28	7.5	5.9	28.20	7.80	6.45
10	8	25	5	28	3.9	3.7	27.58	4.14	3.86
11	4	25	5	29	4.7	2.6	29.11	5.27	3.37
12	4	45	1	47.79	2.9	3.2	48.27	2.94	2.81
13	4	25	1	46	1.4	3.2	45.87	1.39	2.42
14	2.6	35	3	46.09	5.4	3.6	45.91	5.32	3.91
15	9.3	35	3	29.16	6.6	5.3	29.25	6.28	5.32
16	6	35	3	24.5	4.46	6.3	24.59	4.45	6.54
17	6	35	3	24.56	4.41	6.3	24.59	4.45	6.54
18	6	35	0	41.36	3.3	1.1	41.11	3.29	2.24
19	4	45	5	41.44	10.4	5.8	41.34	10.17	5.50
20	6	35	3	25	4.48	6.3	24.59	4.45	6.54

Table 6.2. Quadratic model fitting to the experimental parameters with ANOVA analysis.

Response factor	Quadratic polynomial equation	ANOVA analysis
Surface Tension	$+128.13 - 12.17A - 2.15B - 13.20C - 0.15AB + 0.12AC + 0.32BC + 1.15A^2 + 0.04B^2 + 0.77C^2$	A, B, C, AB, AC, BC, A^2, B^2, C^2 are significant model terms $R^2 = 0.99$
Biosurfactant concentration	$-5.03 + 0.13A + 0.27B + 0.26C - 0.02AB + 0.04\ AC - 0.29BC + 0.12\ A^2 + 0.002B^2 + 0.14C^2$	A, B, C, AC, BC, A^2, C^2 are significant model terms $R^2 = 0.98$
Biomass	$-14.77 + 2.11A + 0.60B + 1.28C + 0.01AB + 0.02AC - 0.02BC - 0.17A^2 - 0.01B^2 - 0.25C^2$	B, C, A^2, B^2, C^2 are significant model terms $R^2 = 0.87$

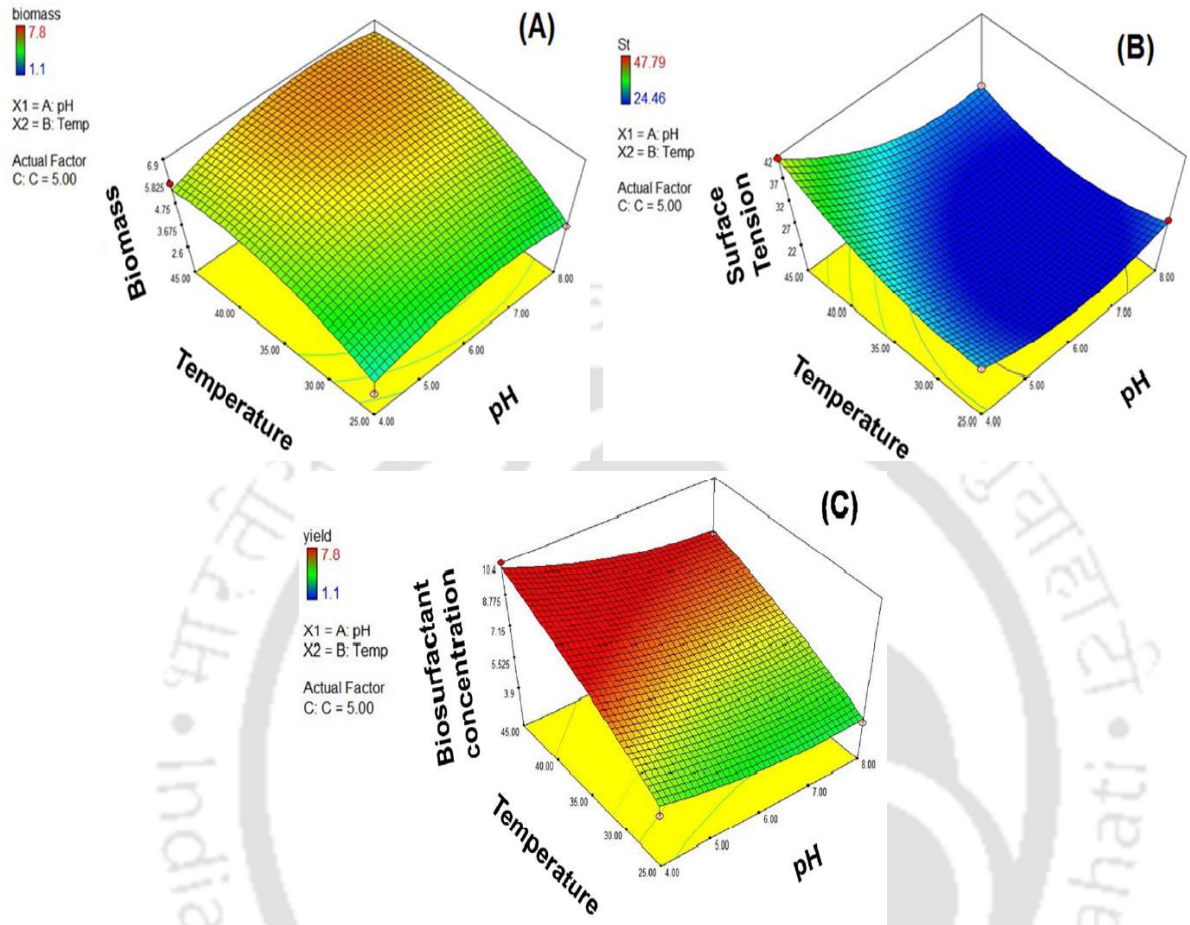

Fig. 6.2: 3D response surface plots for the (A) biomass, (B) ST and (C) biomass concentration considering their independent parameters as pH, temperature and concentration of molasses.

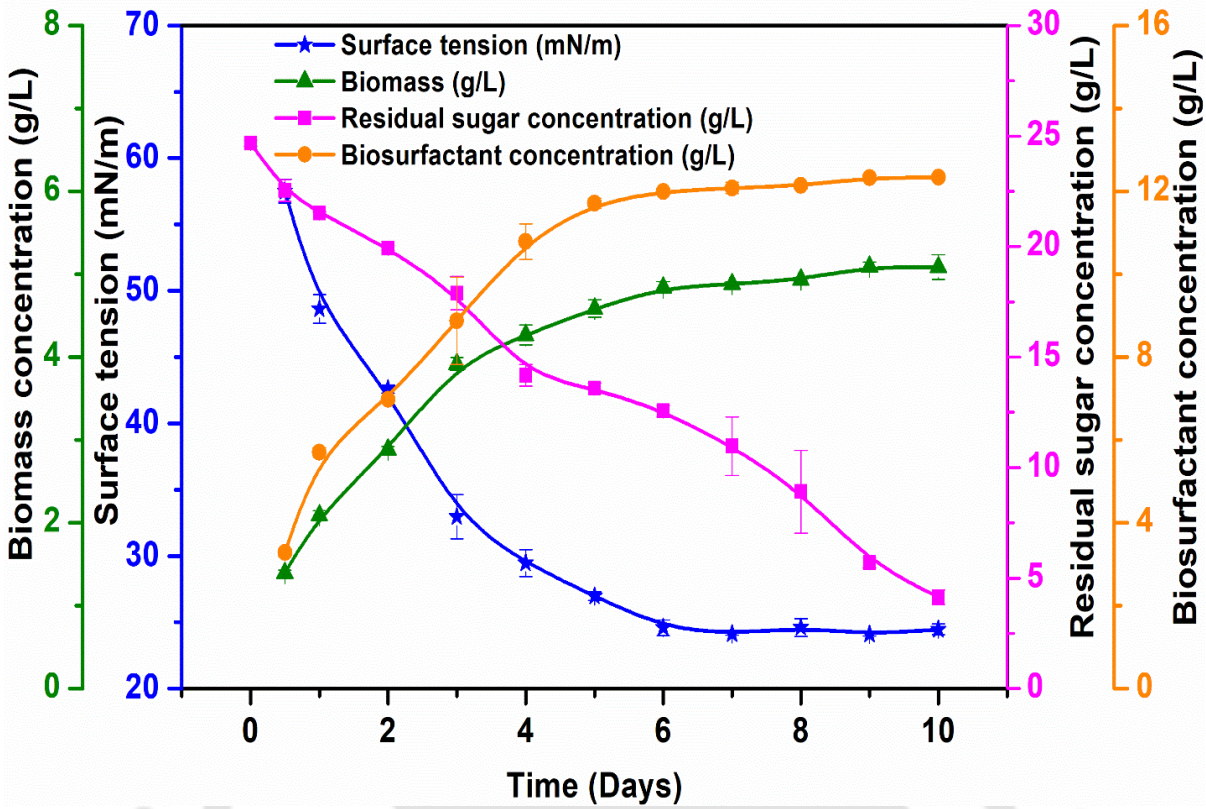

Fig. 6.3: Profile of ST, dry biomass, biosurfactant production and residual sugar at the optimized conditions (pH 6.6, 41 °C and 5 % (w/v) of molasses) in shake-flask study.

6.4.3. Production of biosurfactant at optimized conditions in shake- flask study

Figure 6.3 shows the ST, biomass and biosurfactant concentration profiles of the shake-flask study for the isolated bacterial strain *Bacillus subtilis* RSL-2 at the above predicted optimized conditions of pH 6.6, temperature 41 °C and 5 % of molasses (*w/v*). The ST gradually decreased up to 6 days and reached towards the saturation at 24.09 ± 0.11 mN m^{-1}. Corresponding to the ST decrement, the dry biomass concentration of the culture was increased. The maximum dry biomass concentration was 5.2 ± 0.2 g L^{-1}, which was comparable to the reported data [355]. Dry-biomass and the biosurfactant concentration showed a linear relationship indicating the growth associated production of biosurfactant. The maximum biosurfactant concentration was 12.34 ± 0.1 g L^{-1}. Table

6.3 compares the biosurfactant production ability of various *Bacillus* strains using molasses as the C source. Various literatures have used molasses as a suitable C source along with mineral salt media and other basal media. It is observed that very few bacteria (*Bacillus licheniformis* SA9 and *Bacillus licheniformis* TR7) are capable of using only molasses as a sole nutrient (media). However, in the present study, the biosurfactant concentration was improved by many folds as compared to the literature (see Table 6.3). Further, the surface-active property (i.e. surface tension) of the produced biosurfactant was found to be 24.09 mN m^{-1}, which is comparable or better than the literature [355]. This highlighted the potential of the isolated strain to produce the biosurfactant utilizing using a low-cost substrate (sole medium) like molasses. The economy is the major bottleneck in the biosurfactant production and limits its practical applications. Typically, raw materials account for 10–30 % of the overall production costs in most of the biotechnological processes [377]. The average price of molasses across the globe in about 7–8 INR/kg [378, 379], while the same of minimal media used for bacterial growth is about 7000 INR/kg [380]. This suggested molasses as a suitable low-cost substrate for the production of biosurfactants. It is clear that the use of molasses as the sole raw material is expected to reduce the overall production cost of biosurfactants. Further, during the scale-up process, media choice, geometrical and dynamic similarities play vital roles [381]. Variations in any one of these factors significantly influence the performances of a bioprocess *i.e.*, product yield compared with laboratory-scale experiments. In this laboratory study, molasses was used as the sole raw material and the use of the same raw material during the scale-up shall ensure the similarity of media.

Table 6.3. List of biosurfactant production ability of *Bacillus sp*. using molasses as whole substrate/C source.

S. N.	Microbes	Substrates	Conc. (% w/v)	Culture medium	Reaction conditions (pH, Temp °C, RPM, Time (hr.))	Decrease in ST (mNm^{-1}) /CMC ($mg\ L^{-1}$)	Biosurfa-ctant conc. ($g\ L^{-1}$)	Ref.
1	*Bacillus subtilis* RSL-2	Molasses	5	Whole molasses medium	pH 6.6, 41 °C, 180 rpm, and 240 h	24.09/80	12.34	Present study [216]
2	*Bacillus subtilis* SA9	Molasses	4	Whole molasses medium	pH 6, 30 °C, 150 rpm, and 48–51 h	29.5/30	3.78	[355]
3	*Bacillus lichenifor mis* TR7	Molasses	4	Whole molasses medium	pH 6, 30 °C, 150 rpm, and 48–51 h	28.5/10	3.30	[355]
4	*Bacillus subtilis* B20	Date molasses	8	Basal mineral salt medium	pH 6.5–7.5, 40 °C, 200 rpm and 30 h	25/NA	2.29	[353]
5	*Bacillus lichenifor mis* W16	Molasses	2	Minimal productio n media	pH 7.3-10, 40 °C, and 72 h	38.28/NA	0.52	[382]
6	*Bacillus subtilis* ANR 88	Molasses	4	Minimal medium	pH 7, 30 °C, and 36 h	27.9/NA	0.513	[383]
7	*Bacillus subtilis* ATCC 6633	Molasses	3	Minimal medium	pH 6.8-7.0, 45 °C, 200 rpm, and 48 h	30.48/NA	0.381	[384]
8	*Bacillus subtilis* B30	Date molasses	2	Minimal medium	pH 7, 40 °C, 160 rpm, and 72 h	26.63/33	0.3–0.5	[385]

6.4.4. Analysis of residual sugar

The cell-free supernatant was analysed by DNS method to estimate the residual sugar. The initial sugar concentration (at t = 0) was 24.7 ± 0.1 g L^{-1}, which decreased along with cell growth and biosurfactant production and the final residual sugar at day 10 was 4.10 ± 0.3 g L^{-1}, which

corresponded to the presence of un-fermentable sugar in molasses. This indicated 83.40 % utilization of the sugar to produce biosurfactant and biomass. The overall synthesis reaction is summarized in equation 6.7. The biomass and product (biosurfactant) yield were estimated. The biomass yield $Y_{x/s}$ was found to be 0.25 g g^{-1}, which agreed to the reported data of *Bacillus* strains [386]. The biosurfactant yield $Y_{p/s}$ was estimated to be 0.60 g g^{-1}, which suggested the improved biosurfactant production ability of the present strain. The q_p and q_s were obtained as 0.057 g of biosurfactant g^{-1} of biomass h^{-1} and 0.19 g of substrate g^{-1} biomass h^{-1}. In a study, *Bacillus subtilis* LAMI005 showed $Y_{p/s}$ of 0.11 g g^{-1} when provided with glycerol as C source [387]. Similarly, upon using simple glucose as substrate, *Bacillus subtilis* strains resulted in $Y_{P/S}$ in the range of 0.03−0.05 [386, 388]. Another strain, *Bacillus* sp. BMN 14 was used for the biosurfactant production using simple glucose and exhibited qp and qs as 0.00011 and 0.00027 g g^{-1} h^{-1}, respectively [389]. These findings indicated that the isolated bacterial culture in the present study resulted in the tremendous biomass growth and the remarkable biosurfactant production without using any other media except molasses.

$$Molasses(C_xH_yO_zN_a) \rightarrow Biomass(CH_{1.5}O_{0.5}N_{0.2}) + Biosurfactant(C_{53}H_{93}N_7O_{13}) \quad (6.7)$$

C balance between substrate utilization, biomass and biosurfactant production was performed to determine the fermentation efficiency. The molasses was considered to be sucrose ($C_{12}H_{22}O_{11}$, molecular weight (MW) of 342.3). The molecular structure of biomass (*Bacillus subtilis*) was assumed as $CH_{1.8}O_{0.5}N_{0.2}$ (MW of 24.6). As discussed in the next section, the produced biosurfactant was identified as surfactin ($C_{53}H_{93}N_7O_{13}$, MW of 1036). The substrate (sugar) amount was first utilized for the biomass production and the remaining substrate was considered for the biosurfactant as $C_{Sugar} = C_{Biomass} + C_{Biosurfactant}$. Based on the C-balance, the theoretical product (surfactin) concentration was estimated to be 9.98 g L^{-1}. The higher concentration of the experimental value

(12.34 g L^{-1}) of the biosurfactant than the theoretical one is presumably because of the presence of impurities and moisture in the crude biosurfactant. This confirmed the ~100 % fermentation efficiency and the complete utilization of molasses for the biomass and biosurfactant production.

In general, The hydrophilic head of surfactin contains a peptide chain while the hydrophobic tail is a chain of hydroxylated fatty acids of varying lengths and isoforms [390]. Thus, the biosynthesis of a lipopeptide comprises the production of (i) lipid and (ii) peptide. Further, surfactin synthetase enzymes catalyse the synthesis of surfactin [391].

6.4.5. Batch bioreactor study using sole molasses as nutrient

Figure 6.4 shows the profiles of biomass (*Bacillus subtilis* RSL2) growth and residual sugar during batch culture at previously optimized conditions of pH 6.6, temperature 41°C, and 5 % (w/v) of molasses [216]. The biomass had a short lag phase, an exponential phase up to 68 h, and a short stationary phase followed by the death phase within 96 h of incubation. The specific growth rate during the exponential phase in the batch bioreactor mode of operation was estimated to be 0.059 ± 0.015 h^{-1}, which was 2.5 times greater than the bacterial growth reported during shake-flask incubation [216] as listed in Table 6.4. An exponential reduction in the residual sugar concentration was observed during the exponential phase of culture growth and reached a constant minimum value at the end of the death phase (Figure 6.4). An approximate 90 % of molasses utilization was obtained during batch bioreactor, whereas only 83.4 % of utilization was previously reported during the shake-flask study [216]. A gradual reduction in the COD was also observed along with a decrease in residual sugar and biomass growth in the batch bioreactor (Figure 6.4). 73.4 % decrease in COD value was also obtained. The improved bacterial growth and molasses sugar utilization in the batch bioreactor

as compared to the shake-flask is a result of the enhanced/improved mass transfer in the bioreactor [216].

The supernatant was examined for the reduction in surface tension, which was found to be 25.68 ± 2.8 mN m^{-1}, signifying the production of biosurfactant by the bacteria. The production of biosurfactant was quantified after solvent extraction and lyophilization and estimated to be 13.7 g L^{-1}. The yields, $Y_{P/S}$ and $Y_{X/S}$ were calculated as 0.58 and 0.22 g g^{-1}, respectively, which were comparable to the shake-flask data (Table 6.4).

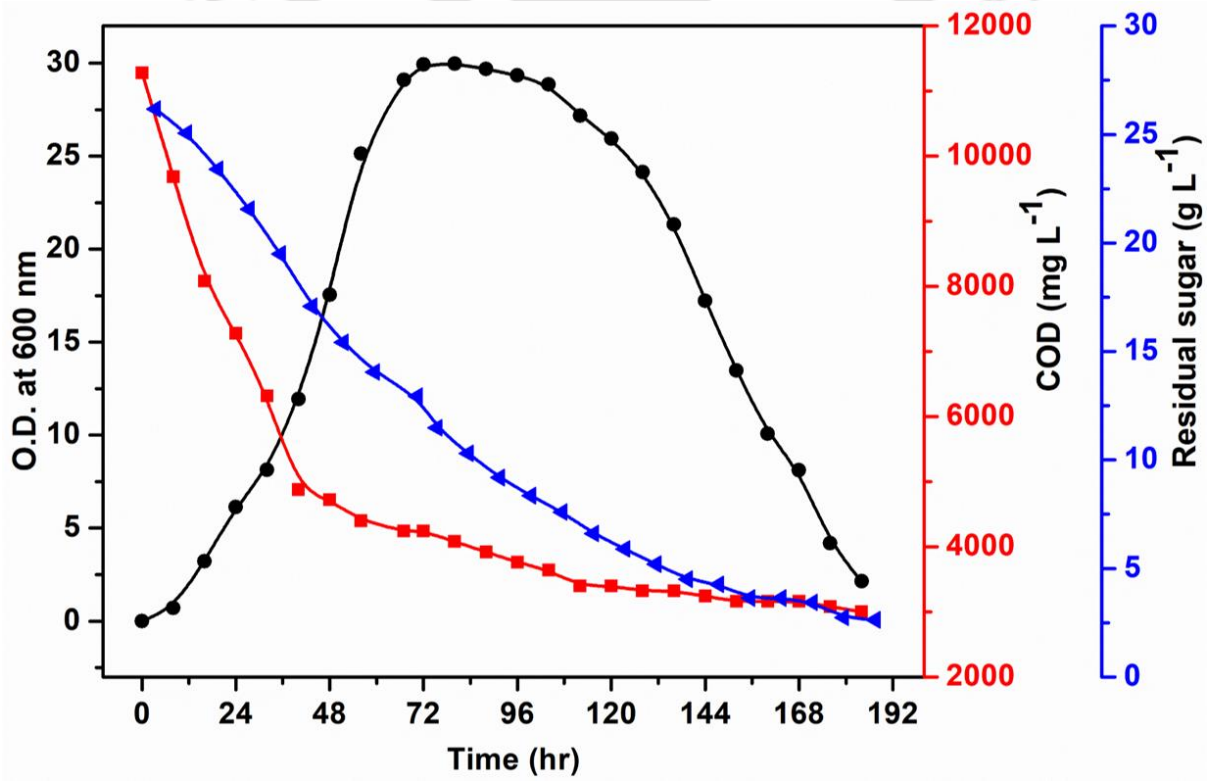

Fig. 6.4: Growth and sugar utilization ability of Bacillus subtilis RSL 2 in batch bioreactor study using 5 % (w/v) molasses as a sole nutrient source at pH 6.6 and temperature 41°C.

Table 6.4. Comparison of the ability of selected bacterial strains to utilize molasses as the sole nutrient source in 3 different growth modes.

Parameters	Shake-flask [216]	Batch bioreactor	Semicontinuous mode of bioreactor
Working volume (L)	0.25	1.50	13.00
Initial sugar (g L^{-1})	26	26	26
Sugar utilization (%)	83.4	90	98.3
Biosurfactant production (g L^{-1})	12.30	13.70	13.92
μ (h^{-1})	0.024	0.059	0.055
$Y_{P/S}$	0.57	0.58	0.97
$Y_{X/S}$	0.25	0.22	0.43

6.4.6. Semicontinuous operation of the bioreactor

In a fermentation process, the exponential phase mainly ceases either due to substrate limitation or product inhibition [392] and biomass enters a short stationary phase followed by the death phase (Figure 6.4). To extend the exponential phase, a semicontinuous mode of bioprocessing was explored. The semicontinuous process started with the batch mode at similar conditions pH 6.6, temperature 41°C, and 5 % (w/v) of molasses. The profiles of biomass growth, residual sugar and biosurfactant concentration are shown in Figure 6.5.

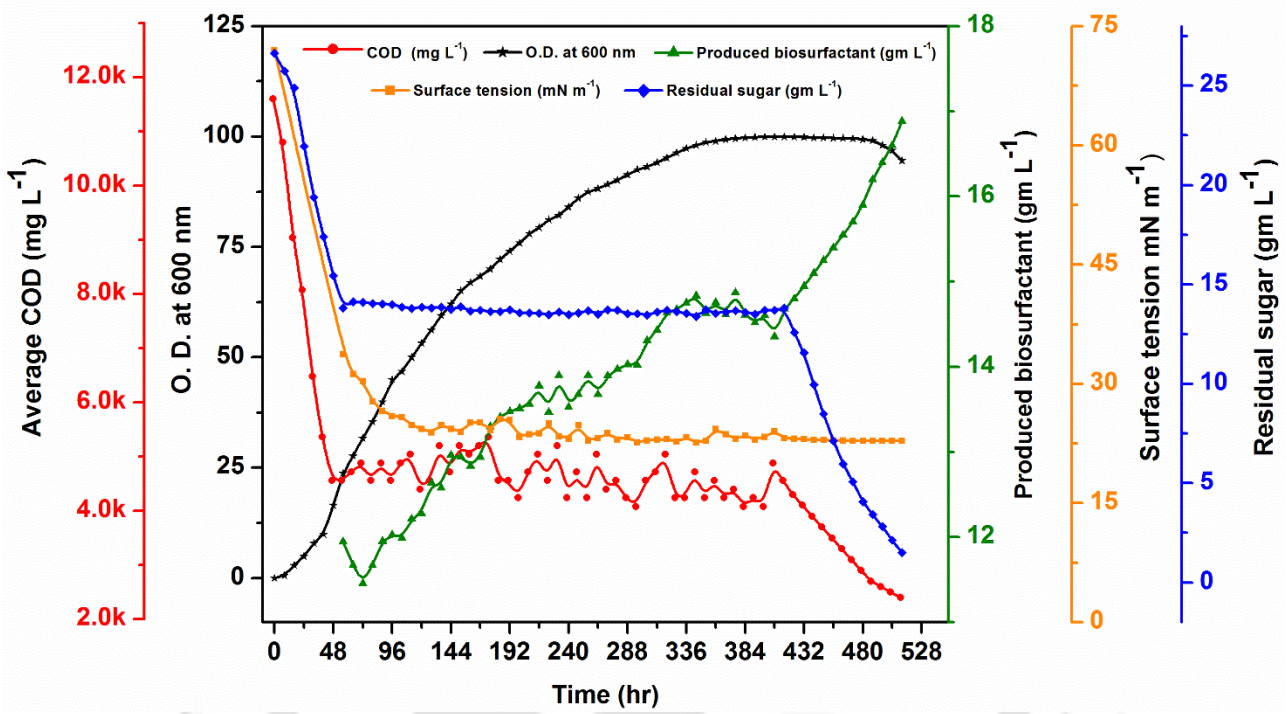

Fig. 6.5: Growth profile of *B.subtilis* RSL2 in a semicontinuous mode reactor with intermittent feeding of 14.05 g L^{-1} per 8 h of incubation.

It was observed that ~50 % of sugar was utilized within the exponential phase of bacterial growth and at the onset of the stationary phase within 64 h of incubation in the batch study (Figure 6.4). Thus residual was about 50 %. This indicated that the accumulation of biosurfactants in the culture media during the exponential phase affected biomass growth. From a batch study, it was found that the bacterial growth rate (μ) started declining with the increase in biosurfactant concentration > 10 g L^{-1} [216]. In the present study, the biosurfactant concentration was observed as 12 g L^{-1} at 64 h of incubation. Thus, to lower the biosurfactant concentration in the bioreactor, a fill-and-draw strategy was performed in the semicontinuous mode for maintaining the biosurfactant concentration of 10 g L^{-1} within the bioreactor. The rate of biosurfactant production up to 64 h was observed to be 0.2 g L^{-1} h^{-1}. Accordingly, 250 mL of culture broth was harvested every 8 h and replenished with sterile molasses of a fixed concentration to maintain (i) biosurfactant concentration of 10 g L^{-1} and (ii)

constant working volume of the bioreactor as 1.5 L. Similarly, the rate of sugar utilization rate ($\Delta S/\Delta t$) during the exponential phase was obtained as 0.17 g L^{-1} h^{-1} and the residual sugar of 14 g L^{-1} was present at 56 h. Hence, an intermittent additional feed of 1.4 g L^{-1} of sugar was added every 8 h i.e. at the rate of 0.17 g L^{-1} h^{-1} to stimulate bacterial growth without substrate deprivation in the semicontinuous mode of bioreactor study.

This fill-and-draw strategy enabled them to extend the stationary phase in the semicontinuous mode as compared to batch operation due to replenishing the nutrients and harvesting product (biosurfactant) from the bioreactor, as shown in Figure 6.5. The strategy extended the exponential phase up to 432 h (18 days). During this period, a constant sugar concentration of 14 g L^{-1} was maintained (Figure 6.5) due to intermitted feeding. This indicated the balance between the rates of utilization and the supply of sugar.

Figure 6.5 evidenced that the growth rate was improved in the semicontinuous feeding mode of bioreactor operation. The specific growth rate 'μ' at the beginning of semicontinuous mode (i.e. batch operation) was calculated as 0.055 h^{-1}, which was comparable to the batch study (Table 6.4). Further, μ values were calculated during the batch and semicontinuous studies at different time intervals. A constant value of μ was observed during the fill-and-draw duration as shown in Figure 6.6, which corresponded to the semicontinuous or the constant volume fed-batch modes of operation [393]. While in the case of the batch study, a gradual decrease in the μ values was observed due to the short stationary phase followed by the death phase (Figures 6.4 and 6.6).

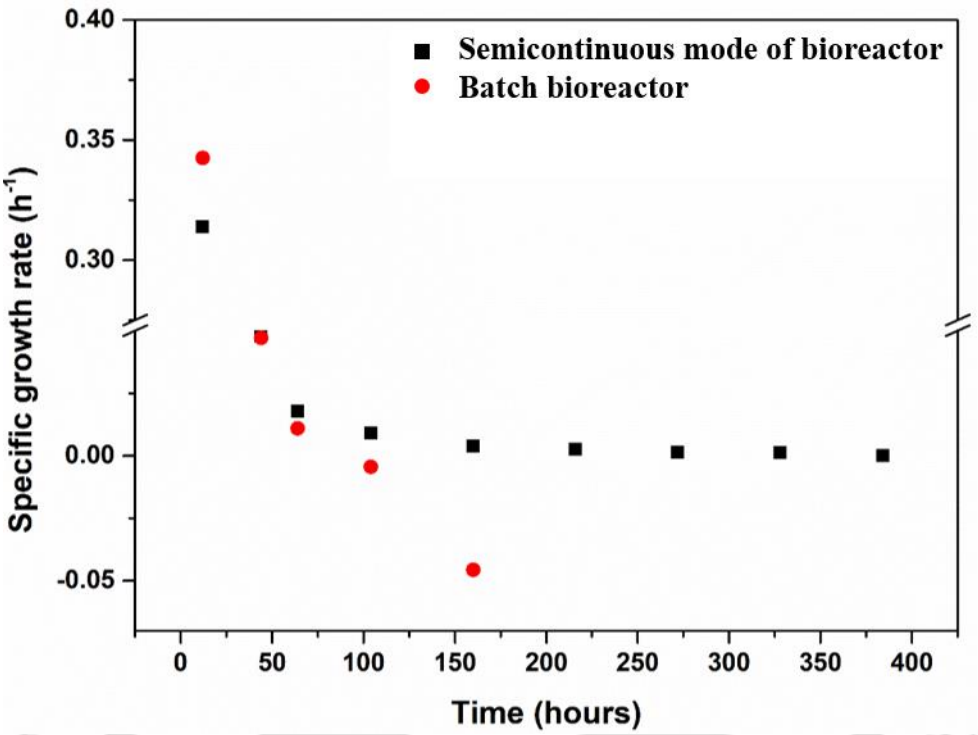

Fig. 6.6: Change in bacterial specific growth rate (μ) with time in the batch and semicontinuous mode of bioreactor studies.

During the extended semicontinuous mode of operation, a total of 13 L of media was fed comparatively 1.5 L of the batch reactor. The overall sugar utilization was 98.3 %, which was better as compared to the batch study (Table 6.4). The biomass yield ($Y_{X/S}$) was improved to 0.43 g g^{-1}. Similarly, the product (biosurfactant) yield ($Y_{P/S}$) was enhanced to 0.97 g g^{-1} i.e. more than 1.5 folds higher yield than batch culture. This also indicated the growth associated with biosurfactant production [216, 366]. The improved yield of biosurfactants was reported in previous studies using a fill-and-draw strategy. Joy *et al.* utilized lignocellulosic hydrolysate for the cost-effective production of rhamnolipid. The enhanced production of rhamnolipid was achieved using a fill-and-draw strategy as compared to a batch study [394]. Chen *et al.* also performed a similar experiment to enhance the

production of rhamnolipid. A pH-stat fed-batch culture with a fill-and-draw strategy resulted in an extended operation period of 500 h and improved rhamnolipid concentration of 9.4 g L^{-1} [395].

The mass balance of C species was done to estimate the theoretical concentration of the biosurfactant using the equation (6.7).

$$\text{Molasses } (C_{12}H_{22}O_{11}) \longrightarrow \text{Biomass } (CH_{1.8}O_{0.5}N_{0.2}) + \text{Biosurfactant } (C_{53}H_{93}N_7O_{13}) \quad (6.7)$$

The molecular weights of molasses, biomass and biosurfactant are 342.3, 24.6 and 1036, respectively. The data of sugar and biomass listed in Table 6.4 were used for the calculation of the product yield. On the basis of the C-balance, the theoretical concentrations of biosurfactant were estimated to be 12.23 and13.08 g L^{-1} in batch and semicontinuous bioreactors, respectively. The experimental values were found to be slightly higher than the theoretical values as listed in Table 6.4 presumably due to the presence of moisture/impurities in the crude biosurfactant.

The synthesis of biosurfactant was corroborated by the decrease in the surface tension as shown in Figure 6.5. The production of biosurfactants and reduction of surface tension are inversely related. In general, an increase in biosurfactant concentration results in a decrease in surface tension. Thus, the reduced surface tension is a better indicator of biosurfactant production. In optimization study, the surface tension was used as a response during the optimization of biosurfactant production [366]. In this study, the surface tension value was reduced to 22.80 mN m^{-1}. Comparative performance of various studies utilizing molasses for the production of biosurfactants is reported in Table 6.5, which highlights the significant yield of biosurfactants and reduction in the surface tension by utilizing molasses as a sole substrate in the present study.

The COD value was also monitored during the fermentation, which followed a similar profile as the residual sugar. At the end of the bioreactor operation, the initial COD of 11600 ± 200 mg L^{-1} declined

to 2400 ± 100 mg L^{-1} (i.e. 79.3 % of reduction). The COD value was found to be 50-80 times lower than that of distillery spent wash with COD of 110000−190000 mg L^{-1} [5, 18]. Overall, the semicontinuous mode of the bioreactor resulted in greater utilization of molasses (sugar) and biosurfactant yield than the batch bioreactor. In addition, downtime of bioreactor also reduces due to extended period of operation in semicontinuous mode. These findings indicate that the semicontinuous mode can be further scaled up.

Table 6.5: Various studies utilizing molasses for the production of biosurfactants

Culture media	Conc. of molasses	Micro-organism	Operation mode	Working volume (mL)	Experimental Conditions	S (mN m^{-1})	CMC (mg L^{-1})	B.S. conc. (g L^{-1})	Ref.
Only sugarcane molasses	4 % (w/v)	*B. licheniformis* TR7	Shake flask study	50	30°C, pH 6 150 rpm, 48 h	28.5	10	3.30	[355]
Only sugarcane molasses	4 % (w/v)	*B. subtilis* SA9	Shake flask study	50	30 °C, pH 6 150 rpm, 48 h	29.5	30	3.78	[355]
Only sugarcane molasses	7 % (v/v)	*P. aeruginosa* GS3	Shake flask study	50	30 °C, pH 7 180 rpm, 48 h	-	-	0.24	[396]
Basal mineral salt + Date molasses	8 % (w/v)	*B. subtilis* B20	Shake flask study	50	40 °C, pH 6.5 200 rpm, 30 h	25	-	2.29	[397]
Minimal production media + Sugarcane molasses	2 % (v/v)	*B. licheniformis* W16	Shake flask study	50	40 °C, pH 7.3 72 h	38.28	-	0.52	[382]
Minimal media + Sugarcane molasses	4 % (v/v)	*B. subtilis* ANR 88	-	-	30 °C, pH 7 160 rpm, 36 h	27.9	-	0.51	[383]
Minimal media + Date molasses	2 % (v/v)	*B. subtilis* B30	Shake flask study	50	40 °C, pH 7 160 rpm, 72 h	26.63	33	0.50	[385]
Basal mineral salt + Sugarcane molasses	6 % (w/v)	*L. paracasei* subsp. *tolerans* N2	Shake flask study	1000	33 °C, pH 6.7	37.85	-	2.70	[398]
Minimal media + Sugarcane molasses	2% (v/v)	*B. subtilis* MTCC 2423	Shake flask study	250	45°C, 200 rpm pH 6.8, 96 h	29		1.0	[399]
Yeast mold agar + Sugarcane molasses	2.5 % (v/v)	*Candida tropicalis* UCP0996	Shake flask study	500	28 °C, pH 5.5 200 rpm, 120 h	30.4	60	4.11	[400]
Only sugarcane molasses	5 % (w/v)	*B. subtilis* RSL-2	Shake flask study	100	41 °C, pH 6.6 180 rpm, 120 h	24.09	80	12.34	[216]
Only sugarcane molasses	5 % (w/v)	*B. subtilis* RSL-2	Batch reactor study	1500	41 °C, pH 6.6 200 rpm, 96 h	25.68	70	13.7	Present study
Only sugarcane molasses	5 % (w/v)	*B. subtilis* RSL-2	Semicontinuous reactor study	13000	41 °C, pH 6.6, 200 rpm, 504 h	22.80	70	13.92	Present study

6.4.7. Analysis of functional groups of crude biosurfactant using FTIR and NMR

The secondary structure of produced biosurfactant was characterized by resolving functional groups using FTIR and NMR analysis (Figure 6.7). The peak at the 2926 cm^{-1} corresponded to the presence of stretching of symmetric aliphatic (CH, CH2 and CH3) chains, and the peak position at the 3414 cm^{-1} represents the presence of stretching bending of –OH groups. The peaks position at 634 cm^{-1} and 779 cm^{-1} correspond to the existence of aromatic CH_2 bending groups. The peak positions of 1146 cm^{-1} and 1240 cm^{-1} represented the presence of alkoxy groups. Similarly, the presence of sharp peaks at the points of 1390 cm^{-1}, 1650 $cm^{-1,}$ and 1726 cm^{-1} represented the presence of stretching of alkane groups (C-H) and amide groups (C=O), respectively. Hence, the produced biosurfactant was obtained as lipopeptide in nature [216, 366] [401]. Similarly, the ^{1}H-NMR spectrum of produced biosurfactant was also analysed to support the function groups identified by the FTIR analysis. The broad peak at the position of 4.75 ppm corresponded to the presence of the solvent D_2O. The peaks at the position of 2.06 and 2.1 ppm corresponded for the presence of alpha carbonyl substrate. The peaks position between 0.98 to 1.17 ppm confirms the presence of $–CH_2C$-O group. The peak at the position of 3.82 confirms the appearance of CH_2 group. These identified groups are reported in various literature for a lipopeptide biosurfactant [402, 403].

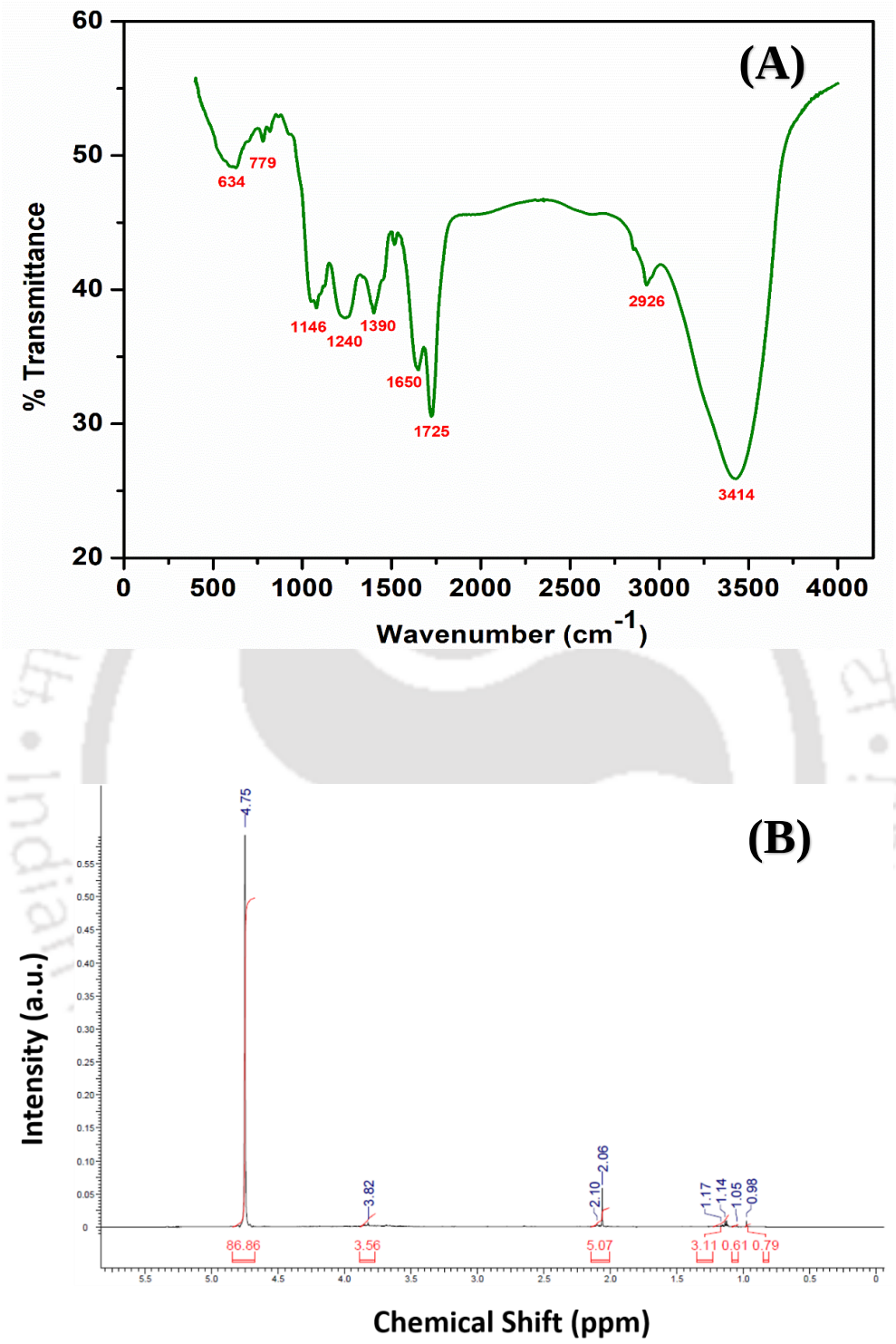

Fig. 6.7: Functional group analysis of the produced biosurfactant by (A) FTIR (B) ^{1}H NMR.

6.4.8. Estimation of molecular weight by using LCMS and MALDI-TOF

The molecular weight of the produced biosurfactant was investigated using LCMS and MALDI-TOF analyses (Figure 6.8 (A and B)). From the LCMS spectrum, the presence of peaks (m/z) at 1086, 1072, 1058, 1044 and 1030 represented $[M + Na]^+$ of C-17 to 13 acyl chains of the surfactin. Similarly, other characteristic peaks (m/z) at 998, 959 and 804 also corresponded to aliphatic surfactin product ions $[M + Na\text{-}H2O]^+$, $[M + Na\text{-}Leu]^+$, $[M + Na\text{-}Leu\text{-}Leu]^+$, respectively. These peaks were in the agreement with the reported peaks in the literature [404, 405]. From MALDI-TOF also, similar results were obtained. Ions at m/z 1007, 1035, and 1022 were hypothesized to be C13$[M + H]^+$, C13 $[M + Na]^+$, and C14 $[M + H]^+$ surfactin, respectively, as also reported in the literature [406-408]. The peak at m/z value of 1144 represented the presence of high molecular weight Iturin A lipopeptide C18$[M + K]^+$ in small amount within the crude biosurfactant mixture [409]. The presence of fragmentation peaks at 895, 918, 695, and 673 represented the disintegration of surfactin C13$[M + H]^+$,[410], C13 $[M + Na]^+$, and C14 $[M + H]^+$ ions respectively, as also reported previously [357, 406, 411]. Therefore, the crude biosurfactant was identified as a heavy molecular weight surfactin of carbon chain C18-C13.

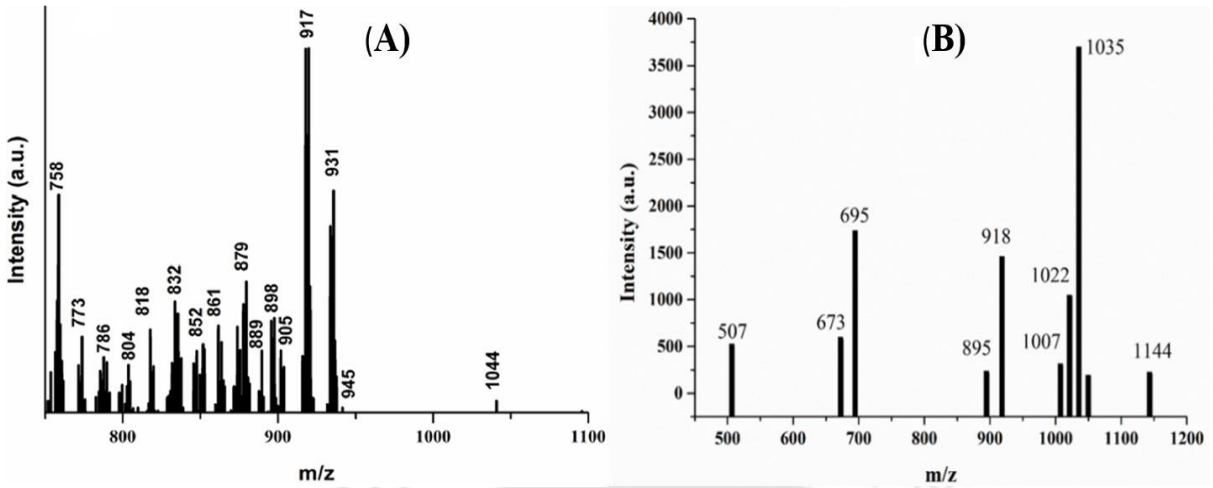

Fig. 6.8: (A) LC–MS and (B) MALDI TOF analysis for the produced biosurfactant.

6.4.9. Determination of CMC of crude biosurfactant

The CMC value is defined as the minimum concentration of biosurfactant at which the optimum reduction of surface tension is achieved and further no decrease in surface tension is observed with an increase in the concentration of biosurfactant. The surface tension was monitored at biosurfactant concentrations ranging from 1 to 1000 mg L^{-1} as shown in Figure 6.9. The surface tension reduction of pure water decreased from 72 mN m^{-1} to the minimum value of 22.80 ± 0.08 mN m^{-1} i.e. 68 % reduction at the minimal concentration of 70 mg L^{-1} of the produced biosurfactant. Further, increasing the biosurfactant concentration did not affect surface tension. Thus, the CMC value of the produced biosurfactant was estimated to be 70 mg L^{-1}. This value was found to be comparable to other reported data [216, 366, 412].

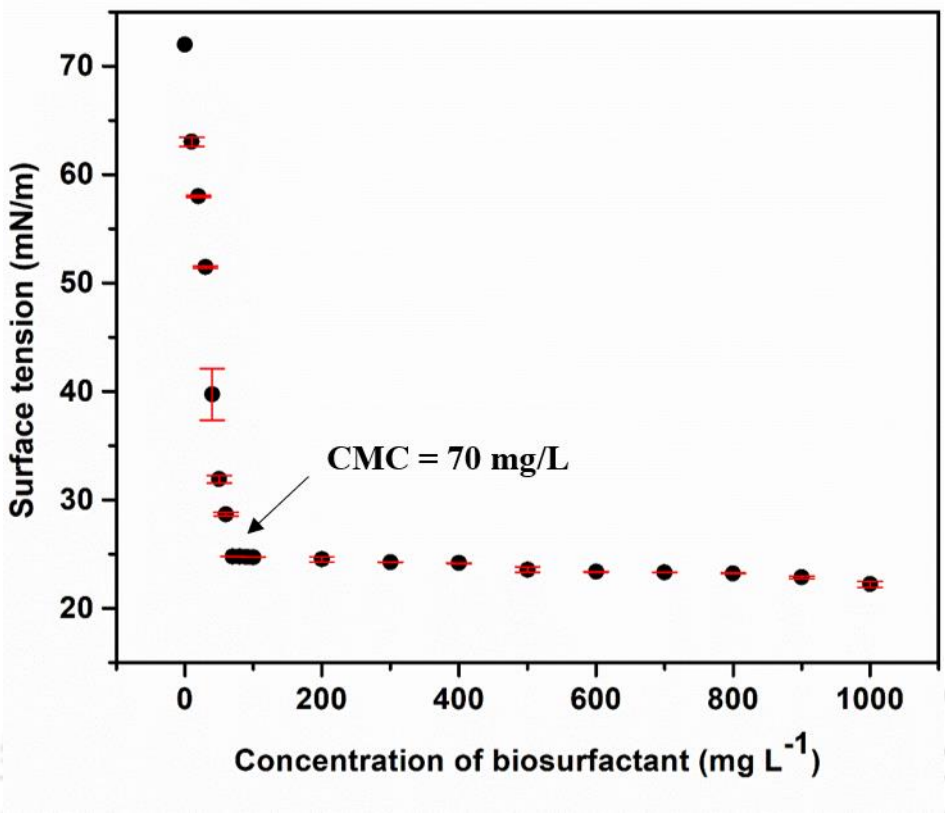

Fig. 6.9: The reduction in surface tension with increased biosurfactant shows the CMC value for crude biosurfactant.

6.4.10. Oil displacement test and emulsification activity

The oil displacement test was performed to check the produced biosurfactant's surface activity and wetting property on oil. The diameter of displaced oil is directly proportional to the surface activity. A clear zone was observed after immediate contact with biosurfactant concentration. The larger diameter of the formed clear zone indicates vigorous biosurfactant surface activity. The experiment was carried out at a CMC concentration (0.07 g L^{-1}). The average diameter of the formed clear zone was found to be 2.1±1 cm (Figure 6.10 (A)), which is relatively better than the reported data. The control experiment was also performed with distilled water, and no clear zone was observed. The

obtained diameter of the clear zone indicates the produced biosurfactant as an excellent surface-active agent.

The surface activity potential screening of produced biosurfactant was also performed by emulsification index analysis. This is the most widely used method for the screening of biosurfactants. The biosurfactant production rate leads to an increase in cell development and biomass concentration in the bioreactor. The produced biosurfactant showed the highest emulsification activity against Paraffin oil, followed by Toluene and hexadecane. The paraffin oil showed 68.75 % emulsification activity, while 37.5 % and 12.5 % emulsification activity were observed with Toluene and hexadecane (Figure 6.10 (B)). The remaining organic solvents were not showing any emulsification activity with produced biosurfactant.

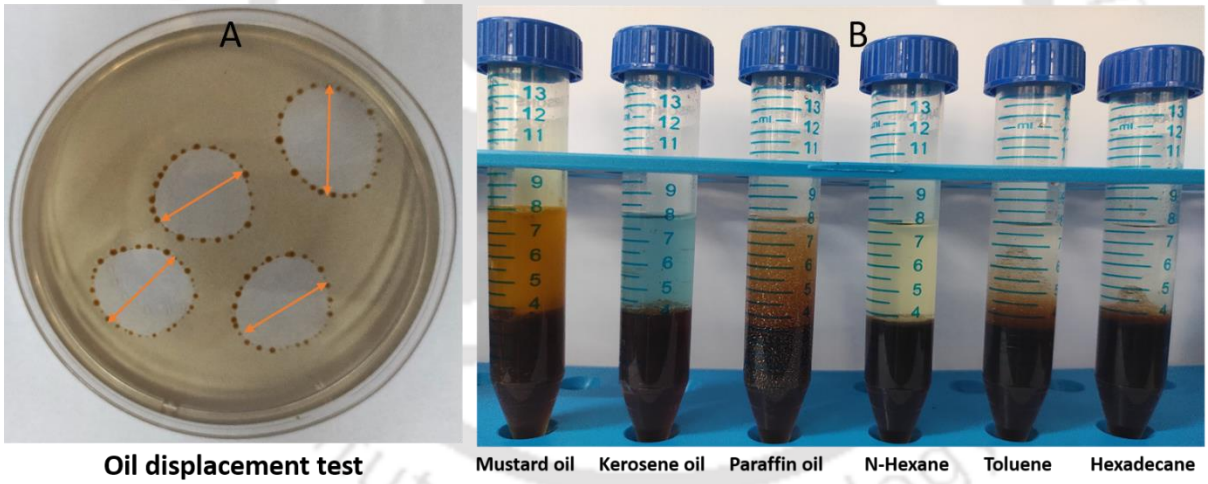

Fig. 6.10: (A) Oil displacement and (B) Emulsification activity of produced biosurfactant.

6.4.11. Colloidal stability and hydrodynamic diameter measurement

The colloidal stability of produced biosurfactant was characterized by measuring the mean zeta potential of produced biosurfactant. The zeta potential of produced biosurfactant was measured at different pH ranging from 3 to 11 act CMC concentration (70 mg L^{-1}). The produced biosurfactant resulted in a mean negative charge of -32.73 ± 0.46 mV at the neutral pH. The negative charge (-ve) of produced biosurfactant strongly demonstrates the anionic nature of the produced biosurfactant (surfactin). A zeta potential ≥ ± 20 mV reflects excellent surface activity and colloidal stability (Figure 6.11) [376]. The hydrodynamic diameter of produced biosurfactant was also estimated at CMC concentration, and it was found to be 148 ± 26 nm, which indicated inter-micelle interactions. It was reported that the formation of inter-micelle H-bonding formed bigger aggregates leading to the increased particle diameter [413]. The colloidal stability and smaller hydrodynamic diameter of produced biosurfactant endorsed its aptness for various applications.

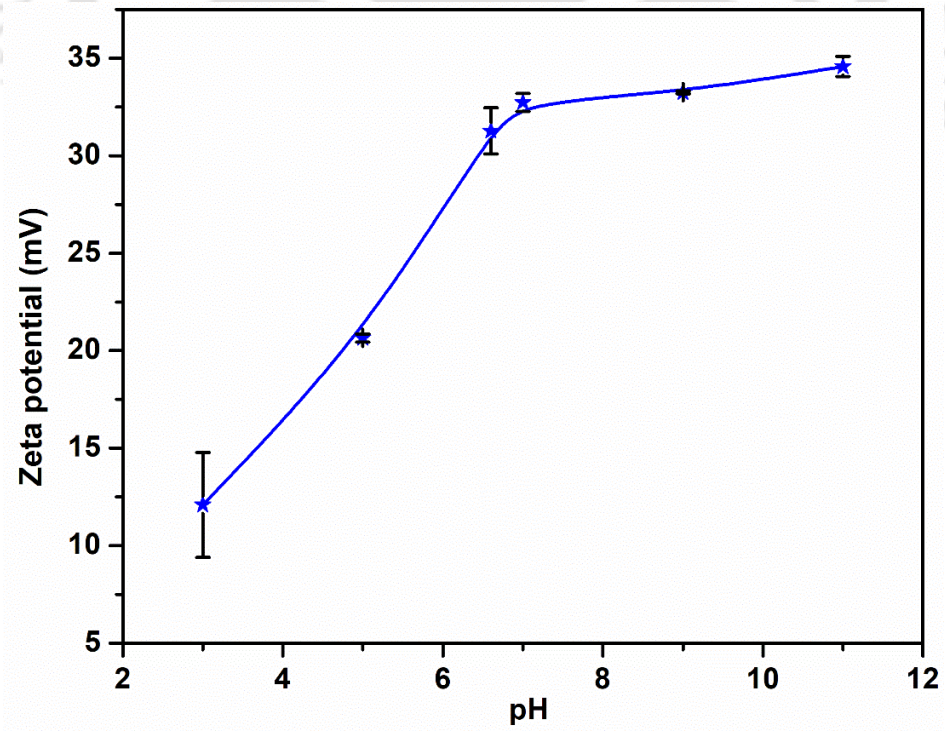

Fig. 6.11: The surface charge of produced biosurfactant at various pH values.

6.4.12. Thermal stability of produced biosurfactant

The thermostability of produced biosurfactant plays an important role in various industrial and environmental applications. The thermal behavior of produced biosurfactant was analyzed by Differential Scanning Calorimetry/ Thermo Gravimetric (DSC/TG). The thermostability was analyzed in the range of temperature 0 to 1000 °C with an increment of 10 °C/min. The thermal behavior of produced biosurfactant can be classified in four-phase as shown in Figure 6.12. The first phase was observed between the temperature 0-100 °C, indicating the slightly unstable (≤ 10 %) due to the moisture content. The second phase was between 100-450 °C indicating the exponential loss of weight (about 60 %). The third phase between the temperature range of 450 °C to 750 °C showing the excellent thermostability of produced biosurfactant and no substantial weight loss (≤ 2%) proved that the produced biosurfactant could be applied for extreme applications such as enhanced oil recovery and remediation of polluted soil. The last phase was from 750-1000 °C, in which exponential weight loss was observed due to thermal degradation [414].

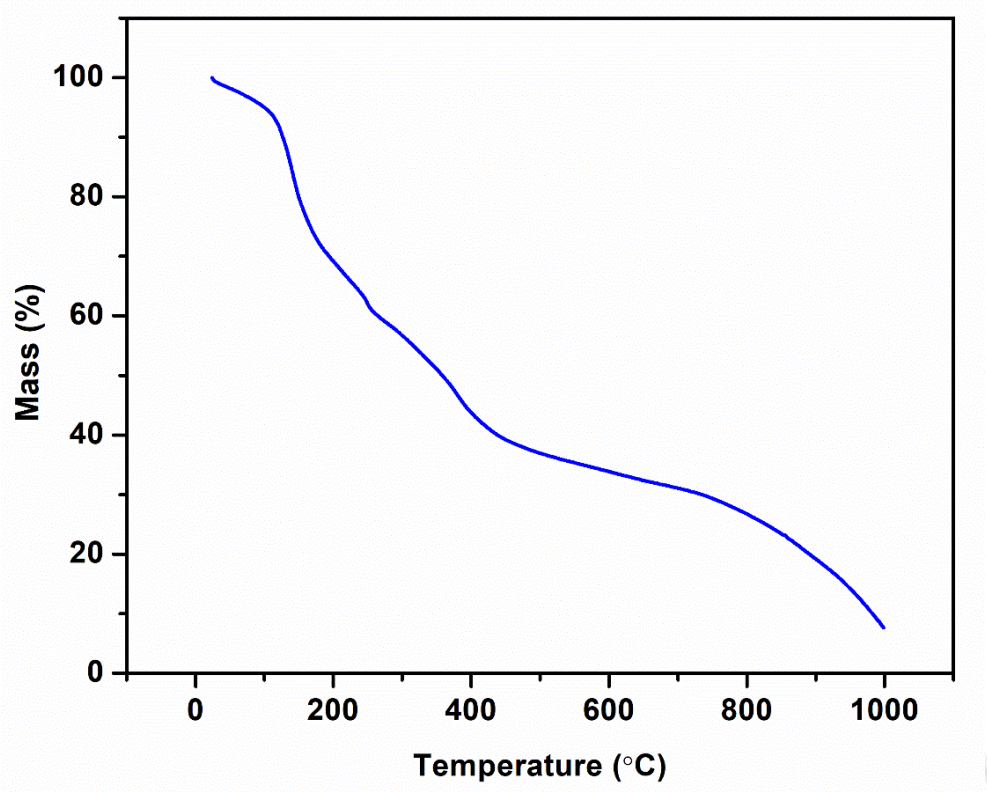

Fig. 6.12: Thermostability analysis of produced biosurfactant using TGA.

6.4.13. Determination of wettability alteration

The amphiphilic nature of biosurfactants is related to wetting behaviour. The wetting property of the produced biosurfactants signifies the alternation in interfacial tension as described by Young's equation [180]. The contact angles of media and produced biosurfactant on a hydrophobic paraffin film (model surface) were measured to analyze the wetting property. The drop shape images are shown in Figure 6.13. The contact angle of un-incubated media containing molasses was found to be 92 ± 1˚, which indicated the hydrophobic paraffin surface. However, the contact angles of cell-free supernatant and the biosurfactant (at CMC) were reduced to be 41 ± 1˚ and 38 ± 1˚, respectively due to a decrease in the liquid-vapor and solid-liquid interfacial tensions. Further, the adsorption of

biosurfactants on the surface also lowers the surface tension of the solid [363]. The hydrophobic nature influences the adhesion on various surfaces such as oil-water, water-air, and solid-surfaces adhesion. This property of the produced biosurfactant is required for tuning the interfacial interactions for various applications like enhanced oil recovery and remediation of crude oil on contaminated sites.

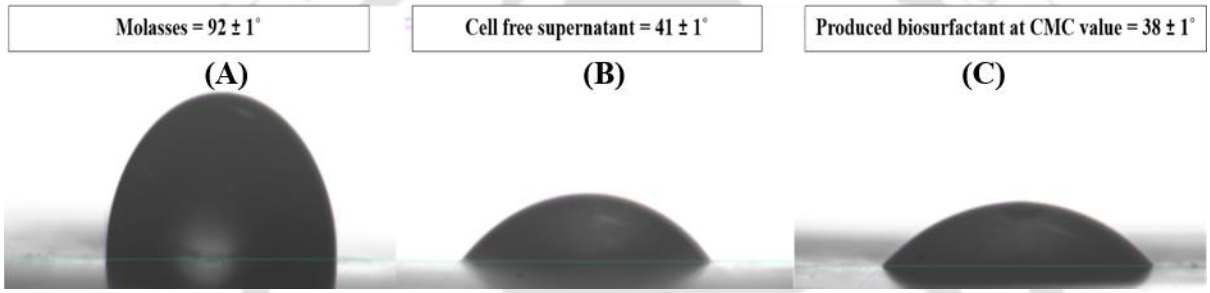

Fig. 6.13: Analysis of wettability alteration by contact angle analysis of (A) Molasses media (B) Cell-free supernatant and (C) produced biosurfactant at CMC value.

6.5. Conclusions

In the present study, sugar cane molasses was explored as a cheap and sole nutrient source (media) for the production of biosurfactant. The RSM-CCD was applied for optimization of experimental parameters (pH, temperature and concentration of molasses) in terms of maximum biosurfactant concentration and minimum ST. The ability of biosurfactant-producing bacteria *B. subtilis* RSL-2 to thrive on a high concentration of molasses (5 %, v/v) as the sole nutrient source was explored using a bioreactor system. In the shake-flask study, the bacteria *Bacillus subtilis* RSL-2 showed

exceptionally high biosurfactant production ability of 12.34 ± 0.1 g L^{-1}. The bacteria showed improved biosurfactant production (13.7 g L^{-1}) and molasses utilization ability (~90 %) in the bioreactor system compared to the shake flask study. To further enhance the molasses biodegradation ability of selected strain, a sequential fed-batch bioreactor study was operated under similar reaction conditions with slight improvisations. Further, the exponential phase got extended up to 18 days by employing a semicontinuous mode of operation. The sugar utilization ability was improved to > 98 % along with 13.92 g L^{-1} of biosurfactant production. The semicontinuous operation for 21 days and a total of 13 L of media was fed as compared to 1.5 L of working volume in the batch reactor. The biosurfactant yield was enhanced by 1.5 times and was found to be 0.97 g g^{-1}. These results demonstrate the potential applicability of *B. subtilis* RSL2 in high biosurfactant production using a semicontinuous mode of operation. The produced biosurfactant was characterized as high molecular weight lipopeptide with characteristically high stability at a broad range of pH and temperature. The biosurfactant showed excellent surface properties in terms of lower ST (24.09 ± 0.11 mN m^{-1}), higher thermostability (160 °C), low CMC value (0.07 g L^{-1}), negative zeta potential (−-32.73 ± 0.46 mV), high emulsification and oil displacement activity. The key finding of this study is the enhanced biosurfactant concentration by many folds using only molasses. These results illustrate the potential applicability of *B. subtilis* RSL-2 in distillery wastewater treatment and high biosurfactant production using a sequential fed-batch mode of operation. These properties of the biosurfactant endorsed its applicability in the medicinal, environmental and food industry applications.

Chapter 7

Overall conclusion and future works

7.1. Overall conclusion

In this adsorption study, the amine-modified *Phyllanthus emblica* leaf powder, formed by SAMs, was explored for melanoidin removal as a cheap, effective and eco-friendly adsorbent. The RSM-CCD was applied to optimize experimental parameters (temperature, pH and adsorbent doses). 2.5 folds enhance the maximum adsorption capacity of the novel adsorbent as compared to unmodified PELP. The adsorption process was described as spontaneous and exothermic. The adsorption mechanism was explained through complexation and electrostatic interactions. Overall the modified PELP can be suggested as a cheap, effective and environment-friendly adsorbent for melanoidin removal in the distilleries.

Similarly, the degradation efficiency at the optimized condition for the photo-Fenton process and photo-Fenton-like catalyst were investigated in real spent wash samples. It was found that the optimized photo-Fenton condition is effectively removing the color (99 ± 1 %) from 5 % v/v real spentwash sample while the FZO sample was effectively removing the 84 ± 1 % of real spentwash sample in a 120 min contact under UV light. Furthermore, the degradation of melanoidin pigments showed efficient colour removal by synthesizing WO_3 nanoparticles at optimized conditions. Effectively removing the colour (73 ± 2 %) from 5 % v/v real spentwash was achieved under visible light illumination. The synthesized nanoparticle was showing reusability up to 8th consecutive cycles, suggested the good stability and efficiency of WO_3. Overall the optimized photo-Fenton condition, Fenton-like catalyst and synthesized WO_3 nanoparticle can be recommended as suitable applications

for melanoidin removal. It can be applied on an industrial scale in distilleries as cheap, effective and environment friendly.

Simultaneously the molasses was explored as a low-cost substrate for the alternative metabolites like biosurfactant for various medicinal, environmental and food applications. Additionally, the batch and fill and draw strategy were investigated for optimum biodegradation of molasses to maximize the production of metabolites (biosurfactant). The produced biosurfactant exhibited excellent CMC value, surface activity, wettability, and colloidal and thermal stability. These characteristics propose the potential applications of produced biosurfactants in various bioremediation and biotechnological sectors. Hence, the obtained biosurfactant holds great potential for diverse environmental remediation, medicinal and material science applications.

7.2. Future Scope

Presently, the sugar industry has occupied a very strong place worldwide, including India. The co-operative sugar factories play a vital role in the rural economy; most distilleries are planted in rural areas. The government strategies on pollution control and environmental management are becoming more and more strict. The government forces distilleries to look for more effective and eco-friendly treatment technologies. The use of such advanced technologies would be not only cost-effective but also be beneficial to the environment. In 2003, the Central Pollution Control board (CPCB) restricted distilleries to achieve zero discharge in the environment. Therefore, distillery wastewater requires extensive treatment to meet the stipulated environmental norms. Based on the existing research gaps, could be focused and fulfilled by considering the following future scopes.

7.2.1. The reaction mechanism of melanoidin breakdown by the physiochemical as well as a biological process is still unknown

Melanoidins are challenging to define because they appear in a variety of sizes and have varying chemical structures depending on the kind of sugar and amino acid involved in the reaction. The elemental composition, structure, and molecular weight of the melanoidins are heavily influenced by reaction circumstances such as the Temp, pH, concentration, duration of the reaction etc. In order to understand the degradation pathway of melanoidin involved by the various physicochemical and biological processes could be focused in the future. The metabolites involved in degradation and intermediate products will strongly depend on multiple factors such as initial concentration, temperature, time, pH of the solution, etc. So it is a very challenging and interesting task to optimize the breakdown pathway.

7.2.2. An integrated approach is required to enhance the efficiency of the melanoidin removal

One of the most challenging aspects of melanoidin degradation is the low yield of treatment efficiencies. Numerous physiochemical and biological experiments have been carried out separately for melanoidin degradation. Yet the treatment efficiencies of these approaches are not validating at a significantly higher concentration of the melanoidin solution. In order to overcome this issue, the use of multiple techniques are required that might result in degradation efficiency. In this regard, the combined approach such as chemical pretreatment followed by biological treatment, Integration of two or more approaches could be examined in the future to enhance the efficiency of melanoidin removal.

7.2.3. Application of genetically modified microorganisms

Biological treatment is not much explored due to its very slow degradation compared to other physiochemical methods or applications. In general, microbial treatment of melanoidin containing wastewater is an eco-friendly and cost-effective approach and the best alternate option of the chemical processes. However, only certain organisms have been identified that have the ability to break down melanoidin and still those are not suitable for melanoidin treatment after a certain limit. In this regard, genetically modified microbial organisms can also be applied for treatment. It is essential to find extreme microbial strains that can be applied to achieve a high yield of melanoidin degradation rate.

7.2.4. Field treatment application can be performed on the contaminated site to investigate real impacts

As discussed initially, the distilleries generate a very large amount of melanoidin containing wastewater. The laboratory-scale treatment approaches are not efficient enough to treat a large volume of melanoidin containing wastewater. Also, it is impossible to expect the same outcomes in the field treatment as in the lab because several environmental factors such as temperature, pH, concentration, light conditions vary in actual conditions. Hence, the melanoidin degradation efficiency will be influenced. So it is important to investigate the real impacts of these methods on melanoidin degradation for field treatment applications. Also, the scale-up studies of various approaches are required to enhance the treatment efficiencies in large volumes.

7.2.5. Production of alternative metabolites using raw materials to reduce the spentwash generation

Microbial biodegradation is the eco-friendliest and economic effluent remediation tool for controlling environmental pollutants. Various species of fungi and bacteria such as *Aspergillus, Fusarium, Stenotrophomonas, Bjerkandera,* and *Bacillus* have been reported to utilize these organometallic compounds as a source of energy for their metabolic activity. In this direction, molasses are low-cost and renewable substrates produced as a bulk by-product of sugarcane industries. Its nutritional composition, enriched in carbohydrates, vitamins and minerals, makes it highly suitable for microbial consumption without any pre-treatment expenditures. In this prospects, molasses/melanoidin-containing wastewater can be applied as a high nutrient source to cultivate various microorganisms. These micro-organisms can be incorporated with these nutrients. Their metabolic activities can produce value-added products such as volatile fatty acids (VFAs), polyphenolic compounds, biosurfactants and polysaccharides, etc.

7.2.6. Cost analysis

The economy is the major bottleneck in the application of various techniques applied for melanoidin degradation as well as the production of value-added substrates. Cost analysis could be investigated with different strategies that would be very helpful to understand the feasibility of these techniques in industrial-based field applications.

Appendices

Appendix Chapter 4

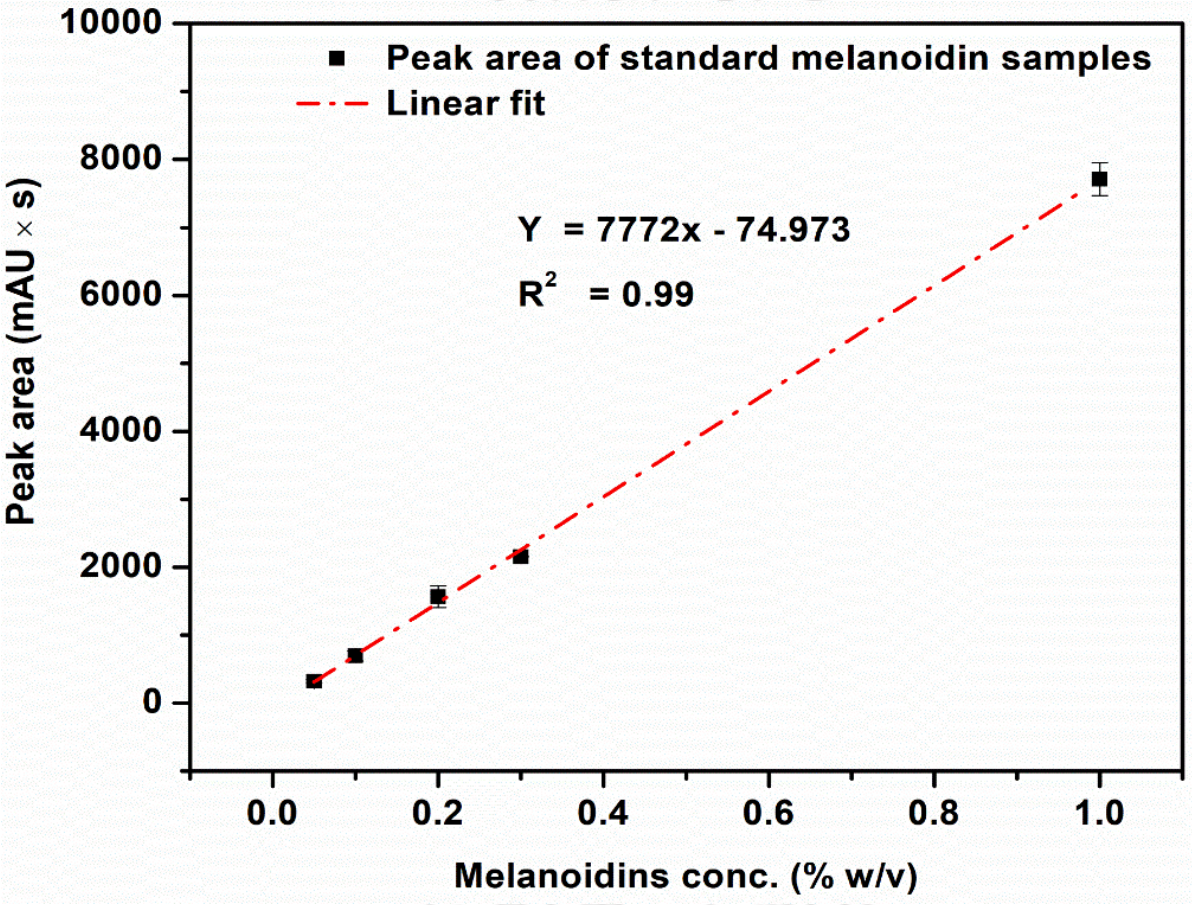

Fig. S4 (A): Standard curve of melanoidin.

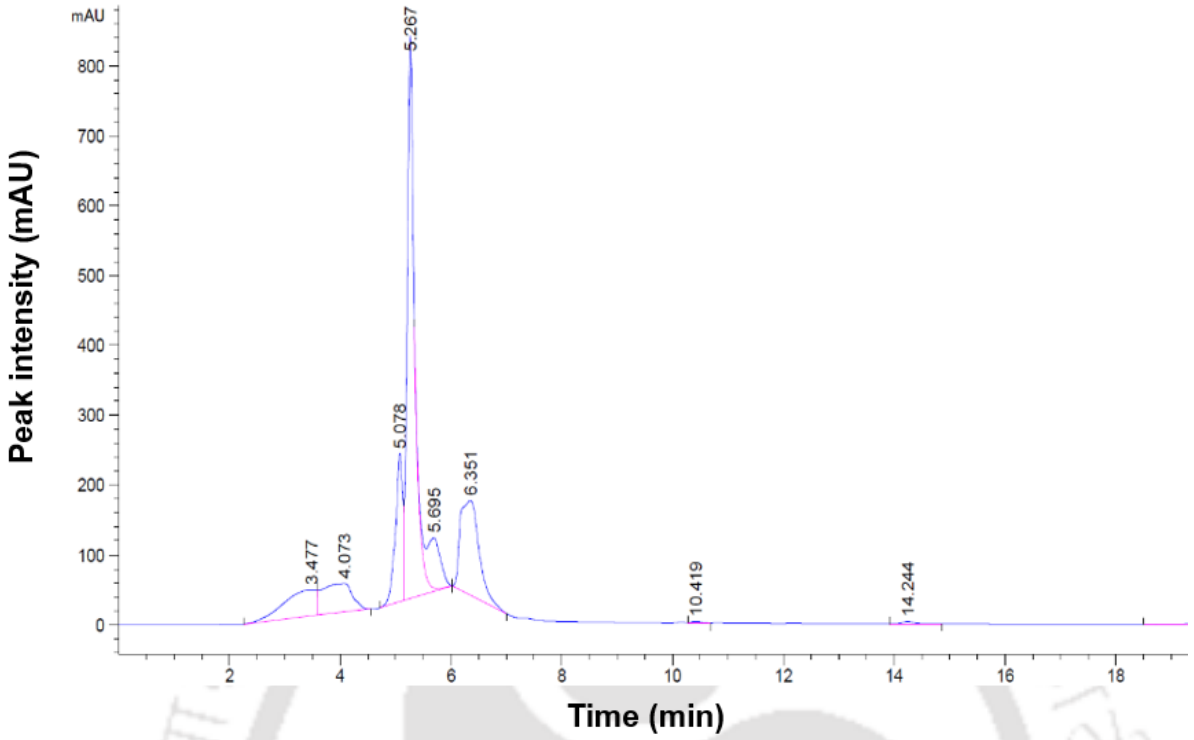

Fig. S4 (B): HPLC chromatogram of a standard melanoidin sample having the initial melanoidin concentration of 10000 ppm (1 % w/v).

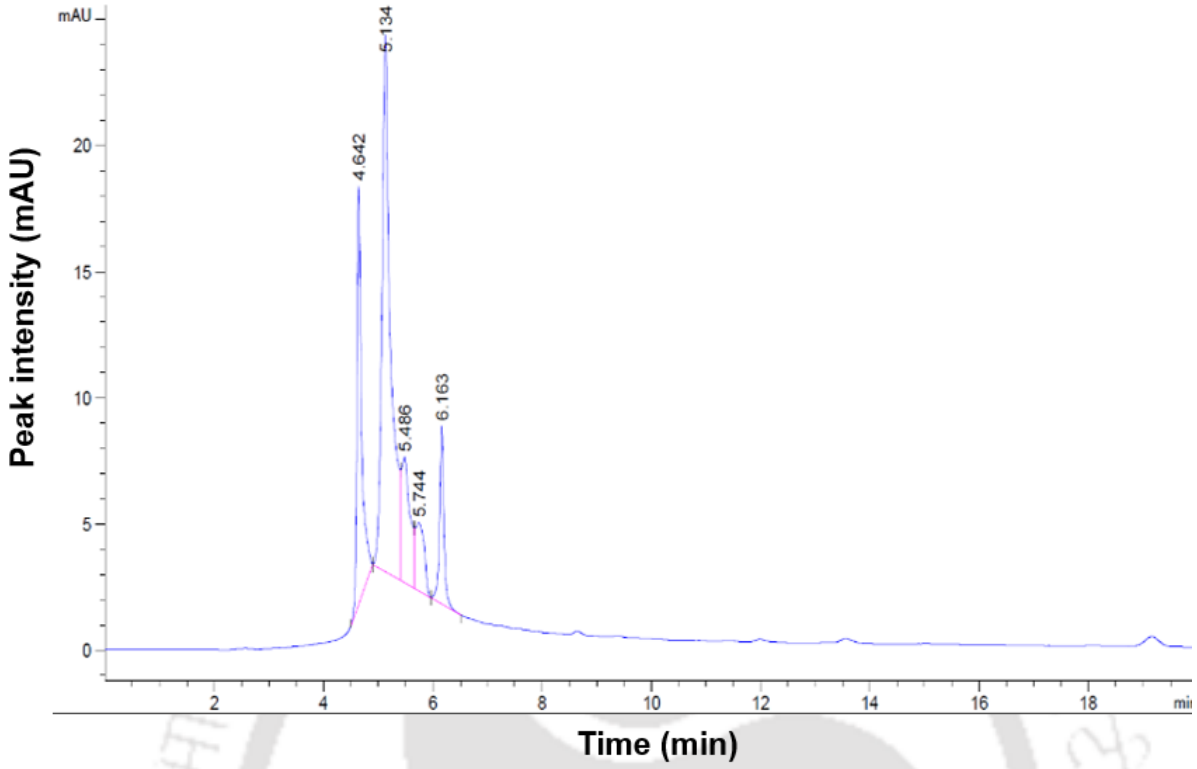

Fig. S4 (C): HPLC chromatogram of a 120 min treated sample at RSM optimized photo-Fenton conditions.

HPLC analysis

The reduction in the peak area of different time intervals samples was compared to control samples to analyse the degradation efficiency of melanoidin. The melanoidin peak was eluted at the retention time of 5.2 minutes (Figure SB). Exponential decrease in peak area and intensity justify the degradation of melanoidin concerning the time. The degradation efficiency was also quantified by HPLC analysis by comparing the chromatograms of standard melanoidin samples of known concentration (Figure SC). The HPLC analysis also evaluated 98 ± 1 % of melanoidin degradation within 120 minutes by photo-Fenton treatment (Figure 4.8 D). Similar peak patterns of melanoidin

were reported by Bharagava *et al.* and Morales *et al.* in their respective studies on HPLC analysis of the melanoidin, which confirms the authentication of the melanoidin compounds [236, 289].

Appendix Chapter 5

Table S5.1. The experimental set-ups of independent variables (Temperature, time, H_2O_2 and WO_3 concentration) and comparison of the experimental and predicted responses (% melanoidin degradation and % COD reduction).

Serial No.	Independent variable				Responses (%)			
					Melanoidin degradation		COD Reduction	
	Temp. °C (A)	Time Min (B)	H_2O_2 mM (C)	WO_3 PPM (D)	Actual Value	Predicted Value	Actual Value	Predicted Value
1	32.5	97.5	57.5	150	52.16	45.21	41.14	33.62
2	47.5	97.5	57.5	150	53.01	49.01	41.14	37.71
3	32.5	232.5	57.5	150	66.42	66.62	57.14	56
4	47.5	232.5	57.5	150	68.04	72.57	59.43	65.23
5	32.5	97.5	152.5	150	67.5	58.51	56	47.62
6	47.5	97.5	152.5	150	66.61	62.53	51.43	48.86
7	32.5	232.5	152.5	150	73.16	77.35	62.88	68.3
8	47.5	232.5	152.5	150	85.03	83.53	75.43	74.67
9	32.5	97.5	57.5	250	67.62	66.58	56	54.48
10	47.5	97.5	57.5	250	74.16	70.52	65.14	60.29
11	32.5	232.5	57.5	250	76.63	81.26	67.43	70.57
12	47.5	232.5	57.5	250	80.9	87.35	75.41	81.51
13	32.5	97.5	152.5	250	92.72	88.74	85.71	80.47
14	47.5	97.5	152.5	250	95.66	92.91	84.57	83.43
15	32.5	232.5	152.5	250	99.39	98.85	93.71	94.86
16	47.5	232.5	152.5	250	99.67	97.17	94.86	92.95
17	25	165	105	200	74.48	78.73	64	70.19
18	55	165	105	200	91.1	88.85	86.86	82.38
19	40	30	105	200	29.56	46.28	17.14	33.62
20	40	300	105	200	96.67	81.95	90.29	75.53
21	40	165	10	200	69.99	68.91	56	56.85
22	40	165	200	200	98.94	98.02	91.43	92.29
23	40	165	105	100	39.49	46.8	29.71	35.14
24	40	165	105	300	97.12	91.81	88	84.28
25	40	165	105	200	90.29	92.58	81.14	82.67
26	40	165	105	200	95.4	92.58	84.57	82.67
27	40	165	105	200	91.65	92.58	82.29	82.67
28	40	165	105	200	93.81	92.58	83.43	82.67
29	40	165	105	200	90.52	92.58	83.43	82.67
30	40	165	105	200	93.79	92.58	81.14	82.67

Table S5.2. ANOVA table of the quadratic model for the % melanoidin degradation by WO_3 photocatalyst.

Source	Sum of squares	df	Mean Square	F-value	p-value
Model	8925.93	14	637.57	9.62	< 0.0001
A (Temp.)	153.62	1	153.62	2.32	0.15
B (Time)	1908.52	1	1908.52	28.79	0.01
C(H_2O_2)	1645.07	1	1645.07	24.82	0.01
D (WO_3)	3039.30	1	3039.30	45.86	0.01
AB	4.62	1	4.62	0.07	0.80
AC	0.05	1	0.05	0.01	0.98
AD	0.02	1	0.02	0.01	0.99
BC	6.60	1	6.60	0.10	0.76
BD	45.36	1	45.36	0.68	0.42
CD	78.59	1	78.59	1.19	0.29
A^2	132.38	1	132.38	2.00	0.18
B^2	1388.77	1	1388.77	20.95	0.01
C^2	86.72	1	86.72	1.31	0.27
D^2	928.47	1	928.47	14.01	0.01
Residual	994.20	15	66.28		
Lack of Fit	972.92	10	97.29	22.86	0.01
Pure Error	21.28	5	4.26		
Cor Total	9920.13	29			

Table S5.3. ANOVA table of the quadratic model for % COD reduction by WO_3 photocatalyst.

Source	Sum of squares	df	Mean Square	F-value	p-value
Model	10572.86	14	755.20	11.55	< 0.01
A (Temp.)	222.77	1	222.77	3.41	0.09
B (Time)	2634.67	1	2634.67	40.29	< 0.01
C(H_2O_2)	1883.64	1	1883.64	28.80	< 0.01
D (WO_3)	3621.62	1	3621.62	55.38	< 0.01
AB	26.37	1	26.37	0.40	0.54
AC	8.15	1	8.15	0.12	0.73
AD	2.94	1	2.94	0.05	0.84
BC	2.91	1	2.91	0.044	0.84
BD	39.63	1	39.63	0.61	0.45
CD	143.88	1	143.88	2.20	0.16
A^2	69.78	1	69.78	1.07	0.32
B^2	1353.14	1	1353.14	20.69	0.01
C^2	112.34	1	112.34	1.72	0.21
D^2	903.31	1	903.31	13.81	0.01
Residual	980.98	15	65.40		
Lack of Fit	971.39	10	97.14	50.64	0.01
Pure Error	9.59	5	1.92		
Cor Total	11553.84	29			

Table S5.4. The experimental set-ups of independent variables (H_2O_2 and FZO concentrations) and comparison of the experimental and predicted responses (% melanoidin degradation and % COD reduction).

Serial No.	Independent variable		Responses (%) melanoidin degradation	
	H_2O_2 mM (A)	WO_3 PPM (B)	Actual Value	Predicted Value
1	37.82	129.29	22.69	25.03
2	172.18	129.29	50.49	59.72
3	37.82	270.71	31.34	36.26
4	172.18	270.71	88.42	89.22
5	10.00	200.00	14.61	12.41
6	200.00	200.00	94.11	82.17
7	105.00	100.00	50.3	45.04
8	105.00	300.00	90.51	81.62
9	105.00	200.00	83.17	82.93
10	105.00	200.00	88.9	82.93
11	105.00	200.00	81.37	82.93
12	105.00	200.00	79.73	82.93
13	105.00	200.00	81.46	82.93

Table S5.5. ANOVA table of the quadratic model for the melanoidin degradation by FZO.

Source	Sum of squares	df	Mean Square	F-value	p-value
Model	9022.60	5	1804.52	22.60	< 0.01
A (H_2O_2)	4866.40	1	4866.40	60.95	< 0.01
B (FZO)	1337.62	1	1337.62	16.75	< 0.01
AB	214.33	1	214.33	2.68	0.15
A^2	2209.03	1	2209.03	27.67	0.01
B^2	667.75	1	667.75	8.36	0.02
Residual	558.94	7	79.85		
Lack of Fit	508.40	3	169.47	13.41	0.02
Pure Error	50.53	4	12.63		
Cor Total	9581.54	12			

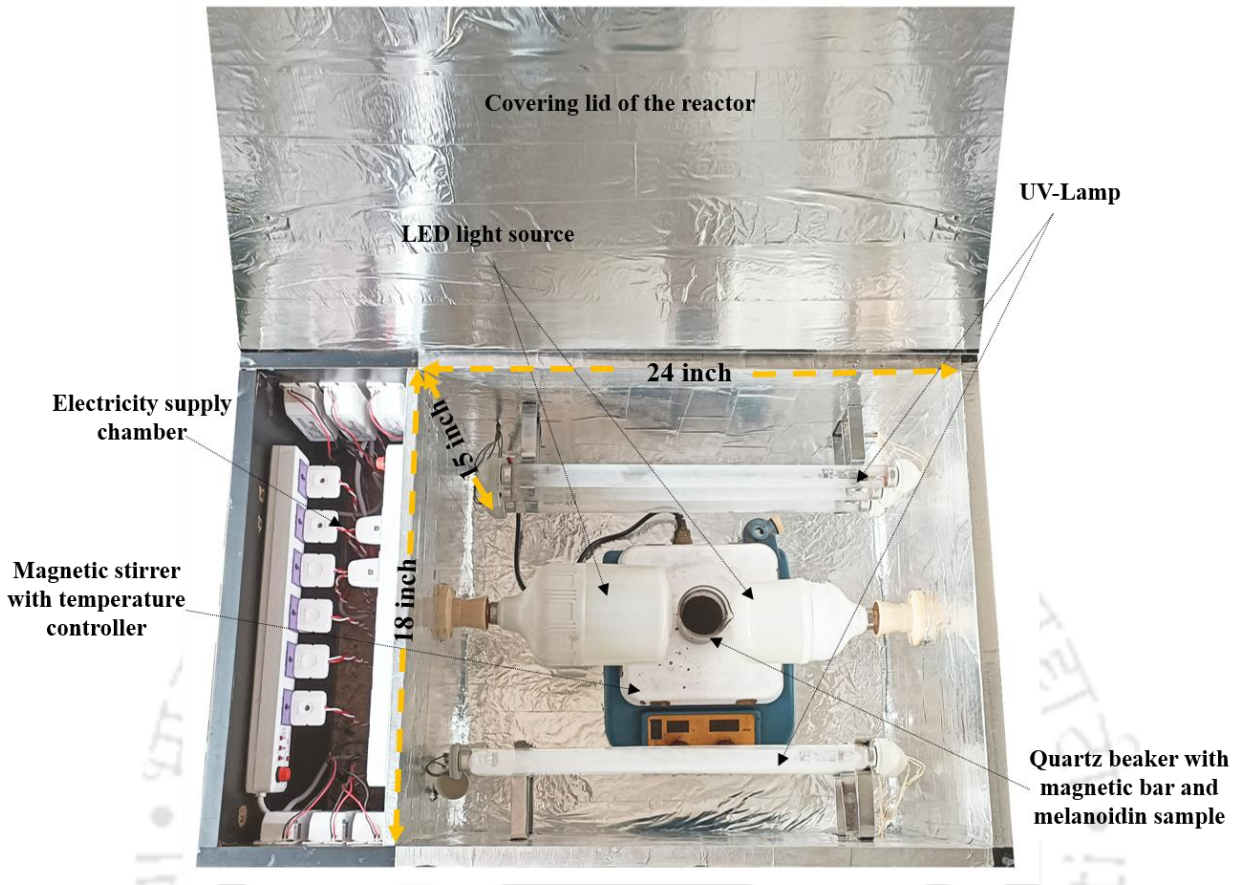

Fig S5.1: Photocatalytic reactor equipped with Visible and UV light sources.

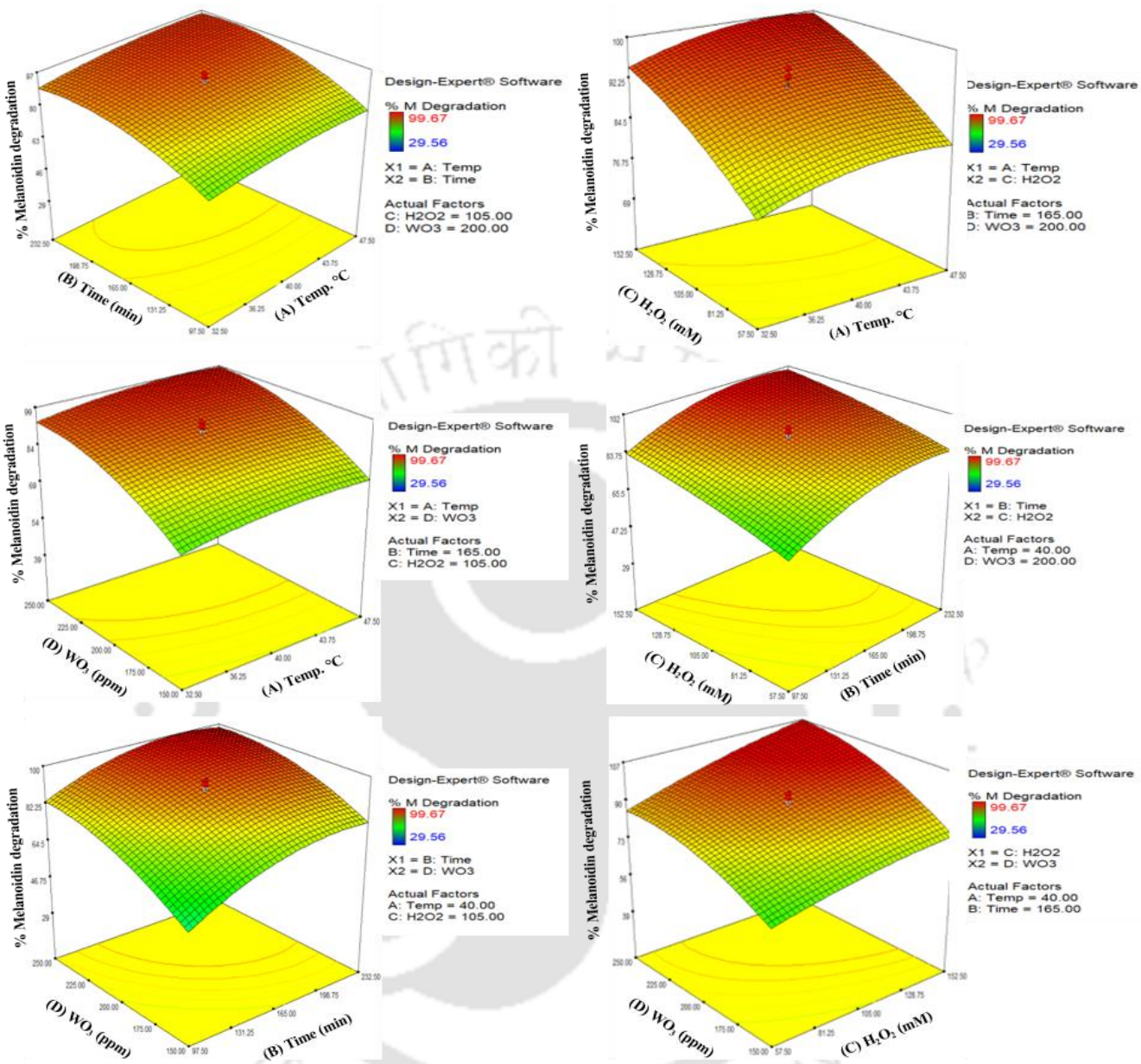

Fig. S5.2: 3D response surface plots for the melanoidin degradation (%) by WO_3 considering their independent parameters as (A) temperature (°C), (B) time (min), (C) H_2O_2 (mM) and (D) WO_3 (ppm) concentrations.

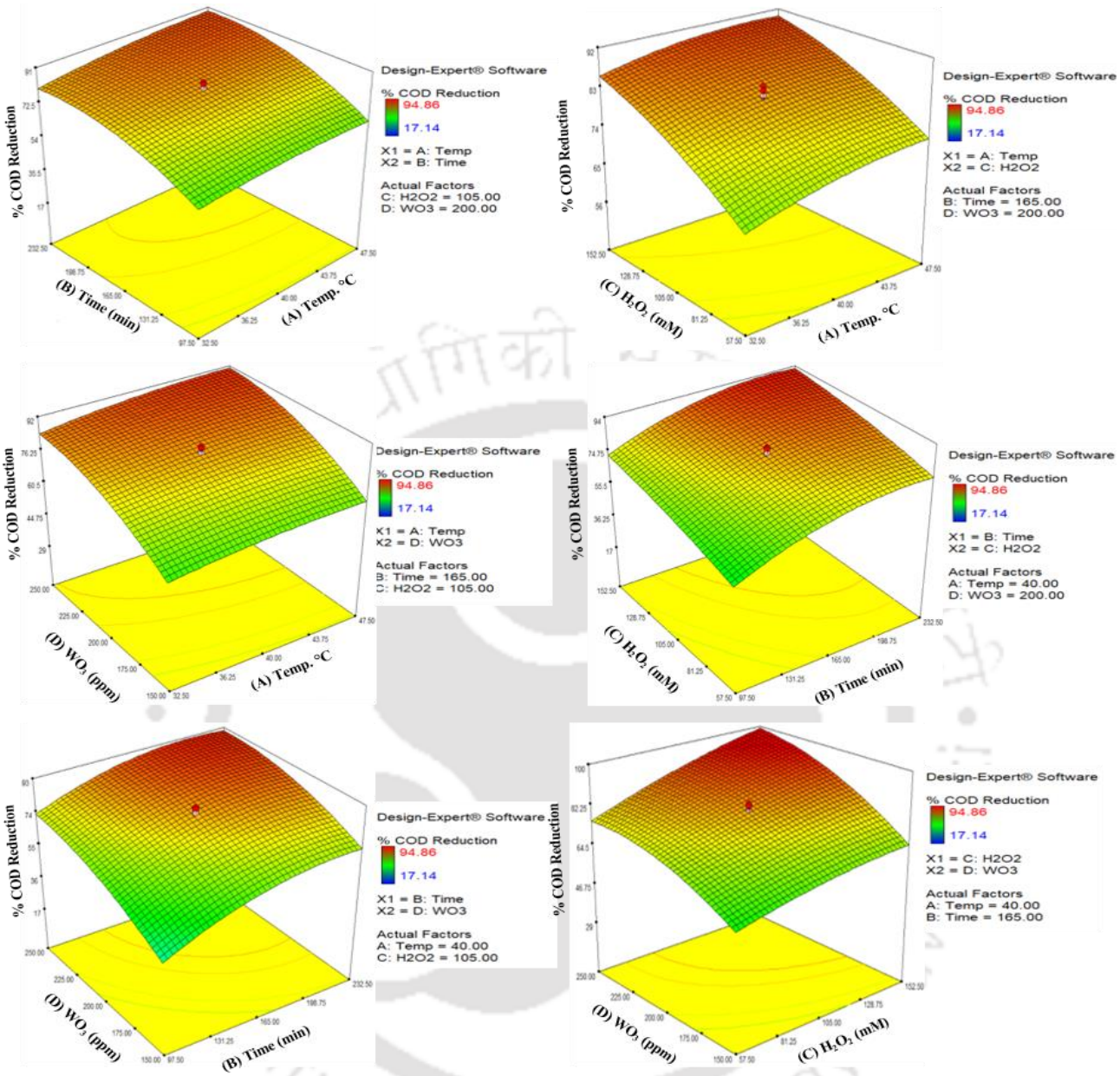

Fig. S5.3: 3D response surface plots for the COD reduction (%) by WO_3 considering their independent parameters as (A) temperature (°C), (B) time (min), (C) H_2O_2 (mM) and (D) WO_3 (ppm) concentrations.

HPLC analysis of the melanoidin degradation by the photocatalyst

The degradation efficiency of the melanoidin was determined by comparing the peak area reduction of samples collected at different time intervals. The melanoidin peak was observed after 5.2 minutes of retention time. The degradation of the melanoidin with time is justified by an exponential decline in peak area and intensity. HPLC analysis was used to determine photocatalytic degradation by evaluating the chromatograms of residual melanoidin samples with known concentrations. As per the HPLC analysis, photocatalyst WO_3 resulted in 97 % of melanoidin degradation (Figure S4) and photocatalyst FZO resulted in 99 % of melanoidin degradation (Figure S6) at their respective RSM optimized conditions.

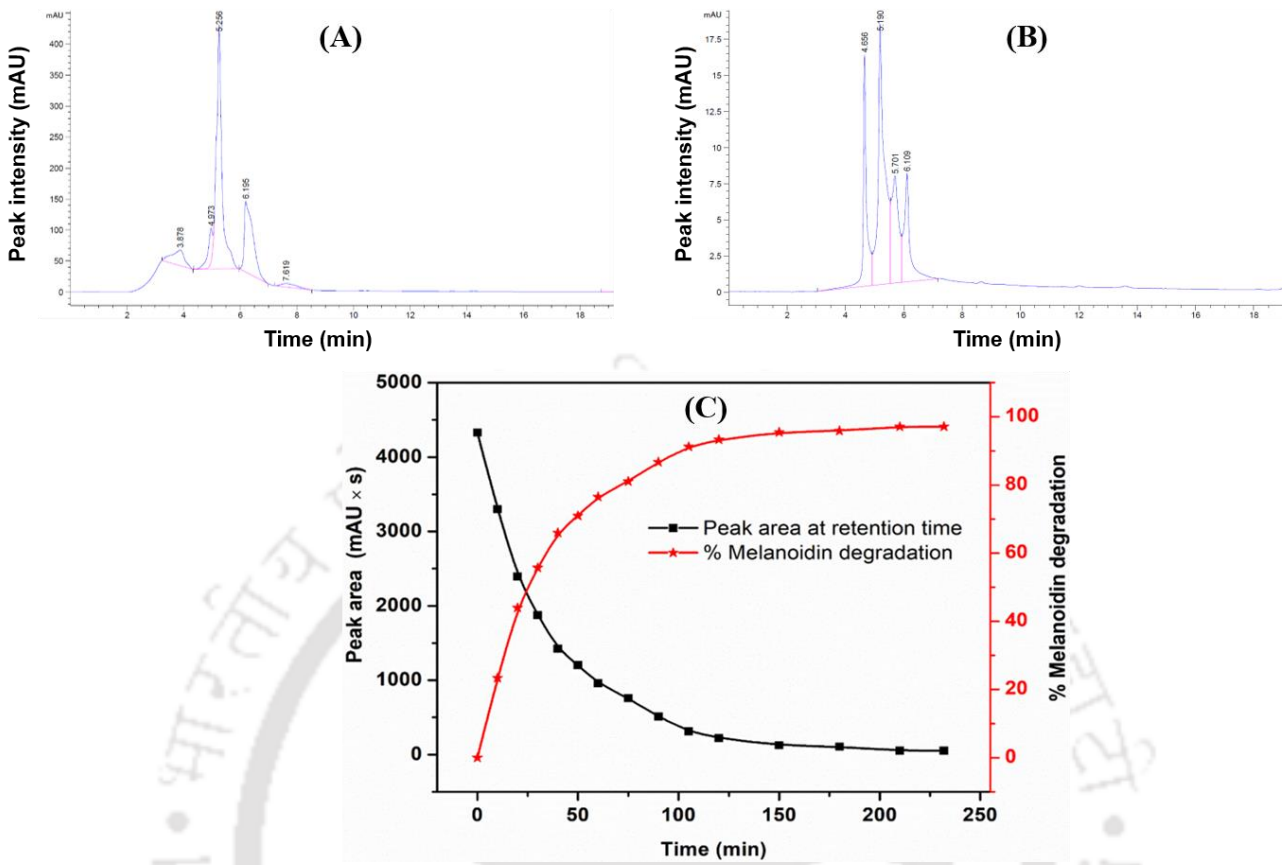

Fig. S5.4: HPLC chromatograms of (A) melanoidin sample at t = 0 min having the initial melanoidin concentration of 5000 ppm (0.5 % w/v), (B) Residual melanoidin at 231 min after photocatalytic degradation using WO_3 at RSM optimized conditions and (C) Reduction in the peak area and degradation of the melanoidin samples at different time intervals evaluated by HPLC analysis.

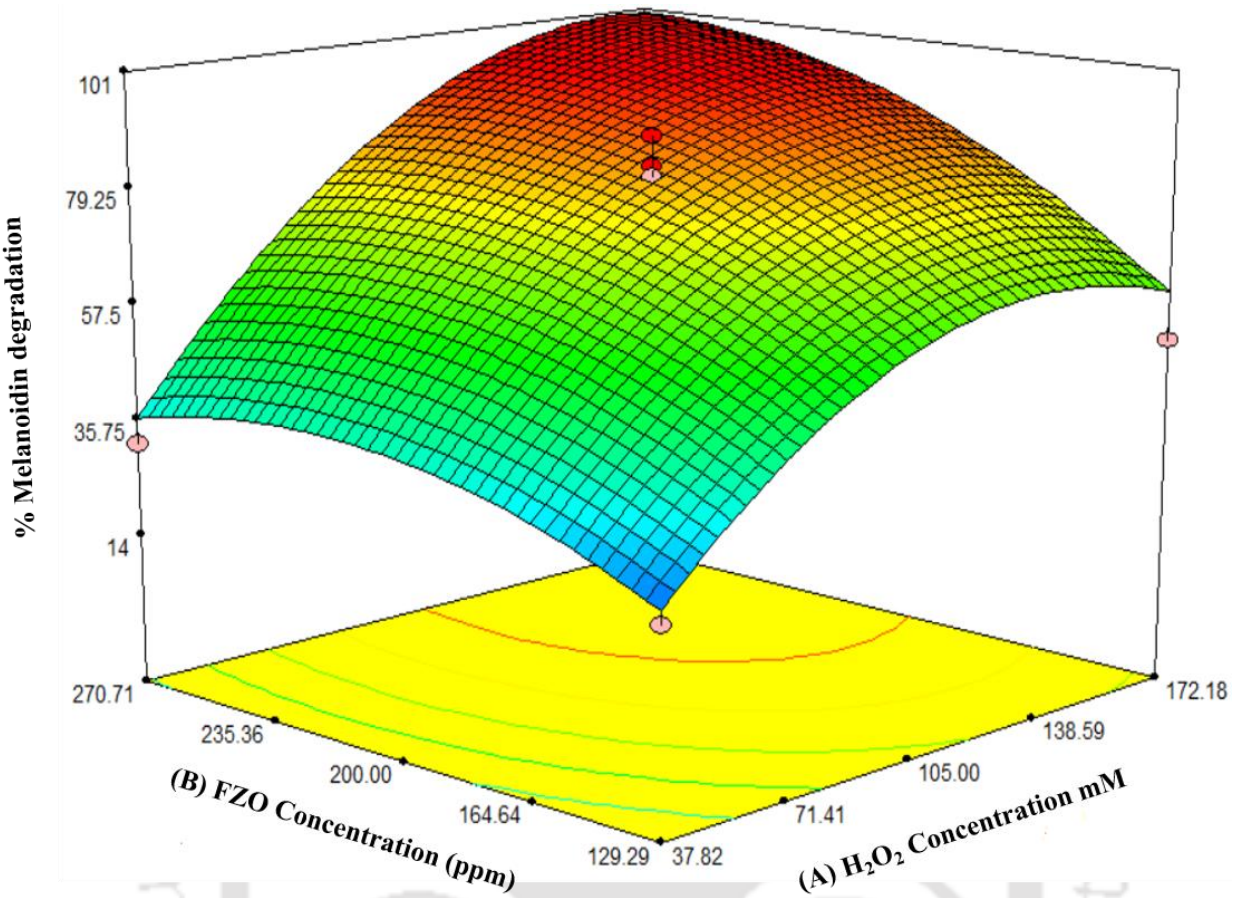

Fig. S5.5: 3D response surface plots for the melanoidin degradation (%) by FZO considering their independent parameters as (A) H_2O_2 (mM) and (B) FZO (ppm) concentrations.

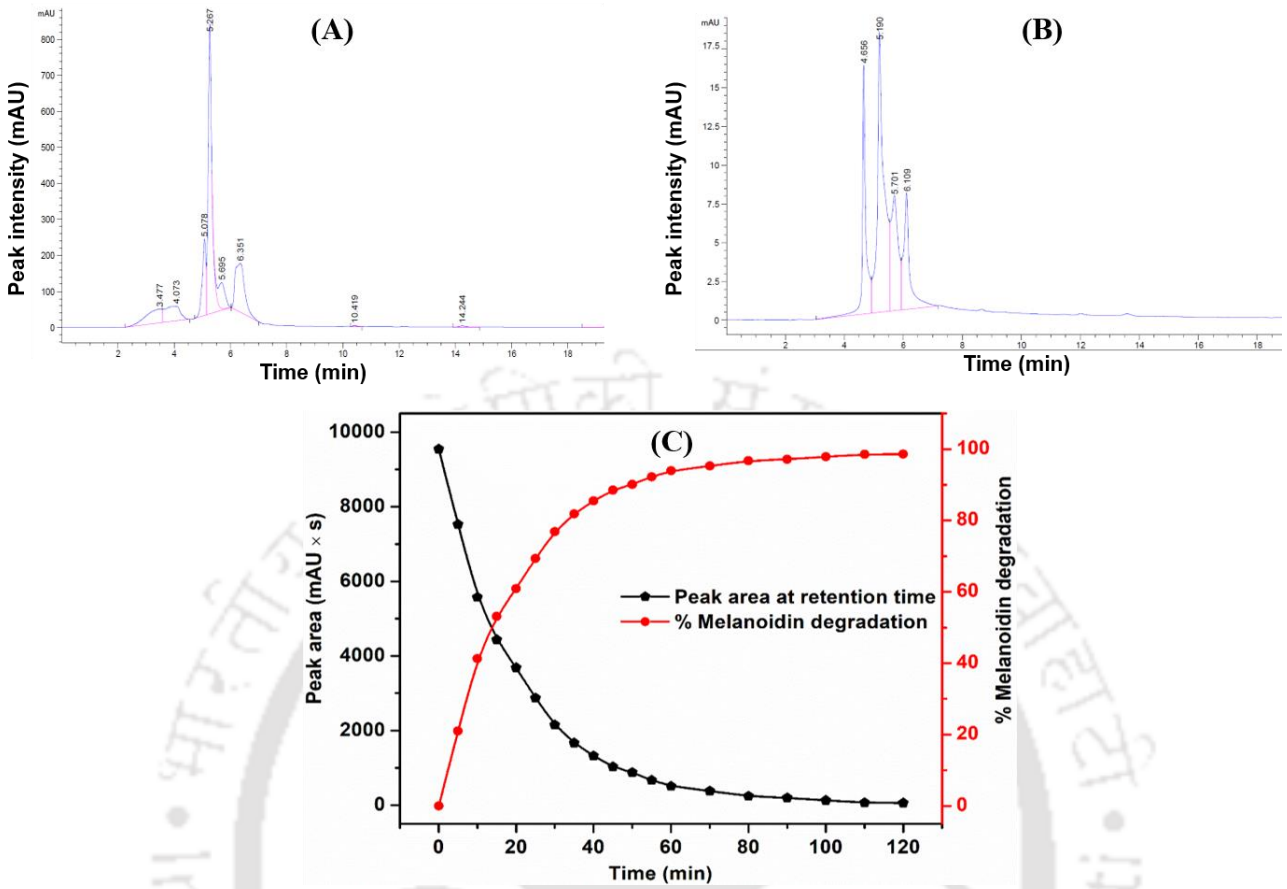

Fig. S5.6: HPLC chromatograms of (A) melanoidin sample at t = 0 min having the initial melanoidin concentration of 10000 ppm (1.0 % w/v), (B) Residual melanoidin at 120 min after photocatalytic degradation using FZO at RSM optimized conditions (C) Standard curve of the melanoidin and (D) Reduction in the peak area and degradation of the melanoidin samples at different time intervals evaluated by HPLC analysis.

References

[1] Adeleye AS, Conway JR, Garner K, Huang Y, Su Y, Keller AA. Engineered nanomaterials for water treatment and remediation: Costs, benefits, and applicability. Chemical Engineering Journal. 2016;286:640-62.

[2] Supply WUJW, Programme SM. Progress on sanitation and drinking water: 2015 update and MDG assessment: World Health Organization; 2015.

[3] Chowdhary P, Raj A, Bharagava RN. Environmental pollution and health hazards from distillery wastewater and treatment approaches to combat the environmental threats: A review. Chemosphere. 2018;194:229-46.

[4] Santal AR, Singh NP, Saharan BS. Biodegradation and detoxification of melanoidin from distillery effluent using an aerobic bacterial strain SAG5 of Alcaligenes faecalis. Journal of Hazardous Materials. 2011;193:319-24.

[5] Verma R, Kundu LM, Pandey LM. Enhanced melanoidin removal by amine-modified Phyllanthus emblica leaf powder. Bioresource Technology. 2021;339:125572.

[6] Verma R, Kundu LM, Pandey LM. 6 - Decontamination of distillery spent wash through advanced oxidation methods. In: Shah MP, editor. Advanced Oxidation Processes for Effluent Treatment Plants: Elsevier; 2021. p. 103-17.

[7] Chandra R, Naresh Bharagava R, Kapley A, Purohit HJ. Characterization of Phragmites cummunis rhizosphere bacterial communities and metabolic products during the two stage sequential treatment of post methanated distillery effluent by bacteria and wetland plants. Bioresource Technology. 2012;103:78-86.

[8] Nooshkam M, Varidi M, Bashash M. The Maillard reaction products as food-born antioxidant and antibrowning agents in model and real food systems. Food Chemistry. 2019;275:644-60.

[9] Zhang Z, Li D, Zhang X. Enzymatic decolorization of melanoidins from molasses wastewater by immobilized keratinase. Bioresource technology. 2019;280:165-72.

[10] Li W, Yu-Yu E, Cheng L-Y, Ding M, Li W-Y, Diao K-S, et al. Rosin-based polymer@ silica core–shell adsorbent: Preparation, characterization, and application to melanoidin adsorption. LWT. 2020;132:109937.

[11] Singh N, Petrinic I, Hélix-Nielsen C, Basu S, Balakrishnan M. Concentrating molasses distillery wastewater using biomimetic forward osmosis (FO) membranes. Water Research. 2018;130:271-80.

[12] Prajapati AK, Chaudhari PK. Physicochemical treatment of distillery wastewater—a review. Chemical Engineering Communications. 2015;202:1098-117.

[13] Arimi MM, Zhang Y, Götz G, Kiriamiti K, Geißen S-U. Antimicrobial colorants in molasses distillery wastewater and their removal technologies. International Biodeterioration & Biodegradation. 2014;87:34-43.

[14] Kamble SKM, Hebbara M, Manjunatha M, Dasog G, GM VP. Influence of long-term irrigation with bio-methanated spentwash on physical and biological properties in a vertisol. Res Environ Life Sci. 2016;9:1-3.

[15] Mohana S, Acharya BK, Madamwar D. Distillery spent wash: Treatment technologies and potential applications. Journal of Hazardous Materials. 2009;163:12-25.

[16] Fagier MA, Elmugdad A, Aziz M, Gabra NM. Identification of some Organic Compounds in Sugarcane vinasse by Gas Chromatography-Mass Spectrometry and Prediction of their Toxicity Using TEST Method. J Chem Pharm Sci. 2015;8:899-905.

[17] Yadav S, Chandra R. Biodegradation of organic compounds of molasses melanoidin (MM) from biomethanated distillery spent wash (BMDS) during the decolourisation by a potential bacterial consortium. Biodegradation. 2012;23:609-20.
[18] Pant D, Adholeya A. Biological approaches for treatment of distillery wastewater: a review. Biores Tech. 2007;98:2321-34.
[19] Prajapati AK, Choudhary R, Verma K, Chaudhari PK, Dubey A. Decolorization and removal of chemical oxygen demand (COD) of rice grain–based biodigester distillery effluent (BDE) using inorganic coagulants. Desalination and Water Treatment. 2015;53:2204-14.
[20] Arimi MM, Zhang Y, Geißen S-U. Color removal of melanoidin-rich industrial effluent by natural manganese oxides. Separation and Purification Technology. 2015;150:286-91.
[21] Chandra R, Pandey P. Decolourisation of anaerobically treated distillery effluent by activated charcoal adsorption method. Indian Journal of Environmental Protection. 2001;21:134-7.
[22] Lalov IG, Guerginov II, Krysteva MA, Fartsov K. Treatment of waste water from distilleries with chitosan. Water Research. 2000;34:1503-6.
[23] Mane JD, Modi S, Nagawade S, Phadnis S, Bhandari V. Treatment of spentwash using chemically modified bagasse and colour removal studies. Biores Tech. 2006;97:1752-5.
[24] Shivayogimath C, Inani S. Treatment of biomethanated distillery spent wash by adsorption process on bagasse activated carbon. International Journal of Applied Science and Engineering Research. 2014;3:1069-78.
[25] Migo VP, Matsumura M, Del Rosario EJ, Kataoka H. Decolorization of molasses wastewater using an inorganic flocculant. Journal of fermentation and bioengineering. 1993;75:438-42.
[26] Sowmeyan R, Swaminathan G. Evaluation of inverse anaerobic fluidized bed reactor for treating high strength organic wastewater. Biores Tech. 2008;99:3877-80.
[27] Bes-Pia A, Mendoza-Roca J, Alcaina-Miranda M, Iborra-Clar A, Iborra-Clar M. Combination of physico-chemical treatment and nanofiltration to reuse wastewater of a printing, dyeing and finishing textile industry. Desalination. 2003;157:73-80.
[28] Pala A, Erden G. Decolorization of a baker's yeast industry effluent by Fenton oxidation. Journal of hazardous materials. 2005;127:141-8.
[29] Sharma A, Ahmad J, Flora SJEr. Application of advanced oxidation processes and toxicity assessment of transformation products. 2018;167:223-33.
[30] Arslan I, Balcioglu IA. Effect of common reactive dye auxiliaries on the ozonation of dyehouse effluents containing vinylsulphone and aminochlorotriazine dyes. Desalination. 2000;130:61-71.
[31] Takashina TA, Leifeld V, Zelinski DW, Mafra MR, Igarashi-Mafra L. Application of response surface methodology for coffee effluent treatment by ozone and combined ozone/UV. Ozone: Science & Engineering. 2018;40:293-304.
[32] Boczkaj G, Fernandes A. Wastewater treatment by means of advanced oxidation processes at basic pH conditions: A review. Chemical Engineering Journal. 2017;320:608-33.
[33] Ghuge SP, Saroha AK. Catalytic ozonation of dye industry effluent using mesoporous bimetallic Ru-Cu/SBA-15 catalyst. Process Safety and Environmental Protection. 2018;118:125-32.
[34] Kasprzyk-Hordern B, Ziółek M, Nawrocki J. Catalytic ozonation and methods of enhancing molecular ozone reactions in water treatment. Applied Catalysis B: Environmental. 2003;46:639-69.
[35] Adiraju B, Saroha AK. Kinetics of ozone oxidation of acid red 131 monoazo dye in aqueous solution. Journal of Hazardous, Toxic, and Radioactive Waste. 2017;21:04016009.
[36] Otieno B, Apollo S, Kabuba J, Naidoo B, Ochieng A. Ozonolysis Post-Treatment of Anaerobically Digested Distillery Wastewater Effluent. Ozone: Science & Engineering. 2019:1-11.
[37] Siles J, García-García I, Martín A, Martín MJJoHM. Integrated ozonation and biomethanization treatments of vinasse derived from ethanol manufacturing. 2011;188:247-53.

[38] Malik SN, Ghosh PC, Vaidya AN, Mudliar SN. Ozone pre-treatment of molasses-based biomethanated distillery wastewater for enhanced bio-composting. Journal of environmental management. 2019;246:42-50.

[39] Mecha AC, Chollom MN. Photocatalytic ozonation of wastewater: a review. Environmental Chemistry Letters. 2020;18:1491-507.

[40] Gu Z, Wang Y, Feng K, Zhang A. A comparative study of dinitrodiazophenol industrial wastewater treatment: Ozone/hydrogen peroxide versus microwave/persulfate. Process Safety and Environmental Protection. 2019;130:39-47.

[41] Farzaneh H, Loganathan K, Saththasivam J, McKay G. Ozone and ozone/hydrogen peroxide treatment to remove gemfibrozil and ibuprofen from treated sewage effluent: Factors influencing bromate formation. Emerging Contaminants. 2020;6:225-34.

[42] Rosenfeldt EJ, Linden KG, Canonica S, von Gunten U. Comparison of the efficiency of OH radical formation during ozonation and the advanced oxidation processes O_3/H_2O_2 and UV/H_2O_2. Water Research. 2006;40:3695-704.

[43] Sushma, Kumari M, Saroha AK. Performance of various catalysts on treatment of refractory pollutants in industrial wastewater by catalytic wet air oxidation: A review. Journal of Environmental Management. 2018;228:169-88.

[44] Tizaoui C, Bouselmi L, Mansouri L, Ghrabi A. Landfill leachate treatment with ozone and ozone/hydrogen peroxide systems. Journal of Hazardous Materials. 2007;140:316-24.

[45] Hadavifar M, Younesi H, Zinatizadeh AA, Mahdad F, Li Q, Ghasemi Z. Application of integrated ozone and granular activated carbon for decolorization and chemical oxygen demand reduction of vinasse from alcohol distilleries. Journal of environmental management. 2016;170:28-36.

[46] Kolte H, Walke A, Nimbakar D, Ghole V, D Student P. Combine Ozonation Treatment Followed byBiological Treatment to Anaerobically Digested Spentwash,". International Journal of Advanced Research in Electrical, Electronics and Instrumentation Engineering. 2014:14082-8.

[47] Padoley K, Tembhekar P, Saratchandra T, Pandit A, Pandey R, Mudliar S. Wet air oxidation as a pretreatment option for selective biodegradability enhancement and biogas generation potential from complex effluent. Biores Tech. 2012;120:157-64.

[48] Gunale TL, Mahajani VV. Studies in mineralization of aqueous aniline using Fenton and wet oxidation (FENTWO) as a hybrid process. Journal of Chemical Technology & Biotechnology: International Research in Process, Environmental & Clean Technology. 2007;82:108-15.

[49] Domínguez CM, Quintanilla A, Casas JA, Rodriguez JJ. Treatment of real winery wastewater by wet oxidation at mild temperature. Separation and Purification Technology. 2014;129:121-8.

[50] Bhoite GM, Vaidya PD. Improved biogas generation from biomethanated distillery wastewater by pretreatment with catalytic wet air oxidation. Industrial & Engineering Chemistry Research. 2018;57:2698-704.

[51] Chandra TS, Malik S, Suvidha G, Padmere M, Shanmugam P, Mudliar S. Wet air oxidation pretreatment of biomethanated distillery effluent: Mapping pretreatment efficiency in terms color, toxicity reduction and biogas generation. Biores Tech. 2014;158:135-40.

[52] Fenton H. LXXIII.—Oxidation of tartaric acid in presence of iron. Journal of the Chemical Society, Transactions. 1894;65:899-910.

[53] De Heredia JB, Torregrosa J, Dominguez J, Partido E. Degradation of wine distillery wastewaters by the combination of aerobic biological treatment with chemical oxidation by Fenton's reagent. Water Science and Technology. 2005;51:167-74.

[54] Pinjari DV, Pandit AB. Cavitation milling of natural cellulose to nanofibrils. Ultrasonics sonochemistry. 2010;17:845-52.

[55] Saharan VK, Pandit AB, Satish Kumar PS, Anandan S. Hydrodynamic cavitation as an advanced oxidation technique for the degradation of acid red 88 dye. Industrial & Engineering Chemistry Research. 2011;51:1981-9.

[56] Padoley K, Saharan VK, Mudliar S, Pandey R, Pandit AB. Cavitationally induced biodegradability enhancement of a distillery wastewater. Journal of hazardous materials. 2012;219:69-74.

[57] Paradkar K, Mudliar S, Sharma A, Pandit A, Pandey R. Hybrid advanced oxidative pretreatment of complex industrial effluent for biodegradability enhancement. International Journal of Chemical and Molecular Engineering. 2016;10:250-8.

[58] Güven G, Perendeci A, Tanyolaç A. Electrochemical treatment of deproteinated whey wastewater and optimization of treatment conditions with response surface methodology. Journal of hazardous materials. 2008;157:69-78.

[59] Benito GG, Miranda MP, De Los Santos DR. Decolorization of wastewater from an alcoholic fermentation process with Trametes versicolor. Biores Tech. 1997;61:33-7.

[60] Rizzo L. Bioassays as a tool for evaluating advanced oxidation processes in water and wastewater treatment. Water research. 2011;45:4311-40.

[61] Prasad RK, Srivastava SJCEJ. Electrochemical degradation of distillery spent wash using catalytic anode: Factorial design of experiments. 2009;146:22-9.

[62] Prasad RK, Kumar RR, Srivastava S. Design of optimum response surface experiments for electro-coagulation of distillery spent wash. Water, air, and soil pollution. 2008;191:5-13.

[63] Legrini O, Oliveros E, Braun A. Photochemical processes for water treatment. Chemical reviews. 1993;93:671-98.

[64] Sharma A, Ahmad J, Flora S. Application of advanced oxidation processes and toxicity assessment of transformation products. Environmental research. 2018;167:223-33.

[65] Lucas MS, Peres JA, Puma GL. Treatment of winery wastewater by ozone-based advanced oxidation processes (O_3, O_3/UV and O_3/UV/H_2O_2) in a pilot-scale bubble column reactor and process economics. Separation and purification technology. 2010;72:235-41.

[66] Asaithambi P, Saravanathamizhan R, Matheswaran M. Comparison of treatment and energy efficiency of advanced oxidation processes for the distillery wastewater. International journal of environmental science and technology. 2015;12:2213-20.

[67] Shah MJAiR, Management W. Industrial Wastewater Treatment: A Challenging Task in the Industrial Waste Management. 2016;2:115.

[68] Navgire M, Yelwande A, Tayde D, Arbad B, Lande M. Photodegradation of molasses by a MoO_3-TiO_2 nanocrystalline composite material. Chin J Catal. 2012;33:261-6.

[69] David C, Arivazhagan Ma, Ibrahim M. Spent wash decolourization using nano-Al_2O_3/kaolin photocatalyst: Taguchi and ANN approach. Journal of Saudi Chemical Society. 2015;19:537-48.

[70] Vineetha M, Matheswaran M, Sheeba KJSE. Photocatalytic colour and COD removal in the distillery effluent by solar radiation. 2013;91:368-73.

[71] Szpyrkowicz L, Juzzolino C, Kaul SN. A comparative study on oxidation of disperse dyes by electrochemical process, ozone, hypochlorite and Fenton reagent. Water research. 2001;35:2129-36.

[72] Davarnejad R, Azizi J. Alcoholic wastewater treatment using electro-Fenton technique modified by Fe_2O_3 nanoparticles. Journal of environmental chemical engineering. 2016;4:2342-9.

[73] David C, Arivazhagan M, Tuvakara F. Decolorization of distillery spent wash effluent by electro oxidation (EC and EF) and Fenton processes: a comparative study. Ecotoxicology and environmental safety. 2015;121:142-8.

[74] Seery MK, George R, Floris P, Pillai SC. Silver doped titanium dioxide nanomaterials for enhanced visible light photocatalysis. Journal of Photochemistry and Photobiology A: Chemistry. 2007;189:258-63.

[75] Qi X-H, Zhuang Y-Y, Yuan Y-C, Gu W-X. Decomposition of aniline in supercritical water. Journal of hazardous materials. 2002;90:51-62.

[76] Pham T-D, Lee B-K. Feasibility of silver doped TiO_2/glass fiber photocatalyst under visible irradiation as an indoor air germicide. International journal of environmental research and public health. 2014;11:3271-88.

[77] Lei X, Xue X, Yang H. Preparation and characterization of Ag-doped TiO_2 nanomaterials and their photocatalytic reduction of Cr (VI) under visible light. Applied Surface Science. 2014;321:396-403.

[78] Carrocci JS, Mori RY, Guimarães OLC, Salazar R, Oliveira M, Peixoto A, et al. Application of heterogenous catalysis with TiO_2 photo irradiated by sunlight and latter activated sludge system for the reduction of vinasse organic load. Engineering. 2012;4:746.

[79] Perendeci NA, Ekinci FY, Godon JJ. Monitoring the performance and microbial diversity dynamics of a full scale anaerobic wastewater treatment plant treating sugar factory wastewater. Environmental Science: Processes & Impacts. 2013;15:494-502.

[80] Villén L, Manjón F, García-Fresnadillo D, Orellana G. Solar water disinfection by photocatalytic singlet oxygen production in heterogeneous medium. Applied Catalysis B: Environmental. 2006;69:1-9.

[81] Bagal MV, Gogate PR. Degradation of diclofenac sodium using combined processes based on hydrodynamic cavitation and heterogeneous photocatalysis. Ultrasonics sonochemistry. 2014;21:1035-43.

[82] Behnajady M, Modirshahla N, Shokri M, Rad B. Enhancement of photocatalytic activity of TiO_2 nanoparticles by silver doping: photodeposition versus liquid impregnation methods. Global NEST Journal. 2008;10:1-7.

[83] Nakata K, Fujishima A. TiO_2 photocatalysis: Design and applications. Journal of photochemistry and photobiology C: Photochemistry Reviews. 2012;13:169-89.

[84] Seck E, Doña-Rodríguez J, Fernández-Rodríguez C, Portillo-Carrizo D, Hernández-Rodríguez M, González-Díaz O, et al. Solar photocatalytic removal of herbicides from real water by using sol–gel synthesized nanocrystalline TiO_2: operational parameters optimization and toxicity studies. Solar Energy. 2013;87:150-7.

[85] Gulyas H, Liriano Jorge CF, Reich M, Otterpohl R. Reclaiming biologically pretreated greywater for reuse by photocatalytic oxidation: qualitative study on the removal of trace organics. Journal of water resource and protection. 2013;5:568-84.

[86] Soto-Verjel J, Maturana AY, Villamizar SE. Advanced catalytic oxidation coupled to biological systems to treat pesticide-contaminated water: A review on technological trends and future challenges. Water Science and Technology. 2021.

[87] David C, Arivazhagan M, Mishrra A. Treatment of spent wash effluent using Kaolin immobilised nano ZnO photocatalyst and material characterisation. Indian Chemical Engineer. 2020;62:138-49.

[88] Kambe T, Shimomura M, Nomura N, Chanpornpong T, Nakahara T. Decolourization of molasses wastewater by Bacillus sp. under thermophilic and anaerobic conditions. Journal of Bioscience and Bioengineering. 1999;87:119-21.

[89] Kumar S, Viswanathan L. Production of biomass, carbon dioxide, volatile acids, and their interrelationship with decrease in chemical oxygen demand, during distillery waste treatment by bacterial strains. Enzyme and microbial technology. 1991;13:179-87.

[90] Dahiya J, Singh D, Nigam P. Decolourisation of molasses wastewater by cells of Pseudomonas fluorescens immobilised on porous cellulose carrier. Biores Tech. 2001;78:111-4.

[91] Ohmomo S, Kainuma M, Kamimura K, Sirianuntapiboon S, Aoshima I, Atthasampunna P. Adsorption of melanoidin to the mycelia of Aspergillus oryzae Y-2-32. Agricultural and biological chemistry. 1988;52:381-6.

[92] Jain N, Minocha A, Verma C. Degradation of predigested distillery effluent by isolated bacterial strains. 2002.

[93] Sirianuntapiboon S, Phothilangka P, Ohmomo S. Decolorization of molasses wastewater by a strain No. BP103 of acetogenic bacteria. Biores Tech. 2004;92:31-9.

[94] Patel A, Pawar R, Mishra S. Tiwari A.,(2001); Exploitation of Marine Cyanobacteria for removal of Colour from Distillery Effluent; Indian. Env Prot.21:1118-21.

[95] Ghosh M, Verma S, Mengoni A, Tripathi A. Enrichment and identification of bacteria capable of reducing chemical oxygen demand of anaerobically treated molasses spent wash. Journal of applied microbiology. 2004;96:1278-86.

[96] Chandra R, Bharagava RN, Rai V. Melanoidins as major colourant in sugarcane molasses based distillery effluent and its degradation. Biores Tech. 2008;99:4648-60.

[97] Patil P, Kapadnis B, Dhamankar V. Decolorisation of synthetic melanoidin and biogas effluent by immobilised fungal isolate of Aspergillus niger UM2. International sugar journal. 2003;105:8-13.

[98] Angayarkanni J, Palaniswamy M, Swaminathan K. Biotreatment of distillery effluent using Aspergillus niveus. Bulletin of environmental contamination and toxicology. 2003;70:0268-77.

[99] Chopra P, Singh D, Verma V, Puniya A. Bioremediation of melanoidin containing digested spentwash from cane-molasses distillery with white rot fungus Coriolus versicolor. Indian J Microbiol. 2004;44:197-200.

[100] Sirianuntapiboon S, Zohsalam P, Ohmomo S. Decolorization of molasses wastewater by Citeromyces sp. WR-43-6. Process biochemistry. 2004;39:917-24.

[101] Malandra L, Wolfaardt G, Zietsman A, Viljoen-Bloom M. Microbiology of a biological contactor for winery wastewater treatment. Water Research. 2003;37:4125-34.

[102] Kim SJ, Shoda M. Batch decolorization of molasses by suspended and immobilized fungus of Geotrichum candidum Dec 1. Journal of bioscience and bioengineering. 1999;88:586-9.

[103] Pant D, Adholeya A. Nitrogen removal from biomethanated spentwash using hydroponic treatment followed by fungal decolorization. Environmental Engineering Science. 2009;26:559-65.

[104] Miyata N, Iwahori K, Fujita M. Manganese-independent and-dependent decolorization of melanoidin by extracellular hydrogen peroxide and peroxidases from Coriolus hirsutus pellets. Journal of fermentation and bioengineering. 1998;85:550-3.

[105] Raghukumar C, Rivonkar G. Decolorization of molasses spent wash by the white-rot fungus Flavodon flavus, isolated from a marine habitat. Applied Microbiology and Biotechnology. 2001;55:510-4.

[106] Chowdhary P, Bharagava RN. Toxicity, Beneficial Aspects and Treatment of Alcohol Industry Wastewater. Emerging and Eco-Friendly Approaches for Waste Management: Springer; 2019. p. 83-97.

[107] Paz A, Outeiriño D, Guerra NP, Domínguez JM. Enzymatic hydrolysis of brewer's spent grain to obtain fermentable sugars. Biores Tech. 2019;275:402-9.

[108] Moriya K, Iefuji H, Shimoi H, Sato S-I, Tadenuma M. Treatment of distillery wastewater discharged from beet molasses-spirits production using yeast. Journal of Fermentation and Bioengineering. 1990;69:138-40.

[109] Dehorter B, Blondeau R. Isolation of an extracellular Mn-dependent enzyme mineralizing melanoidins from the white rot fungus Trametes versicolor. FEMS Microbiology Letters. 1993;109:117-22.

[110] Kumar P, Chandra R. Decolourisation and detoxification of synthetic molasses melanoidins by individual and mixed cultures of Bacillus spp. Bioresource Technology. 2006;97:2096-102.

[111] Tiwari S, Rai P, Yadav SK, Gaur R. A novel thermotolerant Pediococcus acidilactici B-25 strain for color, COD, and BOD reduction of distillery effluent for end use applications. Environmental Science and Pollution Research. 2013;20:4046-58.

[112] Mohana S, Desai C, Madamwar D. Biodegradation and decolourization of anaerobically treated distillery spent wash by a novel bacterial consortium. Biores Tech. 2007;98:333-9.

[113] Naik NM, Jagadeesh K, Alagawadi A. Microbial decolorization of spentwash: a review. Indian journal of microbiology. 2008;48:41-8.
[114] Pal S, Vimala Y. Bioremediation and decolorization of Distillery effluent by novel Microbial Consortium. European Journal of Experimental Biology. 2012;2:496-504.
[115] Ghosh M, Ganguli A, Tripathi A. Decolorization of anaerobically digested molasses spent wash by Pseudomonas putida. Applied biochemistry and microbiology. 2009;45:68.
[116] Potentini MF, Rodriguez-Malaver AJ. Vinasse biodegradation by Phanerochaete chrysosporium. Journal of environmental biology. 2006;27:661-5.
[117] Jiménez AM, Borja R, Martın A. Aerobic–anaerobic biodegradation of beet molasses alcoholic fermentation wastewater. Process Biochemistry. 2003;38:1275-84.
[118] Dahiya J, Singh D, Nigam P. Decolourisation of synthetic and spentwash melanoidins using the white-rot fungus Phanerochaete chrysosporium JAG-40. Biores Tech. 2001;78:95-8.
[119] Guimarães C, Porto P, Oliveira R, Mota M. Continuous decolourization of a sugar refinery wastewater in a modified rotating biological contactor with Phanerochaete chrysosporium immobilized on polyurethane foam disks. Process biochemistry. 2005;40:535-40.
[120] Pant D, Adholeya A. Concentration of fungal ligninolytic enzymes by ultrafiltration and their use in distillery effluent decolorization. World Journal of Microbiology and Biotechnology. 2009;25:1793-800.
[121] Tiwari S, Gaur R, Singh R. Decolorization of a recalcitrant organic compound (Melanoidin) by a novel thermotolerant yeast, Candida tropicalis RG-9. BMC Biotechnology. 2012;12:30.
[122] Kalavathi DF, Uma L, Subramanian G. Degradation and metabolization of the pigment—melanoidin in distillery effluent by the marine cyanobacterium Oscillatoria boryana BDU 92181. Enzyme and Microbial Technology. 2001;29:246-51.
[123] Federici F. Potential applications of viable, immobilized fungal cell systems. World Journal of Microbiology and Biotechnology. 1993;9:495-502.
[124] Shah SS, Desai JD, Ramakrishna C, Bhatt NM. Aerobic biotreatment of wastewater from dimethyl terephthalate plant using biomass support particles. Journal of fermentation and bioengineering. 1998;86:215-9.
[125] Adikane H, Dange M, Selvakumari K. Optimization of anaerobically digested distillery molasses spent wash decolorization using soil as inoculum in the absence of additional carbon and nitrogen source. Biores Tech. 2006;97:2131-5.
[126] Singh N, Pandey G, Rai U, Tripathi R, Singh H, Gupta D. Metal accumulation and ecophysiological effects of distillery effluent on Potamogeton pectinatus L. Bulletin of environmental contamination and toxicology. 2005;74:857-63.
[127] Valderrama LT, Del Campo CM, Rodriguez CM, de-Bashan LE, Bashan Y. Treatment of recalcitrant wastewater from ethanol and citric acid production using the microalga Chlorella vulgaris and the macrophyte Lemna minuscula. Water Research. 2002;36:4185-92.
[128] Saha N, Balakrishnan M, Batra V. Improving industrial water use: case study for an Indian distillery. Resources, Conservation and Recycling. 2005;43:163-74.
[129] Sankaran K, Premalatha M, Vijayasekaran M, Somasundaram V. DEPHY project: Distillery wastewater treatment through anaerobic digestion and phycoremediation—A green industrial approach. Renewable and Sustainable Energy Reviews. 2014;37:634-43.
[130] Travieso L, Benítez F, Sánchez E, Borja R, Leon M, Raposo F, et al. Performance of a laboratory-scale microalgae pond for secondary treatment of distillery wastewaters. Chemical and biochemical engineering quarterly. 2008;22:467-73.
[131] Solovchenko A, Pogosyan S, Chivkunova O, Selyakh I, Semenova L, Voronova E, et al. Phycoremediation of alcohol distillery wastewater with a novel Chlorella sorokiniana strain cultivated in a photobioreactor monitored on-line via chlorophyll fluorescence. Algal Research. 2014;6:234-41.

[132] Murata M, Terasawa N, Homma S. Screening of microorganisms to decolorize a model melanoidin and the chemical properties of a microbially treated melanoidin. Bioscience, biotechnology, and biochemistry. 1992;56:1182-7.

[133] Petta L, De Gisi S, Casella P, Farina R, Notarnicola M. Evaluation of the treatability of a winery distillery (vinasse) wastewater by UASB, anoxic-aerobic UF-MBR and chemical precipitation/adsorption. Journal of environmental management. 2017;201:177-89.

[134] Jo Y, Kim J, Hwang S, Lee C. Anaerobic treatment of rice winery wastewater in an upflow filter packed with steel slag under different hydraulic loading conditions. Biores Tech. 2015;193:53-61.

[135] Tansengco M, Herrera D, Tejano J. Treatment of Molasses-Based Distillery Wastewater in a PilotScale Anaerobic Sequencing Batch Reactor (ASBR). Electronic Journal of Biology. 2016;12:367-77.

[136] Wolmarans B, De Villiers GH. Start-up of a UASB effluent treatment plant on distillery wastewater. Water SA. 2002;28:63-8.

[137] Yu H-Q, Zhao Q-B, Tang Y. Anaerobic treatment of winery wastewater using laboratory-scale multi- and single-fed filters at ambient temperatures. Process biochemistry. 2006;41:2477-81.

[138] Jain M, Bhatnagar L, Zeikus J. Biochemical pathways for methane fermentation and use of granulated biomass for high-rate anaerobic digestion. International Conference on Biogas Technologies and Implementation Strategies Pune (India) 10-15 Jan 19901990.

[139] Nandy T, Shastry S, Kaul S. Wastewater management in a cane molasses distillery involving bioresource recovery. Journal of Environmental Management. 2002;65:25-38.

[140] Jiménez AM, Borja R, Martín A. A comparative kinetic evaluation of the anaerobic digestion of untreated molasses and molasses previously fermented with Penicillium decumbens in batch reactors. Biochemical Engineering Journal. 2004;18:121-32.

[141] Patel H, Madamwar D. Biomethanation of low pH petrochemical wastewater using up-flow fixed-film anaerobic bioreactors. World Journal of Microbiology and Biotechnology. 2000;16:69-75.

[142] Rao BS. A low cost waste treatment method for the disposal of distillery waste (spent wash). Water Research. 1972;6:1275-82.

[143] Singh PN, Robinson T, Dalel S. Treatment of industrial effluents. Distillery effluent. Concise encyclopedia of bioresource technology. 2004:135-42.

[144] Pathade G. A review of current technologies for distillery wastewater treatment. Advances in industrial wastewater treatment: ABD Publishers Jaipur, India; 2003. p. 180-239.

[145] Ruiz C, Torrijos M, Sousbie P, Lebrato Martinez J, Moletta R, Delgenès J-P. Treatment of winery wastewater by an anaerobic sequencing batch reactor. Water science and technology. 2002;45:219-24.

[146] Banerjee S, Biswas G. Studies on biomethanation of distillery wastes and its mathematical analysis. Chemical Engineering Journal. 2004;102:193-201.

[147] Vijayaraghavan K, Ramanujam T. Performance of anaerobic contact filter in series for treating distillery spentwash. Bioprocess Engineering. 2000;22:109-14.

[148] Blonskaja V, Menert A, Vilu R. Use of two-stage anaerobic treatment for distillery waste. Advances in Environmental Research. 2003;7:671-8.

[149] Collins G, Foy C, McHugh S, Mahony T, O'Flaherty V. Anaerobic biological treatment of phenolic wastewater at 15–18 C. Water Research. 2005;39:1614-20.

[150] Goyal S, Seth R, Handa B. Diphasic fixed-film biomethanation of distillery spentwash. Biores Tech. 1996;56:239-44.

[151] Garcia-Calderon D, Buffiere P, Moletta R, Elmaleh S. Anaerobic digestion of wine distillery wastewater in down-flow fluidized bed. Water Research. 1998;32:3593-600.

[152] Akunna JC, Clark M. Performance of a granular-bed anaerobic baffled reactor (GRABBR) treating whisky distillery wastewater. Biores Tech. 2000;74:257-61.

[153] Syutsubo K, Harada H, Ohashi A, Suzuki H. An effective start-up of thermophilic UASB reactor by seeding mesophilically-grown granular sludge. Water Science and Technology. 1997;36:391-8.
[154] Sanchez Riera F, Cordoba P, Siñeriz F. Use of the UASB reactor for the anaerobic treatment of stillage from sugar cane molasses. Biotechnology and bioengineering. 1985;27:1710-6.
[155] Acharya BK, Mohana S, Madamwar D. Anaerobic treatment of distillery spent wash–A study on upflow anaerobic fixed film bioreactor. Biores Tech. 2008;99:4621-6.
[156] Moletta R. Winery and distillery wastewater treatment by anaerobic digestion. Water Science and Technology. 2005;51:137.
[157] Harada H, Uemura S, Chen A-C, Jayadevan J. Anaerobic treatment of a recalcitrant distillery wastewater by a thermophilic UASB reactor. Biores Tech. 1996;55:215-21.
[158] Torrijos M, Moletta R. Winery wastewater depollution by sequencing batch reactor. Water Science and Technology. 1997;35:249-57.
[159] Kannan A, Upreti RK. Influence of distillery effluent on germination and growth of mung bean (Vigna radiata) seeds. Journal of Hazardous Materials. 2008;153:609-15.
[160] Watanabe Y, Sugi R, Tanaka Y, Hayashida S. Enzymatic decolorization of melanoidin by Coriolus sp. No. 20 [melanoidin in distillery waste is one of the source of water pollution]. Agricultural and Biological Chemistry (Japan). 1982.
[161] Ohmomo S, Aoshima I, Tozawa Y, Sakurada N, Ueda K. Purification and some properties of melanoidin decolorizing enzymes, P-III and P-IV, from mycelia of Coriolus versicolor Ps4a. Agricultural and biological chemistry. 1985;49:2047-53.
[162] Mansur M, Suárez T, Fernández-Larrea JB, Brizuela MA, Gonzalez AE. Identification of a laccase gene family in the new lignin-degrading basidiomycete CECT 20197. Applied and Environmental Microbiology. 1997;63:2637-46.
[163] Hayase F, Kim SB, Kato H. Decolorization and degradation products of the melanoidins by hydrogen peroxide. Agricultural and Biological Chemistry. 1984;48:2711-7.
[164] Sirianuntapiboon S, Somchai P, Ohmomo S, Atthasampunna P. Screening of filamentous fungi having the ability to decolorize molasses pigments. Agricultural and biological chemistry. 1988;52:387-92.
[165] Patil P, Kapadnis B, Dhamankar V. Decolorisation of synthetic melanoidin and biogas effluent by immobilised fungal isolate of Aspergillus niger UM2. Indian Sugar. 2003;53:167-73.
[166] Ohmomo S, Kaneko Y, Sirianuntapiboon S, Somchai P, Atthasampunna P, Nakamura I. Decolorization of molasses waste water by a thermophilic strain, Aspergillus fumigatus G-2-6. Agricultural and biological chemistry. 1987;51:3339-46.
[167] Mahugo Santana C, Sosa Ferrera Z, Esther Torres Padrón M, Juan Santana Rodríguez J. Methodologies for the extraction of phenolic compounds from environmental samples: new approaches. Molecules. 2009;14:298-320.
[168] Khezeli T, Daneshfar A, Sahraei R. A green ultrasonic-assisted liquid–liquid microextraction based on deep eutectic solvent for the HPLC-UV determination of ferulic, caffeic and cinnamic acid from olive, almond, sesame and cinnamon oil. Talanta. 2016;150:577-85.
[169] Soquetta MB, Terra LdM, Bastos CP. Green technologies for the extraction of bioactive compounds in fruits and vegetables. CyTA-Journal of Food. 2018;16:400-12.
[170] Ruesgas-Ramón M, Figueroa-Espinoza MC, Durand E. Application of deep eutectic solvents (DES) for phenolic compounds extraction: Overview, challenges, and opportunities. Journal of Agricultural and Food Chemistry. 2017;65:3591-601.
[171] Sarris D, Papanikolaou S. Biotechnological production of ethanol: biochemistry, processes and technologies. Engineering in life sciences. 2016;16:307-29.
[172] Sangave PC, Pandit AB. Ultrasound pre-treatment for enhanced biodegradability of the distillery wastewater. Ultrasonics sonochemistry. 2004;11:197-203.

[173] Zhang X, Zhang Y, Ngo HH, Guo W, Wen H, Zhang D, et al. Characterization and sulfonamide antibiotics adsorption capacity of spent coffee grounds based biochar and hydrochar. Science of The Total Environment. 2020;716:137015.

[174] Ahmed S, Unar IN, Khan HA, Maitlo G, Mahar RB, Jatoi AS, et al. Experimental study and dynamic simulation of melanoidin adsorption from distillery effluent. Environmental Science and Pollution Research. 2020;27:9619-36.

[175] Wongcharee S, Aravinthan V. Application of mesoporous magnetic nanosorbent developed from macadamia nut shell residues for the removal of recalcitrant melanoidin and its fractions. Separation Science and Technology. 2020;55:1636-49.

[176] Arulmathi P, Elangovan G. Applications of response surface methodology and artificial neural network for decolorization of distillery spent wash by using activated Piper nigrum. Journal of environmental biology. 2016;37:1255.

[177] Al Prol AE, Abd El Azzem M, Amer A, El-Metwally ME, Abd El-Hamid HT, El-Moselhy KM. Adsorption of cadmium (II) ions from aqueous solution onto mango leaves. Asian Journal of Physical and Chemical Sciences. 2017:1-11.

[178] Abdolali A, Guo W, Ngo H, Chen S, Nguyen N, Tung K. Typical lignocellulosic wastes and by-products for biosorption process in water and wastewater treatment: a critical review. Biores Tech. 2014;160:57-66.

[179] Hasan A, Pattanayek SK, Pandey LM. Effect of functional groups of self-assembled monolayers on protein adsorption and initial cell adhesion. ACS Biomaterials Science & Engineering. 2018;4:3224-33.

[180] Pandey LM. Surface engineering of nano-sorbents for the removal of heavy metals: Interfacial aspects. Journal of Environmental Chemical Engineering. 2021;9:104586.

[181] Pandey LM, Pattanayek SK. Relation between the wetting effect and the adsorbed amount of water-soluble polymers or proteins at various interfaces. Journal of Chemical & Engineering Data. 2013;58:3440-6.

[182] Pandey LM, Pattanayek SK, Delabouglise D. Properties of adsorbed bovine serum albumin and fibrinogen on self-assembled monolayers. The Journal of Physical Chemistry C. 2013;117:6151-60.

[183] Fito J, Tefera N, Van Hulle SW. Adsorption of distillery spent wash on activated bagasse fly ash: kinetics and thermodynamics. Journal of environmental chemical engineering. 2017;5:5381-8.

[184] Nure JF, Shibeshi NT, Asfaw SL, Audenaert W, Van Hulle SW. COD and colour removal from molasses spent wash using activated carbon produced from bagasse fly ash of Matahara sugar factory, Oromiya region, Ethiopia. Water SA. 2017;43:470-9.

[185] Pandey LM, Pattanayek SK. Hybrid surface from self-assembled layer and its effect on protein adsorption. Applied surface science. 2011;257:4731-7.

[186] Jawed A, Pandey LM. Application of bimetallic Al-doped ZnO nano-assembly for heavy metal removal and decontamination of wastewater. Water Science and Technology. 2019;80:2067-78.

[187] Echavarría A, Pagán J, Ibarz A. Melanoidins formed by Maillard reaction in food and their biological activity. Food Engineering Reviews. 2012;4:203-23.

[188] Tiwari S, Gaur R, Singh R. Decolorization of a recalcitrant organic compound (Melanoidin) by a novel thermotolerant yeast, Candida tropicalis RG-9. BMC biotechnology. 2012;12:1-8.

[189] Kaushik A, Basu S, Singh K, Batra V, Balakrishnan M. Activated carbon from sugarcane bagasse ash for melanoidins recovery. Journal of environmental management. 2017;200:29-34.

[190] Federation WE, Association A. Standard methods for the examination of water and wastewater. American Public Health Association (APHA): Washington, DC, USA. 2005.

[191] Ezechi EH, bin Mohamed Kutty SR, Malakahmad A, Isa MH. Characterization and optimization of effluent dye removal using a new low cost adsorbent: equilibrium, kinetics and thermodynamic study. Process Safety and Environmental Protection. 2015;98:16-32.

[192] Markeb AA, Llimós-Turet J, Ferrer I, Blánquez P, Alonso A, Sánchez A, et al. The use of magnetic iron oxide based nanoparticles to improve microalgae harvesting in real wastewater. Water research. 2019;159:490-500.

[193] Pandey LM. Enhanced adsorption capacity of designed bentonite and alginate beads for the effective removal of methylene blue. Applied Clay Science. 2019;169:102-11.

[194] Sharma S, Hasan A, Kumar N, Pandey LM. Removal of methylene blue dye from aqueous solution using immobilized Agrobacterium fabrum biomass along with iron oxide nanoparticles as biosorbent. Environmental Science and Pollution Research. 2018;25:21605-15.

[195] Al-Sakkari EG, Abdeldayem OM, Genina EE, Amin L, Bahgat NT, Rene ER, et al. New alginate-based interpenetrating polymer networks for water treatment: A response surface methodology based optimization study. International journal of biological macromolecules. 2020;155:772-85.

[196] Shokri A, Daraei P, Zereshki S. Water decolorization using waste cooking oil: An optimized green emulsion liquid membrane by RSM. Journal of Water Process Engineering. 2020;33:101021.

[197] Yazdankish E, Foroughi M, Azqhandi MHA. Capture of I131 from medical-based wastewater using the highly effective and recyclable adsorbent of g-C3N4 assembled with Mg-Co-Al-layered double hydroxide. Journal of hazardous materials. 2020;389:122151.

[198] Sharma S, Malik A, Satya S. Application of response surface methodology (RSM) for optimization of nutrient supplementation for Cr (VI) removal by Aspergillus lentulus AML05. Journal of Hazardous Materials. 2009;164:1198-204.

[199] Langmuir I, Schaefer VJ. The effect of dissolved salts on insoluble monolayers. Journal of the American Chemical Society. 1937;59:2400-14.

[200] Freundlich H. Ueber Kolloidfällung und adsorption. Zeitschrift für Chemie und Industrie der Kolloide. 1907;1:321-31.

[201] Goswami M, Phukan P. Enhanced adsorption of cationic dyes using sulfonic acid modified activated carbon. Journal of Environmental Chemical Engineering. 2017;5:3508-17.

[202] Celebi O, Üzüm Ç, Shahwan T, Erten HN. A radiotracer study of the adsorption behavior of aqueous Ba2+ ions on nanoparticles of zero-valent iron. Journal of Hazardous Materials. 2007;148:761-7.

[203] Tiwari S, Hasan A, Pandey LM. A novel bio-sorbent comprising encapsulated Agrobacterium fabrum (SLAJ731) and iron oxide nanoparticles for removal of crude oil co-contaminant, lead Pb (II). Journal of environmental chemical engineering. 2017;5:442-52.

[204] Patel H. Characterization and adsorptive treatment of distillery spent wash using bagasse fly ash. Arabian Journal for Science and Engineering. 2021:1-11.

[205] Donyagard F, Zarei AR, Rezaei-Vahidian H. Application of magnetic carbon nanocomposites to remove melanoidin from aqueous media: kinetic and isotherm studies. Research on Chemical Intermediates. 2017;43:4639-55.

[206] Dolphen R, Thiravetyan P. Adsorption of melanoidins by chitin nanofibers. Chemical Engineering Journal. 2011;166:890-5.

[207] Figaro S, Avril J, Brouers F, Ouensanga A, Gaspard S. Adsorption studies of molasse's wastewaters on activated carbon: Modelling with a new fractal kinetic equation and evaluation of kinetic models. Journal of hazardous materials. 2009;161:649-56.

[208] Ojijo VO, Onyango MS, Ochieng A, Otieno FA. Decolourization of melanoidin containing wastewater using South African coal fly ash. International Journal of Civil and Environmental Engineering. 2010;2:17-23.

[209] Weber Jr WJ, Morris JC. Kinetics of adsorption on carbon from solution. Journal of the sanitary engineering division. 1963;89:31-59.

[210] Pauletto PS, Lütke SF, Dotto GL, Salau NPG. Adsorption mechanisms of single and simultaneous removal of pharmaceutical compounds onto activated carbon: Isotherm and thermodynamic modeling. Journal of Molecular Liquids. 2021:116203.

[211] Mohsin GF, Schmitt F-J, Kanzler C, Epping JD, Flemig S, Hornemann A. Structural characterization of melanoidin formed from d-glucose and l-alanine at different temperatures applying FTIR, NMR, EPR, and MALDI-ToF-MS. Food chemistry. 2018;245:761-7.
[212] Norde W. Colloids and interfaces in life sciences and bionanotechnology: CRC Press; 2011.
[213] El Haddad M, Regti A, Laamari MR, Slimani R, Mamouni R, El Antri S, et al. Calcined mussel shells as a new and eco-friendly biosorbent to remove textile dyes from aqueous solutions. Journal of the Taiwan Institute of Chemical Engineers. 2014;45:533-40.
[214] Saxena V, Chandra P, Pandey LM. Design and characterization of novel Al-doped ZnO nanoassembly as an effective nanoantibiotic. Applied Nanoscience. 2018;8:1925-41.
[215] Oosterkamp MJ, Bauer S, Ibáñez AB, Méndez-García C, Hong P-Y, Cann I, et al. Identification of methanogenesis and syntrophy as important microbial metabolic processes for optimal thermophilic anaerobic digestion of energy cane thin stillage. Bioresource Technology Reports. 2019;7:100254.
[216] Verma R, Sharma S, Kundu LM, Pandey LM. Experimental investigation of molasses as a sole nutrient for the production of an alternative metabolite biosurfactant. Journal of Water Process Engineering. 2020;38:101632.
[217] Chandra R, Kumar V, Tripathi S, Sharma P. Heavy metal phytoextraction potential of native weeds and grasses from endocrine-disrupting chemicals rich complex distillery sludge and their histological observations during in-situ phytoremediation. Ecological Engineering. 2018;111:143-56.
[218] Ratna S, Rastogi S, Kumar R. Current trends for distillery wastewater management and its emerging applications for sustainable environment. Journal of Environmental Management. 2021;290:112544.
[219] Moran-Salazar R, Sanchez-Lizarraga A, Rodriguez-Campos J, Davila-Vazquez G, Marino-Marmolejo E, Dendooven L, et al. Utilization of vinasses as soil amendment: consequences and perspectives. SpringerPlus. 2016;5:1-11.
[220] Otieno BO, Apollo SO, Naidoo BE, Ochieng A. Photodecolorisation of melanoidins in vinasse with illuminated TiO_2-ZnO/activated carbon composite. Journal of Environmental Science and Health, Part A. 2017;52:616-23.
[221] Hu Q, Fan L, Gao D. Pilot-scale investigation on the treatment of cellulosic ethanol biorefinery wastewater. Chemical Engineering Journal. 2017;309:409-16.
[222] Chowdhary P, Sammi SR, Pandey R, Kaithwas G, Raj A, Singh J, et al. Bacterial degradation of distillery wastewater pollutants and their metabolites characterization and its toxicity evaluation by using Caenorhabditis elegans as terrestrial test models. Chemosphere. 2020;261:127689.
[223] Hanc A, Hrebeckova T, Kuzel S. Vermicomposting of distillery residues in a vertical-flow windrow system. Waste and Biomass Valorization. 2019;10:3647-57.
[224] Jawed A, Verma R, Saxena V, Pandey LM. 9 - Photocatalytic metal nanoparticles: a green approach for degradation of dyes. In: Shah M, Dave S, Das J, editors. Photocatalytic Degradation of Dyes: Elsevier; 2021. p. 251-75.
[225] Sangave PC, Gogate PR, Pandit AB. Combination of ozonation with conventional aerobic oxidation for distillery wastewater treatment. Chemosphere. 2007;68:32-41.
[226] Yavuz Y. EC and EF processes for the treatment of alcohol distillery wastewater. Separation and purification technology. 2007;53:135-40.
[227] Apollo S, Onyango MS, Ochieng A. An integrated anaerobic digestion and UV photocatalytic treatment of distillery wastewater. Journal of hazardous materials. 2013;261:435-42.
[228] Oller I, Malato S, Sánchez-Pérez J. Combination of advanced oxidation processes and biological treatments for wastewater decontamination—a review. Science of the total environment. 2011;409:4141-66.
[229] Aziz ARA, Asaithambi P, Daud WMABW. Combination of electrocoagulation with advanced oxidation processes for the treatment of distillery industrial effluent. Process Safety and Environmental Protection. 2016;99:227-35.

[230] Cesaro A, Naddeo V, Belgiorno V. Wastewater treatment by combination of advanced oxidation processes and conventional biological systems. Journal of Bioremediation & Biodegradation. 2013;4:1-8.

[231] Cañizares P, Hernández-Ortega M, Rodrigo M, Barrera-Díaz C, Roa-Morales G, Sáez C. A comparison between conductive-diamond electrochemical oxidation and other advanced oxidation processes for the treatment of synthetic melanoidins. Journal of Hazardous Materials. 2009;164:120-5.

[232] Saad WF, Othman AM, Abdel-Fattah M, Ahmad MS. Response surface methodology as an approach for optimization of α-amylase production by the new isolated thermotolerant Bacillus licheniformis WF67 strain in submerged fermentation. Biocatalysis and Agricultural Biotechnology. 2021;32:101944.

[233] Yadav V, Ali J, Garg MC. Biosorption of Methylene Blue Dye from Textile-Industry Wastewater onto Sugarcane Bagasse: Response Surface Modeling, Isotherms, Kinetic and Thermodynamic Modeling. Journal of Hazardous, Toxic, and Radioactive Waste. 2021;25:04020067.

[234] Federation WE, Association A. Standard methods for the examination of water and wastewater. American Public Health Association (APHA): Washington, DC, USA. 2005;21.

[235] Bharagava RN, Chandra R, Rai V. Isolation and characterization of aerobic bacteria capable of the degradation of synthetic and natural melanoidins from distillery effluent. World Journal of Microbiology and Biotechnology. 2009;25:737-44.

[236] Morales FJ. Application of capillary zone electrophoresis to the study of food and food-model melanoidins. Food Chemistry. 2002;76:363-9.

[237] Hashemian S. Fenton-like oxidation of Malachite green solutions: kinetic and thermodynamic study. Journal of Chemistry. 2013;2013.

[238] Rodrigues CS, Neto AR, Duda RM, de Oliveira RA, Boaventura RA, Madeira LM. Combination of chemical coagulation, photo-Fenton oxidation and biodegradation for the treatment of vinasse from sugar cane ethanol distillery. Journal of Cleaner Production. 2017;142:3634-44.

[239] Arimi MM. Modified natural zeolite as heterogeneous Fenton catalyst in treatment of recalcitrants in industrial effluent. Progress in Natural Science: Materials International. 2017;27:275-82.

[240] Tokumura M, Ohta A, Znad HT, Kawase Y. UV light assisted decolorization of dark brown colored coffee effluent by photo-Fenton reaction. Water Research. 2006;40:3775-84.

[241] Tokumura M, Znad HT, Kawase Y. Decolorization of dark brown colored coffee effluent by solar photo-Fenton reaction: Effect of solar light dose on decolorization kinetics. Water Research. 2008;42:4665-73.

[242] Fenton HJH. LXXIII.—Oxidation of tartaric acid in presence of iron. Journal of the Chemical Society, Transactions. 1894;65:899-910.

[243] Brillas E, Casado J. Aniline degradation by Electro-Fenton® and peroxi-coagulation processes using a flow reactor for wastewater treatment. Chemosphere. 2002;47:241-8.

[244] Suhan MBK, Shuchi SB, Anis A, Haque Z, Islam MS. Comparative degradation study of remazol black B dye using electro-coagulation and electro-Fenton process: Kinetics and cost analysis. Environmental Nanotechnology, Monitoring & Management. 2020;14:100335.

[245] Burbano AA, Dionysiou DD, Suidan MT, Richardson TL. Oxidation kinetics and effect of pH on the degradation of MTBE with Fenton reagent. Water Research. 2005;39:107-18.

[246] Anipsitakis GP, Dionysiou DD. Transition metal/UV-based advanced oxidation technologies for water decontamination. Applied Catalysis B: Environmental. 2004;54:155-63.

[247] Coca M, Peña M, González G. Chemical oxidation processes for decolorization of brown-colored molasses wastewater. Ozone: Science and Engineering. 2005;27:365-9.

[248] Raji M, Tahroudi MN, Ye F, Dutta J. Prediction of heterogeneous Fenton process in treatment of melanoidin-containing wastewater using data-based models. Journal of Environmental Management. 2022;307:114518.

[249] Raji M, Mirbagheri SA, Ye F, Dutta J. Nano zero-valent iron on activated carbon cloth support as Fenton-like catalyst for efficient color and COD removal from melanoidin wastewater. Chemosphere. 2021;263:127945.

[250] Hakika DC, Sarto S, Mindaryani A, Hidayat M. Decreasing COD in sugarcane vinasse using the fenton reaction: The effect of processing parameters. Catalysts. 2019;9:881.

[251] Bhoite GM, Vaidya PD. Fenton oxidation and adsorption pretreatment for superior biogas recovery from biomethanated spent wash. Chemical Engineering Communications. 2020;207:1347-57.

[252] Hadavifar M, Zinatizadeh AA, Younesi H, Galehdar M. Fenton and photo-Fenton treatment of distillery effluent and optimization of treatment conditions with response surface methodology. Asia-Pacific Journal of chemical engineering. 2010;5:454-64.

[253] Asaithambi P, Sajjadi B, Aziz ARA. Integrated ozone–photo–Fenton process for the removal of pollutant from industrial wastewater. Chinese Journal of Chemical Engineering. 2017;25:516-22.

[254] Martins RC, Pinto FL, Castro-Silva S, Quinta-Ferreira RM. Flocculation, ozonation, and Fenton's process in the treatment of distillery effluents. Journal of Environmental Engineering. 2013;139:110-6.

[255] Rodrigues CSD, Neto AR, Duda RM, de Oliveira RA, Boaventura RAR, Madeira LM. Combination of chemical coagulation, photo-Fenton oxidation and biodegradation for the treatment of vinasse from sugar cane ethanol distillery. Journal of Cleaner Production. 2017;142:3634-44.

[256] Ioannou LA, Fatta-Kassinos D. Solar photo-Fenton oxidation against the bioresistant fractions of winery wastewater. Journal of Environmental Chemical Engineering. 2013;1:703-12.

[257] Ioannou LA, Michael C, Vakondios N, Drosou K, Xekoukoulotakis NP, Diamadopoulos E, et al. Winery wastewater purification by reverse osmosis and oxidation of the concentrate by solar photo-Fenton. Separation and Purification Technology. 2013;118:659-69.

[258] Guimarães V, Lucas MS, Peres JA. Combination of adsorption and heterogeneous photo-Fenton processes for the treatment of winery wastewater. Environmental Science and Pollution Research. 2019;26:31000-13.

[259] Hoarau J, Caro Y, Grondin I, Petit T. Sugarcane vinasse processing: Toward a status shift from waste to valuable resource. A review. Journal of Water Process Engineering. 2018;24:11-25.

[260] Solomon S. Sugarcane production and development of sugar industry in India. Sugar Tech. 2016;18:588-602.

[261] Wang H-Y, Qian H, Yao W-R. Melanoidins produced by the Maillard reaction: Structure and biological activity. Food Chemistry. 2011;128:573-84.

[262] Mishra D, Kumari S, Jaiswal A, Arya S, Yadav BR, Thul ST, et al. Evaluation of distillery sludge as a soil amendment for improving soil quality and sugarcane (CO-265) yield. Environmental Technology & Innovation. 2021;23:101624.

[263] Chowdhary P, Yadav A, Kaithwas G, Bharagava RN. Distillery wastewater: a major source of environmental pollution and its biological treatment for environmental safety. Green technologies and environmental sustainability: Springer; 2017. p. 409-35.

[264] Castro LEN, Santos JVF, Fagnani KC, Alves HJ, Colpini LMS. Evaluation of the effect of different treatment methods on sugarcane vinasse remediation. Journal of Environmental Science and Health, Part B. 2019;54:791-800.

[265] Espana-Gamboa E, Mijangos-Cortes J, Barahona-Perez L, Dominguez-Maldonado J, Hernández-Zarate G, Alzate-Gaviria L. Vinasses: characterization and treatments. Waste management & research. 2011;29:1235-50.

[266] Bhardwaj S, Ruhela M, Bhutiani R, Ahamad F, Bhardwaj R. Distellery spent wash (DSW) treatment methodogies and challenges with special reference to incineration: An overview. Environment Conservation Journal. 2019;20:135-44.

[267] Umair Hassan M, Aamer M, Umer Chattha M, Haiying T, Khan I, Seleiman MF, et al. Sugarcane distillery spent wash (dsw) as a bio-nutrient supplement: a win-win option for sustainable crop production. Agronomy. 2021;11:183.

[268] MiarAlipour S, Friedmann D, Scott J, Amal R. TiO_2/porous adsorbents: Recent advances and novel applications. Journal of Hazardous Materials. 2018;341:404-23.

[269] Vineetha M, Matheswaran M, Sheeba K. Photocatalytic colour and COD removal in the distillery effluent by solar radiation. Solar Energy. 2013;91:368-73.

[270] Lee KM, Lai CW, Ngai KS, Juan JC. Recent developments of zinc oxide based photocatalyst in water treatment technology: A review. Water Research. 2016;88:428-48.

[271] Shindhal T, Rakholiya P, Varjani S, Pandey A, Ngo HH, Guo W, et al. A critical review on advances in the practices and perspectives for the treatment of dye industry wastewater. Bioengineered. 2021;12:70-87.

[272] Rajeshwar K, Osugi ME, Chanmanee W, Chenthamarakshan CR, Zanoni MVB, Kajitvichyanukul P, et al. Heterogeneous photocatalytic treatment of organic dyes in air and aqueous media. Journal of Photochemistry and Photobiology C: Photochemistry Reviews. 2008;9:171-92.

[273] Samsami S, Mohamadizaniani M, Sarrafzadeh M-H, Rene ER, Firoozbahr M. Recent advances in the treatment of dye-containing wastewater from textile industries: Overview and perspectives. Process Safety and Environmental Protection. 2020;143:138-63.

[274] Jawed A, Kar P, Verma R, Shukla K, Hemanth P, Thakur VK, et al. Integration of biological control with engineered heterojunction nano-photocatalysts for sustainable and effective management of water hyacinth weed. Journal of Environmental Chemical Engineering. 2022;10:106976.

[275] Zhang Q, Li H, Ma Y, Zhai T. ZnSe nanostructures: Synthesis, properties and applications. Progress in Materials Science. 2016;83:472-535.

[276] Zhao X, Li M, Lou X. Sol–gel assisted hydrothermal synthesis of ZnO microstructures: Morphology control and photocatalytic activity. Advanced Powder Technology. 2014;25:372-8.

[277] Nishioka S, Hyodo J, Vequizo JJM, Yamashita S, Kumagai H, Kimoto K, et al. Homogeneous electron doping into nonstoichiometric strontium titanate improves its photocatalytic activity for hydrogen and oxygen evolution. ACS Catalysis. 2018;8:7190-200.

[278] Rahman M, Sarmah T, Dihingia P, Verma R, Sharma S, Kirti, et al. Bulk synthesis of tungsten-oxide nanomaterials by a novel, plasma chemical reactor configuration, studies on their performance for waste-water treatment and hydrogen evolution reactions. Chemical Engineering Journal. 2022;428:131111.

[279] Heng ZW, Chong WC, Pang YL, Koo CH. An overview of the recent advances of carbon quantum dots/metal oxides in the application of heterogeneous photocatalysis in photodegradation of pollutants towards visible-light and solar energy exploitation. Journal of Environmental Chemical Engineering. 2021;9:105199.

[280] Kumar S, Kumar A, Kumar A, Krishnan V. Nanoscale zinc oxide based heterojunctions as visible light active photocatalysts for hydrogen energy and environmental remediation. Catalysis Reviews. 2020;62:346-405.

[281] Apollo S, Onyongo MS, Ochieng A. UV/H_2O_2/TiO_2/Zeolite hybrid system for treatment of molasses wastewater. Iranian Journal of Chemistry and Chemical Engineering (IJCCE). 2014;33:107-17.

[282] Apollo S, Otieno B, Onyango M, Ochieng A. Influence of Zeolite Support on Integrated Biodegradation and Photodegradation of Molasses Wastewater for Organic Load Reduction and Colour Removal. Phyto and Rhizo Remediation: Springer; 2019. p. 287-300.

[283] Benton O, Apollo S, Naidoo B, Ochieng A. Photodegradation of molasses wastewater using TiO_2–ZnO nanohybrid photocatalyst supported on activated carbon. Chemical Engineering Communications. 2016;203:1443-54.

[284] Li X, Ouyang S, Kikugawa N, Ye J. Novel Ag_2ZnGeO_4 photocatalyst for dye degradation under visible light irradiation. Applied Catalysis A: General. 2008;334:51-8.

[285] Takle SP, Naik SD, Khore SK, Ohwal SA, Bhujbal NM, Landge SL, et al. Photodegradation of spent wash, a sugar industry waste, using vanadium-doped TiO_2 nanoparticles. RSC advances. 2018;8:20394-405.

[286] Saldaña-Flores KE, Flores-Estrella RA, Alcaraz-Gonzalez V, Carissimi E, de Souza BG, Ruotolo LAM, et al. Regulation of Hydrogen Peroxide Dosage in a Heterogeneous Photo-Fenton Process. Processes. 2021;9:2167.

[287] Dwyer J, Kavanagh L, Lant P. The degradation of dissolved organic nitrogen associated with melanoidin using a UV/H_2O_2 AOP. Chemosphere. 2008;71:1745-53.

[288] Prabakar C, Muthukumaran S, Raja V. Structural, magnetic and photoluminescence behavior of Ni/Fe doped ZnO nanostructures prepared by co-precipitation method. Optik. 2020;202:163714.

[289] Bharagava RN, Chandra R, Rai V. Isolation and characterization of aerobic bacteria capable of the degradation of synthetic and natural melanoidins from distillery effluent. World Journal of Microbiology and Biotechnology. 2009;25:737.

[290] Mohan L, Avani AV, Kathirvel P, Marnadu R, Packiaraj R, Joshua JR, et al. Investigation on structural, morphological and electrochemical properties of Mn doped WO_3 nanoparticles synthesized by co-precipitation method for supercapacitor applications. Journal of Alloys and Compounds. 2021;882:160670.

[291] Thilagavathi T, Venugopal D, Marnadu R, Chandrasekaran J, Thangaraju D, Palanivel B, et al. WO_3/CoWO4 nanocomposite synthesis using a facile co-precipitation method for enhanced photocatalytic applications. Journal of Physics and Chemistry of Solids. 2021;154:110066.

[292] Martínez-de la Cruz A, Martínez DS, Cuéllar EL. Synthesis and characterization of WO_3 nanoparticles prepared by the precipitation method: Evaluation of photocatalytic activity under vis-irradiation. Solid State Sciences. 2010;12:88-94.

[293] Supothina S, Seeharaj P, Yoriya S, Sriyudthsak M. Synthesis of tungsten oxide nanoparticles by acid precipitation method. Ceramics International. 2007;33:931-6.

[294] Saxena V, Pandey LM. Bimetallic assembly of Fe(III) doped ZnO as an effective nanoantibiotic and its ROS independent antibacterial mechanism. Journal of Trace Elements in Medicine and Biology. 2020;57:126416.

[295] Ngigi EM, Nomngongo PN, Ngila JC. Synthesis and application of Fe-doped WO_3 nanoparticles for photocatalytic degradation of methylparaben using visible–light radiation and H_2O_2. Catalysis Letters. 2019;149:49-60.

[296] Chandra R, Kumar V, Tripathi S. Evaluation of molasses-melanoidin decolourisation by potential bacterial consortium discharged in distillery effluent. 3 Biotech. 2018;8:1-16.

[297] Jawed A, Saxena V, Pandey LM. Engineered nanomaterials and their surface functionalization for the removal of heavy metals: A review. Journal of Water Process Engineering. 2020;33:101009.

[298] Fopase R, Pathode SR, Sharma S, Datta P, Pandey LM. Lipopeptide and essential oil based nanoemulsion for controlled drug delivery. Polymer-Plastics Technology and Materials. 2020;59:2076-86.

[299] Ferreira LC, Ferreira LC, Cardoso VL, Coutinho Filho U. Mn (II) removal from water using emulsion liquid membrane composed of chelating agents and biosurfactant produced in loco. Journal of Water Process Engineering. 2019;29:100792.

[300] Harifi T, Montazer M. A novel magnetic reusable nanocomposite with enhanced photocatalytic activities for dye degradation. Separation and Purification Technology. 2014;134:210-9.

[301] Munir M, Wong K, Xagoraraki I. Release of antibiotic resistant bacteria and genes in the effluent and biosolids of five wastewater utilities in Michigan. Water research. 2011;45:681-93.

[302] Dutta V, Sharma S, Raizada P, Thakur VK, Khan AAP, Saini V, et al. An overview on WO_3 based photocatalyst for environmental remediation. Journal of Environmental Chemical Engineering. 2021;9:105018.
[303] Mohsin M, Bhatti IA, Ashar A, Khan MW, Farooq MU, Khan H, et al. Iron-doped zinc oxide for photocatalyzed degradation of humic acid from municipal wastewater. Applied Materials Today. 2021;23:101047.
[304] Mohsin M, Bhatti IA, Ashar A, Khan MW, Farooq MU, Khan H, et al. Iron-doped zinc oxide for photocatalyzed degradation of humic acid from municipal wastewater. Applied Materials Today. 2021;23:101047.
[305] Reddy IN, Reddy CV, Sreedhar M, Shim J, Cho M, Kim D. Effect of ball milling on optical properties and visible photocatalytic activity of Fe doped ZnO nanoparticles. Materials Science and Engineering: B. 2019;240:33-40.
[306] Nanakkal A, Alexander L. Graphene/BiVO4/TiO_2 nanocomposite: tuning band gap energies for superior photocatalytic activity under visible light. Journal of Materials Science. 2017;52:7997-8006.
[307] Klubnuan S, Suwanboon S, Amornpitoksuk P. Effects of optical band gap energy, band tail energy and particle shape on photocatalytic activities of different ZnO nanostructures prepared by a hydrothermal method. Optical Materials. 2016;53:134-41.
[308] Abdullin KA, Azatkaliev A, Gabdullin M, Kalkozova ZK, Mukashev B, Serikkanov AJPotSS. Preparation of Nanosized Tungsten and Tungsten Oxide Powders. 2018;60:2634-9.
[309] Abdullin KA, Azatkaliev A, Gabdullin M, Kalkozova ZK, Mukashev B, Serikkanov A. Preparation of Nanosized Tungsten and Tungsten Oxide Powders. Physics of the Solid State. 2018;60:2634-9.
[310] Ram J, Singh R, Gupta R, Kumar V, Singh F, Kumar R. Effect of annealing on the surface morphology, optical and and structural properties of nanodimensional tungsten oxide prepared by coprecipitation technique. Journal of Electronic Materials. 2019;48:1174-83.
[311] Sungpanich J, Thongtem T, Thongtem S. Large-scale synthesis of WO_3 nanoplates by a microwave-hydrothermal method. Ceramics International. 2012;38:1051-5.
[312] Pang HF, Xiang X, Li ZJ, Fu YQ, Zu XT. Hydrothermal synthesis and optical properties of hexagonal tungsten oxide nanocrystals assisted by ammonium tartrate. physica status solidi (a). 2012;209:537-44.
[313] Abbaspoor M, Aliannezhadi M, Tehrani FS. Effect of solution pH on as-synthesized and calcined WO_3 nanoparticles synthesized using sol-gel method. Optical Materials. 2021;121:111552.
[314] Hunge Y, Yadav A, Mohite B, Mathe V, Bhosale C. Photoelectrocatalytic degradation of sugarcane factory wastewater using WO_3/ZnO thin films. Journal of Materials Science: Materials in Electronics. 2018;29:3808-16.
[315] Hunge Y, Mahadik M, Mohite V, Kumbhar S, Deshpande N, Rajpure K, et al. Photoelectrocatalytic degradation of methyl blue using sprayed WO_3 thin films. Journal of Materials Science: Materials in Electronics. 2016;27:1629-35.
[316] Fakhri A, Behrouz S. Photocatalytic properties of tungsten trioxide (WO_3) nanoparticles for degradation of Lidocaine under visible and sunlight irradiation. Solar Energy. 2015;112:163-8.
[317] Li M, Pokhrel S, Jin X, Mädler L, Damoiseaux R, Hoek EM. Stability, bioavailability, and bacterial toxicity of ZnO and iron-doped ZnO nanoparticles in aquatic media. Environmental science & technology. 2011;45:755-61.
[318] Azeez F, Al-Hetlani E, Arafa M, Abdelmonem Y, Nazeer AA, Amin MO, et al. The effect of surface charge on photocatalytic degradation of methylene blue dye using chargeable titania nanoparticles. Scientific reports. 2018;8:1-9.
[319] Saxena V, Sharma S, Pandey LM. Fe(III) doped ZnO nano-assembly as a potential heterogeneous nano-catalyst for the production of biodiesel. Materials Letters. 2019;237:232-5.

[320] Chen G, Peng J, Song C, Zeng F, Pan F. Interplay between chemical state, electric properties, and ferromagnetism in Fe-doped ZnO films. Journal of Applied Physics. 2013;113:104503.
[321] Subramani K, Sathish M. Facile synthesis of ZnO nanoflowers/reduced graphene oxide nanocomposite using zinc hexacyanoferrate for supercapacitor applications. Materials Letters. 2019;236:424-7.
[322] Srivastava VC. Photocatalytic oxidation of dye bearing wastewater by iron doped zinc oxide. Industrial & Engineering Chemistry Research. 2013;52:17790-9.
[323] Sharma N, Jandaik S, Kumar S, Chitkara M, Sandhu IS. Synthesis, characterisation and antimicrobial activity of manganese-and iron-doped zinc oxide nanoparticles. Journal of Experimental Nanoscience. 2016;11:54-71.
[324] Akbar Jan F, Wajidullah, Ullah R, Ullah N, Salman, Usman M. Exploring the environmental and potential therapeutic applications of Myrtus communis L. assisted synthesized zinc oxide (ZnO) and iron doped zinc oxide (Fe-ZnO) nanoparticles. Journal of Saudi Chemical Society. 2021;25:101278.
[325] Zhang Y, Ram MK, Stefanakos EK, Goswami DY. Enhanced photocatalytic activity of iron doped zinc oxide nanowires for water decontamination. Surface and Coatings Technology. 2013;217:119-23.
[326] Santos L, Silveira CM, Elangovan E, Neto JP, Nunes D, Pereira L, et al. Synthesis of WO_3 nanoparticles for biosensing applications. Sensors and Actuators B: Chemical. 2016;223:186-94.
[327] Kolhe PS, Mutadak P, Maiti N, Sonawane KM. Synthesis of WO_3 nanoflakes by hydrothermal route and its gas sensing application. Sensors and Actuators A: Physical. 2020;304:111877.
[328] Jiang N, Zhao Y, Shang K, Lu N, Li J, Wu Y. Degradation of toluene by pulse-modulated multistage DBD plasma: Key parameters optimization through response surface methodology (RSM) and degradation pathway analysis. Journal of Hazardous Materials. 2020;393:122365.
[329] Fang H, Oberoi AS, He Z, Khanal SK, Lu H. Ciprofloxacin-degrading Paraclostridium sp. isolated from sulfate-reducing bacteria-enriched sludge: Optimization and mechanism. Water Research. 2021;191:116808.
[330] Saien J, Shahrezaei F. Organic pollutants removal from petroleum refinery wastewater with nanotitania photocatalyst and UV light emission. International Journal of Photoenergy. 2012;2012.
[331] Ani IJ, Akpan UG, Olutoye MA, Hameed BH. Photocatalytic degradation of pollutants in petroleum refinery wastewater by TiO_2- and ZnO-based photocatalysts: Recent development. Journal of Cleaner Production. 2018;205:930-54.
[332] Suganthi KS, Rajan KS. Temperature induced changes in ZnO–water nanofluid: Zeta potential, size distribution and viscosity profiles. International Journal of Heat and Mass Transfer. 2012;55:7969-80.
[333] Tang C-c, Fang Y-f, Cao X-q, Tian H-l, Huang Y-p. Regulation of visible-light-driven photocatalytic degradation of Rhodamine B on BiOBr via zeta potential. Research on Chemical Intermediates. 2020;46:509-20.
[334] Rafigh SM, Rahimpour Soleymani A. Melanoidin removal from molasses wastewater using graphene oxide nanosheets. Separation Science and Technology. 2020;55:2281-93.
[335] Bredemeier D, Walter D, Schmidt J. Light-induced lifetime degradation in high-performance multicrystalline silicon: Detailed kinetics of the defect activation. Solar Energy Materials and Solar Cells. 2017;173:2-5.
[336] Chen D, Cheng Y, Zhou N, Chen P, Wang Y, Li K, et al. Photocatalytic degradation of organic pollutants using TiO_2-based photocatalysts: A review. Journal of Cleaner Production. 2020;268:121725.
[337] Patil AB, Patil KR, Pardeshi SK. Enhancement of oxygen vacancies and solar photocatalytic activity of zinc oxide by incorporation of nonmetal. Journal of Solid State Chemistry. 2011;184:3273-9.
[338] Anju S, Yesodharan S, Yesodharan E. Zinc oxide mediated sonophotocatalytic degradation of phenol in water. Chemical Engineering Journal. 2012;189:84-93.

[339] Satori H, Kawase Y. Decolorization of dark brown colored coffee effluent using zinc oxide particles: The role of dissolved oxygen in degradation of colored compounds. Journal of Environmental Management. 2014;139:172-9.

[340] Meshram S, Limaye R, Ghodke S, Nigam S, Sonawane S, Chikate R. Continuous flow photocatalytic reactor using ZnO–bentonite nanocomposite for degradation of phenol. Chemical Engineering Journal. 2011;172:1008-15.

[341] Zhu H-Y, Xiao L, Jiang R, Zeng G-M, Liu L. Efficient decolorization of azo dye solution by visible light-induced photocatalytic process using SnO2/ZnO heterojunction immobilized in chitosan matrix. Chemical Engineering Journal. 2011;172:746-53.

[342] Vineetha MN, Matheswaran M, Sheeba KN. Photocatalytic colour and COD removal in the distillery effluent by solar radiation. Solar Energy. 2013;91:368-73.

[343] Yu Q, Yan Y, Lin H, Li H, Zheng Y, Jiao B, et al. Biosurfactants enhanced electrokinetic treatment of Cr from chromite ore processing residue based on chemical fractions. Journal of Water Process Engineering. 2020;36:101252.

[344] Gudiña EJ, Rangarajan V, Sen R, Rodrigues LR. Potential therapeutic applications of biosurfactants. Trends in pharmacological sciences. 2013;34:667-75.

[345] Sharma S, Datta P, Kumar B, Tiwari P, Pandey LM. Production of novel rhamnolipids via biodegradation of waste cooking oil using Pseudomonas aeruginosa MTCC7815. Biodegradation. 2019;30:301-12.

[346] Sharma S, Tiwari S, Hasan A, Saxena V, Pandey LM. Recent advances in conventional and contemporary methods for remediation of heavy metal-contaminated soils. 3 Biotech. 2018;8:1-18.

[347] Mishra B, Varjani S, Kumar G, Awasthi MK, Awasthi SK, Sindhu R, et al. Microbial approaches for remediation of pollutants: innovations, future outlook, and challenges. Energy & Environment. 2021;32:1029-58.

[348] Srivastava RK, Shetti NP, Reddy KR, Aminabhavi TMJSotTE. Sustainable energy from waste organic matters via efficient microbial processes. 2020;722:137927.

[349] Duncan J, Bokhary A, Fatehi P, Kong F, Lin H, Liao BJBt. Thermophilic membrane bioreactors: a review. 2017;243:1180-93.

[350] Singh G, Bakshi S, Bandyopadhyay K, Bose S, Nayak R, Paul DJB, et al. Enhanced biodegradation of melanoidin pigment from spentwash using PDMS-immobilized microbes via 'repeated addition'strategy. 2021;33:101990.

[351] Kumar V, Wati L, Nigam P, Banat I, Yadav B, Singh D, et al. Decolorization and biodegradation of anaerobically digested sugarcane molasses spent wash effluent from biomethanation plants by white-rot fungi. Process Biochemistry. 1998;33:83-8.

[352] Zhang B, Zhao H, Zhou S, Shi C, Wang C, Ni J. A novel UASB–MFC–BAF integrated system for high strength molasses wastewater treatment and bioelectricity generation. Bioresource Technology. 2009;100:5687-93.

[353] Al-Bahry S, Al-Wahaibi Y, Elshafie A, Al-Bemani A, Joshi S, Al-Makhmari H, et al. Biosurfactant production by Bacillus subtilis B20 using date molasses and its possible application in enhanced oil recovery. International Biodeterioration & Biodegradation. 2013;81:141-6.

[354] De Vrieze J, Plovie K, Verstraete W, Boon N. Co-digestion of molasses or kitchen waste with high-rate activated sludge results in a diverse microbial community with stable methane production. Journal of Environmental Management. 2015;152:75-82.

[355] Saimmai A, Sobhon V, Maneerat S. Molasses as a whole medium for biosurfactants production by Bacillus strains and their application. Applied biochemistry and biotechnology. 2011;165:315-35.

[356] Sohsalam P, Sirianuntapiboon S. Feasibility of using constructed wetland treatment for molasses wastewater treatment. Bioresource technology. 2008;99:5610-6.

[357] Verma R, Sharma S, Kundu LM, Pandey LMJJoWPE. Experimental investigation of molasses as a sole nutrient for the production of an alternative metabolite biosurfactant. 2020;38:101632.
[358] Shinde AB, Nakade DB. Decolourization of Distillery Spent Wash by Bacillus coagulans ABS012. 2021.
[359] Kumar P, Chandra RJBoec, toxicology. Detoxification of distillery effluent through Bacillus thuringiensis (MTCC 4714) enhanced phytoremediation potential of Spirodela polyrrhiza (L.) Schliden. 2004;73:903-10.
[360] Kumar P, Chandra RJBT. Decolourisation and detoxification of synthetic molasses melanoidins by individual and mixed cultures of Bacillus spp. 2006;97:2096-102.
[361] Kaczorek E, Pacholak A, Zdarta A, Smułek WJC, Interfaces. The impact of biosurfactants on microbial cell properties leading to hydrocarbon bioavailability increase. 2018;2:35.
[362] Mnif I, Maktouf S, Fendri R, Kriaa M, Ellouze S, Ghribi DJES, et al. Improvement of methyl orange dye biotreatment by a novel isolated strain, Aeromonas veronii GRI, by SPB1 biosurfactant addition. 2016;23:1742-54.
[363] Sharma S, Pandey LM. Production of biosurfactant by Bacillus subtilis RSL-2 isolated from sludge and biosurfactant mediated degradation of oil. Bioresource Technology. 2020;307:123261.
[364] Thanapimmetha A, Srinophakun P, Amat S, Saisriyoot M. Decolorization of molasses-based distillery wastewater by means of pulse electro-Fenton process. Journal of Environmental Chemical Engineering. 2017;5:2305-12.
[365] Farias D, Maugeri-Filho F. Sequential fed batch extractive fermentation for enhanced bioethanol production using recycled Spathaspora passalidarum and mixed sugar composition. Fuel. 2021;288:119673.
[366] Datta P, Tiwari P, Pandey LM. Isolation and characterization of biosurfactant producing and oil degrading Bacillus subtilis MG495086 from formation water of Assam oil reservoir and its suitability for enhanced oil recovery. Bioresource Technology. 2018;270:439-48.
[367] Sharma S, Pandey LMJLiAM. Integration of biosorption and biodegradation in a fed-batch mode for the enhanced crude oil remediation. 2021;73:471-6.
[368] Miller GL. Use of dinitrosalicylic acid reagent for determination of reducing sugar. Analytical chemistry. 1959;31:426-8.
[369] Lima RB, de Aguiar CL, Galaverna R, Baptista AS, Eberlin MN, Arthur V. Sucrose and color profiles in sugarcane (Saccharum sp.) juice analyzed by UFLC-ELSD and Synapt High-Definition Mass Spectrometry during radiation treatment. Radiation Physics and Chemistry. 2016;121:99-105.
[370] Panda SK, Maiti SK. An approach for simultaneous detoxification and increment of cellulase enzyme production by Trichoderma reesei using rice straw. Energy Sources, Part A: Recovery, Utilization, and Environmental Effects. 2019;41:2691-703.
[371] Jo M-S, Rene ER, Kim S-H, Park H-S. An analysis of synergistic and antagonistic behavior during BTEX removal in batch system using response surface methodology. Journal of hazardous materials. 2008;152:1276-84.
[372] Işildar A. Two-step leaching of valuable metals from discarded printed circuit boards, process kinetics, and optimization using response surface methodology. Metal Recovery from Electronic Waste: Biological Versus Chemical Leaching for Recovery of Copper and Gold: CRC Press; 2018. p. 145-68.
[373] Datta P, Tiwari P, Pandey LM. Oil washing proficiency of biosurfactant produced by isolated Bacillus tequilensis MK 729017 from Assam reservoir soil. Journal of Petroleum Science and Engineering. 2020;195:107612.
[374] Sharma S, Verma R, Dhull S, Maiti SK, Pandey LM. Biodegradation of waste cooking oil and simultaneous production of rhamnolipid biosurfactant by Pseudomonas aeruginosa P7815 in batch and fed-batch bioreactor. Bioprocess Biosyst Eng. 2021.

[375] Sharma S, Tiwari P, Pandey L. Identification of Various Metabolites like Gases, Biopolymers and Biosurfactants. Microbial Enhanced Oil Recovery: Springer; 2022. p. 197-220.
[376] Sharma S, Pandey LMJBt. Production of biosurfactant by Bacillus subtilis RSL-2 isolated from sludge and biosurfactant mediated degradation of oil. 2020;307:123261.
[377] Makkar R, Cameotra S. An update on the use of unconventional substrates for biosurfactant production and their new applications. Applied microbiology and biotechnology. 2002;58:428-34.
[378] Castañeda-Ayarza JA, Cortez LAB. Final and B molasses for fuel ethanol production and some market implications. Renewable and Sustainable Energy Reviews. 2017;70:1059-65.
[379] Leal MRLV, Leite JGDB, Chagas MF, Da Maia R, Cortez LAB. Feasibility assessment of converting sugar mills to bioenergy production in Africa. Agriculture. 2016;6:45.
[380] Mahanty B, Pakshirajan K, Dasu VV. A two liquid phase partitioning bioreactor system for the biodegradation of pyrene: comparative evaluation and cost–benefit analysis. Journal of Chemical Technology & Biotechnology. 2010;85:349-55.
[381] Shuler ML. Bioprocess enzineering. Prentice-Hall. 1992:412-20.
[382] Joshi SJ, Al-Wahaibi YM, Al-Bahry SN, Elshafie AE, Al-Bemani AS, Al-Bahri A, et al. Production, characterization, and application of Bacillus licheniformis W16 biosurfactant in enhancing oil recovery. Frontiers in microbiology. 2016;7:1853.
[383] Rane AN, Baikar VV, Ravi Kumar V, Deopurkar RL. Agro-industrial wastes for production of biosurfactant by Bacillus subtilis ANR 88 and its application in synthesis of silver and gold nanoparticles. Frontiers in microbiology. 2017;8:492.
[384] Kashkouli YR, Mogharei A, Mousavian S, Vahabzadeh F. Performance of artificial neural network for predicting fermentation characteristics in biosurfactant production by Bacillus subtilis ATCC 6633 using sugar cane molasses. International Journal of Food Engineering. 2011;7.
[385] Al-Wahaibi Y, Joshi S, Al-Bahry S, Elshafie A, Al-Bemani A, Shibulal B. Biosurfactant production by Bacillus subtilis B30 and its application in enhancing oil recovery. Colloids and Surfaces B: Biointerfaces. 2014;114:324-33.
[386] Willenbacher J, Zwick M, Mohr T, Schmid F, Syldatk C, Hausmann R. Evaluation of different Bacillus strains in respect of their ability to produce Surfactin in a model fermentation process with integrated foam fractionation. Applied microbiology and biotechnology. 2014;98:9623-32.
[387] Sousa M, Dantas I, Feitosa F, Alencar A, Soares S, Melo V, et al. Performance of a biosurfactant produced by Bacillus subtilis LAMI005 on the formation of oil/biosurfactant/water emulsion: study of the phase behaviour of emulsified systems. Brazilian Journal of Chemical Engineering. 2014;31:613-23.
[388] Willenbacher J, Rau J-T, Rogalla J, Syldatk C, Hausmann R. Foam-free production of Surfactin via anaerobic fermentation of Bacillus subtilis DSM 10T. Amb Express. 2015;5:1-9.
[389] Heryani H, Putra MD. Kinetic study and modeling of biosurfactant production using Bacillus sp. Electronic Journal of Biotechnology. 2017;27:49-54.
[390] Yang H, Li X, Li X, Yu H, Shen Z. Identification of lipopeptide isoforms by MALDI-TOF-MS/MS based on the simultaneous purification of iturin, fengycin, and surfactin by RP-HPLC. Analytical and Bioanalytical Chemistry. 2015;407:2529-42.
[391] Nakano M, Magnuson R, Myers A, Curry J, Grossman A, Zuber P. srfA is an operon required for surfactin production, competence development, and efficient sporulation in Bacillus subtilis. Journal of bacteriology. 1991;173:1770-8.
[392] Sharma S, Verma R, Dhull S, Maiti SK, Pandey LM. Biodegradation of waste cooking oil and simultaneous production of rhamnolipid biosurfactant by Pseudomonas aeruginosa P7815 in batch and fed-batch bioreactor. Bioprocess and Biosystems Engineering. 2022;45:309-19.
[393] Doran PM. Bioprocess engineering principles: Academic Press; 2013.

[394] Joy S, Rahman PKSM, Khare SK, Soni SR, Sharma S. Statistical and sequential (fill-and-draw) approach to enhance rhamnolipid production using industrial lignocellulosic hydrolysate C6 stream from Achromobacter sp. (PS1). Bioresource Technology. 2019;288:121494.

[395] Chen S-Y, Wei Y-H, Chang J-S. Repeated pH-stat fed-batch fermentation for rhamnolipid production with indigenous Pseudomonas aeruginosa S2. Applied Microbiology and Biotechnology. 2007;76:67-74.

[396] Patel R, Desai A. Biosurfactant production by Pseudomonas aeruginosaGS3 from molasses. Letters in Applied Microbiology. 1997;25:91-4.

[397] Al-Bahry SN, Al-Wahaibi YM, Elshafie AE, Al-Bemani AS, Joshi SJ, Al-Makhmari HS, et al. Biosurfactant production by Bacillus subtilis B20 using date molasses and its possible application in enhanced oil recovery. International Biodeterioration & Biodegradation. 2013;81:141-6.

[398] Hippolyte MT, Augustin M, Hervé TM, Robert N, Devappa S. Application of response surface methodology to improve the production of antimicrobial biosurfactants by Lactobacillus paracasei subsp. tolerans N2 using sugar cane molasses as substrate. Bioresources and Bioprocessing. 2018;5:1-16.

[399] Makkar RS, Cameotra SS. Utilization of molasses for biosurfactant production by two Bacillus strains at thermophilic conditions. Journal of the American Oil Chemists' Society. 1997;74:887-9.

[400] Almeida DG, Soares da Silva RdCF, Meira HM, Brasileiro PPF, Silva EJ, Luna JM, et al. Production, Characterization and Commercial Formulation of a Biosurfactant from Candida tropicalis UCP0996 and Its Application in Decontamination of Petroleum Pollutants. Processes. 2021;9:885.

[401] Fanaei M, Emtiazi G. Microbial assisted (Bacillus mojavensis) production of bio-surfactant lipopeptide with potential pharmaceutical applications and its characterization by MALDI-TOF-MS analysis. Journal of Molecular Liquids. 2018;268:707-14.

[402] Pereira JF, Gudiña EJ, Costa R, Vitorino R, Teixeira JA, Coutinho JA, et al. Optimization and characterization of biosurfactant production by Bacillus subtilis isolates towards microbial enhanced oil recovery applications. Fuel. 2013;111:259-68.

[403] Nalini S, Parthasarathi R, Prabudoss V. Production and characterization of lipopeptide from Bacillus cereus SNAU01 under solid state fermentation and its potential application as anti-biofilm agent. Biocatalysis and Agricultural Biotechnology. 2016;5:123-32.

[404] Sarwar A, Hassan MN, Imran M, Iqbal M, Majeed S, Brader G, et al. Biocontrol activity of surfactin A purified from Bacillus NH-100 and NH-217 against rice bakanae disease. Microbiological research. 2018;209:1-13.

[405] Bernat P, Paraszkiewicz K, Siewiera P, Moryl M, Płaza G, Chojniak J. Lipid composition in a strain of Bacillus subtilis, a producer of iturin A lipopeptides that are active against uropathogenic bacteria. World Journal of Microbiology and Biotechnology. 2016;32:1-13.

[406] Yang H, Li X, Li X, Yu H, Shen ZJA, chemistry b. Identification of lipopeptide isoforms by MALDI-TOF-MS/MS based on the simultaneous purification of iturin, fengycin, and surfactin by RP-HPLC. 2015;407:2529-42.

[407] Vater J, Kablitz B, Wilde C, Franke P, Mehta N, Cameotra SSJA, et al. Matrix-assisted laser desorption ionization-time of flight mass spectrometry of lipopeptide biosurfactants in whole cells and culture filtrates of Bacillus subtilis C-1 isolated from petroleum sludge. 2002;68:6210-9.

[408] Lin L-Z, Zheng Q-W, Wei T, Zhang Z-Q, Zhao C-F, Zhong H, et al. Isolation and Characterization of Fengycins Produced by Bacillus amyloliquefaciens JFL21 and Its Broad-Spectrum Antimicrobial Potential Against Multidrug-Resistant Foodborne Pathogens. 2020;11:3319.

[409] Athukorala SN, Fernando WD, Rashid KYJCjom. Identification of antifungal antibiotics of Bacillus species isolated from different microhabitats using polymerase chain reaction and MALDI-TOF mass spectrometry. 2009;55:1021-32.

[410] Hong S-Y, Lee D-H, Lee J-H, Haque M, Cho K-MJM. Five Surfactin Isomers Produced during Cheonggukjang Fermentation by Bacillus pumilus HY1 and Their Properties. 2021;26:4478.

[411] Ma Y, Kong Q, Qin C, Chen Y, Chen Y, Lv R, et al. Identification of lipopeptides in Bacillus megaterium by two-step ultrafiltration and LC–ESI–MS/MS. AMB Express. 2016;6:79.

[412] Zou C, Wang M, Xing Y, Lan G, Ge T, Yan X, et al. Characterization and optimization of biosurfactants produced by Acinetobacter baylyi ZJ2 isolated from crude oil-contaminated soil sample toward microbial enhanced oil recovery applications. Biochemical Engineering Journal. 2014;90:49-58.

[413] Taira T, Yanagisawa S, Imura T. Influence of inorganic and organic counter-cations on the surface properties and self-assembly of cyclic lipopeptide surfactin. Colloids and Surfaces A: Physicochemical and Engineering Aspects. 2021;626:126973.

[414] Chandankere R, Yao J, Cai M, Masakorala K, Jain AK, Choi MM. Properties and characterization of biosurfactant in crude oil biodegradation by bacterium Bacillus methylotrophicus USTBa. Fuel. 2014;122:140-8.

Research output

Publications

1. **Rahul Verma**, L M Kundu, and L M Pandey (2021), "*Enhanced melanoidin removal by amine-modified Phyllanthus emblica leaf powder*." **Bioresource Technology**, 339, 125572.

2. **Rahul Verma**, S Sharma, L M Kundu, and L M Pandey (2020), "*Experimental investigation of molasses as a sole nutrient for the production of an alternative metabolite biosurfactant*". **Journal of Water Process Engineering**, 38, 101632.

3. **Rahul Verma**, S Sharma, L M Kundu, S K Maiti and L M Pandey (2022), "*Enhanced Production of Biosurfactant by Bacillus subtilis RSL2 in Semicontinuous Bioreactor Utilizing Molasses as A Sole Substrate*." **Journal of Biotechnology**, 362, 24-35.

4. **Rahul Verma**, L M Kundu, and L M Pandey (2021, "*Decontamination of distillery spentwash through advanced oxidation methods*." **Advanced Oxidation Processes for Effluent Treatment Plants, Elsevier**. p. 103-117.

5. **Rahul Verma**, A Jawed, V Saxena and L M Pandey (2021), "**Photocatalytic Degradation of Dyes: Current trends and future perspectives." Elsevier** 251-275.

6. S Sharma, **Rahul Verma** and L M Pandey (2019), "*Crude oil degradation and biosurfactant production abilities of isolated Agrobacterium fabrum SLAJ731."* **Biocatalysis and Agricultural Biotechnology,** 21, 101322.

7. S Sharma, **Rahul Verma**, S Dhull, S K Maiti, L M Pandey (2021), "*Biodegradation of waste cooking oil and simultaneous production of rhamnolipid biosurfactant by Pseudomonas aeruginosa P7815 in batch and fed-batch bioreactor."* **Bioprocess and Biosystems Engineering**, 45 (2), 309-319.

8. A Jawed, P Kar, **Rahul Verma**, K Shukla, P Hemanth, V K Thakur, L M Pandey and R K Gupta (2022), *"Integration of biological control with engineered heterojunction nano-photocatalysts for sustainable and effective management of water hyacinth weed."* **Journal of Environmental Chemical Engineering**, 10, 106976.

9. M Rahman, T Sarmah, P Dihingiaa, **Rahul Verma**, S Sharma, N Divesh. Kriti, N D Srivastavad, L M Pandey, and M Kakati (2021), *"Bulk synthesis of tungsten-oxide nanomaterials by a novel, plasma chemical reactor configuration, studies on their performance for wastewater treatment and hydrogen evolution reactions."* **Chemical Engineering Journal**, 428, 131111.

10. **Rahul Verma**, L M Kundu, and L M Pandey, *"Optimization of process variables of photo-Fenton degradation of melanoidins under visible/UV irradiations"* **(Under review).**

11. **Rahul Verma**, L M Kundu, and L M Pandey, *"Synthesis of WO_3 nanomaterial to enhance photocatalytic degradation of melanoidin under Visible/UV light: A kinetic insight*" **(Under review).**

Conferences, Seminars and Workshops

1. **Rahul Verma**, Lalit M. Pandey and Lal Mohan Kundu, Particle Size & Zeta Potential Measurement by Dynamic Light Scattering (DLS) & Electrophoretic Light Scattering (ELS) Techniques, Antoon Paar 2021 (Webinar).

2. **Rahul Verma**, Lalit M. Pandey and Lal Mohan Kundu, Advances and challenges in the measurement of contaminants of emerging concern (and transformation products) in environmental matrices, international PhD school on advanced oxidation Processes 2020 (Webinar).

3. **Rahul Verma**, Lalit M. Pandey and Lal Mohan Kundu, Enhanced melanoidin removal by surface-modified *Phyllanthus emblica* leaf powder as a potential low-cost bio-adsorbent. ICONN – 2021 SRM **29.**

4. **Rahul Verma**, Lalit M. Pandey and Lal Mohan Kundu, Characterization and optimization study of biosurfactant produced from molasses using isolated bacterial strain *Bacillus subtilis RSL-2*, 2nd International Conference on Bioprocess for Sustainable Environment and Energy, ICBSEE-2020 at NIT Rourkela.

5. **Rahul Verma**, Lalit M. Pandey and Lal Mohan Kundu, Photocatalytic decolorization of molasses-based spentwash using UV/ZnO/TiO_2/H_2O_2, Workshop cum Symposium on Bioinspired Nanomaterials for Environmental Applications; February 12-13, 2020, Centre for the Environment, Indian Institute of Technology Guwahati, Assam.

6. **Rahul Verma**, L M Kundu and L M Pandey. "Performance study of the UV-light/radiation-assisted reactor for melanoidin degradation: insight into the kinetics and mechanism". International Conference on Biotechnology for Sustainable Bioresources and Bioeconomy (BSBB-2022), Indian Institute of Technology Guwahati, Assam.